

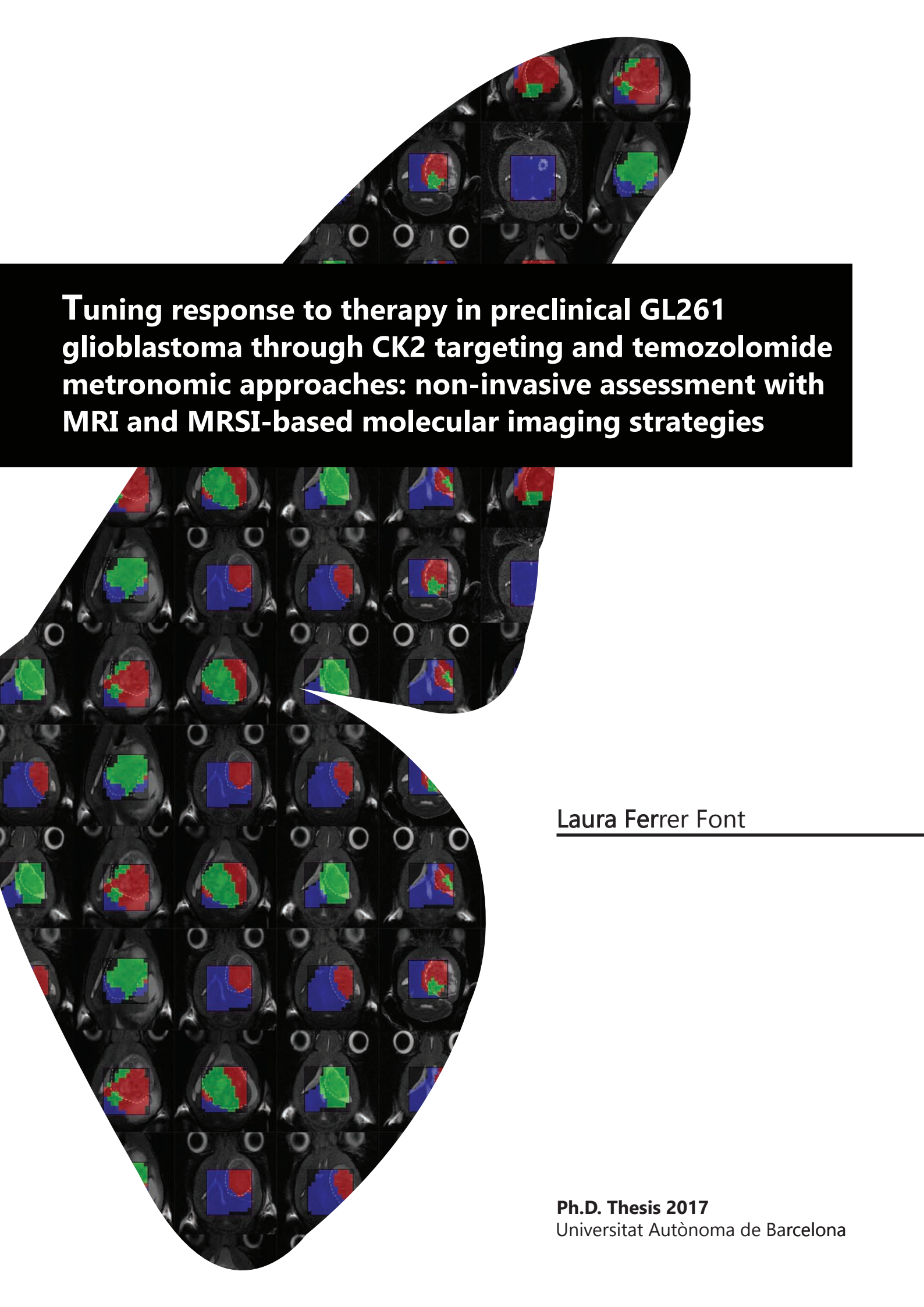


Universitat Autònoma de Barcelona

**ADVERTIMENT.** L'accés als continguts d'aquesta tesi queda condicionat a l'acceptació de les condicions d'ús establertes per la següent llicència Creative Commons:  [http://cat.creativecommons.org/?page\\_id=184](http://cat.creativecommons.org/?page_id=184)

**ADVERTENCIA.** El acceso a los contenidos de esta tesis queda condicionado a la aceptación de las condiciones de uso establecidas por la siguiente licencia Creative Commons:  <http://es.creativecommons.org/blog/licencias/>

**WARNING.** The access to the contents of this doctoral thesis it is limited to the acceptance of the use conditions set by the following Creative Commons license:  <https://creativecommons.org/licenses/?lang=en>



**Tuning response to therapy in preclinical GL261 glioblastoma through CK2 targeting and temozolomide metronomic approaches: non-invasive assessment with MRI and MRSI-based molecular imaging strategies**

Laura Ferrer Font

**Ph.D. Thesis 2017**  
Universitat Autònoma de Barcelona







**Universitat Autònoma  
de Barcelona**

Departament de Bioquímica i Biologia Molecular

**Tuning response to therapy in  
preclinical GL261 glioblastoma through  
CK2 targeting and temozolomide  
metronomic approaches: non-invasive  
assessment with MRI and MRSI-based  
molecular imaging strategies**

**Laura Ferrer Font**

**Ph. D. Thesis**

**2017**



Dissertation presented by

**Laura Ferrer Font**

Submitted for the Degree of PhD of Biochemistry, Molecular Biology and

Biomedicine at the

**Universitat Autònoma de Barcelona**

of the doctoral program in

**Biochemistry, Molecular Biology and Biomedicine**

of the department of

**Biochemistry and Molecular Biology**

supervised by

**Ph. D. Carles Arús Caraltó and Ph. D. Ana Paula Candiota**

**Signatures of the supervisors**

---

Prof. Carles Arús Caraltó

---

Ph.D. Ana Paula Candiota

**Signature of the Ph. D. thesis author**

---

Laura Ferrer Font

*Cerdanyola del Vallès, 9<sup>th</sup> February, 2017.*





*Als meus pares, qui em van donar les ales,  
em van ensenyar a volar i em van deixar volar.*

*"If you always do what you always did,  
you will always get what you always got."*

-Albert Einstein-



## ACKNOWLEDGEMENTS

Podríem dir que aquesta tesi ha estat com el procés d'elaboració d'una gran recepta, i com a tal, ha requerit de la participació de grans mestres del món de la cuina i d'ingredients exquisits de la millor qualitat del mercat.

Vull agrair als meus directors de tesi, Dr. Carles Arús i Dra. Ana Paula Candiota, que m'acceptessin com a doctoranda i que em donessin l'oportunitat de realitzar aquesta recepta de quatre anys sota la seva direcció. Ells han estat els mestres cuiners que m'han guiat i assessorat durant aquests temps i que m'han aportat coneixements i visions científiques essencials per al desenvolupament de la tesi. Per tenir èxit amb una recepta, cal planificar bé els temps de cocció, anticipar-se a preparar i coure alguns dels aliments, entre d'altres. I així ha estat, i us n'estic molt agraïda.

A tots els companys del *Grup d'Aplicacions Biomèdiques de la Ressonància Magnètica Nuclear* (GABRMN), que s'han convertit en els ingredients claus, que hagin estat al meu costat quan els he necessitat. A la Teresa, la Myriam, l'Alina, el Víctor i la Magda, que des del primer dia em guiessin i m'ensenyessin a cuinar; a la Lucía i l'Elena, les nombroses hores de debats al bar que, de ben segur, han ajudat a millorar el producte final; a la Marga, la predisposició per aportar idees per millorar la recepta i el seu bon humor, molt important per a l'ambient de la cuina; i, sobretot, a la Nuria, la cuinera que va entrar a la cuina en el mateix moment que jo, l'ajuda a preparar cada plat en tot moment —quan una feia de xef, l'altra feia d'ajudant, i viceversa—.

A la gent del Departament de Bioquímica i Biologia Molecular, especialment a l'Helena Carbó i al Salvador Bartolomé, per la seva atenció i ajuda. I al Santi i a la Magda, per l'ajuda prestada en tot moment a fer altres petites receptes preparades en paral·lel, les pràctiques. També, agrair als membres del *Servei de ressonància*, en especial a la Sílvia i al Miquel, la paciència per ensenyar-me a fer funcionar el Biospec, la màquina principal per a l'elaboració de la recepta.

Al grup de Kinasics, en especial, a la Fani, que fos la meva mentora en el món de la cuina dels Western blots (WB), i al Jordi Vilardell, un cuiner expert, la seva disposició a donar-me un cop de mà i consells que m'han estat molt útils. I, també, a l'Emili Itarte, un gran mestre cuiner de CK2, la compartició del seu coneixement. També agrair al Martí Pumarola, un ingredient important, la seva col·laboració i interès pel treball del grup i el seu assessorament en el diagnòstic histopatològic, i a l'Ester Blasco, el seu bon tracte i predisposició.

Al grup d'Itàlia, el fet de donar el punt exòtic a la recepta, i especialment a la Maria Ruzzene, la qual va dirigir d'una manera exhaustiva el treball; al Daniele, poder compartir tots els dinars de tupper a la vora del riu, i a tota la colla de post-docs, que em van fer sentir com a casa. *Grazzie mille per tutto!*

A tots els companys del *bus sharing*, que hagin estat el maridatge de la recepta (cafès als viatges d'anada i cerveses, als de tornada). Amb ells, els viatges a la UAB han estat molt agradables. Gràcies nois!

Qualsevol plat en l'alta gastronomia cal que estigui molt ben presentat perquè entri pels ulls del consumidor; així doncs, gràcies, Carles, per la portada de la tesi, per haver entès tan bé què volia sense tenir ni idea del tema.

Vull agrair a totes les espècies (julivert, pebre, orenga...), imprescindibles per a una recepta gustosa, com l'escoltisme i tots els meus companys de viatge de l'equip de la taula permanent d'on he format part aquests 3 anys, que entenguessin que la tesi passava per davant, que vinguessin a fer reunions als bancs de fora de la UAB quan jo havia de passar ratolins, i que m'obliguessin a no oblidar que la vida no només passava dins la cuina. Els lemes de l'escoltisme, *Tant com puc* i *Sempre a punt*, han estat directrius claus per a l'elaboració d'aquesta recepta. I, també, a tots els amics i amigues per fer-me sortir de la cuina els caps de setmana, i haver-me ajudat a distreure anant a la muntanya per tornar els dilluns amb energia per continuar cuinant.

Vull fer un agraïment molt especial a la meva família, per estar incondicionalment al meu costat, perquè, sense ells, no existiria la recepta. Als meus avis, per haver tingut la sort de créixer al seu costat i haver pogut aprendre'n tantes coses. Al meu tiet, per estar sempre disposat a donar-me un cop de mà. Al meu germà, per haver-me fet sempre la guitza i aconseguir, així, que fos millor persona. I, sobretot, als meus pares, per ser el mirall en què intento reflectir-me cada dia. Per últim, vull agrair al Mario *tot* el que ha fet per al *nostre doctorat* durant aquests anys, no solament m'ha animat i aguantat quan les forces defallien, sinó que s'ha tornat un expert en el tema i m'ha donat consells en tot moment perquè fes més i millor.

A tots, gràcies, moltes gràcies, per haver fet possible aquesta gran recepta i haver-me acompanyat durant tot el seu procés d'elaboració.

**TABLE OF CONTENTS**

<b>ABBREVIATIONS .....</b>	<b>XI</b>
<b>1 INTRODUCTION .....</b>	<b>1</b>
<b>1.1 BRAIN TUMORS .....</b>	<b>1</b>
1.1.1 Epidemiology, classification and etiology .....	1
1.1.2 Genetic pathways in GBM progression .....	4
1.1.3 Relevance of cancer stem cells (CSCs) in cancer progression .....	6
1.1.4 Brain tumor diagnosis .....	10
1.1.5 GBM therapy .....	11
<i>1.1.5.1 Surgical resection .....</i>	<i>12</i>
<i>1.1.5.2 Radiotherapy (RT).....</i>	<i>13</i>
<i>1.1.5.3 Chemotherapy.....</i>	<i>15</i>
<i>1.1.5.4 Evidence of the immune system role in response to therapy.....</i>	<i>19</i>
<i>1.1.5.5 Other therapeutic strategies .....</i>	<i>25</i>
<b>1.2 PROTEIN CASEIN KINASE CK2 (CK2) .....</b>	<b>27</b>
1.2.1 Structure of CK2 .....	27
1.2.2 Regulation of CK2 activity in cells.....	31
<i>1.2.2.1 Expression and assembly.....</i>	<i>31</i>
<i>1.2.2.2 Protein-protein regulatory interactions .....</i>	<i>32</i>
<i>1.2.2.3 CK2 phosphorylation .....</i>	<i>32</i>
1.2.3 The localization of CK2 subunits.....	33
1.2.4 CK2 and cancer .....	33

1.2.4.1 Role of CK2 in cell cycle and cell division .....	33
1.2.4.2 Function of CK2 in cell survival and apoptosis.....	34
1.2.4.3 CK2 and Epithelial-Mesenchymal Transition (EMT) .....	35
1.2.4.4 CK2 in angiogenesis.....	36
1.2.4.5 CK2 and signalling pathways.....	38
1.2.5 CK2 as a therapeutic target .....	41
<b>1.3 PRECLINICAL MODELS OF GBM.....</b>	<b>44</b>
<b>1.4 NUCLEAR MAGNETIC RESONANCE (NMR).....</b>	<b>47</b>
1.4.1 Basic concepts and relevant parameters .....	47
1.4.1.1 Relaxation times.....	51
1.4.2 Biomedical applications of NMR in cancer.....	54
1.4.2.1 Magnetic resonance imaging (MRI).....	54
1.4.2.2 Magnetic resonance spectroscopy (MRS) and Magnetic Resonance Spectroscopic Imaging (MRSI).....	58
1.4.2.3 Pattern recognition (PR) analysis of NMR data.....	63
1.4.3 Nosological imaging of the response to therapy .....	65
<b>2 GENERAL OBJECTIVES .....</b>	<b>67</b>
<b>3 GENERAL MATERIALS AND METHODS .....</b>	<b>69</b>
<b>3.1 GL261 cells.....</b>	<b>69</b>
3.1.1 Cell count.....	70
<b>3.2 Animal Model (GL261 cells growing into C57BL/6 mouse).....</b>	<b>70</b>
3.2.1 Generation of tumors by stereotactic injection of cells.....	71

---

<b>3.3 Tissue preservation for post-mortem procedures .....</b>	<b>73</b>
<b>3.4 <i>In vivo</i> MRI/MRS/MRSI .....</b>	<b>73</b>
3.4.1 MRI acquisition.....	74
3.4.1.1 Tumor volume calculation from MRI acquisitions.....	74
3.4.2 MRS/MRSI .....	75
<b>4 RESULTS .....</b>	<b>77</b>
<b>4.1 CK2 CONTENT IN GBM .....</b>	<b>77</b>
4.1.1 Specific objectives .....	77
4.1.2 Specific materials and methods .....	77
4.1.3 Results .....	79
4.1.4 Discussion.....	81
4.1.5 Conclusion .....	82
<b>4.2 TARGETING PROTEIN KINASE CK2: EVALUATING CX-4945 POTENTIAL FOR GL261 GLIOBLASTOMA THERAPY IN IMMUNOCOMPETENT MICE .....</b>	<b>83</b>
4.2.1 Specific objectives .....	83
4.2.2 Specific materials and methods .....	83
4.2.3 Results .....	92
4.2.4 Discussion.....	105
4.2.5 Conclusions.....	111
<b>4.3 CYCLOPHOSPHAMIDE AND TEMOZOLOMIDE METRONOMIC TREATMENT IN IMMUNOCOMPETENT MICE: POTENTIAL FOR GL261 GLIOBLASTOMA TREATMENT</b>	<b>113</b>
4.3.1 Specific objectives .....	113

4.3.2 Specific materials and methods .....	113
4.3.3 Results .....	121
4.3.4 Discussion.....	132
4.3.5 Conclusions.....	142
<b>5 GENERAL DISCUSSION.....</b>	<b>143</b>
<b>6 GENERAL CONCLUSIONS .....</b>	<b>153</b>
<b>7 BIBLIOGRAPHY .....</b>	<b>155</b>
<b>8 ANNEXES .....</b>	<b>173</b>
<b>8.1 ANNEX 1: SUPERVISION OF LABORATORY ANIMALS .....</b>	<b>173</b>
<b>8.2 ANNEX 2: Article “Protein kinase CK2 content in GL261 mouse glioblastoma” ..</b>	<b>175</b>
<b>8.3 ANNEX 3: Article “Improving Ribosomal RNA Integrity in Surgically Resected Human Brain Tumor Biopsies” .</b>	<b>181</b>



**INDEX OF FIGURES**

<b>Figure 1.1</b> Distribution of malignant primary brain and CNS tumors by histology subtypes. ....	4
<b>Figure 1.2</b> Genetic changes pathways leading to primary and secondary GBM .....	5
<b>Figure 1.3</b> Two models for tumor heterogeneity and propagation in solid tumors.....	8
<b>Figure 1.4</b> Management for diagnostic and treatment of GBM.....	12
<b>Figure 1.5</b> Direct and indirect actions of radiation .....	14
<b>Figure 1.6</b> TMZ activation and resistance pathways scheme. ....	17
<b>Figure 1.7</b> Scheme of the immune system actuation .....	19
<b>Figure 1.8</b> Scheme of the cycle for immune response against a tumor .....	21
<b>Figure 1.9</b> Crystal structure of the CK2 holoenzyme. ....	28
<b>Figure 1.10</b> Cellular mechanisms involved in angiogenesis in GBM .....	37
<b>Figure 1.11</b> iCK2s molecular structures .....	42
<b>Figure 1.12</b> Preclinical cancer models scheme. ....	45
<b>Figure 1.13</b> Diagram representing a magnetic moment of a nucleus .....	48
<b>Figure 1.14</b> Effect of an external magnetic field ( $B_0$ ) on the magnetic moments of a sample...	48
<b>Figure 1.15</b> Representation of the perturbation of the macroscopic magnetization of a sample in a coordinate system. ....	50
<b>Figure 1.16</b> Free induction decay (FID) transformation.....	50
<b>Figure 1.17</b> Diagram showing the process of $T_1$ relaxation. ....	51
<b>Figure 1.18</b> Diagram showing the process of $T_2$ relaxation .....	53
<b>Figure 1.19</b> Mice brain MRI in axial orientation .....	55
<b>Figure 1.20</b> Spin-Echo (SE) pulse sequence for acquisition of diffusion weighted imaging .....	57

<b>Figure 1.21</b> Apparent diffusion coefficient (ADC) maps and T <sub>2w</sub> axial images.....	58
<b>Figure 1.22</b> Scheme of the magnetic field scanned from left to right, from low to high values	60
<b>Figure 1.23</b> Representative SV spectra. ....	63
<b>Figure 1.24</b> Examples of nosological semi-supervised maps .....	66
<b>Figure 3.1</b> Scheme for unique identification in mice by ear punching. ....	71
<b>Figure 3.2</b> A C57BL/6 mouse immobilized in a stereotactic holder. ....	72
<b>Figure 3.3</b> Scheme of the tumor volume measurement.....	74
<b>Figure 4.1</b> CK2 WB quantification in GL261 GBM compared to contralateral parenchyma and control mice .....	80
<b>Figure 4.2</b> Therapy administration scheme protocols .....	90
<b>Figure 4.3</b> GL261 cells viability after treatment.....	93
<b>Figure 4.4</b> CK2 activity in GL261 cells and tumor samples.....	95
<b>Figure 4.5</b> Mice body weight (MTD studies) .....	97
<b>Figure 4.6</b> Tumor volumes, survival rate and CK2 activity and expression in CX-4945 treated mice. ....	99
<b>Figure 4.7</b> Body weight averages of treated and control mice .....	100
<b>Figure 4.8</b> MRI of CX-4945 treated mice.....	101
<b>Figure 4.9</b> Tumor volume and Kaplan-Meier survival curve of mice treated with TMZ combined with CX-4945. ....	103
<b>Figure 4.10</b> Survival Kaplan-Meier curve for 3 cycles of TMZ vs. control. ....	103
<b>Figure 4.11</b> Tumor volumes and survival rate for 6-day metronomic treatment.....	104
<b>Figure 4.12</b> Tumor and edema volumes of mice treated with TMZ .....	119
<b>Figure 4.13</b> Tumor volumes, survival rate and nosological images of mice treated with CPA.	122

**Figure 4.14** Body weight of mice from different experimental groups ..... 123

**Figure 4.15** Tumor volumes and Kaplan-Meier curve of control mice and metronomic TMZ treated mice ..... 125

**Figure 4.16** Examples of volume evolution follow-up and MRSI acquisitions ..... 128

**Figure 4.17** Coronal  $T_{2w}$  MRI of “cured” mice from TMZ 140 mg/Kg metronomic therapy treatment ..... 129

**Figure 4.18** Tumor and edema volume evolution ..... 130

**Figure 4.19** Example of thymic lymphoma appearance in one mouse treated with TMZ metronomic 140 mg/Kg ..... 131

**Figure 4.20** Correlation between volume at therapy starting point ..... 135

**Figure 4.21** Responding pattern average spectra after semi-supervised source analysis ..... 136

**Figure 5.1** Relationship between tumor volume evolution and nosological images obtained 149



**INDEX OF TABLES**

<b>Table 1.1</b> Summary of the most important metabolite resonances that can be found in human brain in vivo <sup>1</sup> H spectra at 1.5T in human brain .....	61
<b>Table 4.1</b> Normalized values of CK2 expression levels. ....	80
<b>Table 4.2</b> Average ± standard deviation (AV ± SD) for tumor volume (mm <sup>3</sup> ) and body weight (g) for mice before starting CX-4945 therapy every day .....	86
<b>Table 4.3</b> Average ± standard deviation (AV± SD) for tumor volume (mm <sup>3</sup> ) and body weight (g) for mice before starting CX-4945 therapy in alternated days .....	86
<b>Table 4.4</b> Average ± standard deviation (AV± SD) for tumor volume (mm <sup>3</sup> ) and body weight (g) for mice before starting combined TMZ±CX-4945 therapy .....	86
<b>Table 4.5</b> Average ± standard deviation (AV± SD) for tumor volume (mm <sup>3</sup> ) and body weight (g) for mice before starting metronomic therapy .....	87
<b>Table 4.6</b> Doses for CX-4945, TDB and TMZ administration in MTD calculation experiments...	88
<b>Table 4.7</b> Symptoms and signals guidance to decide the MTD .....	88
<b>Table 4.8</b> Average ± standard deviation (AV±SD) for tumor volume (mm <sup>3</sup> ) and body weight (g) for mice before starting therapy, at day 8 p.i. ....	114
<b>Table 4.9</b> Treatments performed with CPA and TMZ therapy.....	115



**ABBREVIATIONS**

<b>ADC</b>	Apparent diffusion coefficient
<b>ALDH</b>	Aldehyde dehydrogenase
<b>APC</b>	Antigen presenting cells
<b>APG</b>	Apigenin
<b>AS</b>	Surface area
<b>ASCII</b>	American Standard Code for Information Interchange
<b>ATP</b>	Adenosine triphosphate
<b>BBB</b>	Blood–brain barrier
<b>BER</b>	Base excision repair
<b>B<sub>0</sub></b>	External magnetic field
<b>CA</b>	Contrast agent
<b>CD5</b>	Cluster of differentiation 5
<b>CK2</b>	Casein Kinase 2
<b>c-Myc</b>	Myc proto-oncogene protein
<b>CNS</b>	Central nervous system
<b>CPA</b>	Cyclophosphamide
<b>CSCs</b>	Cancer stem cells
<b>CT</b>	Computed tomography
<b>CTL</b>	Cytotoxic T-lymphocytes
<b>CX-4945</b>	5-(3-Chlorophenylamino)benzo[c][2,6] naphthyridine-8-carboxylic acid
<b>DC</b>	Dendritic cell
<b>DMSO</b>	Dimethyl sulfoxide
<b>DNA</b>	Deoxyribonucleic acid
<b>DSB</b>	Double-strand break
<b>DWI</b>	Diffusion weighted imaging
<b>EC<sub>50</sub></b>	Half maximal effective concentration
<b>EDTA</b>	Ethylenediaminetetraacetic acid
<b>EGFR</b>	Epidermal growth factor receptor
<b>EMT</b>	Epithelial-to-mesenchymal transition
<b>ERK</b>	Extracellular signal-regulated kinase
<b>ETL</b>	Echo train length
<b>FID</b>	Free induction decay
<b>FOV</b>	Field of view

<b>FT</b>	Fourier transform
<b>GABRMN</b>	Grup d'Aplicacions Biomèdiques de la Ressonància Magnètica Nuclear
<b>GBM</b>	Glioblastoma
<b>GEM</b>	Genetically engineered mouse
<b>Gln</b>	Glutamine
<b>Glu</b>	Glutamate
<b>GSK3<math>\beta</math></b>	Glycogen synthase kinase 3 $\beta$
<b>HE</b>	Hematoxylin-Eosin
<b>HIF-1<math>\alpha</math></b>	Hypoxia-inducible factor 1-alpha
<b>HR</b>	High resolution
<b><math>^1\text{H}</math></b>	Proton
<b>iCK2</b>	CK2 inhibitor
<b>IC<sub>50</sub></b>	Half maximal inhibitory concentration
<b>IDH</b>	Isocitrate dehydrogenase
<b>IL</b>	interleukin
<b>IR</b>	Ionizing radiation
<b>IT</b>	inter-slice thickness
<b>JAK</b>	Janus kinase
<b>LDA</b>	Linear Discriminant Analysis
<b>LN</b>	Lymph node
<b>LOH</b>	Loss of heterozygosity
<b>MGMT</b>	O6-methylguanine-DNA-methyltransferase
<b>mi</b>	Myo-inositol
<b>MMR</b>	Mismatch repair
<b>MR</b>	Magnetic resonance
<b>MRI</b>	Magnetic resonance imaging
<b>MRS</b>	Magnetic Resonance Spectroscopy
<b>MRSI</b>	Magnetic resonance spectroscopic imaging
<b>MTD</b>	Maximum tolerated dose
<b>MTIC</b>	Methyl-triazeno imidazole-carboxamide
<b>MTX</b>	Matrix size
<b>MV</b>	Multi-voxel
<b>Mxy</b>	Transversal plane of magnetization
<b>Mz</b>	Longitudinal plane of magnetization
<b>NA</b>	Number of averages



<b>NF-kB</b>	Nuclear factor kappa-light-chain-enhancer of activated B cells
<b>NMF</b>	Non-negative matrix factorization
<b>NMR</b>	Nuclear Magnetic Resonance
<b>NS</b>	Number of slices
<b>NSCs</b>	Neural stem cells
<b>N3-MeA</b>	N3-methyl-adenine
<b>N7-MeG</b>	N7-methyl-guanine
<b>OA</b>	Oligoastrocytoma
<b>ODG</b>	Oligodendroglioma
<b>O6-MeG</b>	O6-methyl-guanine
<b>PBS</b>	Phosphate buffered saline
<b>PDGF</b>	Platelet-derived growth factor
<b>PDGFR</b>	Platelet-derived growth factor receptor
<b>p.i.</b>	post-inoculation
<b>PIM-1</b>	Proviral Integration of Moloney virus
<b>Pin-1</b>	Peptidyl-prolyl cis-trans isomerase NIMA-interacting 1
<b>PI3K</b>	Phosphatidylinositol 3-kinase
<b>ppm</b>	Part per million
<b>PR</b>	Pattern recognition
<b>PRH</b>	Proline-Rich-Homeo
<b>PTBE</b>	Peritumoral brain edema
<b>PTEN</b>	Phosphatase and tensin homolog
<b>PUFAs</b>	Polyunsaturated fatty acids
<b>PVDF</b>	Polyvinylidene fluoride
<b>RARE</b>	Rapid acquisition with relaxation enhancement
<b>RF</b>	Radiofrequency
<b>ROI</b>	Region of interest
<b>RPMI</b>	Roswell Park Memorial Institute
<b>RT</b>	Radiotherapy
<b>SCs</b>	Stem cells
<b>SDS-PAGE</b>	Sodium dodecyl sulfate polyacrylamide gel electrophoresis
<b>SE</b>	Spin-echo
<b>Ser</b>	Serine
<b>SSB</b>	Single-strand break
<b>ST</b>	Slice thickness

<b>STAT</b>	Signal transducer and activator of transcription
<b>SV</b>	Single voxel
<b>TAT</b>	Total acquisition time
<b>TBB</b>	4,5,6,7-Tetrabromobenzotriazole
<b>TDB</b>	Tetra-bromo-deoxyribofuranosyl-benzimidazole
<b>TE</b>	Echo time
<b>TE<sub>eff</sub></b>	Effective echo time
<b>Thr</b>	Threonine
<b>TMZ</b>	Temozolomide
<b>TNF<math>\alpha</math></b>	Tumor necrosis factor $\alpha$
<b>T-PBS</b>	Tween phosphate buffered saline
<b>TP53</b>	Tumor protein P53
<b>T<sub>2w</sub></b>	T <sub>2</sub> -weighted
<b>TR</b>	Recycling time
<b>UV</b>	Ultraviolet
<b>VEGF</b>	Vascular endothelial growth factor
<b>VEGFR</b>	Vascular endothelial growth factor receptor
<b>WB</b>	Western blot
<b>WHO</b>	World health organization
<b>wt</b>	Wild type
<b>2D</b>	Two dimensional
<b>3D</b>	Three dimensional

## 1 INTRODUCTION

### 1.1 BRAIN TUMORS

#### 1.1.1 Epidemiology, classification and etiology

Tumors of the central nervous system (CNS) comprise around 1.8% of all cancer cases diagnosed each year worldwide. Still, they account for a higher mortality rate percentage of 2.3% among all cancer patients [1] in comparison with other tumors, for which mortality is lower than incidence, such as breast or colorectal cancer.

Among CNS tumors, brain tumors are a common designation for tumors arising in intracranial regions: brain itself (neurons, glial cells, lymphatic tissue or blood vessels), cranial nerves (Schwann cells), brain envelopes (meninges), skull, pituitary and pineal gland. These tumors, which originate in the brain, are called primary brain neoplasms. Secondary brain neoplasms, on the other hand, have a metastatic origin, and can derive, for example, from lung cancer, breast, melanomas, colorectal and kidney cancers, mainly [2, 3]. While primary brain tumors are named for cell type of origin or its location in the brain, the secondary brain tumors are named after the organ or the tissue in which they arose.

The tumors of CNS are classified according to criteria published by World Health Organization (WHO) 2007 [4] and, more recently, WHO 2016 [5], based on the type and location of the originating cells, while the degree of malignancy is characterized by the grade. The grade of a tumor is established taking into account essentially four histopathological criteria: mitotic activity, nuclear atypia, endothelial hyperplasia and necrosis. These characteristics describe how abnormal the cancer cells are and how quickly the tumor is likely to grow and spread, determining the patient survival probability. There are four grades of malignancy:

- **Grade I:** tumors that have low proliferative potential, diffused nature and the possibility of cure following surgical resection alone (e.g. pilocytic astrocytoma).

- **Grade II:** infiltrating tumors with low mitotic activity and potential of recurrence after surgery; most tend to progress to higher grades of malignancy (e.g. astrocytomas and oligodendrogliomas (ODGs)).
- **Grade III:** tumors with present histological evidence of malignancy, such as nuclear atypia, elevated mitotic activity, clearly expressed infiltrative capabilities and anaplasia (e.g. anaplastic ODG).
- **Grade IV:** tumors that are cytologically malignant, mitotically active with vascular proliferation, necrosis and are generally associated with a rapid preoperative and postoperative progression of disease and fatal outcome. Still, widespread infiltration of surrounding tissue characterizes some grade IV neoplasms. (e.g. glioblastoma (GBM)).

The most common primary brain tumors are gliomas, neoplasms that arise from glial cells, accounting for 27% of CNS tumors and 80% of malignant CNS tumors [6]. Gliomas are classified according to different parameters:

- Their presumed *cell of origin* (which include astrocytomas, derived from astrocytes; ODGs, derived from oligodendrocytes; and oligoastrocytomas (OAs), derived from astrocytes and/or oligodendrocytes)
- Their *location* (supratentorial, in the cerebrum, and infratentorial, in the cerebellum)
- The *extent of brain infiltration* (circumscribed or diffusely infiltrating)
- Their *grade of malignancy*

Astrocytomas make up the most frequent gliomas and represent 33.3% of all newly diagnosed brain tumor cases [7]. They can be divided into: pilocytic astrocytoma (grade I), low-grade diffuse astrocytomas (grade II) and anaplastic astrocytomas (grade III). ODGs have a less favourable prognosis than diffuse astrocytomas, but also less likely to progress to more

aggressive stages. The incidence rate of OAs can vary from 1.8% to 19% among all gliomas and this variation is due to different diagnosis criteria among laboratories, as they are often confused with ODGs and astrocytomas. In the new report of WHO 2016, it is offered a more precise way to differentiate between them based on using both genotype (i.e. Isocitrate dehydrogenase (IDH) mutation and 1p/19q codeletion status) and phenotype [5]. The prognosis and malignancy depends on the proportions of the different cell types that constitute these mixed oligoastrocytic tumors.

The most common of all malignant primary brain tumors is GBM (46.1%) [6] (Figure 1.1), and with a grade of IV, it is the most malignant and aggressive form of glioma. The average survival of GBM patients is of 14-15 months, even when an aggressive treatment is applied [8, 9]. Moreover, malignant brain tumours such as GBM have devastating social effects, presenting the highest mean when measuring the “Years of potential life lost (YPLL)” [10], which is an estimation of how much a patient’s life is likely to be shortened by his or her cancer, especially relevant in case of young patients. Temozolomide (TMZ) plus radiotherapy (RT) is the standard therapeutic choice for GBM treatment producing, at present, the best survival rates [11] (more details will be found in section 1.1.5.3 and 1.1.5.2, respectively). The histopathological features of GBM include: nuclear atypia, cellular pleomorphism, vascular thrombosis, microvascular proliferation and necrosis, and is characterized by a diffuse tissue-distribution pattern, with extensive dissemination of the tumor cells within the brain that hampers complete surgical resection. To date, routine screening for early detection of brain tumors is not currently available, as it is for some common cancers (e.g, prostate, breast, colorectal...). Given the poor GBM prognosis, there is an urgent need of developing better GBM treatments and to improve non-invasive detection techniques.

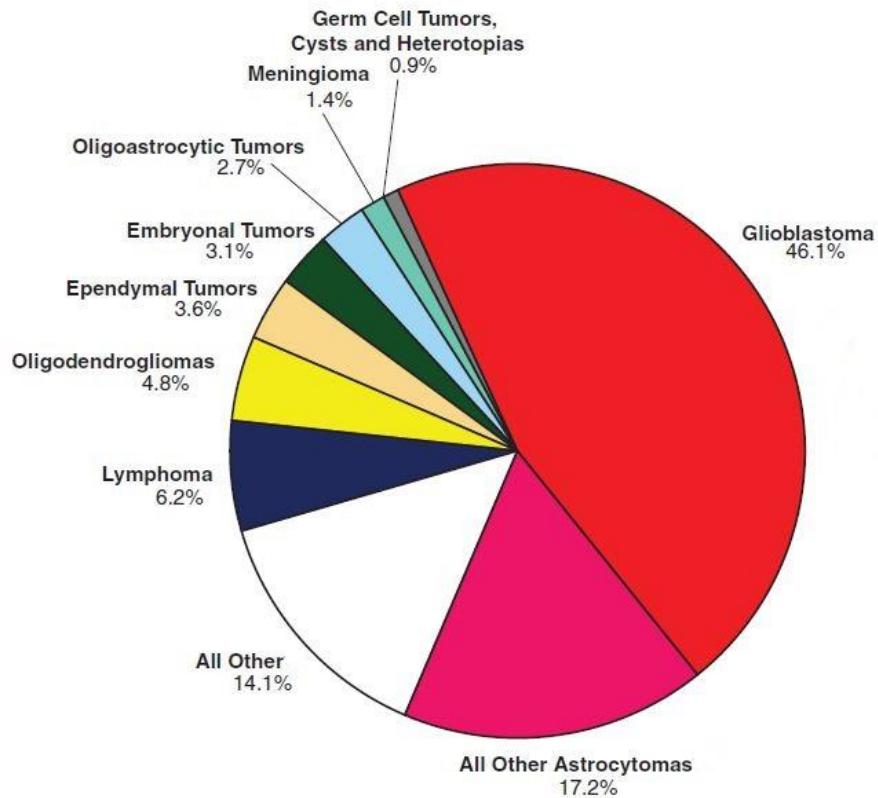


**Figure 1.1** Distribution of malignant primary brain and CNS tumors by histology subtypes (CBTRUS statistical Report 2007-2011). Modified from [6].

### 1.1.2 Genetic pathways in GBM progression

Mainly, two pathways of glioma development have been identified: primary GBM that arise *de novo* without lower grade precursors, or astrocytomas which start as grade II or III and then progress into secondary GBM, and ODGs that can transform into anaplastic ODG, both finally evolving into secondary GBM (Figure 1.2). GBMs can be alternatively divided following the 2016 CNS WHO classification [5] into (1) GBM, IDH wild type (wt) (about 90% of cases), which corresponds most frequently with the clinically defined primary or *de novo* GBM and predominates in patients over 55 years of age and (2) GBM, IDH-mutant (about 10% of cases), which mainly corresponds closely to the so-called secondary GBM, with a history of prior lower grade diffuse glioma and preferentially arising in younger patients.

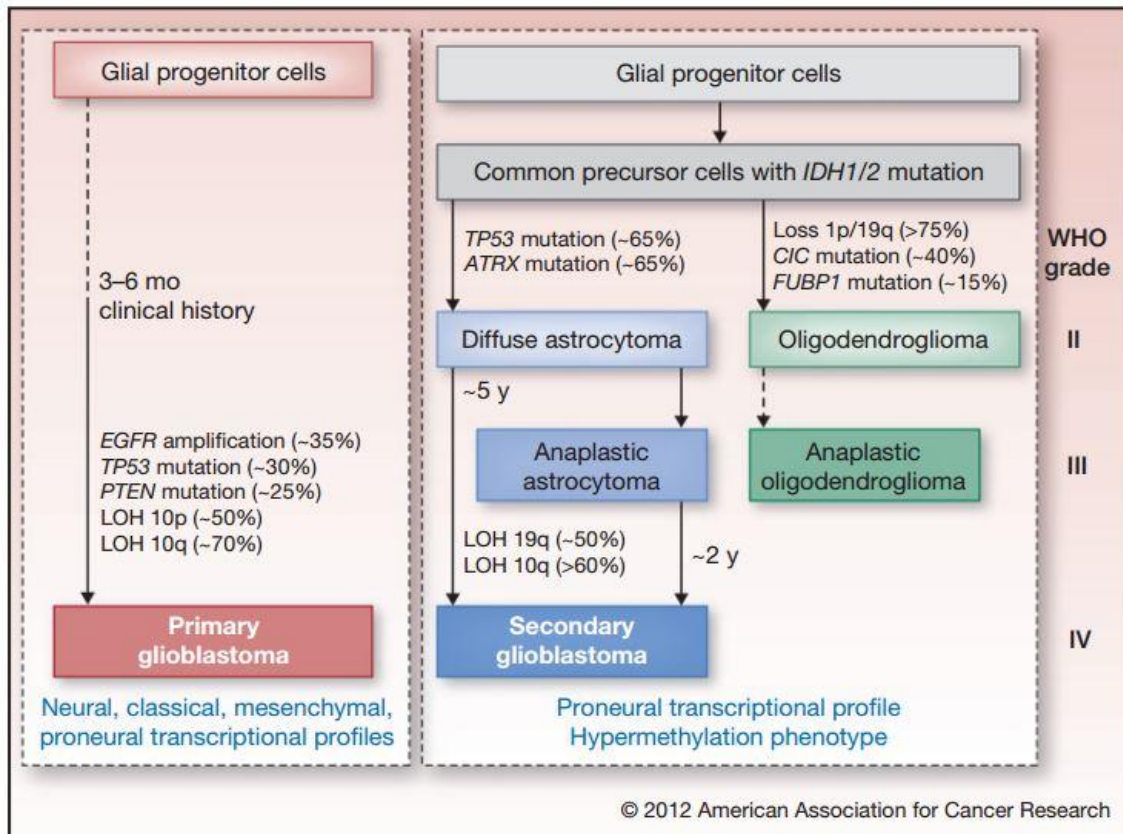


**Figure 1.2 Genetic changes pathways leading to primary and secondary GBM.** ATRX: transcriptional regulator ATRX, CIC: protein capicua homolog, EGFR: epidermal growth factor receptor, FUBP1: Far Upstream Element Binding Protein 1, LOH: loss of heterozygosity, PTEN: phosphatase and tensin homolog and TP53: tumor protein P53. Taken from [12].

Cancer development is a multistep process and morphologic changes observed during the process of malignant transformation reflect the sequential acquisition of genetic alterations [13]. It has been suggested that between four and seven independent alterations must occur within a normal somatic cell before a cancerous phenotype results [14]. These genetic alterations, that drive the development and progression of malignancies, include deoxyribonucleic acid (DNA) sequence changes; copy number aberrations, chromosomal rearrangements and modification in DNA methylation. Some alterations associated with primary and secondary GBM are presented in Figure 1.2; it is worth noting that, on the basis of histopathological criteria, it is impossible to distinguish a secondary GBM a from a primary one with a single time point sampling.

Primary GBMs are characterized by epidermal growth factor receptor (EGFR) gene amplification and mutation; loss of heterozygosity (LOH) of chromosome 10q containing phosphatase and tensin homolog (PTEN); overexpression of murine double minute 2 (MDM2); and deletion of p16. The hallmarks of secondary GBMs include mutations of tumor protein P53 (TP53) and retinoblastoma (RB); overexpression of platelet-derived growth factor A and platelet-derived growth factor receptor alpha (PDGFA/PDGFR $\alpha$ ) and LOH of 19q [15, 16]. Moreover, these alterations tend to occur in a defined order during the progression to a high-grade tumor: the TP53 mutation seems to be a relatively early event during the development of an astrocytoma, whereas the loss or mutation of PTEN and amplification of EGFR are characteristic of higher-grade tumors [17].

The nicotinamide adenine dinucleotide phosphate (NADP<sup>+</sup>)-dependent IDH1 and IDH2 play functions in cellular metabolism in lipid synthesis, cellular defence against oxidative stress, oxidative respiration, and oxygen-sensing signal transduction. Although the molecular pathogenesis of IDH1 and IDH2 mutations in the development of gliomas is still unclear, several theories have been proposed, including: increased angiogenesis due to accumulation of hypoxia-inducible factor 1-alpha (HIF-1 $\alpha$ ) [18] and increased vulnerability to oxidative stress because of depletion of antioxidants [19]. IDH1 or IDH2 have been found mutated in the vast majority of WHO grade II or III gliomas and in the secondary GBMs that develop from these precursors [20]. Patients with driver mutations in the IDH1 and IDH2 of their GBM have improved prognosis compared to gliomas with wild-type IDH [21]. Lately, a very important effect seems to be inhibition of DNA demethylases by the generated onco-metabolite 2-oxoglutarate of DNA demethylases [22].

### **1.1.3 Relevance of cancer stem cells (CSCs) in cancer progression**

Stem cells (SCs) are defined as cells that have the ability to perpetuate themselves through self-renewal and to generate mature cells of a particular tissue through stepwise



differentiation. Increasing evidence, from hematopoietic malignancies and solid tumors (including brain), has strongly supported the concept that only subpopulation of cancer cells in each tumor has the capability of cancer initiation and repopulation [23–25]. These cells have been called CSCs because they share some characteristics with normal SCs, including the capacity of self-renewal, multi-lineage differentiation, and maintained proliferation [26]. The origins of CSCs within tumors have not been clarified and may vary from one tumor type to another. In some tumors, normal tissue SCs may serve as the cells-of-origin that undergo oncogenic transformation to yield CSCs; in others, they may arise from restricted progenitor cells or more differentiated cells that have suffered oncogenic transformation and acquiring more “stem-like” character [27].

There is evidence that cancer arises from a series of the oncogenic and tumor suppressor mutations (see Section 1.1.2) that occurs in few or even a single founder cell, defining cancer as a DNA-associated disease. Tumor cells eventually acquire unlimited and uncontrolled proliferation potential that drive tumor progression forward [14]. Two hypothetical models exist, which can explain this phenomenon (Figure 1.3).

Traditionally, cancer cells within tumors were portrayed as heterogeneous cell populations due to distinct clonal subpopulations, reflected in histopathological diversity and containing regions of various degrees of differentiation, proliferation, vascularity, inflammation, and/or invasiveness [28], considering that all the cells in a tumor would have a similar tumorigenic potential to proliferate extensively to form new tumors (Figure 1.3A) [29]. Afterwards, however, a hierarchical model emerged (Figure 1.3B), pointing to the existence of a new dimension of intratumor heterogeneity and a subset of cells within the tumor that have significant proliferation capacity and the ability to generate new tumors, termed CSCs, with the remainder of the tumor cells representing terminally differentiated cells [26]. The essential difference between these possibilities is the prediction, according to the second possibility,

that whatever the environment or mutational status of the cells, only a small, phenotypically distinct subset cells has the ability to proliferate extensively or form a new tumor. Although considerable controversy remains as to which tumor types are hierarchically organized and how to define CSCs, this developmental and/or hierarchical model has generated considerable interest because CSCs appear to possess properties that make them clinically relevant.

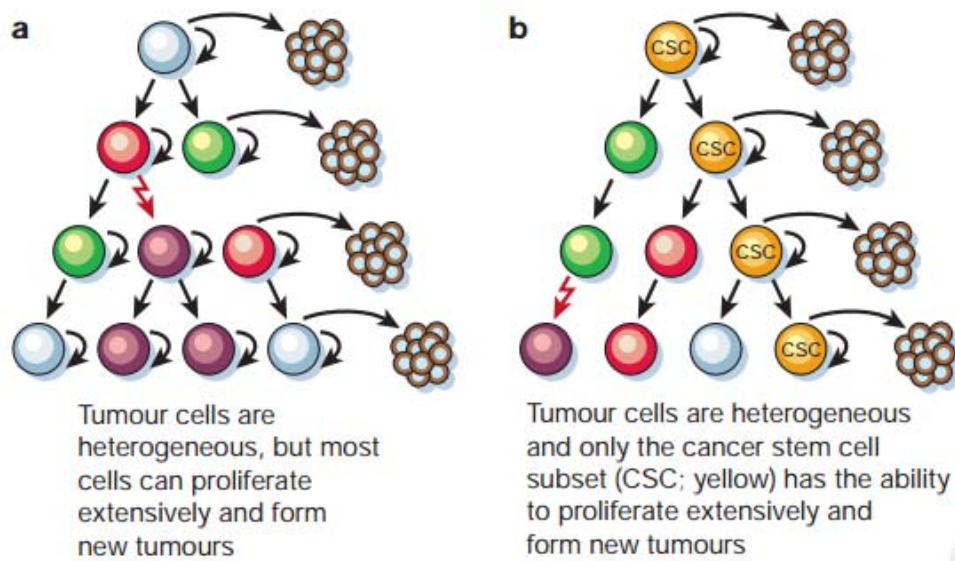


**Figure 1.3 Two models for tumor heterogeneity and propagation in solid tumors. a)** In the clonal evolution model all undifferentiated cells have similar tumorigenic capacity. **b)** In the cancer stem cells (CSCs) model, most cancer cells only limited proliferative potential and only a subset of cancer cells consistently proliferate extensively in clonogenic assays and can form new tumors on transplantation [30, 31]. CSCs can generate a tumor, based on their self-renewal properties and enormous proliferative potential. Extracted from [26].

SCs and their more differentiated progeny express a variety of markers, ranging from surface markers to transcription factors, thus, SCs and CSCs share many common marker genes [32], making it possible to identify and isolate CSCs. Currently, the marker-based flow cytometry (FCM) and magnetic cell sorting (MACS) techniques are the most effective cell isolating methods. For characterizing GBM CSCs, some of the usually accepted enrichment markers are

CD133, nestin, signal transducer and activator of transcription (STAT3) and Myc proto-oncogene protein (c-Myc), among others.

Evidence from both experimental models and clinical studies indicate that CSCs survive many commonly employed cancer therapeutics, being resistant to chemotherapy and RT [33, 34] (see also sections 1.1.5.2 and 1.1.5.3).

The lack of persistent response of GBM tumors to therapy is probably due to the existence of GBM CSCs within the tumor which are not depleted by classical therapies, being crucial for driving invasive tumor growth and relapse [35]. GBM CSCs have been demonstrated to also have the potential to differentiate into astrocytes, oligodendrocytes and neurons [24]. Although the origin of GBM CSCs is not clearly defined, GBM CSCs share similar properties with normal neural stem cells (NSCs) that endow these cells with key traits of carcinogenesis, including enhanced potentials of proliferation, angiogenesis and invasion. Thus, initiation and recurrence of primary GBM may be caused by a subpopulation of GBM CSCs which may derive from mutated NSC and precursor cells [36].

Heterogeneity among GBM tumor cells arises within a single tumor as a result of genetic and epigenetic changes, as well as different microenvironments within different regions of the tumors [37]. In GBM CSCs, there is clonal heterogeneity at the genetic level with distinct tumorigenic potential and defined GBM CSC marker expression resulting from clonal evolution which is likely to influence disease progression and response to treatment [28]. Another level of complexity in GBM is the dynamic equilibrium between GBM CSCs and differentiated non-GBM CSCs, and the potential for non-GBM CSCs to dedifferentiate to GBM CSCs due to epigenetic alteration which confers phenotypic plasticity to the tumor population [38]. Moreover, it has been observed that exposure to differentiated GBM cells to therapeutic doses of TMZ or ionizing radiation (IR) increases the GBM CSC pool both *in vitro* and *in vivo* [39]. This could lead to replenishment of the original tumor CSCs population, leading to a more

infiltrative phenotype and enhanced chemoresistance, representing a potential mechanism for therapeutic relapse.

Therefore, it would be critically important to develop therapeutic strategies that contain agents targeting different signalling pathways and/or employing effective multi-targeting agents for the eradication of those GBM CSCs.

#### **1.1.4 Brain tumor diagnosis**

Detection of brain tumors does not take place until marked clinical symptoms occur in affected patients, which is usually a late event. The absence of pain receptors in the brain allows tumors to grow 'silently', although this would also depend on the tumor location. In general, by the time a glioma becomes symptomatic, it is almost always too late in its biological course for complete remission [40]. Brain tumors cause symptoms for two reasons: firstly, because they take up space inside the skull as they grow and compress other brain structures, and secondly, they can cause specific symptoms due to their position in the brain. Persistent headache, nausea, vomiting, seizures, visual disturbances, memory loss and altered mental functions are common signs that can manifest once the intracranial pressure rises due to the mass effect of the lesion [41]. Often more than one symptom is present, and this leads to a suspicion of an abnormal brain mass presence. Diagnosis begins with appropriate brain imaging. Techniques such as Positron Emission Tomography (PET), Computed Tomography (CT), Magnetic Resonance Imaging (MRI), and Magnetic Resonance Spectroscopy (MRS) are used to perform the initial assessment and localization of the tumor, as well as to perform the follow-up of treatment and determine tumor progression. Initial diagnosis is usually followed by histopathological analysis (biopsy, surgical resection) depending on the location of the tumor, which for now, is the gold standard method to confirm the diagnosis, tumor grading, classification and give a prognosis to guide treatment decisions.

Despite high grade glioma is a disease diagnosed usually in the fifth or sixth decade of life, younger patients are also affected. An accurate histopathological diagnosis is essential as tumor type and grade may condition the treatment. Magnetic resonance (MR) imaging with gadolinium chelate contrast enhancement (see also section 1.4.2.1) is considered the standard noninvasive technique for detection and treatment follow-up and it is usually followed by tissue sampling (stereotactic biopsy, debulking surgery) and histopathology analysis.

### **1.1.5 GBM therapy**

For GBM patients, surgery, followed by radiotherapy plus chemotherapy are the basis of these patients treatment, with the best results obtained when the three of them can be used [42].

Completely resected patients in good performance status and aged less than 75 years are candidates to chemoradiotherapy followed by additional adjuvant TMZ cycles [11]. Additionally, selected cases with complete resection without ventricular exposure can be offered carmustine (BCNU) wafers as a first line therapy [43] (0).

There are no relevant data regarding the role of chemoradiotherapy with TMZ in patients older than 75 years. In addition, a small randomized trial in patients of 70 years of age or older demonstrated that radiotherapy results in a modest improvement in survival, without reducing the quality of life or cognition in elderly patients with glioblastoma [44]. Also, there is a phase II trial suggesting that chemotherapy alone with TMZ can be considered as safe, easily administered, and effective therapeutic approach for elderly (>70 years) patients with newly diagnosed GBM [45].

In cases in which resection is not possible, a stereotactic biopsy may be performed. These patients are good candidates for trials of neoadjuvant chemotherapy [46] and, if possible, their treatment should be individualized according to their characteristics (age, tumor location, genetic profile, among others) by a multidisciplinary committee.

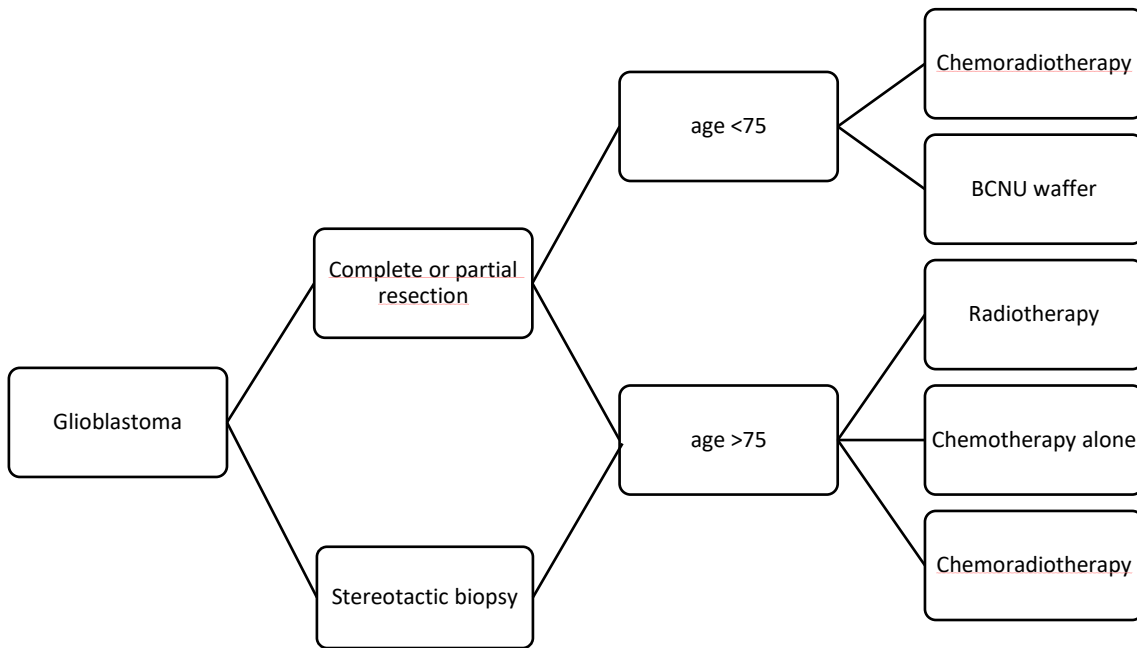


**Figure 1.4 Management for diagnostic and treatment of GBM.** BCNU: carmustine.

### 1.1.5.1 Surgical resection

Surgery is usually the first step in treating most benign and many malignant brain tumors. It is often the preferred treatment when a tumor can be removed without unnecessary risk of neurological damage. The primary objective of the surgery is to remove as much tumor mass as possible to achieve a better overall survival [47, 48]. Additionally, in some cases it can be used to provide a tumor tissue sample for an accurate histopathological diagnosis or genomic testing and to remove at least part of the tumor to relieve pressure inside the skull (intracranial pressure). Surgery also allows reducing the amount of tumor mass to be treated with radiation or chemotherapy, and enables direct access for intra-surgical chemotherapy or radiation of malignant tumors. Nevertheless, complete removal should be the ideal outcome without compromising the neurological functions of the patient. This may be the best strategy and provide a cure in some tumor cases, for example meningiomas, which are usually well-circumscribed lesions, but may be insufficient or impossible in others, due to the extension, location or the infiltrative nature in case of high grade gliomas.

Current advances in neurosurgery, such as minimally invasive techniques [49], intraoperative brain mapping [50] and intraoperative MRI [51, 52], have led to an improved safety and an increased extent of resection in glioma patients. However, complete surgical resection of high grade gliomas is virtually impossible due to their infiltrative nature. That is why surgery must be followed by adjuvant RT, chemotherapy, or both.

#### **1.1.5.2 Radiotherapy (RT)**

RT is a major tool in the treatment and improvement of prognosis and survival of patients. The main aim of RT is to kill tumor cells while leaving normal brain tissue unharmed, so that the vital functions and the patient's quality of life is not affected.

RT involves administration of IR (photon or a charged subatomic particle) to the location of the tumor from an external source (the most common approach), from a source placed inside the body (brachytherapy), or through the use of radioactive drugs (systemic). Effects such as cell death, chromosomal aberrations, DNA damage, mutagenesis, and carcinogenesis result from direct ionization of cell structures, particularly DNA, or from indirect damage through reactive oxygen species produced by radiolysis of water. These biological effects are attributed to irreparable or misrepaired DNA damage in cells directly hit by radiation (Figure 1.5). Although radiation affects both normal cells and tumor cells, healthy cells have longer time to repair themselves than tumor cells, so resulting in differential cancer cell killing [53]. RT may be used subsequent or, in some cases, in place of resection of the tumor and it is the most common treatment for secondary brain tumors. Radiation with an external beam has been shown to be effective in the treatment of newly diagnosed malignant gliomas increasing the median survival of the treated patients from 5 months to 9 months with adjuvant RT compared to surgery alone [54, 55].

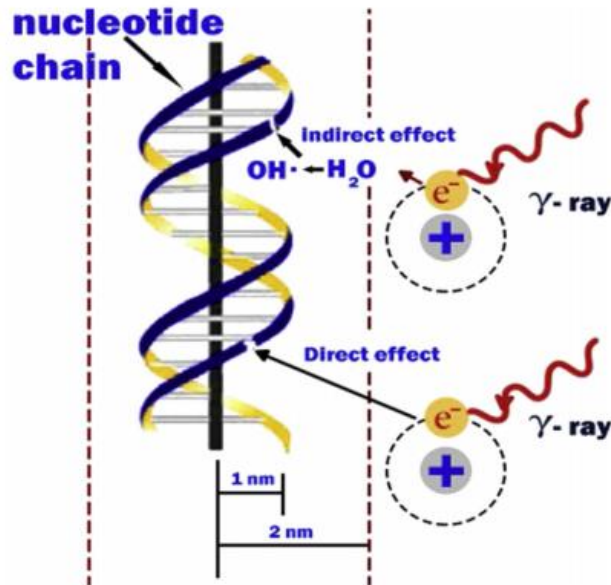


**Figure 1.5 Direct and indirect actions of radiation.** Direct ionization of DNA or indirect damage through reactive oxygen species produced by radiolysis of water. These are biological effects producing irreparable or misrepaired DNA damage in cells directly hit by radiation. Extracted from [56].

Since radiation is not completely selective and can affect both normal cells and tumor cells, a special type of radiation protocol that focuses the high-dose zone of radiation on the target area was developed, and was called stereotactic radiosurgery [57]. Other techniques have been helpful at the time of distinguishing the border of normal brain around the tumor, as seen on imaging, most commonly by MRI or CT. Although MRI provides greater definition of the neoplastic extension in comparison with CT imaging, it may still be advisable to complement the zone delineation with other non-invasive techniques, such as perfusion or diffusion MRI or magnetic resonance spectroscopy imaging (MRSI), due to the highly infiltrative nature of glial tumors. Thus, the aforementioned techniques would be helpful for proper discrimination between healthy and tumoral tissue and to set better irradiation margins for a given case to improve the prognosis and increase survival [58].

Nevertheless, gliomas are heterogeneous tissues and some cells seem to be resistant to RT [59], implicating that even after application of the clinically best tolerated maximum RT dose to tumors, glioma will not be completely eradicated.



### **1.1.5.3 Chemotherapy**

Chemotherapy is a category of cancer treatment that uses one or more anti-cancer drugs (chemotherapeutic agents) as part of a standardized chemotherapy regimen. Chemotherapy may be given with a curative intent (chemotherapeutic agents either alone or in combination), or it may aim to prolong life or to reduce symptoms (palliative chemotherapy). The use of therapeutic agents poses a major challenge for neuro-oncologists, because CNS tumors represent a variety of growth patterns and response to therapy, making it difficult to find a specific therapeutic target. Additionally, the fundamental problem with systemic chemotherapy for brain tumors is reaching an effective dose within the tumor. The unique physiology of tumor tissue and mechanisms at the blood-tumor interface, i.e. increased intratumor oncotic pressure, bad perfusion or collapsed vessels make it difficult for blood-borne drugs to reach the tumor's inner core.

#### **1.1.5.3.1 Alkylating agents: TMZ and CPA**

##### **Temozolomide (TMZ)**

The standard chemotherapy for GBM is based mainly on alkylating agents, such as TMZ. This is considered the most effective drug for the treatment of this tumor, although only a small improvement in survival time is achieved in the clinical practice: Stupp et al. [60] assigned 573 GBM patients to treatment; 278 (97%) of the 286 patients in the radiotherapy-alone group and 254 (89%) of 287 in the combined treatment radiotherapy and TMZ group died during the 5 years of follow-up. Overall survival rates were 27% at 2 years, 16% at 3 years, 12% at 4 years, and 10% at 5 years (for the combined RT+TMZ treatment) versus 11%, 4%, 3%, and 2% (for radiotherapy alone), respectively [60]. TMZ is also one of the few agents with the ability to penetrate the blood-brain barrier (BBB), achieving cytotoxic concentrations in cerebrospinal fluid and brain parenchyma, which may be also of interest in the treatment of tumors with yet intact BBB.

TMZ in aqueous solution is chemically converted to methyl-triazeno imidazole-carboxamide (MTIC) at physiologic pH (Figure 1.6), and MTIC degrades to the inactive 5-aminoimidazole-4-carboxamide (AIC) and to the electrophilic alkylating methyldiazonium cation that may transfer a methyl group to DNA. The most common site of methylation is N7 of guanine (N7-MeG), 60-80%, and the N3 of adenine (N3-MeA), 10-20%. Methylation of the O6 of guanine (O6-MeG) accounts for only about 5-10% of DNA adducts, but is the primary responsible for the cytotoxic effects of TMZ. The O6-MeG lesion leads to DNA double-strand breaks (DSBs) and subsequent cell death via apoptosis and/or autophagy. When active O6-methylguanine-DNA-methyltransferase (MGMT) is present, O6-MeG is repaired without cytotoxicity and this is thought to contribute to resistance to TMZ treatment. The repair occurs by transferring the methyl group from the adduct to its own cysteine residue and the methylated MGMT is then degraded. Resistance to alkylating agents is mainly due to overexpression of the MGMT protein, and it is a major, currently unresolved problem with TMZ therapy. Therefore, mechanisms to deplete MGMT in tumor cells are being developed in an attempt to increase sensitivity to TMZ. Despite this, a subset of GBM does not respond to treatment even after MGMT inactivation, suggesting that other DNA repair mechanisms may also modulate the tolerance to TMZ. The possible roles of the single-strand breaks (SSBs) and DSBs repair pathways in mediating therapeutic resistance to TMZ have also begun to emerge [61]. Authors affirm that when MGMT is inactivated or has not potential to completely repair O6-meG, the unrepaired O6-meG would be continuously repaired by the futile cycle of mismatch repair (MMR) which ultimately induces cell death by provoking DSBs. Additionally, N7-MeG and N3-meA are repaired by base excision repair (BER). If not repaired, alkylated bases cause replication stall and collapse the replication fork, generating SSBs, which ultimately would induce DSBs. It is possible that SSB and DSB repair pathways are activated and diminish the cytotoxic effects of TMZ (Figure 1.6) [61].

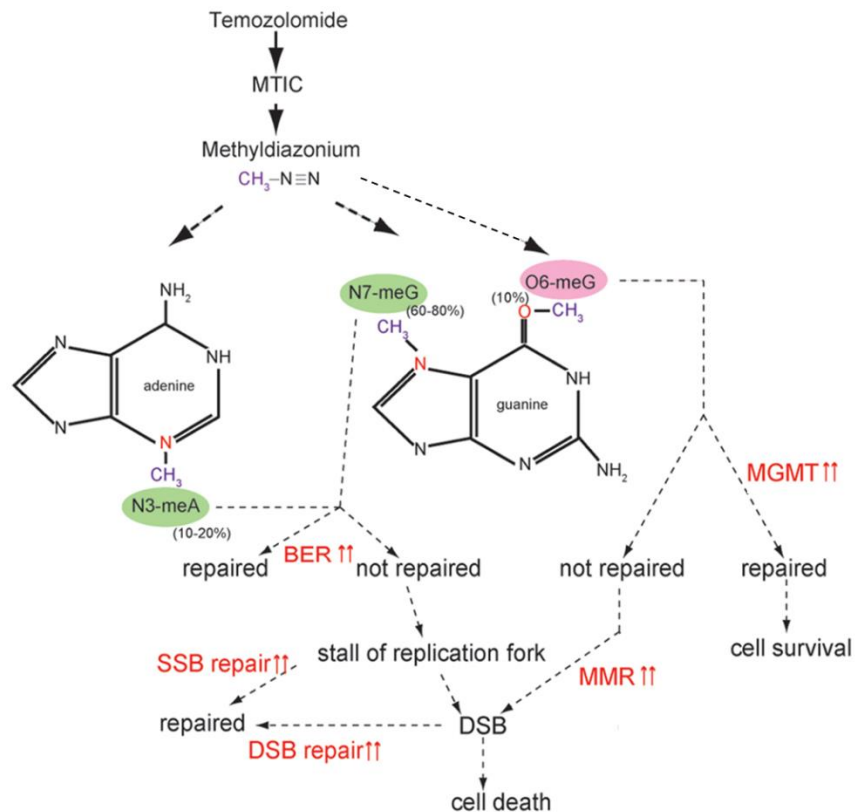


**Figure 1.6 TMZ activation and resistance pathways scheme.** O6-meG DNA adducts account for only 10% of TMZ-induced DNA lesions, but they are responsible for the cytotoxic effect. MGMT repairs the lesions, resulting in resistance to TMZ. If MGMT is depleted or suppressed by methylation of its gene promoter, cytotoxicity of TMZ is enhanced. MMR recognizes the abnormal base pairs containing O6-meG, eventually leading to DNA DSB and cell death. N3-meA and N7-meG adducts are also cytotoxic, but are usually repaired by the BER system. It is possible that SSB and DSB repair pathways are activated and diminish the cytotoxic effects of TMZ. BER: base excision repair, DSB: double-strand break, MGMT:O6-methylguanine-DNA-methyltransferase, MMR: mismatch repair, N3-meA:N3-methyl-adenine, N7-meG: N7-methyl-guanine, O6-meG:O6-methyl-guanine and SSB: single-strand break. Adapted from [61].

TMZ improves outcome in treated patients when administered alone [62] or in combination with RT [60] or with other agents like procarbazine [63] or lomustine [64], among others. Unluckily, GBM CSCs are known to produce chemoresistance, indicating that GBM CSCs persist in GBM even when a standard treatment is applied [35]. Additionally, cellular exposure to DNA damaging agents, such as TMZ, could develop mutations and clastogenic effects which can result in additional malignant transformation [65]. As well, in human GMB patients treated

with TMZ, secondary effects, mainly related to blood toxicity (leucopenia, thrombopenia), are known [66].

### **Cyclophosphamide (CPA)**

Another chemotherapeutic agent with purported activity for high-grade gliomas is CPA [67–69], but CPA induces larger side effects than TMZ and more significant toxicity at therapeutic doses in humans [70]. CPA is a prodrug that is converted by hepatic microsomal enzymes to 4-hydroxycyclophosphamide and aldophosphamide. These compounds diffuse into cells and are converted into the active alkylating compound, phosphoramidate mustard, an alkylating agent, which adds an alkyl group to DNA. It attaches the alkyl group to the guanine base of DNA, at the number 7 nitrogen atom of the imidazole ring. This interferes with DNA replication by forming intrastrand and interstrand DNA crosslinks that results in inhibition of DNA synthesis and cell death. The major mechanism of CPA detoxification appears to be inactivation of aldophosphamide by cellular aldehyde dehydrogenase (ALDH) [71]. CPA's unique metabolism and inactivation by ALDH is responsible for its distinct cytotoxic properties. Differential cellular expression of ALDH has an effect on the anticancer therapeutic index and immunosuppressive properties of CPA [71].

The alkylating agent CPA was first approved by the food and drug administration for cancer treatment in 1959 and is currently used to treat a variety of diseases, including breast and ovarian cancer, hematological malignancies, and autoimmune diseases [72]. CPA is commonly delivered to cancer patients on a maximum tolerated dose (MTD) schedule, but often show modest anti-cancer activity on their own [69] or in combination with irradiation or/and other agents like carboplatin [73, 74]. This limited efficacy is in part due to high toxicity to the host, usually considerable hematological toxicity [67], which necessitates a long drug-free break, during which chemotherapy-resistant tumor cell populations may emerge and residual tumors can neovascularize, leading to tumor regrowth [75, 76].

#### 1.1.5.4 Evidence of the immune system role in response to therapy

Research over the past decades has shown evidence that the immune system not only interacts with developing neoplasms, but also removes damaged and stressed cells, which are generally more prone to become malignant (process named anticancer immunosurveillance) [77]. In addition, it has been observed that the immune system plays an important role in the response of numerous malignancies to therapy [78].

The development of effective antitumor immune response depends on coordinated interactions of host immunocompetent cells, as well as on the generation of tumor antigen-specific cytotoxic T lymphocytes (CTLs). CTLs recognise specific antigenic peptides presented on the surface of transformed cells, so they represent an important role in the defence against cancer. To become competent killer cells, naïve lymphocytes require efficient instructing by dendritic cells (DCs), which are professional antigen-presenting cells (APCs), as well as proper CD4+ cell helper ( Figure 1.7).

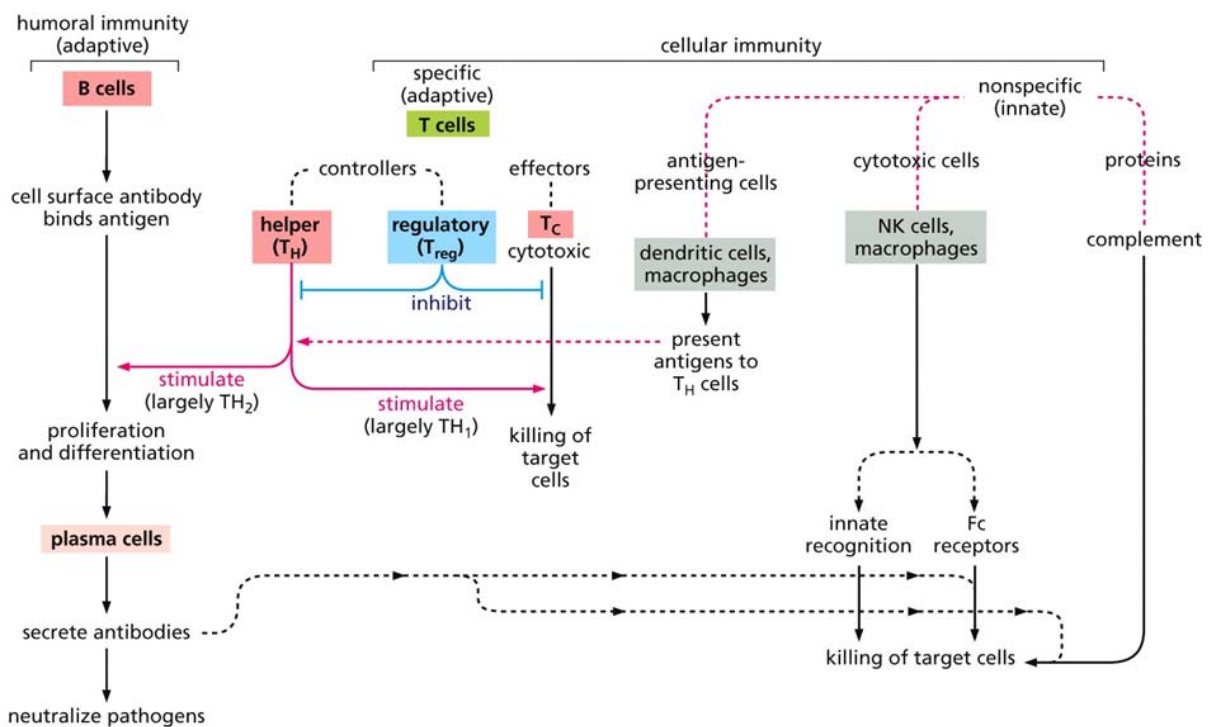


**Figure 1.7 Scheme of the immune system actuation.** Humoral immunity and cellular (specific and non-specific) immunity with the participation of T and B lymphocytes. Extracted from [79].

Malignant cells express pathogen-associated molecular patterns (PAMPs) that can be recognized on dendritic cell (DC) precursors, triggering the local release of cytokines and chemokines. This results in the recruitment and activation of innate immunity effector cells, including macrophages ( $m\phi$ ), natural killer (NK) and natural killer T (NKT) cells, all of which are able to kill cancer cells. DCs engulf apoptotic tumor cells, undergo a maturation process and then migrate to regional lymph nodes, where they present processed tumor-derived peptides to CD8<sup>+</sup> and CD4<sup>+</sup> T cells upon the upregulation of MHC Class I and II molecules. Activated CTLs then clonally expand and leave lymph nodes (LN), infiltrating tumor tissues and eventually get activated to mediate effector functions (Figure 1.8) [80]. Additionally, some of this CD4<sup>+</sup> T cells help activate antigen-specific CD8<sup>+</sup> T cells, and these activated CD8<sup>+</sup> T cells also traffic into the brain, showing brain accumulation peaking at about 7 days after initial antigen presentation to DCs in the tumor [81], suggesting that this time period is needed for the activation of the full immune response to the tumor.

However, the immune response is complex and depending on several factors, multiple immune suppressive mechanisms may inhibit T cell function in the cancer context [82]. Thus, adaptive immune responses in GBM patients are deficient as the tumor microenvironment is rich in immunosuppressive factors secreted by the tumor [83], like transforming growth factor beta (TGF- $\beta$ ) and vascular endothelial growth factor (VEGF) which suppress T cell proliferation and cytotoxic function [84]. Additionally, it is known that T cell unresponsiveness occurs during the growth of hematologic and solid tumors in complex microenvironments which can strongly influence the growth and progression of the tumor cells and can act as a barrier, limiting the efficacy of cancer immunotherapy [85]. Moreover, most of the antigens expressed by tumor cells are also expressed in normal cells resulting in immunotolerance and a failure of the immune system, allowing the development of solid tumors [85] and immune escape mechanisms which have been described for some tumor types and stages [86].

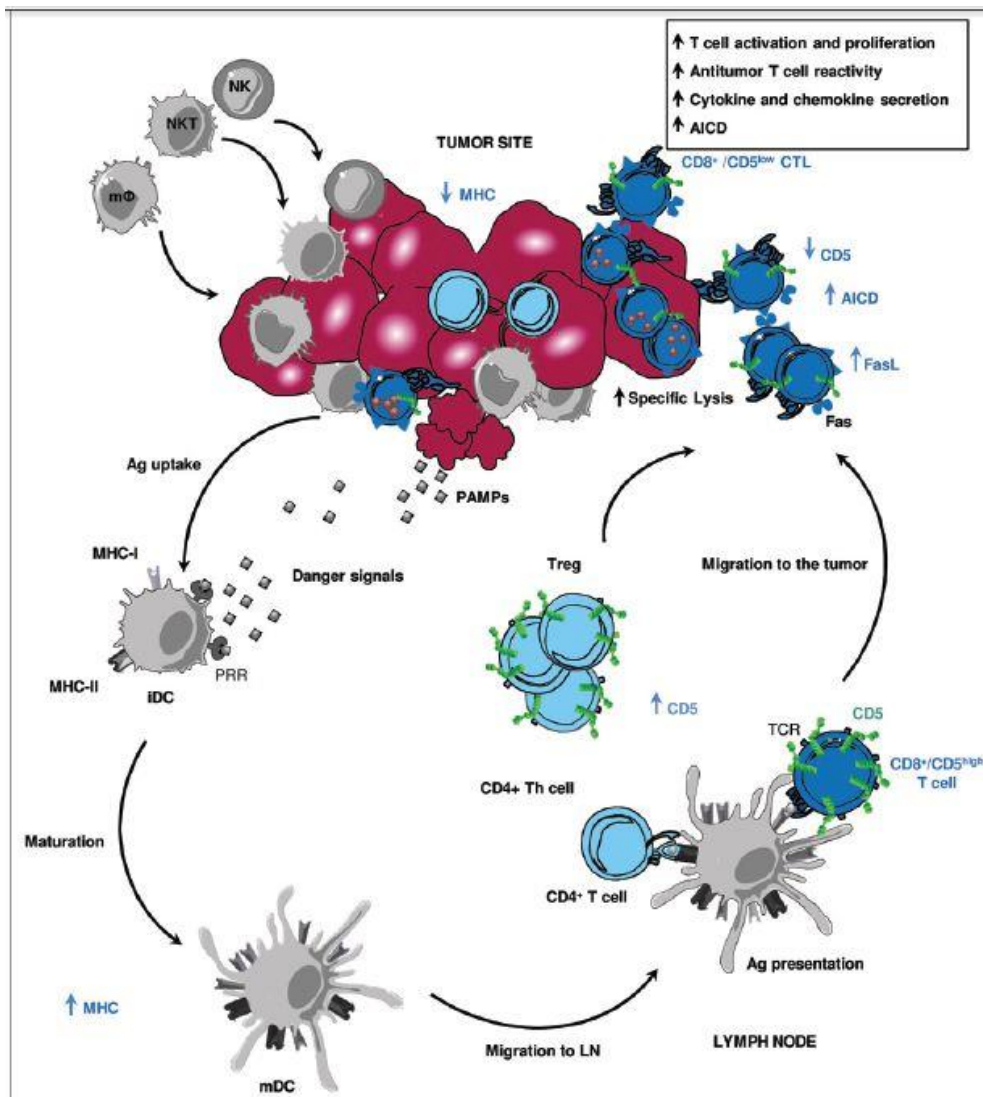


**Figure 1.8** Scheme of the cycle for immune response against a tumor. The whole cycle in mouse brain is assumed to take 7 days [81]. The malignant cells may express pathogen-associated molecular patterns (PAMPs) that can be recognized by pattern recognition receptors (PRRs) on dendritic cells (DCs) precursors, triggering the local release of cytokines and chemokines. Then, DCs migrate to local lymph nodes (LN) and present processed tumor-derived peptides to naïve T and B-lymphocytes, which are then activated in case of Antigen (Ag) match to become plasma cells producing antibodies and CD4<sup>+</sup> helper T lymphocytes or CD8<sup>+</sup> cytotoxic T lymphocytes (CTLs). Activated CTLs leave LN to infiltrate tumor tissues and exert effector functions. Immunotolerance may be induced by downregulation of cluster of differentiation 5 (CD5) in CTLs infiltrating the tumor causing activation-induced cell death (AICD). FASL: FAS ligand, MHC: Major histocompatibility complex, M $\phi$ : macrophages, NK: natural killer, NKT: natural killer T, TCR: T-cell receptor, and Treg: Lymphocyte T regulatory. Taken from [80].

As immunosuppression plays an important role in tumor progression, it is reasonable to hypothesize that the reversion of the immune suppression could allow more effective immune targeting of glioma, resulting in less tumor progression and improved outcomes. Moreover, it has been long observed that changes in the immune system relate with cancer survival. For instance, patients that had postoperative infections, showed a better outcome [87]. Indeed, a direct correlation between survival of patients with primary GBM and tumor infiltration of cytotoxic and helper T cells has been observed [88].

#### **1.1.5.4.2 Therapeutic strategies to potentiate or interfere with the immune system**

##### **Metronomic approach schedule**

Despite chemotherapy represents the mainstay of cancer medicine for both locally and advanced neoplasms, with the MTD being the most used administration scheme for the past 50 years [89] and being TMZ the standard selected drug for GBM therapy [60], no cure for this tumor is available at present [90]. In preceding years, several groups began to study a modality of drug administration called “metronomic therapy” [91, 92], referring to equally spaced, low doses of chemotherapeutic drugs without extended rest periods. Efforts have also been devoted to study new therapeutic regimens with conventional drugs in order to activate immune responses that enhance tumor regression and prevent tumor regrowth [93]. Specifically in GL261 GBM tumors growing subcutaneously in immunocompetent mice (see also section 1.3), CPA metronomic therapy has proven to not only activate antitumor CD8<sup>+</sup> T-cell response, but also to induce long-term, specific T-cell tumor memory [92]. The same authors have also proven that a metronomic 6-day intermittent was the optimum timing for this therapy, and this could be in agreement with the 7-day cycle for immune cell recruitment in mice brain described by other authors in [81]. This agrees with several authors that affirm that immune system could intervene in therapy response [93], having the CTLs a relevant role in the defence against cancer as they recognize antigens presented on the surface of transformed cells, following a complex cycle described in [80].



The limitation of toxicity effects to the host due to TMZ and CPA administered at MTD can be addressed, in part, by administration of TMZ and CPA on a metronomic schedule [94], which maintains TMZ and CPA cytotoxicity to tumor-associated endothelial cells and can increase overall therapeutic activity while reducing host toxicity [95–97]. CPA and TMZ metronomic low doses schedules have been demonstrated to increase tumor cell autophagy, to elicit antitumor immune responses in humans, and to show promising safety and efficacy [98]. Daily, oral low dose metronomic CPA schedules have shown promising results in preclinical models [99, 100] and are currently being tested in clinical trials [101, 102].

### **Immunotherapy**

Recent studies have raised hopes regarding immunotherapy, which has recently established itself as a proven therapy for several types of cancer improving the body's immune response to a tumor [103]. Moreover, in early-stage clinical trials, several different immunotherapeutic strategies have shown promise against GBM [104]. Therefore, at present the immunotherapy effectiveness is being assessed in clinical trials for brain cancer with strategies such as cancer vaccines, oncolytic virus therapy, adoptive cell therapy, monoclonal antibodies, amongst others.

As with immunization for infections, immunization against tumors can theoretically occur in the form of passive or active immunotherapy [104]. The passive form gives the patient immune cells (active *in vitro*) or antibodies capable of targeting tumor cells, so, there is no activation of patient's own immune system. On the other hand, active immunization is intended to stimulate the patient's own immune response.

In broad terms, passive/adoptive immunotherapy can be further divided into 3 approaches: The first is the direct injection of monoclonal antibodies, in which antibodies known to interact with an antigen associated with a tumor are administered to the patient [105]. In GBM, only one monoclonal antibody has been approved for treatment, which is Bevacizumab, a

humanized Immunoglobulin 1 monoclonal antibody that binds to and neutralizes the VEGF [106], a tumor-associated protein that is the central mediator of tumor angiogenesis. The second approach to cancer passive immunotherapy is to stimulate the immune system with cytokines. Cytokine stimulation with interleukin (IL)-2 have been studied in a variety of cancers, but it has not shown benefit in GBM [107]. A third strategy is adoptive cell therapy [104] in which immune cells activated *ex vivo* are administered to patients, either by systemic injection or directly into the tumor. In this last instance, if DNA mutation occurs in the cancer antigen being targeted, the immunization will not be effective any longer. Accordingly, this type of immunotherapy may not represent a permanent solution to eradicate the tumor.

Active immunotherapy boosts the patient's immune system. There are two approaches to active immunization: peptide based therapy and cell based therapy [108]. In peptide based therapy, peptides corresponding to tumor antigens are injected as a vaccine to induce immune activation being capable to bind to Major Histocompatibility Complex (MHC) class I molecules, which will lead to activation of CTLs and tumor cell killing. On the other hand, cell based active immunotherapy involves obtaining DCs from a patient and pulsing them with glioma antigens derived from a tumor resection. Since DCs are professional APCs, they are an obvious choice for active immunotherapy and have to date been the most studied cell based vaccine [104, 108]. The activated DCs are then injected back into the patient. This approach is also being explored as a way to target glioma SCs, a radioresistant and chemoresistant subpopulation of cells within a patient's tumor. In a phase I trial, patients with newly diagnosed GBM which were given a DC-based vaccine with a combination of glioma SC antigens, increased survival was observed, and, in some patients, their tumor biopsy had a decrease or absence of cells positive for CD133, a glioma SC marker [109]. Additionally, it has been demonstrated that DC vaccines can be given safely to patients with GBM undergoing TMZ alone or in combination with RT [110]. Still, one of the major challenges in cancer immunotherapy is the induction of strong and durable antitumor immune responses, not yet achieved in patients.

### **1.1.5.5 Other therapeutic strategies**

#### **Targeted therapies**

Common genetic abnormalities in GBM are associated with aberrant activation or suppression of cellular signal transduction pathways and resistance to radiation and chemotherapy. Special attention has been focused on other therapeutic strategies that target intracellular signalling pathways determining the key functions of tumor biology, such as proliferation and apoptosis or angiogenesis. Examples of targets are several growth factor receptors, such as EGFR, vascular endothelial growth factor receptor (VEGFR) and PDGFR, which are overexpressed, amplified and/or mutated in cancer cells and this leads to uncontrolled cell proliferation, angiogenesis, migration, survival and differentiation [111]. Several signal transduction inhibitors have been examined in preclinical and clinical trials with malignant gliomas, including antiangiogenic agents (bevacizumab, enzastaurin), inhibitors of EGFR tyrosine kinase (gefitinib and erlotinib) [112], mammalian target of rapamycin (temsirolimus, everolimus) and integrin (cilengitide). Some of them have reached the clinical practice (e.g. bevacizumab), although they are not used yet as a first choice. Although preliminary clinical results of the use of targeted agents have not translated into significantly better survival, more recent phase II trials are exploring the combination of multitargeted drugs with cytotoxic chemotherapy and RT in order to overcome the resistance of tumors to single-agent targeted therapies [113].

#### **Small molecular weight kinase inhibitors**

Inhibition of protein kinases has become a standard of modern clinical oncology, and it could improve GBM patients' survival. Protein and lipid kinases play essential roles in many signalling pathways that regulate cell functions. Deregulation of these kinase activities leads to a variety of pathologies ranging from cancer to diabetes, infectious diseases, cardiovascular disorders, cell growth and survival. More than 500 protein kinases are encoded by the human genome, and since many human diseases result from overactivation of protein and lipid kinases due to mutations and/or overexpression, this enzyme category represent an important target for the

pharmaceutical industry. In past decades, around 20 small-molecule kinase inhibitors have been approved for clinical use, mainly for oncological indications, such as Sorafenib or Erlotinib [114]. These drugs target stages of signal transduction from the receptor protein tyrosine kinases that initiate intracellular signalling, through second-messenger-dependent lipid and protein kinases that regulate the cell cycle.

- **CK2 inhibitors (iCK2s)**

Protein Casein Kinase CK2 (CK2), an oncogenic protein kinase, contributes to tumor development, proliferation, and apoptosis suppression in cancer [115]. Different iCK2s have been studied for cancer applications, such as 4,5,6,7-Tetrabromobenzotriazole (TBB) [116, 117] or apigenin (APG) [118, 119]. Additionally, a more specific iCK2, 5-(3-Chlorophenylamino)benzo[c][2,6] naphthyridine-8-carboxylic acid (CX-4945) [120–124] has been reported as the first iCK2 in clinical stage<sup>1,2</sup>. *In vitro* studies of breast cancer [122] and studies with an intracranial murine glioma model [124] have also presented successful results for CX-4945. Moreover, other promising iCK2s are in development, such as tetra-bromo-deoxyribofuranosyl-benzimidazole (TDB), a dual inhibitor of CK2 and Proviral Integration of Moloney virus 1 (PIM-1) [125]. These results highlight the relevance of CK2 and its interwoven signalling targets in tumor growth and progression. More insight in this issue can be found in section 1.2.5.

---

<sup>1</sup> <http://www.cancer.gov/clinicaltrials/search/view?cdrid=642699&version=HealthProfessional>

<sup>2</sup> <http://www.prnewswire.com/news-releases/cylene-presents-encouraging-clinical-data-for-oral-ck2-inhibitor-at-asco-123219423.html>

## **1.2 PROTEIN CASEIN KINASE CK2 (CK2)**

For many years, it has been clear that the reversible phosphorylation of proteins is a major mechanism for the regulation of a broad spectrum of fundamental cellular processes. So, it is not surprising that the human genome encodes many distinct protein kinases [126]. Some protein kinases are very specific and can phosphorylate a restricted number of substrates, while other protein kinases, can phosphorylate hundreds of proteins within cells, which is the case of CK2.

CK2 is a ubiquitously expressed protein kinase which exhibits extensive sequence and functional conservation across species. In addition, it is a highly pleiotropic and constitutively active Serine (Ser)/threonine (Thr) protein kinase in eukaryotic organisms, where is known to phosphorylate more than 300 physiological targets [127]. While the number of targets known to be phosphorylated by CK2 continues growing, it becomes evident that CK2 has a decisive role in the regulation of diverse cellular processes, including cell differentiation, proliferation and survival [127].

### **1.2.1 Structure of CK2**

The analysis of amino acid sequences, as well as crystallography studies have allowed to elucidate the structural and biochemical features of CK2. As said before, protein CK2 is distributed ubiquitously in eukaryotic organisms, where it mostly appears to exist in tetrameric complexes consisting of two catalytic subunits (CK2 $\alpha$  and/or CK2 $\alpha'$ ) and two regulatory subunits (CK2 $\beta$ ) (Figure 1.9). In many organisms, distinct isoenzymic forms of the catalytic subunit of CK2 have been identified [128]. For example, in humans, two catalytic isoforms, designated CK2 $\alpha$  and CK2 $\alpha'$  encoded by the gene CSNK2A1 and CSNK2A2, respectively, have been well characterized, while a third isoform, designated CK2 $\alpha''$ , has been recently identified [129]. In humans, only a single regulatory subunit, designated CK2 $\beta$ , has

been identified, while in other organisms, such as plants, a broad range of CK2 $\beta$  forms have been recognised [130].

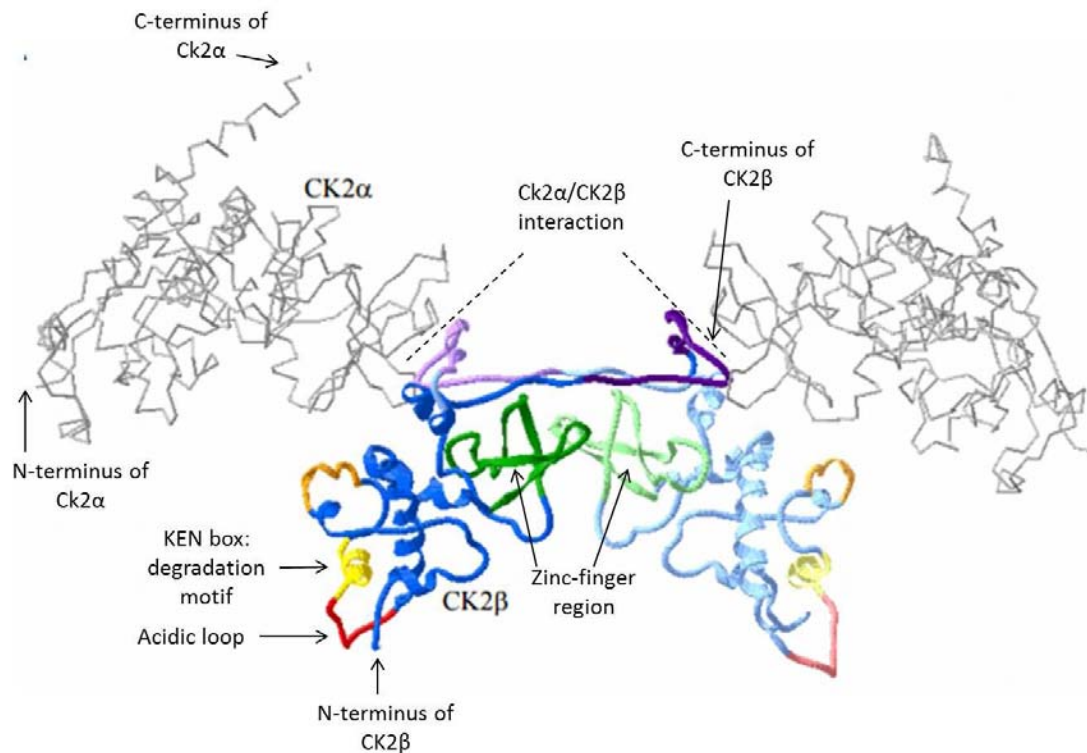


**Figure 1.9 Crystal structure of the CK2 holoenzyme.** The CK2 $\beta$  dimer forms the core of the enzyme. Important motifs of CK2 $\beta$  are marked: the putative degradation motif (KEN box), the acidic loop involved in modulation of catalytic subunit activity and the zinc-finger motif which mediates between CK2 $\beta$  dimer formation and CK2 $\alpha$  coordination. Adapted from [131].

At a very early stage after its discovery, CK2 was distinguished among known protein kinases for its ability to phosphorylate Ser or Thr residues that are proximal to acidic amino acids. This is the reason why it is said that CK2 is a dual-specificity kinase. Additionally, systematic studies led to the definition of a minimal consensus sequence for phosphorylation of CK2 (i.e. Ser-Xaa-Xaa-Acidic, where the acid residue may be glutamate (Glu), aspartate (Asp), pSer or phosphotyrosine (pTyr)) that remains distinct from the minimal consensus sequence for any other protein kinase that has been characterized to date [132]. The delineation of this minimal consensus sequence has greatly facilitated the identification of many new potential CK2

targets, although some limitations have been found, namely: sites phosphorylated by CK2 that are not conform with this consensus [133], or sites with the consensus sequence without guaranteed phosphorylation, since there may be additional determinants within the sequence that modulate phosphorylation efficiency [134].

With mammalian CK2, tetrameric CK2 complexes may contain either identical (two CK2 $\alpha$  or two CK2 $\alpha'$ ) or non-identical (one CK2 $\alpha$  and one CK2 $\alpha'$ ) catalytic subunits. In the CK2 complex, the regulatory subunit forms a stable dimer, which links the two catalytic subunits, allowing no direct interaction between them [135]. The catalytic subunits contact with both regulatory chains, predominantly via C-terminal tails of the regulatory subunit.

#### **CK2 $\alpha$ : catalytic subunit**

Despite being the products of separate genes, the two catalytic subunits (CK2 $\alpha$  and CK2 $\alpha'$ ) exhibit more than 90% sequence identity in the N-terminal 330 amino acids. On the other hand, the C-terminal domains of the two isoenzymes are completely unrelated [136]. There is evidence for functional specialization of the individual CK2 isoforms in yeast, mice and mammal cells [137].

The structure of CK2 $\alpha$  is subdivided in different regions, which are responsible for the main functional characteristics of this subunit, such as its monomeric form constitutive activity, the structure of substrate recognition, as well as the basis of dual-cosubstrat (Ser/Thr) specificity.

#### **CK2 $\beta$ : regulatory subunit**

CK2 $\beta$  does not display extensive homology with other protein kinase regulatory subunits, but it has a remarkably sequence and functional conservation among species [136]. Several complementary lines of evidence indicate that dimers of CK2 $\beta$  are at the core of the tetrameric CK2 complexes [138]. Additionally, a large proportion of CK2 $\beta$  has been shown to be phosphorylated at an autophosphorylation site, near the amino terminus of the protein, most

likely at serine 2 and serine 3 [139]. In the structure of CK2 $\beta$  the three most important regions are the zinc-binding motif, the CK2 $\alpha$ -binding interface of CK2 $\beta$  and the acidic loop [131] (Figure 1.9). The crystal structure of dimeric CK2 $\beta$  demonstrated that a zinc finger mediates CK2 $\beta$  dimerization [140]. It is characterized by four cysteine residues which mediate the interaction allowing the CK2 $\beta$  dimer to form the core of the CK2 holoenzyme [141]. As expected, it has been demonstrated that disruption of the zinc-finger by mutation of cysteine (Cys) 109 and 114, resulted in a loss of CK2 $\beta$  dimer formation [140], pointing that this region is responsible for the ability of CK2 $\beta$  to stabilize CK2 activity [141].

Another additional sequence of relevance within CK2 $\beta$  is a surface exposed acidic loop. This acidic region has been identified as the site where CK2 binds polyamines, which are known to stimulate CK2 activity *in vitro* [142]. Despite precise details remain to be defined, it seems that the acidic loop may play a role in CK2 regulation. In addition, CK2 $\beta$  contains a sequence resembling that of the nine amino acid motif called the “destruction box” that plays a key role in the specific degradation of cyclin B at the end of mitosis [143]. While this motif is situated on a surface exposed  $\alpha$ -helix where it is available for recognition by the cellular degradation machinery, the functional relevance of KEN boxes of CK2 $\beta$  have not been characterized in detail yet [131].

Although the role of CK2 $\beta$  has been usually considered as restricted to form the tetrameric CK2 complexes, nowadays, this view has changed and CK2 $\beta$  is presently accepted to have both, CK2 dependent, and CK2 activity independent functions. Several proteins have been identified to bind to the tetrameric form of CK2 through binding sites on CK2 $\beta$ , thus, CK2 $\beta$  appears to be a substrate docking protein. Some proteins, such as M-phase inducer phosphatase 2 (Cdc25B) or cyclin-dependent kinase inhibitor 1B (p27<sup>KIP1</sup>), among others, have been shown to bind to the N-terminal region of CK2 $\beta$  [131]. This study and others provide alternative mechanisms by which CK2 $\beta$  modulates the ability of CK2 to phosphorylate specific cellular targets. Moreover,



there are proteins that bind to CK2 $\beta$  in the absence of CK2 $\alpha$ , including Ser/Thr-protein kinases A-Raf (A-Raf) , c-Mos and check point kinase 1 (Chk1) [144–146]. These proteins contain a sequence of amino acids in the N-terminal which resembles the sequence present in the catalytic subunits CK2 $\alpha$  and CK2 $\alpha'$ .

*In vitro* phosphorylation by CK2 can be performed by the free CK2 $\alpha$  or by the tetrameric form and that is why CK2 substrates were classified in three groups [147]: CLASS 1 (phosphorylated only by CK2 $\alpha$  and CK2 $\alpha/\beta$ , the majority of the cases), CLASS II (only phosphorylated by CK2 $\alpha$ ) and CLASS 3 (only phosphorylated by CK2 $\alpha/\beta$ , a minority respect to CLASS I substrates).

### **1.2.2 Regulation of CK2 activity in cells**

A major controversial area has been the debate about CK2 activity regulation in cells. Then, CK2 is constitutively active, that is to say: CK2 activity is generally detected in cell or tissue extracts even in the absence of any stimulation factors [148]. Further studies have reported that CK2 responds to diverse stimuli, and that a number of different mechanisms contribute to its regulation. They include regulated expression and assembly, regulation by covalent modification and regulatory interactions by protein and/or non-protein molecules [137].

#### **1.2.2.1 Expression and assembly**

The regulatory subunit (CK2 $\beta$ ) controls the catalytic activity and substrate specificity of CK2, as well as the assembly of the CK2 tetramer. However, there have been evidences suggesting that the catalytic subunits of CK2 also exist in a free form and then, they could bind and phosphorylate specific proteins independently of the CK2 $\beta$  subunit [149].

It is clear that CK2 is involved in the regulation of cell cycle progression [150], and it is known that all CK2 subunits are expressed throughout the cell cycle [151]. It has been observed that, in several types of cells, CK2 $\beta$  is synthesized in a large excess over the catalytic subunit  $\alpha$ , and the fraction of  $\beta$  subunit that do not enters the tetramer is rapidly degraded [152, 153].

Moreover, it has been stated that CK2 $\alpha$  may regulate the transcription of the regulatory subunit, binding to a sequence upstream of the human CK2 $\beta$  gene, positively regulating its transcription. This notion is supported by more recent evidences, which indicate that the catalytic subunits of CK2 stimulate the expression of both CK2 $\alpha$  and CK2 $\beta$  genes [154], probably through the phosphorylation of transcription factors.

#### **1.2.2.2 Protein-protein regulatory interactions**

Large evidence suggests that protein-protein interactions represent a major mechanism for the regulation of specific protein kinases [155]. It is known that, directly or indirectly, CK2 is regulated by interacting proteins. There are different proteins that are identified as CK2-interacting partners, which could be considered in different categories: enzyme-substrate interaction, for instance nucleolar and coiled-body phosphoprotein 1 (Nopp140) [156], or other proteins like Heat shock protein 90 (HSP 90) that may directly alter or stabilize CK2 catalytic activity [157]. Another category of protein would be the ones involved in targeting CK2 to specific sites or structures within the cell, for example, tubulin [158]. Moreover, there are several proteins that interact specifically with CK2 in response to a stimulus which modulate its activity. This is the case of Peptidyl-prolyl cis-trans isomerase NIMA-interacting 1 (Pin-1), which interacts with CK2 in a phosphorylation-dependent manner [159]. CK2 also interacts with the facilitates chromatin transcription (FACT) complex in response to ultraviolet (UV) radiation [160].

#### **1.2.2.3 CK2 phosphorylation**

Although there is scarce support for the hypothesis that phosphorylation is required for CK2 activity [161], it has been shown that this mechanism may participate in the modulation of CK2 activity. In mammalian cells, CK2 $\beta$  and CK2 $\alpha$  are phosphorylated in a cell cycle-dependent manner at different sites [162]. Moreover, phosphorylation in the C-terminal region of CK2 $\alpha$

allows CK2 $\alpha$  to interact indirectly with Pin-1. This interaction does not appear to influence the activity of CK2, but modulates the activity of CK2 towards topoisomerase II $\alpha$  [159].

### **1.2.3 The localization of CK2 subunits**

CK2 is present at different sites within cells, and CK2 $\alpha/\alpha'$  and CK2 $\beta$  subunits are not always co-localized. For example, in mammalian cells, immunofluorescence studies have demonstrated that the three subunits of CK2 were localized to the smooth endoplasmic reticulum and the Golgi complex, whereas only CK2 $\alpha$  and CK2 $\alpha'$  subunits could be detected in the rough endoplasmic reticulum [163]. These studies reveal an asymmetric distribution of the individual CK2 subunits. Moreover, it has been shown that, despite there are predominant nuclear and moderated cytoplasmic localization of both CK2 subunit types, each of the CK2 subunits is independently imported and both are highly mobile within the nucleus. This subcellular localization of CK2 subunits is highly regulated and may be a key to its function and modulation towards specific substrates that are distributed in different cellular compartments (reviewed in [131]).

### **1.2.4 CK2 and cancer**

CK2, an oncogenic protein kinase, contributes to tumor development, proliferation, migration and invasion as well as apoptosis suppression in cancer [115, 164]. It is a constitutively active Ser/Thr kinase and elevated CK2 expression levels have been demonstrated in several cancer types in comparison with normal tissue [165–167]. Its overexpression has been also proved in human GBM biopsies compared to adjacent normal tissue [168]. Several explanations stated below support the relationship between CK2 and cancer processes.

#### **1.2.4.1 Role of CK2 in cell cycle and cell division**

CK2 has been functionally implicated in every stage of the cell cycle [169, 170], as antisense oligonucleotides directed against CK2 $\alpha$  or CK2 $\beta$ , as well as iCK2s block the cell cycle progression [171]. Evidence in mammals suggests that CK2 is required at multiple transitions

in the cell cycle ( $G_0/G_1$ ,  $G_1/S$  and  $G_2/M$ ) [172–174], and roles associated to CK2 in the  $G_2/M$  transition and mitosis come from the observation that CK2 is associated with the mitotic spindle and centrosomes [175, 176]. Additionally, CK2 does participate in the regulation of various stages of the cell cycle, presumably through the phosphorylation and regulation of proteins that have important functions associated with cell cycle progression. Examples could be p34<sup>cdc2</sup> or topoisomerase II [177, 178], cell cycle regulatory proteins identified as likely physiological targets of CK2.

#### 1.2.4.2 Function of CK2 in cell survival and apoptosis

CK2 has been demonstrated to be essential for cell viability, for example in an experiment in *Dictyostelium discoideum* [179] in which CK2 is essential for its vegetative growth. As well, in mammalian cells, forced expression of kinase-inactive CK2 $\alpha$  or CK2 $\alpha'$  also compromises cell proliferation events [180].

It appears that CK2 has a dual role in cell function, namely its involvement in growth and proliferation, as well as in suppression of apoptosis. The latter function of CK2 is of particular significance with respect to its role in neoplasia since CK2 has been found to be consistently elevated in cancer cells which are known to demonstrate remarkable resistance to death [181].

Taking into account that phosphorylation of CK2 can protect specific proteins from caspase-mediated degradation, it is not surprising that a robust similarity was found between the sequences of the recognition for caspase degradation and the CK2 consensus phosphorylation sequence. So, CK2 phosphorylates several proteins such as BH3-interacting domain death agonist (Bid), Protein max (Max) and PTEN, in a position close to the caspase recognition sequence, inhibiting such caspase cleavage [137]. Moreover, CK2 phosphorylation also directly affects proteins that are components of the apoptotic machinery. For instance, CK2 phosphorylates procaspase-2, preventing caspase activity by blocking its dimerization [182].

CK2 also impacts on apoptotic activity in cells mediated by chemical agents and also by physical stress, as forced overexpression of CK2 prior to treatment of cells with etoposide or diethylstilbestrol strongly protected them against apoptosis [183]. Analogous observations employing radiation or UV treatment of cells have reached similar conclusions [184]. It was previously suggested that CK2 may be involved in phosphorylation of ser-392 induced by UV damage of DNA [185]. In addition, recent documentation indicating that CK2 mediates DNA repair following single strand damage [186] may also be relevant for explaining its role in cell death regulation.

#### **1.2.4.3 CK2 and Epithelial-Mesenchymal Transition (EMT)**

The EMT is characterized by the loss of epithelial characteristics and the acquisition of mesenchymal characteristics: namely, loss of epithelial markers such as E-cadherin and the induction of mesenchymal markers including N-cadherin and vimentin are hallmark early-stage and late-stage events of EMT, respectively. During EMT, cells acquire invasiveness and migratory characteristics and elevated resistance to apoptosis. EMT is a necessary mechanism in embryonic development, but also is a major phenotype of cancer metastasis and invasion [187]. Although little is known about CK2 in the EMT mechanism, there is an increasing interest in its role in cell invasion and migration. Thus, it has been reported that CK2 $\alpha$  modulates cell proliferation and invasion by regulating EMT-related genes [188]. The progression from normal intestinal mucosa to adenocarcinoma in colorectal cancer is closely correlated with the EMT process and changes in the expression of a series of genes, such as E-cadherin, vimentin, and  $\beta$ -catenin [189]. Additionally, CK2 $\alpha$  knockdown decreases the expressions of snail1 and smad2/3, and the downregulation of snail1 and smad2/3 facilitates an increase in E-cadherin expression and EMT repression [188]. Another study has reported that CK2 $\beta$  downregulation induced EMT characteristics, such as morphological changes, and anchorage-independent growth, increased cell migration, as well as the induction of EMT-related markers including Snail 1 [190].

Moreover, another concept is emerging, pointing that the unbalanced expression of CK2 subunits may drive EMT, thereby contributing to tumor progression [190]. So, an imbalance of CK2 subunits resulting in the decrease of CK2 $\beta$  has been correlated with the induction of EMT-related markers, and CK2 $\beta$ -depleted epithelial cells display Snail-dependent EMT characteristics like morphological changes, enhanced migration, and anchorage-independent growth [190]. Thus, these studies support the notion that CK2 is a protein which may play an important role in processes related with EMT, for example cancer invasion and metastasis.

#### **1.2.4.4 CK2 in angiogenesis**

Angiogenesis is a biological mechanism by which new blood vessels arise from existing ones. Some of the normal situations where angiogenesis is important include wound healing, skeletal development and placenta formation during pregnancy. Even though, angiogenesis has a critical role in pathological processes, including tumor growth, as it provides oxygen and nutrients to new tumor cells. GBMs are among the most vascular tumors in humans, with angiogenesis being a known hallmark of the transition from a lower-grade to a higher-grade glioma [191]. In normal tissue and low-grade gliomas, there is a balance between proangiogenic and antiangiogenic factors, but at some point, a change in this balance occurs and causes the tumor to switch to a proangiogenic state [191]. It is believed that certain mutations in GBM, such as those involving PTEN, IDH1, and EGFR, may contribute to the angiogenic switch by helping to stabilize HIF-1 $\alpha$ , which leads to increased transcription of VEGF [191], Figure 1.10.

As said above, one of the most important extracellular factors that are required in this process is VEGF, which regulates the function of vascular and non-vascular cells and modulates different steps of angiogenesis [192]. There are some studies that support the notion that CK2 is a key protein in angiogenesis: proline-Rich-Homeo (PRH) domain protein inhibits the transcription of genes that are needed for VEGF-signalling, while PRH domain protein

phosphorylation by CK2 blocks its DNA binding activity and abrogates its inhibitory effect over VEGF signalling pathway components [193]. Besides VEGF, other factors are important in angiogenesis, such as fibroblast growth factor (FGF), which is a binding partner of CK2 $\beta$  subunit, or PDGF, which is also phosphorylated by CK2.

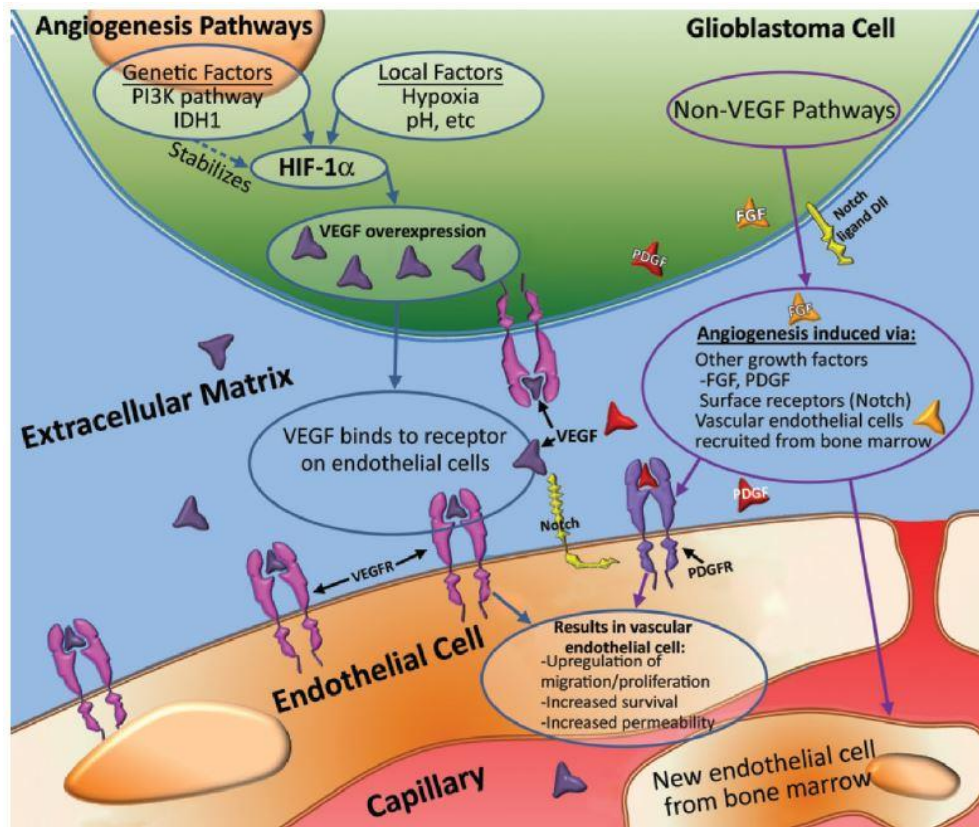


**Figure 1.10 Cellular mechanisms involved in angiogenesis in GBM.** The combination of genetic alterations and local factors results in increased HIF-1 $\alpha$  and, ultimately, VEGF shown in purple, which diffuses out of GBM cells to nearby VEGF receptors (VEGFR) shown in pink on capillary endothelial cells. This process that results in an increase in proliferation, migration, and survival of endothelial cells, as well as increased permeability. FGF: fibroblast growth factor, HIF-1 $\alpha$ : hypoxia-inducible factor 1 $\alpha$ , IDH1: isocitrate dehydrogenase 1, PDGF: platelet-derived growth factor and VEGF: vascular endothelial growth factor. Extracted from [192].

Therefore, it has been observed that inhibition of CK2 reduces endothelial cell proliferation, survival and migration and suppresses neovascularization in a mouse model of retinopathy

[194]. More recently, it has been described that CK2 inhibition by quinalizarin blocks vascularization of developing endometriotic lesions [195].

#### **1.2.4.5 CK2 and signalling pathways**

In cell survival regulation, apoptosis, autophagy, EMT, and angiogenesis, there are multiple signalling networks involved, in which CK2 assumes important roles. Notably, CK2 could have a role in the activation of the Wnt/ $\beta$ -catenin, phosphatidylinositol 3-kinase (PI3K)/AKT, janus kinase (JAK)/ STAT and nuclear factor kappa-light-chain-enhancer of activated B cells (NF- $\kappa$ B) pathways, which have been implicated in GBM development [196]. Despite this, the mechanism by which CK2 can affect these signalling pathways has not yet been fully understood.

##### **1.2.4.5.1 CK2 in NF- $\kappa$ B pathway**

The NF- $\kappa$ B/p65 transcription factors play critical roles in regulating the expression of a variety of genes involved in immune and inflammatory responses, cell proliferation, and apoptosis [197]. In addition, NF- $\kappa$ B signalling pathway is highly activated in GBM [196] and it is one of the signalling pathways which are linked with CK2 pro-survival effects.

NF- $\kappa$ B is normally sequestered in the cytosol by binding to its inhibitor I $\kappa$ B $\alpha$ , whose proteolytic degradation is therefore required before NF- $\kappa$ B is released and translocated to the nucleus where it will act as transcription factor for anti-apoptotic and pro-proliferative genes. Many extracellular stimuli, such as tumor necrosis factor (TNF $\alpha$ ), cause rapid phosphorylation of I $\kappa$ B $\alpha$  at N-terminal Ser residues leading to ubiquitination and degradation of the inhibitor. Nuclear translocation and DNA binding are apparently not sufficient to activate an NF- $\kappa$ B-dependent reporter, so *in vitro* studies suggest that TNF $\alpha$  induces phosphorylation of RelA/p65 that enhances NF- $\kappa$ B DNA binding ability [198].



CK2 activates the NF- $\kappa$ B pathway phosphorylating and promoting I $\kappa$ B $\alpha$  degradation [124]. Additionally, inhibition of CK2 reduced TNF $\alpha$ -induced phosphorylation of p65/RelA at ser592 and the expression of downstream targets, I $\kappa$ B $\alpha$  and IL-8 [124] which lead to NF- $\kappa$ B activation [199].

#### **1.2.4.5.2 CK2 and PTEN/PI3K/AKT cascade**

The PTEN/PI3K/AKT pathway is one of the most commonly deregulated pathway in cancer and it is involved in cell proliferation, resistance to apoptosis and EMT. This pro-survival signalling cascade can be activated in response to a variety of stimuli, including cytokines and growth factors [200]. About a 36% of GBM samples have mutations or homozygous deletions of PTEN and alterations of genes encoding subunits of PI3K [196] and high levels of phosphorylated AKT (p-AKT) have been reported to correlate with a poor prognosis in patients with GBM [201].

CK2 seems to act in multiple points within the PI3K pathway and it has a key role in promoting survival signals. CK2 can regulate AKT activity indirectly by controlling the activity of PTEN through proteasome-dependent phosphorylation, as well as activating AKT by direct phosphorylation [115]. The residues whose phosphorylation is known to be most responsible for Akt activation are Thr308 (in the activation loop), by 3-phosphoinositide dependent protein kinase-1 (PDK<sub>1</sub>) and Ser473, (in the hydrophobic domain outside the catalytic domain), by mammalian target of rapamycin complex 2 (mTORC<sub>2</sub>). It has been described that Akt can be further stimulated through phosphorylation of Ser129 by CK2 [202]. Thus, CK2 phosphorylates AKT at Ser129, which promotes cell survival by generating a constitutively active form of AKT [203]. In this situation, the pro-survival signalling of the PI3K pathway is continually active when AKT is phosphorylated by CK2 leading to the development of tumorigenesis [115].

PTEN is a tumor suppressor involved in the regulation of cell survival and found to be frequently mutated in a number of cancers. The major role of PTEN in tumor suppression is

through the negative regulation of the PI3K pathway that promotes cell survival [204]. Phosphorylation of PTEN by CK2 has been reported to result in the stabilization of PTEN in its inactive form. Therefore, phosphorylation of PTEN by CK2 is thought to inhibit PTEN activity and perpetuate the PI3K survival signal, leading to oncogenesis in affected cells [115].

#### **1.2.4.5.3 CK2 and JAK/STAT pathway**

The JAK/STAT pathway transmits signals from IL-6 family cytokines by activation of STAT-3, which induces expression of genes that regulate anti-apoptotic behaviour, angiogenesis and proliferation. It has been demonstrated that levels of activated STAT-3 are elevated in GBM tissues [205], and additionally, JAK1 and JAK2 are also activated in human GBM xenografts [206]. Evidence for cross-talk between CK2 and JAK-STAT signalling has been described, having CK2 the ability to intensify JAK/STAT signalling [207]. Moreover, CK2 inhibition, down modulates the NF- $\kappa$ B and STAT3 survival pathways [208].

#### **1.2.4.5.4 CK2 and Wnt pathway**

The Wnt signaling pathway plays an essential role in embryogenesis; however, when the pathway is activated in adult tissues, it promotes transformation and tumorigenesis [209].  $\beta$ -catenin and components of the Wnt canonical pathway are commonly overexpressed in GBM [210].

In turn, CK2 is involved in the reactivation of the Wnt pathway observed in some cancers. In the presence of a Wnt signal, glycogen synthase kinase 3  $\beta$  (GSK3 $\beta$ ) is inactivated, allowing in turn the phosphorylation of  $\beta$ -catenin by CK2, which is proposed to promote the dissociation of  $\beta$ -catenin from its chaperones [115]. This would allow the translocation of  $\beta$ -catenin to the nucleus, leading to the activation of transcription pro-survival factors such as c-Myc, c-Jun and cyclin D1. Phosphorylation of  $\beta$ -catenin by CK2 seems to be a pivotal event in the development of tumorigenesis by stabilizing  $\beta$ -catenin and protecting it from proteasome degradation [211].

Transgenic mouse models overexpressing CK2 present also overexpress  $\beta$ -catenin, leading to the development of mammary tumors [212].

The GSK3 $\beta$  is an AKT target, so when AKT is activated, translocates to the various subcellular compartments where it phosphorylates several targets, including GSK3 $\beta$ . Ser9 is the GSK3 $\beta$  phosphorylation site for AKT, and the phosphorylation of this residue leads to the inactivation of GSK3 $\beta$  and downregulated  $\beta$ -catenin expression and suppressed proliferation of GBM cells [213].

### **1.2.5 CK2 as a therapeutic target**

CK2 has emerged as a new therapeutic target due to the growing number of evidences that support its involvement in several biological processes, such as cancer development and progression [167], as stated in previous sections. There is an increasing interest in new ways to identify, or design, inhibitors of CK2 that may allow higher specificity against it. Over the last years, several inhibitors of CK2 have been described. These molecules can be classified in diverse groups, depending on the ability to bind to the adenosine triphosphate (ATP) site (ATP competitive inhibitors), or the other different regions (non-competitive inhibitors), as well as other alternative strategies which target the assembling part of the tetrameric holoenzyme complex or the regulatory subunit of CK2.

The ATP competitive inhibitors mimic adenine or adenosine, binding to the ATP pocket and blocking the interaction with substrates that would bind to the ATP site. Several chemical compounds have been developed as competitive inhibitors. The first competitive inhibitor developed was the nucleoside adenosine analog 5,6-1-( $\beta$ -D-ribofuranosyl) benzimidazole (DRB). Subsequently, inhibitors from a novel class were synthesized with higher specificity, one of them was TBB [116, 117] (molecular structure in Figure 1.11A). In addition, it has also been observed that natural compounds, such as flavonoids (APG, molecular structure in Figure 1.11B), are also potent inhibitors of CK2 [118, 119]. Although many ATP-competitive inhibitors

have been characterised, only CX-4945 [120–124] (molecular structure in Figure 1.11C) has entered phase II clinical trials as anticancer target<sup>3,4</sup>.

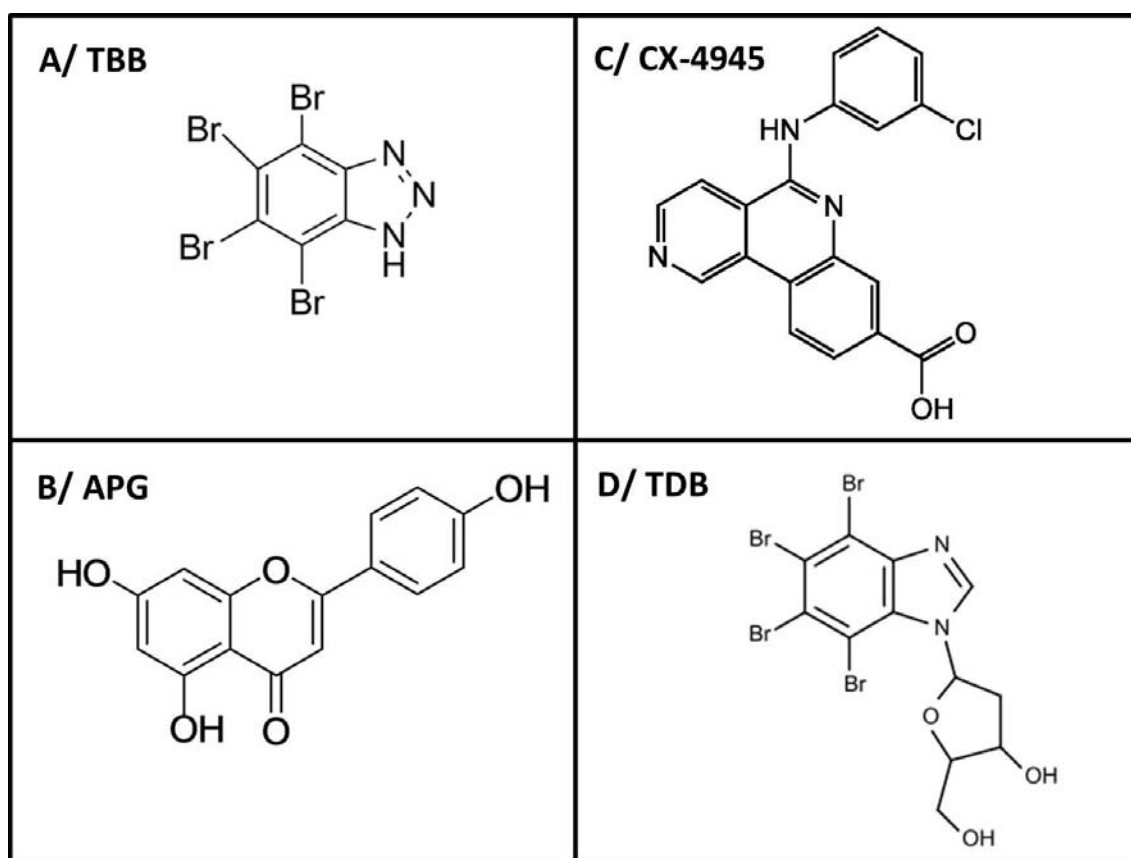


**Figure 1.11 iCK2s molecular structures. A)** TBB: 4,5,6,7-Tetrabromobenzotriazole, **B)** APG: apigenin (5,7-dihydroxy-2-(4-hydroxyphenyl)-4H-chromen-4-one), **C)** CX-4945: 5-(3-Chlorophenylamino)benzo[c][2,6]naphthyridine-8-carboxylic acid and **D)** TDB: tetra-bromo-deoxyribofuranosyl-benzimidazole.

Constitutive phosphorylation of AKT at Ser129 and Ser473 in GBM cells was inhibited by CX-4945 in a dose dependent manner [124]. Moreover, CX-4945 inhibited the activity of CK2 $\alpha$ /CK2 $\alpha'$ , suppressed cell cycle progression, angiogenesis and PI3K/AKT signalling, and exhibited antitumor activity in breast, pancreatic and prostate xenograft models [122, 123]

<sup>3</sup> <http://www.cancer.gov/clinicaltrials/search/view?cdrid=642699&version=HealthProfessional>

<sup>4</sup> <http://www.prnewswire.com/news-releases/cylene-presents-encouraging-clinical-data-for-oral-ck2-inhibitor-at-asco-123219423.html>

(please check section 1.2.5.2 for further details about the PTEN/PI3K/AKT cascade). In addition, CK2 phosphorylates JAK 1 and 2 promoting the JAK-STAT pathway activation [207] and regulates expression of IL-6 [214]. Moreover, CX-4945 treatment to human GBM cells reduced the JAK2 expression level, inhibited epidermal growth factor (EGF)-induced and IL-6-induced STAT3 and STAT5 activation [207].

Several studies have demonstrated the effect of CX-4945 as an antiproliferative agent, like *In vitro* studies of breast cancer [122]. In addition, studies of *in vivo* administration of CX-4945 to a subcutaneous leukemia xenotransplanted mice [215] and an intracranial murine glioma model [124] have also presented successful results for CX-4945. Moreover, other promising iCK2s are in development, such as TDB (molecular structure in Figure 1.11D), a dual inhibitor of CK2 and PIM-1 [125].

### **1.3 PRECLINICAL MODELS OF GBM**

The use of animal models in tumour research is mandatory in the search for new therapeutic targets due to obvious ethical restrictions related to human patients. It is not possible to perform repeated exams in patients afflicted with a brain tumour or to repeatedly collect biopsy samples at given time points of tumour growth/progression for research purposes, especially if surgical resection or chemotherapy are practicable. For this reason, animal models of human brain tumours have been developed to facilitate studies of tumour characterisation, progression and response to therapy.

The utility of any preclinical model depends on how closely it replicates the original human disease, and in Figure 1.12, a broad range of preclinical cancer models are shown. Ideal animal models of human glioma should be orthotopic and mimic relevant characteristics such as infiltration in the cerebral parenchyma that characterizes their aggressiveness. In this respect, subcutaneous models are known to provide over-optimistic therapy response results with respect to intracerebral models [216]. Subcutaneous implanted tumours experience a different micro-environment from the tissue of origin, and are not always able to recapitulate the originating phenotype. In this sense, intracranial brain tumours are no longer assessable by calliper measurements such as the subcutaneous ones, and rely on survival endpoints, which provide limited insight into tumour burden. To properly follow-up tumour evolution and response to therapy in intracranial brain tumor models, non-invasive techniques such as MRI should be used [217]. Bioluminescent methods to follow up orthotopic tumors growth are also available, but, the need for transformed cell lines, such as luciferase expression, has been reported to trigger an immune response on its own [218], complicating the evaluation of immune system associated parameters.

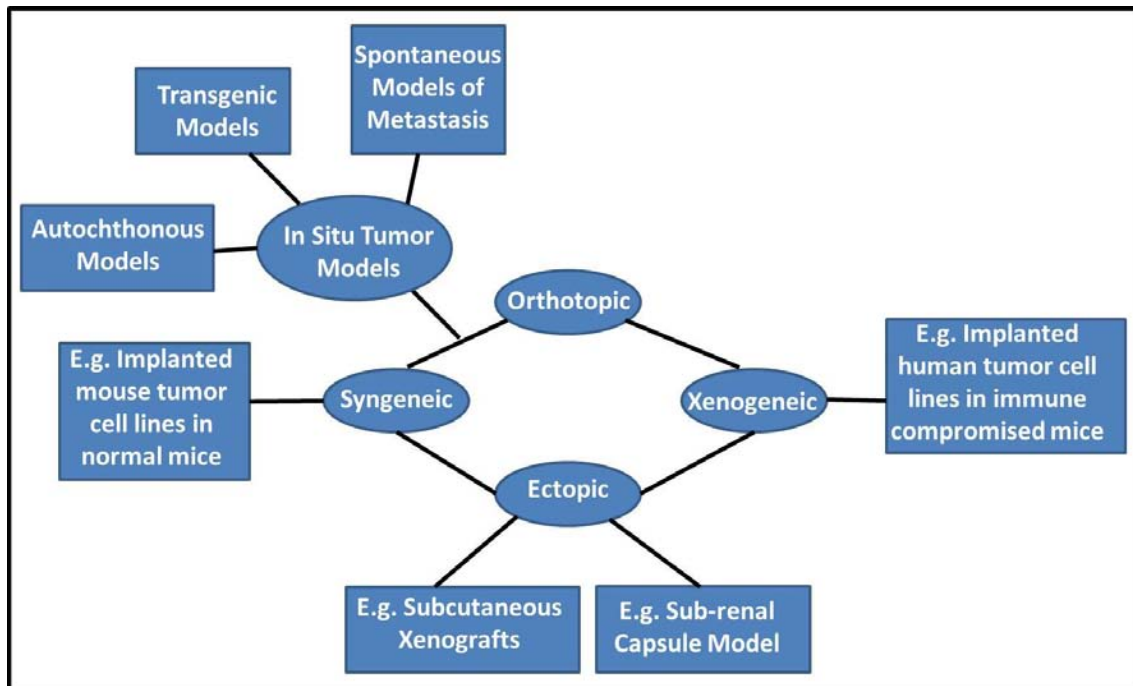


**Figure 1.12 Preclinical cancer models scheme.**

GL261 glioma cells growing in a C57BL/6 genetic background is one of the best characterised orthotopic allograft mouse models of malignant glioma [219, 220], resulting in tumors with invasive and infiltrative characteristics similar to those of human GBMs [221]. These tumors grow exponentially for about three weeks; after this period, the tumor kills animals due to mass effect. They probably belong to the “venerable” tumor classes [222] where no or few immunological effects are expected against the tumor when inoculating these cells in immunocompetent mice. Other models have been described, either through subcutaneous growth in immune-compromised mice [223] or through neurosphere culture, followed by intracranial stereotactic injection [224–227]. These immunodeprived mice models are widely used [228] to preclude remaining immune response effects. However, the use of these models also prevents the possibility of studying the role of the immune system in tumor progression or response to therapy. Nude mice, which are widely used for these models, have the Nu gene knocked out, resulting in animals unable to generate T lymphocytes [229]. Furthermore, the severe combined immunodeficient (SCID) mice lack functional T and B cells [230], and T cells have proven to be relevant in therapy response [231] (see also section 1.1.5.4). In this sense, it

is well known that the study of agents that trigger immune system response would require the use of orthotopic, syngeneic tumors in immunologically intact mice [232]. On the other hand, it is known that transplantable models, despite having the advantage of rapid tumor development and reproducibility, do not fully resemble the characteristics of angiogenesis and invasiveness of human brain tumors. A better recapitulation of human tumors is achieved with genetically engineered mouse (GEM) which arise spontaneously along animals life [233, 234] and reproduce the most common genetic modifications seen in human tumors [233]. Nevertheless, the lack of standardization in tumours developed by GEM, make it difficult to achieve a homogeneous group of tumor-bearing mice to evaluate therapy response effects. In addition, the experience of our group with GEM mice demonstrated a very low tumor incidence in one GEM mice, S-colony (*S100B-v-erbB/INK4A-ARF(+)*), reaching a value of 16% [235], being far from the initially described by the developers of this model (>90%, as reported in [234]).

Therefore, considering its advantages and disadvantages, the GL261 orthotopically implanted immunocompetent mice model was chosen for the work developed in this thesis. Although GEM models would indeed mimic better the spontaneous appearance of a tumour, the GL261 model presents a high incidence rate and produces homogeneous experimental groups to assess therapy response, which is not straightforward with GEM models. A relevant advantage is that the GL261 model growing into C57BL/6 mice, has been used for more than 20 years in different therapy evaluation approaches [221, 236, 237], and behaves as an immunocompetent model, which is suitable for assessing brain tumor metronomic therapies and their possible interaction with the host immune system. It is worth mentioning, however, that therapy response becomes more complex when the GBM is growing orthotopically inside the brain, compared to the ectopic inoculation, an environment which does not mimic intracranial conditions.



## 1.4 NUCLEAR MAGNETIC RESONANCE (NMR)

NMR, better known in clinical practice as MR, is a valuable research tool that has been used for the past decades to non-invasively investigate human tumors. The NMR phenomenon was first described by Bloch and Purcell, but it was only until 1970's, when Raymond V. Damadian invented the first whole-body MR scanner and performed a full human body scan, and Paul Lauterbur (Nobel Prize 2003) [238] generated the first usable NMR images. Since then, remarkable progress has been made in both technological improvements of the method itself and its applications, including MRI, MRS and MRSI, which provide *in vivo* medical images and metabolomics information about tissues, making as well an advance in cancer diagnoses.

### 1.4.1 Basic concepts and relevant parameters

The NMR phenomenon is based on the physical properties of atoms, having the property of absorbing radiofrequency (RF) energy which is released to their surroundings during the transition to their original state when they are placed in a magnetic field. This RF absorption property is determined by a quantum feature, present within nuclei of atoms with an odd number of protons and/or neutrons, and called the nuclear spin. These nuclei with spin different from zero are said to be MR active. In the biomedical research field, the most used MR active atoms are proton ( $^1\text{H}$ ), carbon ( $^{13}\text{C}$ ) and phosphorus ( $^{31}\text{P}$ ), because of their spin  $I = \frac{1}{2}$  and natural abundance (in case of  $^{13}\text{C}$ , this is low, 1.1%, but allows selective enrichment). So, if nuclei behave as charged particles in motion, those with non-zero spin have a magnetic moment ( $\vec{\mu}$ ) that have a magnitude and direction specific for each type of nucleus (Figure 1.13).

In the absence of an external magnetic field ( $B_0$ ), the magnetic moments are randomly oriented and the net magnetization is zero (Figure 1.14). When a  $B_0$  is applied, they orient either parallel or antiparallel to the applied field, in the case of nuclei with spin  $\frac{1}{2}$ . In a sample

containing a large number of nuclei, the lower energy state, with an orientation parallel to the  $B_0$ , is slightly more populated than the upper energy antiparallel state.

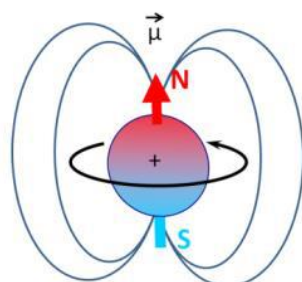


**Figure 1.13** Diagram representing a magnetic moment of a nucleus (caused by the rotation of the nucleus with a nuclear spin different from 0) resembling a magnet with north (N) and south (S) poles. Blue and red arrows show the magnetic field direction, Black circular arrow represents the rotation of the magnetic moment ( $\vec{\mu}$ ) around its axis. Circular blue lines represent the magnetic field. Extracted from [239].

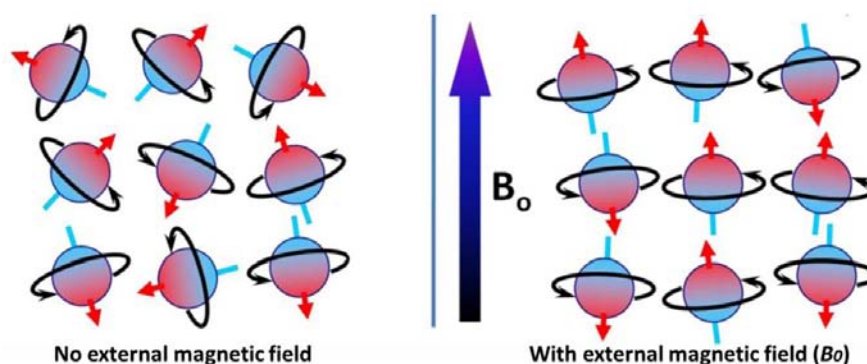


**Figure 1.14** Effect of an external magnetic field ( $B_0$ ) on the magnetic moments of a sample. Due to Brownian motion, the population of nuclei is oriented in all possible directions (left). Applying a  $B_0$ , the nuclei align in two different directions: parallel or anti-parallel to the field (right). Extracted from [239].

The resonance phenomenon is based on the ability of nuclei to transition between energy states. If an amount of energy equal to the difference in energies ( $\Delta E$ ) of the two nuclear spin orientations is applied to the nuclei, the transition between energy levels is induced. This is usually obtained by applying an additional magnetic field ( $B_1$ ) in the electromagnetic RF range,

as short pulses in the plane perpendicular to  $B_0$ . The absorption of energy by the nuclei spins causes transitions from lower to higher energy state.

The energy required to induce flipping and obtain an NMR signal should match the energy difference between the two nuclear orientations and it is shown in equation 1 to depend on the strength of the magnetic field  $B_0$  in which the nucleus is placed:

$$\Delta E = \frac{\gamma h B_0}{2\pi} \quad \text{EQ. 1}$$

where  $h$  is Planck's constant that correlates energy with turning (precession) frequency,  $\gamma$  is the gyromagnetic constant of the nucleus (varies from one nuclear isotope to another) and  $B_0$  is the external magnetic field. The Bohr condition ( $\Delta E = h\nu_0$ ) enables the precession frequency ( $\nu_0$ ) of the nuclear transition to be written as:

$$\nu_0 = \frac{\gamma B_0}{2\pi} \quad \text{EQ. 2}$$

Equation 2 is often referred to as the *Larmor equation*. Applying  $B_1$  in the direction of the  $xy$  plane, the net magnetization of the nuclei changes by an angle  $\theta$  (flip angle), changing the orientation of the net magnetization of the nuclei in thermal equilibrium ( $\vec{M}_0 = Mz$ ) to the transversal plane of magnetization ( $Mxy$ ) (Figure 1.15). When the RF ceases, the magnetization recovers its initial orientation emitting the energy absorbed during the transition through relaxation processes, described later in this section, while an electrical signal is collected by the receiving coil. Namely, the transverse component of the magnetization of the sample ( $Mxy$ ) revolves around  $B_0$  with the *Larmor frequency* and induces a small alternating current in a detection coil. Thus, the detected signal is obtained as an attenuated sinusoid, called free induction decay (FID), and must be processed mathematically by Fourier Transform (FT), which untangles all the different frequency components of the FID, transforming time domain signal to frequency domains. The frequency signal that is obtained after the FT is known as the MR

spectrum (Figure 1.16). This signal, proportional to the initial magnetization of the sample, is quite low considering the small differences between low and high energy populations, and amplification is needed before processing.

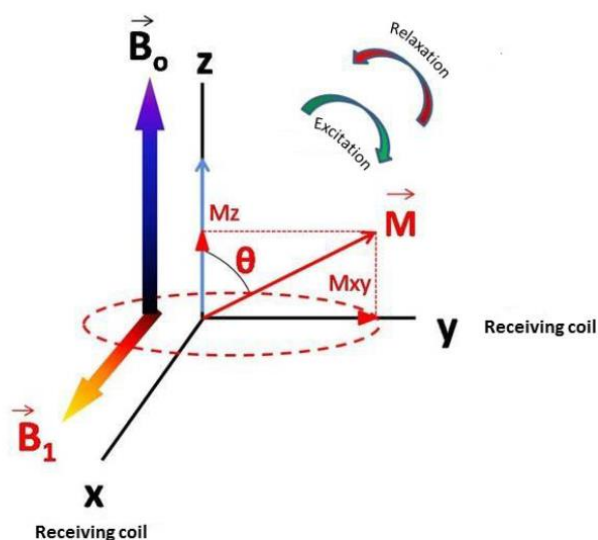


**Figure 1.15** Representation of the perturbation of the macroscopic magnetization of a sample in a coordinate system (rotating at the resonance frequency). Applying an additional magnetic field ( $B_1$ ) perpendicular to  $B_0$  and excitation causes net magnetization  $\vec{M}$  to move by an angle  $\vartheta$ , flipping it into the  $M_{xy}$  (transverse plane of magnetization). When  $B_1$  is removed, the system returns to its initial thermal equilibrium (relaxation). The transversal plane of magnetization ( $M_{xy}$ ) component will be collected by the receiver coils as alternating electrical current signal.  $M_z$ : longitudinal plane of magnetization. Taken from [239].

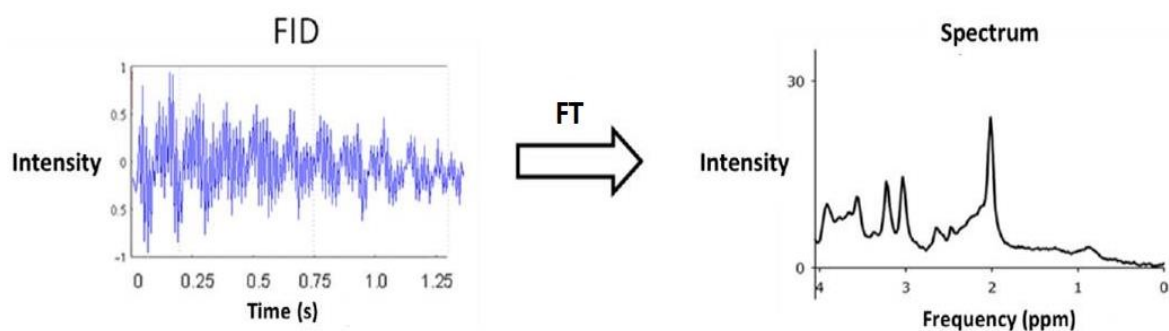


**Figure 1.16** Free induction decay (FID) transformation (left, time domain) recorded in an NMR experiment, to a spectrum (right, frequency domain), after application of the Fourier transform (FT). Extracted from [239].

### 1.4.1.1 Relaxation times

The relaxation phenomena determine the return to equilibrium of both longitudinal and transverse magnetization, called “spin-lattice” and “spin-spin” interactions, respectively. These two processes cause  $T_1$  relaxation and  $T_2$  relaxation respectively, and are exponential in nature with time constants  $T_1$  and  $T_2$ . These processes are relevant in the interpretation of tissue and spectral features in MRI and MRS.

#### $T_1$ relaxation time

$T_1$  relaxation or longitudinal relaxation describes the transfer of energy from the spin system to its surroundings, otherwise known as the lattice. The energy transfer process causes the longitudinal plan of magnetization ( $M_z$ ) to gradually recover exponentially towards its initial equilibrium value (Figure 1.17).

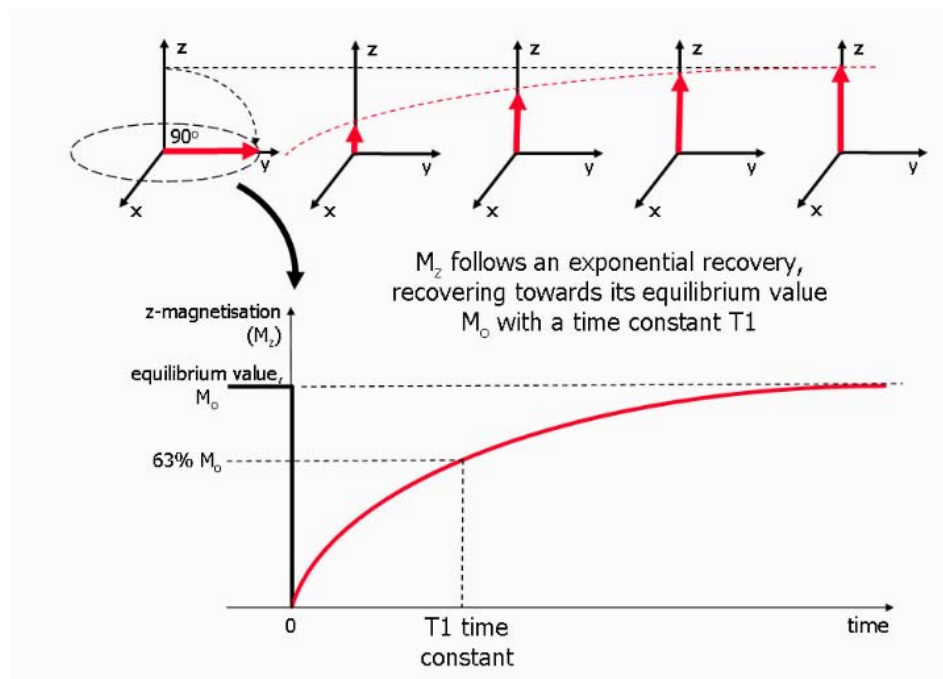


**Figure 1.17** Diagram showing the process of  $T_1$  relaxation after a  $90^\circ$  RF pulse is applied at equilibrium.

The  $z$  component of the net magnetization, longitudinal plane of magnetization ( $M_z$ ) is reduced to zero, but then recovers gradually back to its equilibrium value if no further RF pulses are applied. The recovery of  $M$  is an exponential process with a time constant  $T_1$ . This is the time at which the magnetization has recovered to 63% of its value at equilibrium. Taken from [240].

$T_1$  relaxation is also known as longitudinal relaxation or  $T_1$  recovery. The time it takes to recover 63% of the initial magnetization is called  $T_1$  relaxation constant. The  $T_1$  rate constant depends on the strength of the applied magnetic field  $B_0$ , tissue composition, structure, molecular motion and surroundings. Protons in different tissues and metabolites therefore have different  $T_1$  recovery rates. The repetition time between pulses determines the rate of signal recovery/signal saturation, which is important in tissue appearance (MRI) and metabolite absolute quantifications (MRS/MRSI).

### **$T_2$ relaxation time**

$T_2$  relaxation or transverse relaxation is defined as a time constant for the decay of transverse magnetization arising from natural interactions at the atomic or molecular levels within the tissue or substance of interest, used as measurement of those processes contributing to the transverse decay of MR signal. Each spin experiences the external magnetic field,  $B_0$ . However, one spin affects the other by slightly altering the magnetic field experienced by the second spin. Thus, these dipole-dipole interactions between magnetic moments cause the precession rates of the individual spins to vary slightly. The result is that they lose phase coherence and the resultant  $M_{xy}$  decays gradually to zero as shown in Figure 1.18. The time it takes the magnetization to decay a 37% of the initial phase coherence ( $M_{xy}$ ) is called  $T_2$  relaxation constant. However, the actual decay of global coherence is usually faster due local static variations (inhomogeneities) in  $B_0$ . Therefore, the actual time the system takes to lose 37% of the initial magnetization is called  $T_2^*$  relaxation constant (Figure 1.18).  $T_2^*$  can be considered as “effective”  $T_2$ , whereas the first  $T_2$  can be considered the “natural” or “intrinsic”  $T_2$  of the tissue analysed.  $T_2^*$  is always less than or equal to  $T_2$ .

Spin-spin relaxation time depends on the molecular environment of the spins, and so  $T_2$  for the resonance of interest vary between tissues. Free molecules (i.e. spins) in fluids influence the phase of each other less than if they were close to one another as in solids. Thus, fluids have

the longest  $T_2$  (on the order of seconds), and water based tissues are in the 40–200 ms range, while fat based tissues are in the 10–100 ms range. The echo time (TE) used in acquisition sequences (see section 1.4.2.1) will have an impact in tissue appearance (MRI) and also in metabolite intensity signals (MRS).

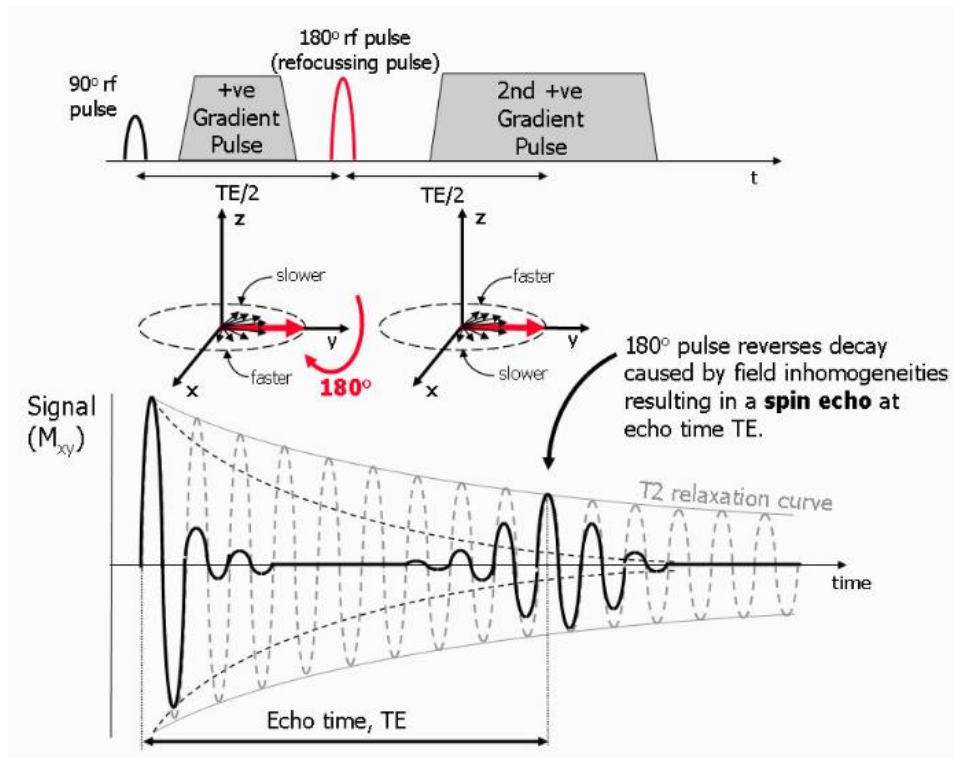


**Figure 1.18 Diagram showing the process of  $T_2$  relaxation.** The presence of magnetic field inhomogeneities causes additional de-phasing of the proton magnetic moments. The Larmor frequency is slower where the magnetic field is reduced and faster where the field is increased resulting in a loss or gain in relative phase respectively. After a period of half of the echo time (TE), the application of a  $180^\circ$  radio frequency (RF) pulse causes an instantaneous change in sign of the phase shifts by rotating the spins (in this example) about the y axis. As the differences in Larmor frequency remain unchanged, the proton magnetic moments then move back into phase over a similar time period, reversing the de-phasing effect of the magnetic field inhomogeneities to generate a spin echo. In addition to the effect of the  $180^\circ$  refocussing pulse, gradients are applied to de-phase and re-phase the signal for imaging purposes. Note that for spin echo pulse sequences, the second gradient has the same sign as the first, as the  $180^\circ$  pulse also changes the sign of the phase shifts caused by the first gradient. Still, the loss of signal due to intrinsic  $T_2$  relaxation mechanisms remains after refocusing. Extracted from [240].

$T_1$  and  $T_2$  relaxation occur simultaneously but are independent of each other. Nonetheless,  $T_2$  relaxation generally proceeds more rapidly than  $T_1$  recovery. For this reason, longitudinal magnetization can never be re-established until all the transverse magnetization has decayed away.

#### **1.4.2 Biomedical applications of NMR in cancer**

The most popular way of diagnosing brain tumors is by MRI, which apart from providing a spatial anatomic location of the tumor in its initial stages, provides an opportunity to noninvasively follow the tumor morphology and how it develops over time. NMR is a non-IR methodology and repeated explorations can be performed for patient follow-up. In addition, it can be used to measure parameters of physiological and biophysical interest, such as the cerebral blood flow or the diffusion coefficients of water. Complementary to MRI, MRS obtains physiological and biochemical information and metabolomics profile of the tissue under investigation. In addition, MRSI [241] combines both techniques and provides a two dimension (2D) or three dimension (3D) mapping of the spatial distribution of the metabolites in the region of interest (ROI). Furthermore, statistical pattern recognition (PR) techniques [242] are applied nowadays to perform automatic categorization of individual MRSI data (MR spectra) obtained from different types of tissue. This MRSI imaging capability may be relevant, since tumors are commonly heterogeneous. This PR approach can be applied to MRSI data [243, 244] both from human brain tumors and preclinical animal models.

##### **1.4.2.1 Magnetic resonance imaging (MRI)**

In clinical and research MRI,  $^1\text{H}$  atoms are most-often used to generate a detectable RF signal that is received by coils in close proximity to the anatomy being examined.  $^1\text{H}$  atoms exist naturally in biological organisms in abundance, particularly in water and fat. For this reason, most MRI scans essentially map the location of water and fat in the body and the intensity of the signals is converted in grey scale information which would shape and provide contrast to



the image. The RF pulses excite the nuclear spin energy transition, and magnetic field gradients are used in order to localize the signal in space. The intrinsic contrast of images obtained in MRI is primarily achieved due to differences in proton density (hydrogen concentration) between tissues of the sample under study, and also to their characteristic relaxation times ( $T_1$  and  $T_2$ ). Those differences, for example between normal tissues and tumors, result in contrast differences in the image.

There is a great variety of pulse sequences available for MRI, combining in different ways the recycling time (TR) (time between two RF excitation pulses) and TE (or echo time), elapsed between the application of the excitation pulse and the final signal collection, to obtain contrast. There are three major types of images, defined by the parameter in which the contrast is based, that can be generated during the classical MRI acquisition:  $T_1$ -weighted ( $T_{1w}$ ) (which is more sensitive to the standard anatomical details),  $T_2$ -weighted ( $T_{2w}$ ) (which is more sensitive to the water content and the presence of disease) and proton density weighted (Figure 1.19). As classical sequences used to obtain MRI images, spin-echo (SE) or gradient-echo (GRE) sequences can be found, and more optimized sequences to obtain higher resolution images in a reduced time, such as fast spin echo (FSE) or fast gradient recalled echo (FGRE) sequences are also available.

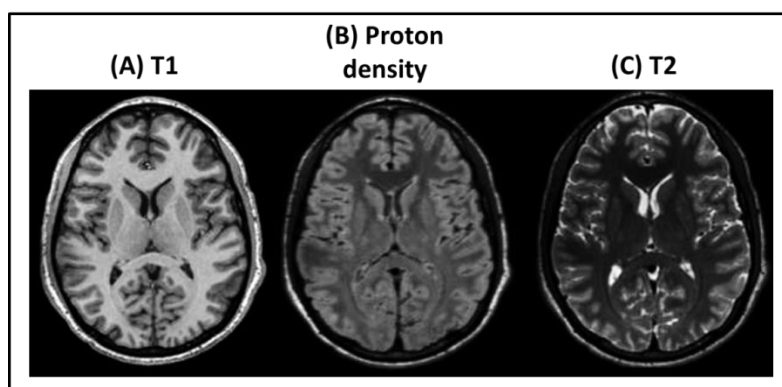


**Figure 1.19** Mice brain MRI in axial orientation showing how image weighting can be used to vary the contrast between grey matter, white matter and cerebrospinal fluid. (A)  $T_1$ -weighted, (B) proton density-weighted, and (C)  $T_2$ -weighted MRI sequences. Extracted from [245].

Moreover, the intrinsic contrast can be modified or enhanced with the use of contrast agents (CA) which increase the specificity and sensitivity of detection of abnormal masses. The most commonly used compounds for contrast enhancement in the clinical practice are gadolinium-based. Such MRI CAs alter the relaxation times of water in tissues following administration and therefore increase contrast. The CAs used in the clinical practice usually shorten the value of  $T_1$  of nearby water protons thereby producing signal intensity increase (positive contrast). CAs altering  $T_2$  (usually negative contrast) are less frequent in clinics, and several of them have been withdrawn or discontinued in preceding years. Most of the clinically available CAs are not able to cross an intact BBB, but they can reach a lesion if BBB is disrupted, also providing information about this parameter.

Nowadays a broad number of MRI techniques are being used, such as diffusion, perfusion, functional imaging, amongst others, designed for diagnoses and follow up of distinct pathologies. Only diffusion weighted imaging (DWI) will be reviewed, because no other specific MRI techniques were used in this thesis.

### **Diffusion weighted imaging (DWI) and Apparent diffusion coefficient (ADC) maps**

Nowadays DWI is included in the imaging protocol in some cases, since it has important diagnostic implications. For instance it can be helpful, jointly with MRS, in the differentiation of abscesses from tumors [246], as distinguishing brain abscesses from cystic or necrotic tumors is sometimes difficult with CT or MRI techniques alone.

Diffusion images are based in water molecules mobility, which have a random thermic movement (*Brownian movement*). This movement is isotropic in the free water. However, water movement in the brain is restricted due to limiting structures such as cell membranes. Thus, water has a preferred movement in the direction where there is no barrier, so an anisotropic movement may take place. Both restriction and anisotropy provide information of interest.

There are NMR specific sequences that permit to obtain a diffusion weighted image. These sequences incorporate a pair of gradients separated by one pulse and with a limited duration (Figure 1.20). To generate a diffusion-weighted image, the gradient effects cancel one another if spins are not moving, but if spins are moving, they experiment a change of phase with signal attenuation, which depends on the amplitude and the direction of the gradients applied, that can be in different directions (x, y and z) allowing anisotropy evaluation.

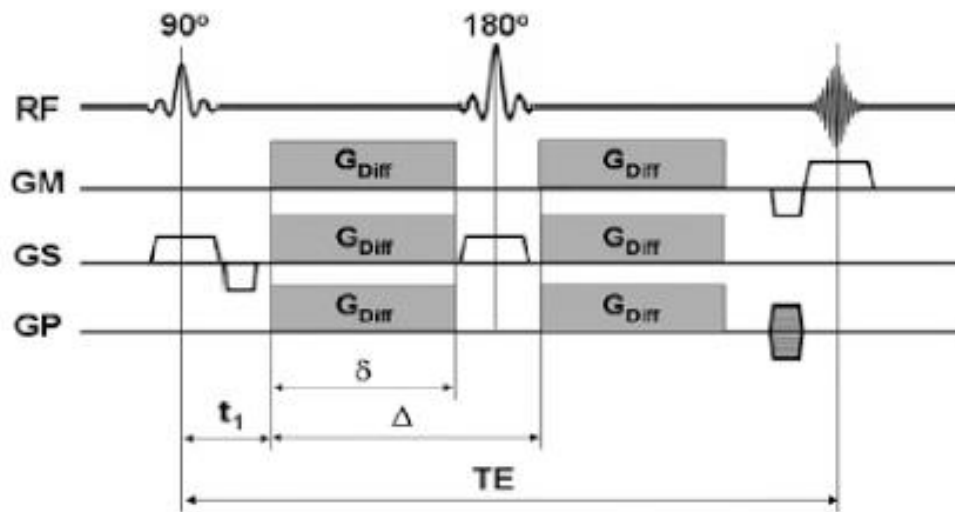


**Figure 1.20 Spin-Echo (SE) pulse sequence for acquisition of diffusion weighted imaging (DWI).** RF: radiofrequency pulse, GS: slice selection direction, GP: phase codification direction,  $G_{Diff}$ : diffusion gradient,  $t_1$ : time between application of the first RF pulse and the first diffusion gradient,  $\Delta$ : time between two diffusion-weighted gradients,  $\delta$ : application time of diffusion gradient and TE: echo time. Extracted from [247].

The diffusion sensibility is controlled by parameter “b” (EQ. 3) which determines the attenuation of the diffusion, which in turn depends of the duration time and the diffusion amplitude gradient. The attenuation also depends on the molecular translation magnitude and the diffusion ponderation. In equation 3,  $gd$  is the amplitude of the applied gradient,  $\Delta$  the time between gradients and  $\delta$  the duration of the gradient.

$$b = (\gamma^2 \cdot gd^2 \cdot \delta^2) \cdot \left(\Delta - \frac{\delta}{3}\right) \quad \text{EQ. 3}$$

As it is not possible to obtain the water diffusion coefficient from a unique image, different images with different b values are needed, maintaining constant the remaining experimental variables. Furthermore, in ADC maps, each pixel intensity is proportional to the apparent diffusion in the corresponding voxel. The hyperintense zones in ADC maps show higher coefficient of diffusion, which means that the signal loss in diffusion weighted images is directly proportional to the water diffusion coefficient value (example in Figure 1.21).

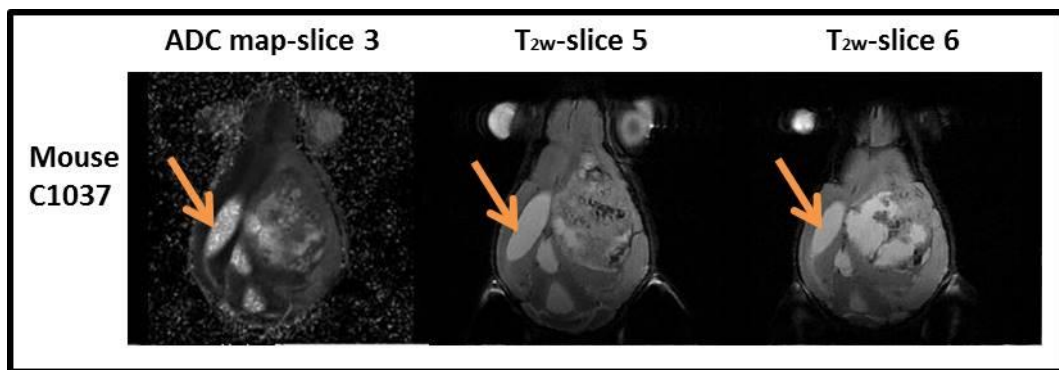


**Figure 1.21** Apparent diffusion coefficient (ADC) maps and  $T_{2w}$  axial images from the head of mouse C1037 harbouring a GBM during this thesis (see section 4.3.3 for further details). Ventricles have been marked with an orange arrow, and are high in mobile water with high ADC and long  $T_{2w}$  are seen as hiperintensity region both in ADC map and  $T_{2w}$  images. For ACD maps 5 coronal slices were acquired and for  $T_{2w}$  images, 10 coronal slices were acquired. Thus, ADC map-slice 3 and  $T_{2w}$ -slices 5 and 6, correspond in the same region.

#### 1.4.2.2 Magnetic resonance spectroscopy (MRS) and Magnetic Resonance Spectroscopic Imaging (MRSI)

MRI is the most used technique for diagnosis and management of brain tumors, providing detailed anatomic information. This can be supported by MRS and MRSI, which allow the biochemical characterization of tissues *in vivo* non-invasively, providing important clues about tumor biology and response to treatment. The suppression of the intense water signal allows the visualization of other metabolites of interest that are present in much lower concentrations. In Single voxel (SV) MRS, a spectrum is acquired from a small volume of tissue

defined by the intersection of three orthogonal planes. On the other hand, the MRS signal can be obtained from multiple voxels, multi-voxel (MV), giving rise to what is called MRSI, also named chemical shift imaging (CSI). MRSI is a powerful technique since it allows simultaneous visualization of the metabolic state of different regions of the tissue of interest, which may be superimposed to anatomical MRI acquisitions. MV localization techniques can be in one dimension (1D), 2D or 3D and produce a matrix of contiguous voxels. MRS, SV spectroscopy and 2D and 3D MRSI have been consistently used, in both, clinical [248] and preclinical studies [249].

### Chemical shift

In MRS the chemical shift is the resonant frequency of a nucleus relative to a standard at the same magnetic field and is informative about the chemical environment of the nucleus (e.g. proton) being measured. This makes it possible for metabolites to be distinguishable in a spectrum, and in turn differences in spectral pattern can be useful for distinguishing between different tissue types, classes of tumors, or the same tumor under different conditions (e.g. treatment).

When a nucleus is placed in a magnetic field,  $B_0$ , its electrons circulate in such a manner that there is an induced magnetic field,  $B_e$ , which opposes to the main field  $B_0$ . Thus the effective  $B = B_0 - B_e$ . It is therefore, said that the nucleus is shielded from the external magnetic field. The resonating frequency  $\nu_0$  varies because the actual magnetic field  $B$  at the nucleus is always less than the external field  $B_0$ . The extent of shielding is influenced by many structural features within the molecule. Put in the form of an equation this becomes:

$$\delta = \frac{\nu_s - \nu_R}{\text{spectrometer frequency}} \times 10^6 \quad \text{EQ. 4}$$

Where  $\delta$  is the chemical shift,  $\nu_{\text{SAMPLE}}$  is the resonant frequency of the sample and  $\nu_{\text{REF}}$  is the reference frequency of a standard compound, measured in the same applied field ( $B_0$ ). For the

reference frequency, conventionally, the tetramethylsilane (TMS) dissolved in organic sample may be used as a standard signal, which will have a chemical shift of zero if chosen as the reference. The shielding effect is expressed in terms of the chemical shift,  $\delta$ , in a part per million (ppm) scale independent of  $B_0$ , with respect to an internal or external reference. For aqueous samples or *in vivo* studies other references may be used. Accordingly, it is advisable to check the reference used in each instance for minor possible differences that may need correction for proper comparison to be made.

In the original continuous wave method of measuring NMR spectra, the magnetic field was scanned from left to right, from low to high values. This is often convenient to describe the relative positions of the resonances in an NMR spectrum. For example, a peak at a chemical shift,  $\delta$ , of 10 ppm is said to be downfield or deshielded with respect to a peak at 5 ppm, or if you prefer, the peak at 5 ppm is upfield or shielded with respect to the peak at 10 ppm (Figure 1.22).

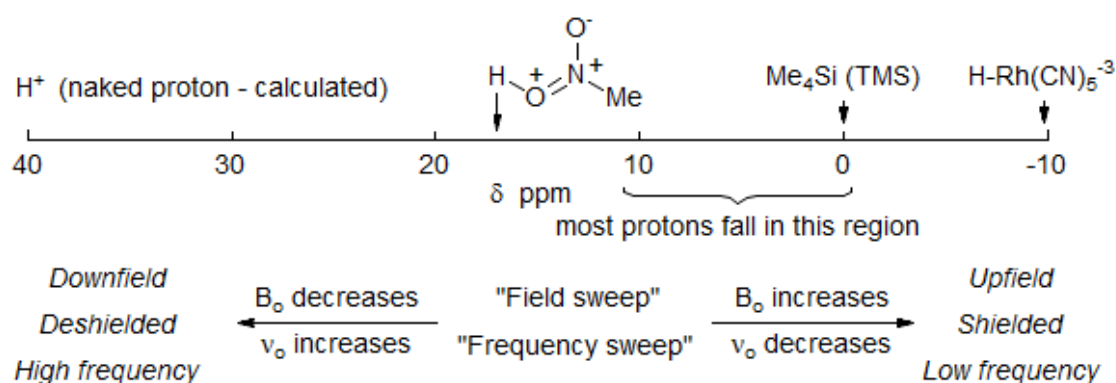


**Figure 1.22** Scheme of the magnetic field scanned from left to right, from low to high values. Signals on the right as upfield or shielded, and signals to the left as downfield or deshielded. Taken from [250].

## Resonances and biological significance of the major $^1\text{H}$ NMR detectable compounds of brain tissue

There is a long list of metabolites from which several resonances (also named peaks, signals) can be detected in human brain, human brain tumors and other pathologies in MR spectra (see Table 1.1 for an abrogated summary).

Metabolite	Abreviaton	ppm
Mobil Lipids and/or macromolecules	ML and/or MM	0.9, 1.3-1.4 and 2.0-2.9
Lactate	Lac	1.31 and 4.10
N-Acetylaspartate	NAA	2.01, 2.49, 2.67, 4.38 and 6.13
Glutamate	Glu	2.04, 2.12, 2.34, 2.35 and 3.74
Glutamine	Gln	2.11, 2.13, 2.43, 2.45 and 3.75
Creatine total	TCre	3.03 and 3.91
Choline total	TCh	3.19, 3.50 and 4.05
Myo-inositol	ml	3.26, 3.52, 3.61 and 4.05
Glycine	Gly	3.55

**Table 1.1 Summary of the most important metabolite resonances that can be found in human brain in vivo  $^1\text{H}$  spectra at 1.5T in human brain. Data extracted from [251].**

N-Acetylaspartate (NAA) with a peak at 2.01 ppm, is the largest signal in the normal adult brain spectrum, and usually represents neuronal functional integrity, being it reduced or absent in most brain tumors [252]. Elevated levels of choline-containing metabolites, total Choline (TCho) with a peak at 3.21 ppm, when compared to normal brain are indicative of tumors, as abnormal Choline metabolism with increased phosphocoline at 3.21 ppm is emerging as a metabolic hallmark that is associated with oncogenesis and tumor progression [253]. Total Creatine (TCre), presenting two signals at 3.03 and 3.91 ppm, is involved in energy metabolism and it is known to be decreased in tumors [254]. Lactate (Lac), with two signals around 1.31 and 4.10 ppm, is an end product of anaerobic glycolysis, usually present in brain tissue at low concentrations under normal conditions. Its signal increases in cases of hypoxia and blood flow impairment such as stroke, trauma, tumor, necrotic tissue and cystic masses [255] but also in tumor regions where the Warburg effect produces increased glycolytic flow [256]. Myo-inositol (ml), with a major signal around 3.52, is considered a glial marker and ml

levels have been shown to decrease with astrocytic grade *in vivo* between low-grade astrocytoma and GBM [257]. Glu with major resonance signals in the region 2.04-2.35 ppm acts as the major excitatory neurotransmitter in the CNS. In turn, glutamine (Gln) with major signals in the region 2.11-2.46, is a precursor and storage form of Glu located in astrocytes. Glycine (Gly), with a peak at 3.55, has an elevated concentration in certain gliomas [258]. Mobile Lipids (ML) and macromolecules (MM) resonances occur at various regions of the spectrum: around 0.9, 1.3-1.4 and 2.0 -2.9 ppm. *In vivo* NMR detectable ML are known to be significant markers of tumor malignancy. Their levels correlate with necrosis [259] which is a histopathological feature of high grade gliomas caused by hypoxic stress [260].

Despite metabolites differential expression enables the differentiation between tumor types [261], in this thesis, we will focus in one type of tumor (GBM) under different conditions (treated and non-treated), as small but consistent differences can be observed using MRS/MRSI [262]. Some metabolites, such as polyunsaturated fatty acids (PUFAs) [263], that in normal brain conditions display very low detectable content, appear to change in a consistent way after therapy is administered to brain tumors, as seen in SV spectra shown in Figure 1.23 and in [263].

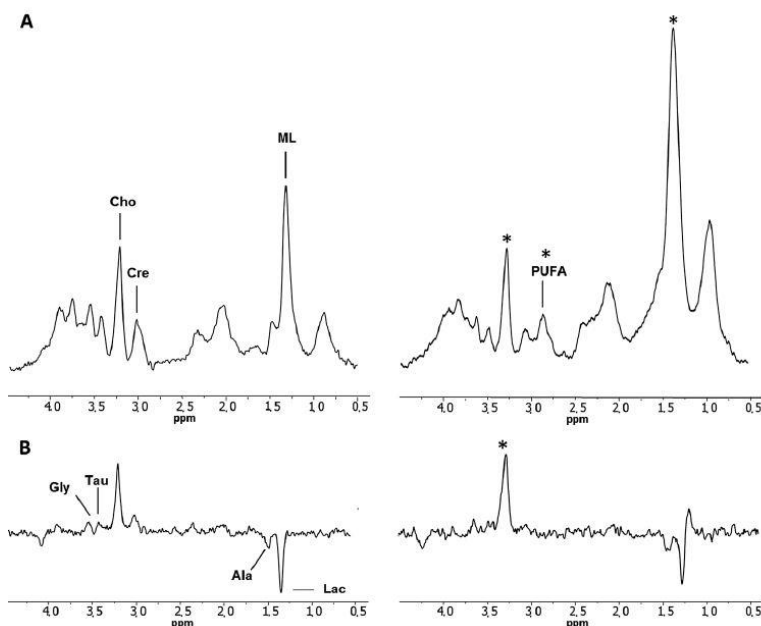




**Figure 1.23 Representative SV spectra** from mouse C356 GL261 GBM treated with 3-cycles of TMZ, at short **(A)** and long **(B)**  $T_E$ . Left, the spectra acquired before treatment; right, the spectra registered after therapy (day 28 p.i. of GL261 cells). The main resonances used for ratio calculations are labeled as follows: Cho (choline) at 3.21 ppm, Cre (creatine) at 3.03 ppm, MLs at 1.28 ppm, polyunsaturated fatty acids (PUFAs) at 2.82 ppm, Tau (taurine) at 3.42 ppm, Gly (glycine) at 3.54 ppm, Ala (alanine) at 1.45 ppm and Lac (lactate) at 1.32 ppm. The peak height ratios choline/creatine, PUFA/Cre and ML/Cre were significantly higher in short  $T_E$  spectra after treatment. The Cho/Cre ratio was also significantly higher in long  $T_E$  spectra after treatment in comparison with spectra acquired before treatment. Significant differences for peak height ratios between pre and post therapy are marked with an asterisk. Extracted from [237].

#### 1.4.2.3 Pattern recognition (PR) analysis of NMR data

Classification methods for data vectors are usually described under the general heading of pattern recognition (PR), a term which encompasses a wide range of techniques which try to find patterns in groups of data and to distinguish between different subgroups. Once these patterns are identified, they can be used to assign unknown individuals to a particular classification. In certain instances the term “machine learning” is also used for this purpose.

The analysis of metabolites through MRS gives access to biochemical information about specific processes ongoing within the evaluated pathology. Accordingly, PR is the process of classifying input data into categories or classes based on key features. Nonetheless, the richness of information contained in MRS spectra presents difficulties to interpret the measurements and associated changes in more than a few metabolites within a particular clinical condition. Coupling the techniques of MRS with reliable algorithms of PR allow to identify relationships between the quantitative changes of different metabolites simultaneously and detect even small differences in metabolic profiles. There are three major classification strategies used in PR: supervised, unsupervised and semi-supervised classification.

### **Supervised PR**

The supervised PR methods involve the use of a known training group of cases to develop a mathematical model. A new data vector (e.g. a spectrum) is assigned to a certain class based on a previous classification, so, for brain tumor spectra this is normally done through histopathological analysis criteria [264]. Once trained, the classifier and the mathematical algorithms can be tried for validation of samples assigning the input data to appropriate class labels and comparing those with gold standard reference values [265].

Supervised classification basically consists of three steps: First step, dimensionality data reduction, allowing the detection of the relevant characteristics of spectra that may better represent one class. Secondly, spectra classification in different classes taking into account differential descriptive characteristics and, last, evaluation of the robustness of the classification in terms of their descriptive characteristics (which allows discrimination of differences between groups) and predictive (allowing to assign a new spectrum to one of the previously established classes) [261]. Several types of supervised techniques exist that can be applied to MR data, but the most classical one is Linear Discriminant Analysis (LDA) [266].

### **Unsupervised PR**

The main difference between the unsupervised and supervised methodology is that in the unsupervised case, the investigator does not assign the possible training cases to a determined class. Instead, classes are created in base of similar patterns between different cases with clustering of them. Thus, unsupervised classification is performed without using prior information (for example, regarding tumor type and grade in case of brain tumors); it tries to group cases based on their similarities between each other, without knowing the exact final grouping structure. The similarity measure can be based on the distance of the samples in the multi-dimensional feature space constructed by the observed data features. Clustering techniques, such as Principal Component Analysis (PCA) [242] or non-negative matrix

factorization (NMF) [267] are examples of common unsupervised techniques. These NMF techniques offer an advantage, as each class is represented by a complete spectroscopic pattern characteristic “metabolic state”, called source. From the biochemical point of view, the source extraction technique to classify MRS data assumes that in each voxel there is a mixture of heterogeneous tissues pattern and the contribution of each source to the final pattern can be calculated [249]. The obvious advantage of this approach lies in the fact that the labelling procedure becomes independent of the availability of labelled MRSI datasets and the negative effect of mislabelled cases on the generalization capabilities of the model will be prevented.

### **Semi-supervised PR**

The semi-supervised PR methodology as described in [268] makes use of both labelled and unlabelled data for training and proposes to take benefit from the use of prior knowledge derived from class membership of the spectra to guide the source extraction. The first stage is the definition of a Fisher Information (FI) metric [269] to model pairwise similarities and dissimilarities between data points, using a Multi-Layer Perceptron (MLP) classifier to estimate the conditional probabilities of class membership. Second part would be the approximation of the empirical data distribution in an Euclidean projective space in which NMF-based techniques can be applied. This was done in [268] with Multidimensional Scaling methods, specifically with the iterative algorithm and the last part is the application of Convex-NMF for the source decomposition of the data.

#### **1.4.3 Nosological imaging of the response to therapy**

Molecular imaging of tumours based on the objective classification of MRSI data brings us closer to the nosologic imaging concept [237, 248]. The PR analysis of different spectra of treated and untreated animals can be used to classify which voxels from MRSI matrices correspond to each class, namely normal brain tissue, treated/responding and untreated/unresponsive tumour [262]. For the analysis, each individual voxel in the MRSI grid

was referred to as spectral vector (spv) and considered as an individual case. After the PR studies, the classification result obtained for each voxel was colour-coded and represented as nosological maps for each matrix. For the generation of colour-coded nosological images of each individual mouse the colour assigned was the one corresponding to the source which was contributing most to each voxel being either responding or untreated/unresponsive/relapsing or normal brain. Nosological images were produced throughout the course of therapy to track full or partial response changes (in case of treated animals). Nosological images were also produced for untreated control animals for comparison (an example is shown in Figure 1.24).

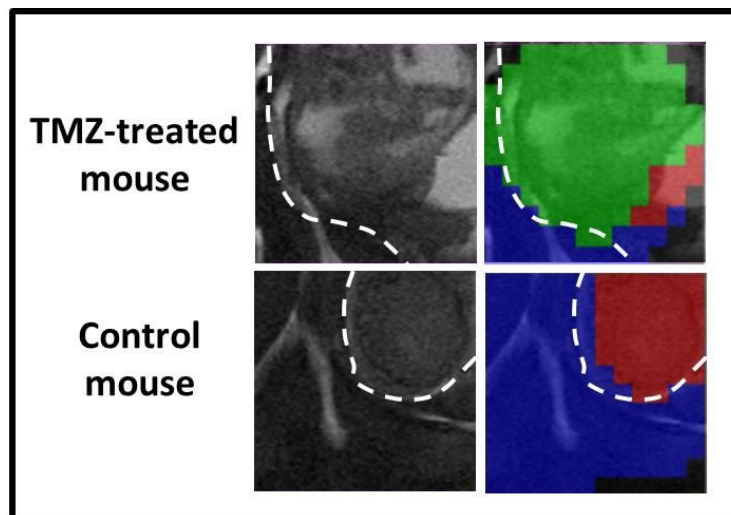


**Figure 1.24** Examples of nosological semi-supervised maps corresponding to mice C967 (control GL261) and C1011 (GL261 responding to TMZ). The Cxxx notation corresponds to the internal research group unique mouse identifier code. The boundaries of the T<sub>2w</sub> abnormal masses are marked with a white discontinuous line. On the left of each map, the high resolution T<sub>2w</sub> images used as references for MRSI studies are shown. For each map, colour coding is as follows: blue represents normal tissue, red, actively proliferating tumor, green, tumor responding to therapy, and black undetermined tissue.

## **2 GENERAL OBJECTIVES**

The major goals of this thesis were:

1. Optimization of therapy response in C57BL/6 mice bearing GL261 GBM, mainly through the use of iCK2s or using chemotherapy, both, alone or in combination.
2. Improvement of non-invasive protocols for therapy response monitoring using MRSI-based PR techniques and nosological imaging.



### 3 GENERAL MATERIALS AND METHODS

This section describes the common materials and methods used in different experimental parts (chapters) described in this thesis. Further on, each chapter contains specific materials and methods for the work described in that particular section. Cross references will be stated towards general materials and methods, in case of need, to avoid repeating methods already described here.

#### 3.1 GL261 cells

GL261 mouse glioma cells were obtained from the Tumor Bank Repository at the National Cancer Institute (*Frederick, MD, USA*). These cells had been previously used and characterised by our group [220, 270] and the work with this cell line was continued due to their highly reproducible behaviour (close to 100% penetrance) in generating high grade gliomas (GBM) when implanted into wt C57BL/6 mice.

The cells were cultured in flasks of 75 cm<sup>2</sup> (*Nunc, LabClinics SA, Barcelona*), and were grown as previously described in [270], using Roswell Park Memorial Institute (RPMI)-1640 medium (*Sigma-Aldrich, Madrid, Spain*) supplemented with 2.0 g/L of sodium bicarbonate, 0.285 g/L gln, 1% penicillin-streptomycin (all from *Sigma-Aldrich, Madrid, Spain*) and 10% fetal bovine serum (FBS) (*Gibco, Invitrogen, UK*). The time period to reach confluence (i.e. cells covering 75-85% of the flask surface) was 7 days from the time of subculture (day 0). The culture medium was changed on the days 3 and 5. Cell cultures were incubated at 37°C in a 5% CO<sub>2</sub> and 95% humidity (*incubator HERAcell, 150i, Thermo Scientific*). Upon reaching confluence, cells were subcultured; the medium was removed by aspiration with a vacuum pump and the cells were washed with 10 ml of sterile phosphate buffered saline (PBS). Then, after removing PBS, cells were detached from the flask using 2 ml of trypsin-ethylenediaminetetraacetic acid (EDTA) (0.5 g/L and 0.2 g/L, respectively) (*Sigma-Aldrich, Madrid, Spain*) and resuspended in 8 ml RPMI medium (10 ml total volume of resuspension). The resuspension, containing ca. 7x10<sup>5</sup> cells,

was seeded into new flasks containing 25 ml RPMI medium. Cells were subcultured until passage 40, at which time they were discarded to avoid possible accumulation of genetic alterations. In this case, a new aliquot was thawed from an initial amplification made at the start of cell culture work for this thesis.

### **3.1.1 Cell count**

The cell counts were performed in the TC20™ automater cell counter (*Biorad, Hercules, California*) using Trypan Blue dye (*Sigma-Aldrich, Madrid, Spain*) to distinguish viable from dead cells, since the latter are not able to extrude the dye and appear dark blue when observed in the screen, being also detected by the counter. Aliquots of 20 µl of a cell suspension, obtained during the subculturing step described above (Section 3.1), were added to 20 µl of Trypan Blue dye. A volume of 10 µl of the mixture was added to each side (duplicate samples) of the cell counting slide (*Biorad, Hercules, California*). The number of cells/µl was obtained for each sample, and numbers were averaged.

### **3.2 Animal Model (GL261 cells growing into C57BL/6 mouse)**

Animals used for this work were C57BL/6 female wt mice weighting 18-24g and aged 12-16 weeks, which were obtained from Charles River Laboratories (*Charles River Laboratories Internacional, l'Abresle, France*) and housed in the animal facility of the *Universitat Autònoma de Barcelona*. The wt C57BL/6 mice were used either as control animals or to generate the stereotactically induced tumors as described in section 3.2.1.

The experiments were conducted according to experimental protocols, previously approved by the local ethics committee (*Comissió d'Ètica en l'Experimentació Animal i Humana*) according to regional and state legislations (protocol DMAH-8236/CEEAH-2785). The protocol of supervision of laboratory animals described in Annex 1 was followed by the *Servei d'Estabulari* veterinary staff to assess mice physical state and to inform the researcher whether the



ethanization of an animal was recommended and halting of the experimental protocol should be considered.

Each mice evaluated was given a unique alphanumeric identifier. For example, identifiers of the type CXXX belong to mice bearing GL261 tumors and WTXXX to wt mice without tumors. In order to differentiate animals in the same cage, unique ear notch combinations were made with an ear punch device. For this, 1, 2 or 3 notches and their combinations were made in one or both ears, as shown in **¡Error! No se encuentra el origen de la referencia..**



**Figure 3.1** Scheme for unique identification in mice by ear punching.

### 3.2.1 Generation of tumors by stereotactic injection of cells

After the cell counting (Section 3.1.1), the cell suspension was transferred into a 15ml Falcon tube (*Deltalab SLU, Barcelona, Spain*) and centrifuged 1.5 minutes at 1,400 x g (*Centrifuge Selecta S-240, ALCO, Terrassa, Spain*). The supernatant was removed and the pellet resuspended in the RPMI medium, so that each 4 $\mu$ l contained 10<sup>5</sup> of cells, according to the equation 5:

$$V_f = (4\mu\text{l} \times C_f)10^5 \quad \text{EQ. 5}$$

where  $V_f$  is the volume of the medium for cells to be resuspended in  $\mu$ l and  $C_f$  is the total number of cells in the pellet obtained with the automated cell counter (section 3.1.1).

Analgesia was administered subcutaneously to each animal 15 minutes prior to anaesthesia and also 24 and 48 hours after surgery, with meloxicam (*Metacam, Boehringer Ingelheim*), at 1.0 mg/kg. The animals were anesthetized with a mixture of ketamine (*Parke-Davis SL, Madrid*) and xylazine (*Carlier, Barcelona, Spain*) (80 and 10 mg/kg, respectively) administered intraperitoneally, and after that, mice were immobilized in a stereotaxic holder (*Kopf Instruments, Tujunga / CA, USA*), as shown in Figure 3.2. Afterwards, the head area was shaved and the incision site was sterilized, a 1 cm incision was made exposing the skull, and a 1 mm hole was drilled 0.1 mm posterior to the Bregma and 2.32 mm lateral (right) to the midline using a microdrill (*Fine Science Tools, Heidelberg, Germany*). A 26G Hamilton syringe (*Reno/NV, USA*), positioned on a digital push-pull microinjector (*Harvard Apparatus, Holliston/MA, USA*) was then used for injection of 4  $\mu$ l RPMI medium containing  $10^5$  GL261 cells at a depth of 3.35 mm from the skull surface at a rate of 2  $\mu$ l/min. Once the injection was completed, the syringe was left untouched for two additional minutes before its removal, in order to allow the cells to settle and to prevent them from leaking outside the skull. Then, the Hamilton syringe was gently taken out, the scission site closed with suture silk 5.0 (*Braun, Barcelona, Spain*) and the animal was left in a warm environment ( $\sim 25$  °C) to recover from anaesthesia.



**Figure 3.2** A C57BL/6 mouse immobilized in a stereotaxic holder.

### **3.3 Tissue preservation for post-mortem procedures**

When tumor-bearing animals died or were euthanized by cervical dislocation (refer to annex 1 for the criteria used to decide about animal euthanization) due to symptoms of suffering, the brains were excised and either fixed or frozen. In case of fixation, tissue was preserved in 4% formaldehyde and embedded in paraffin until further histopathological analysis (Hematoxylin-Eosin (HE) staining). In case of freezing, tumors were dissected away and separated from contralateral normal brain parenchyma, and in some cases cerebellum was also dissected. These tissues were resected after visual inspection of the whole brain and tumor, avoiding as much as possible the crossed contamination of tissues. Samples were frozen in a liquid nitrogen container, for further CK2 activity and expression analysis. Histopathological analysis was done under supervision of Dr. Martí Pumarola (*Departament de Medicina i Cirurgia Animals, Universitat Autònoma de Barcelona*).

### **3.4 *In vivo* MRI/MRS/MRSI**

MR studies were carried out at the joint NMR facility of the Universitat Autònoma de Barcelona and CIBER-BBN (*Cerdanyola del Vallès, Spain*) Unit 25 of the ICTS NANOBIOSIS (<http://www.nanbiosis.es/>) with a 7T horizontal magnet (*BioSpec 70/30, Bruker BioSpin, Ettlingen, Germany*) equipped with actively shielded gradients (B-GA12 gradient coil inserted into a B-GA20S gradient system) and a quadrature receive surface coil, actively decoupled from a volume resonator with 72 mm inner diameter.

Mice were placed in the scanner bed and anesthetized with 0.5-2.0% isoflurane in O<sub>2</sub>, keeping the respiratory frequency at 60-80 breaths/min. The body temperature was controlled using a recirculating water system incorporated to the animal bed. Breathing was constantly monitored (*SA Instruments, Inc., New York, USA*).

### 3.4.1 MRI acquisition

GL261 tumor-bearing mice were screened by acquiring high resolution (HR) coronal  $T_{2w}$  images (TR/TE<sub>eff</sub> = 4200/36 ms) using Rapid Acquisition with Relaxation Enhancement (RARE) sequence to detect brain tumor presence and monitor its evolution stage. The acquisition parameters were as follows: turbo factor: 8, field of view (FOV): 19.2 x 19.2, mm matrix size (MTX): 256 x 256 (75 x 75  $\mu\text{m}/\text{pixel}$ ), number of slices: 10, slice thickness (ST): 0.5 mm, inter-slice thickness (IT): 0.6 mm, number of averages (NA): 4, total acquisition time (TAT): 6 min and 43 s.

MRI data were acquired and processed on a Linux computer using ParaVision 5.1 software (Bruker BioSpin GmbH, Ettlingen, Germany).

#### 3.4.1.1 Tumor volume calculation from MRI acquisitions

The tumor area was calculated in each slice, using an automated system for generating ROIs available in the Paravision 5.1 software. The IT volume was not registered and it was estimated adding the IT to the corresponding ST in Equation 6 (Figure 3.3).

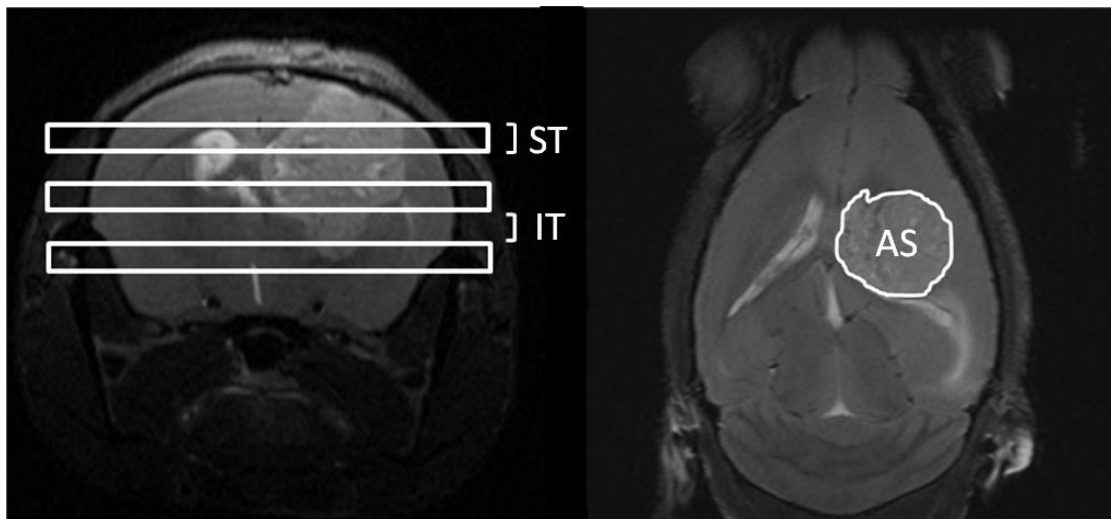


**Figure 3.3** Scheme of the tumor volume measurement. HR axial  $T_{2w}$  images (right) were acquired for this purpose. The surface area (AS) of the tumor (white line contour at right) was measured in each slice of the axial sequence. The slice thickness (ST) and the inter-slice thickness (IT) (represented by horizontal slices over a coronal image on the left) were taken into account for final volume calculation.

Tumor volumes in the evaluated mice were calculated from  $T_{2w}$  HR axial images using the following equation:

$$TV (mm)^3 = [(AS_1 \times ST) \pm [(AS_2 \pm (\dots) \pm AS_{10}) \times (ST \pm IT)]] \times 0.075^2 \quad \text{EQ. 6}$$

where  $TV$  is the tumor volume, the surface area ( $AS$ ) is the number of pixels contained in the ROI delimited by the tumor boundaries in each slice of the MRI acquisition,  $ST$  is 0.5 mm,  $IT$  is 0.1 mm and  $0.075^2 \text{ mm}^2$  the individual pixel surface area.

### 3.4.2 MRS/MRSI

MRS and MRSI methodology have been described in detail in specific materials and methods of chapter 4.3 (section 4.3.2).



## **4 RESULTS**

### **4.1 CK2 CONTENT IN GBM**

Most of the content of this section have been published in the *Pathology and Oncology Research Journal*, entitled “*Protein CK2 content in GL261 mouse glioblastoma*” by Ferrer-Font L, Alcaraz E, Plana M, Candiota AP, Itarte E and Arús C. The published manuscript can be found in Annex 2.

#### **4.1.1 Specific objectives**

- To assess the CK2 content in GL261 GBM compared to mice normal brain parenchyma, in order to check if CK2 could be a suitable target for the treatment of these tumors.

#### **4.1.2 Specific materials and methods**

##### **Animal Models**

A total of 6 C57BL/6 female wt mice that weighed  $18\pm 2$  g were used for this study. Tumors were induced in 3 C57BL/6 mice by intracranial stereotactic injection of  $10^5$  GL261 cells in the caudate nucleus, as previously described in general materials and methods (section 3.2.1). Tumor volumes were followed using  $T_{2w}$  MRI acquisitions, until the tumor reached the desired size to be able to obtain enough tumor sample and normal brain parenchyma sample for WB studies. This was equivalent to a tumour of about  $77.3\pm 10.9$  mm<sup>3</sup> (15 days after implantation), taking into account previous work from our group. Both tumor-bearing and wt animals were euthanized, their brains were removed and tumor resected (in case of tumor-bearing animals). The brain parenchyma from three wt mice was used as control, while contralateral brain parenchyma from tumor-bearing animals was employed to determine the possible effects outside the tumor volume, as recently described by other authors [271]. The contralateral tissue was obtained after visual inspection of the whole brain and tumor, avoiding as much as possible the tumoral zone. Samples were stored in liquid nitrogen until further processing.

### **Protein extraction**

Tissue samples were weighed and 250 µl of cold lysis buffer for each 100 mg of tissue was added (cold lysis buffer: 50 mM Tris-HCl pH 7.7, 150 mM NaCl, 15 mM MgCl<sub>2</sub>, 0.4 mM EDTA, 0.5 mM DTT, 100 µg/mL Leupeptin, 100 µg/mL Aprotinin, 10 mM Benzamidin, 2 mM phenylmethylsulfonyl fluoride). Samples were homogenized with a Sonics sonicator (*Vibra-cell, Newtown, USA*) 10 times for 10-second intervals, and after, 0.5% Triton-X-100 was added. After remaining 15 min on ice, the lysate was centrifuged at 13,000 × g for 20 min at 4 °C. Supernatants were used for WB analysis.

### **WB analysis**

The differential expression of protein CK2α and CK2β in mice brain was assessed for wt brain, GL261 tumor and contralateral brain parenchyma (non tumoral). The protein content of tissue extracts was quantified with the Bradford assay [272]. For WB analysis, 50 µg of total protein were separated by 12% Sodium Dodecyl Sulfate Polyacrylamide Gel Electrophoresis (SDS-PAGE) and transferred onto Polyvinylidene fluoride (PVDF) membranes by electroblotting. The membranes were then blocked in 5% milk powder in 0.02% Tween Phosphate buffered saline (T-PBS) for 1 hour and washed three times for 10 min with T-PBS. Membranes were incubated with antibodies against CK2α (CK2α (sc-6479 C-18), 42 kD, 1:300, *Santacruz, Texas USA*) or CK2β (CK2β EP1995Y, 24-25kD, 1:200, *Merck Millipore, Darmstadt, Germany*), and tubulin was used as a loading control (β-tubulin, 55 kD, 1:1000, Cell signalling technology (*Danvers, Massachusetts, USA*)). Incubation was performed overnight at 4°C. The next day, three T-PBS washing steps were carried out and incubation with the secondary antibodies took place during 1 hour (anti-goat for CK2α and anti-rabbit for CK2β and tubulin, 1:5000, *Biorad, Hercules, California*) and three washing steps with T-PBS were repeated. The specific antibody binding was detected with the enhanced chemiluminescence technique with Lumi-Light Western blotting substrate (*Roche, Basel, Germany*).



WB films were scanned and quantified with the *ImageJ* software (*National Institutes of Health, USA*, <http://imagej.nih.gov/ij/>) at the Laboratory of Luminescence and Biomolecular Spectroscopy (LLEB) at UAB and data obtained was normalized to tubulin.

### **Statistical analysis**

Normality was first inspected in each group by the Kolmogorov-Smirnov test and variance homogeneity was assessed with the Levene's test. A two-tailed Student's t-test for independent measurements was used for comparisons when data followed a normal Gaussian distribution. If data presented a non-normal distribution, Mann-Whitney U test was used for comparisons. The significance level for all tests was  $p < 0.05$ .

### **4.1.3 Results**

The expression level of CK2 catalytic subunit (CK2 $\alpha$ ) was about four-fold higher in tumor and more than two-fold higher in contralateral brain parenchyma than in wt brain parenchyma (Figure 4.1 and Table 4.1). On the other hand, no significant changes were detected in the expression of the CK2 regulatory subunit (CK2 $\beta$ ), as shown in Figure 4.1, for selected samples, and quantitatively summarized in Table 4.1. Furthermore, the here named "unbalancedness" ratio CK2 $\alpha$ /CK2 $\beta$ , significantly increased about four-fold in tumors with respect to normal brain parenchyma.

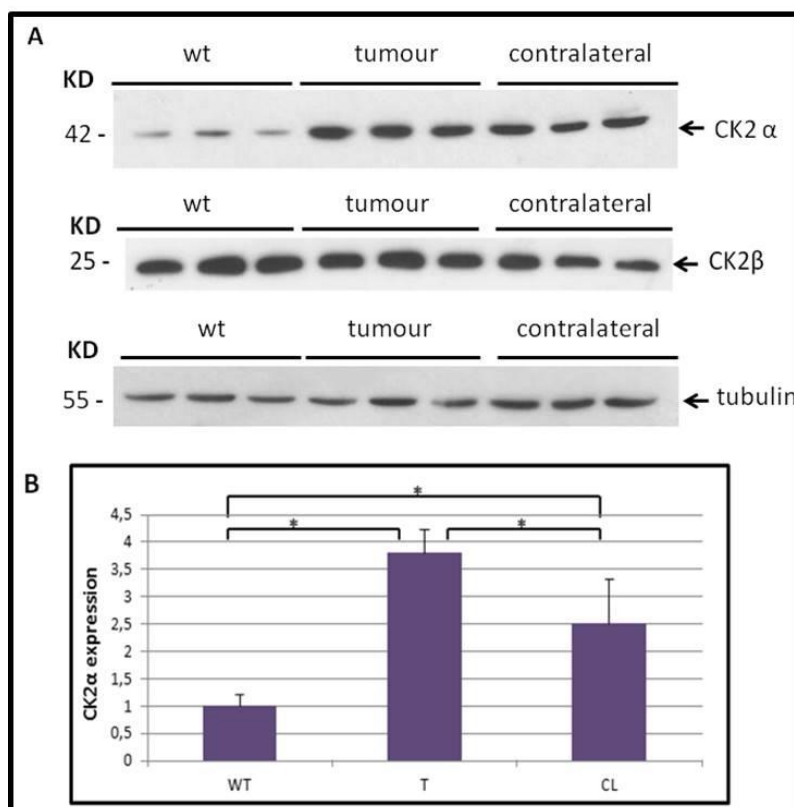


**Figure 4.1 CK2 WB quantification in GL261 GBM compared to contralateral parenchyma and control mice (A)** WB of characteristic tissue samples using 50  $\mu$ g of total protein, detection with anti-CK2 $\alpha$  antibody, anti-CK2 $\beta$  antibody and with anti-tubulin antibody. From left to right, wt brain parenchyma samples, tumor samples and contralateral brain parenchyma samples. **(B)** Quantification (bar;  $\pm$ SD) carried out of the normalized CK2 $\alpha$  to tubulin expression ratio in tissue samples using 50  $\mu$ g of total protein. WT=wild type brain parenchyma, T=tumor, CL=contralateral brain parenchyma \*=  $p < 0.05$ .

CK2 $\alpha$				CK2 $\beta$				CK2 $\alpha$ /CK2 $\beta$	
WT	1.00 $\pm$ 0.2 $\yen$	T/WT	3.85 $\pm$ 0.5 $^f$	WT	0.70 $\pm$ 0.3	T/WT	1.34 $\pm$ 0.2	WT	1.34 $\pm$ 0.5 $\yen$
T	3.80 $\pm$ 0.4 $^*$	CL/WT	2.51 $\pm$ 0.4 $^s$	T	1.00 $\pm$ 0.2	CL/WT	1.10 $\pm$ 0.1	T	3.82 $\pm$ 0.3 $^*$
CL	2.50 $\pm$ 0.8 $^{*\yen}$	T/CL	1.54 $\pm$ 0.2 $^{f\$}$	CL	0.90 $\pm$ 0.2	T/CL	1.06 $\pm$ 0.2 $^f$	CL	2.68 $\pm$ 0.5 $^{*\yen}$

**Table 4.1 Normalized values of CK2 expression levels ( $\pm$ SD) and their unbalancedness ratios ( $\pm$ SD)**

**T/WT, CL/WT and T/CL for CK2 $\alpha$  and CK2 $\beta$  quantifications.** Abbreviations as in Figure 4.1 legend. (\*) significance compared with WT, ( $\yen$ ) significance compared with T, (E) significance compared with T/WT and (\$) significance compared with CL/W.

#### **4.1.4 Discussion**

It has been consistently reported by other authors that high levels of CK2 $\alpha$  are expressed in solid human tumors [165], for example in colorectal carcinomas and breast carcinomas [166]. Our results in preclinical GL261 GBM agree with authors in [166], in the fact that we found higher expression levels of CK2 $\alpha$  in tumor, in comparison with the normal tissue (wt brain parenchyma). In our study, the Tumor/Normal ratio of CK2 $\alpha$  normalized expression values was of 3.8 (Figure 4.1). For CK2 $\beta$ , a non-significant increased expression was detected for the Tumor/Normal brain parenchyma ratio, which reached a value of 1.34.

A somewhat unexpected result found in our study was the significantly higher CK2 $\alpha$  expression level detected in the contralateral non-affected brain parenchyma, which has not been described in the literature as far as we are aware. In this respect, Figure 4.1A and B show a significantly higher CK2 $\alpha$  expression in contralateral tissue in comparison with the wt brain parenchyma, although this expression is clearly lower than the expression found in tumors (Table 4.1). This could be partially explained due to the well-known infiltration pattern of the GBM, invading adjacent non-tumoral tissue and even producing a precancerous stage in apparently uninvolved parenchyma [271]. In this respect, Lama and collaborators [273] also described an increased ERK1/2 expression in GBM peritumoral tissue from patients. Taking into account that ERK1/2 seems to be activated for translocation to the nucleus by CK2 phosphorylation [274] our results on the increased CK2 content in the contralateral/peritumoral area would agree with those reports and reinforce the idea of a “precancerous stage” away from the tumor mass, also for the CK2 content.

Regarding the different CK2 subunits evaluated (CK2 $\alpha$  and CK2 $\beta$ ), our results suggest that an unbalanced expression is taking place in the GL261 GBM (see Figure 4.1A and Table 4.1), with a predominance of an overexpression of CK2 $\alpha$  in the studied tumors. This imbalance of CK2 subunits was also seen in [274], being produced in this case by a relative decrease in the CK2 $\beta$

regulatory subunit in biopsies of human breast cancer tumors having suffered EMT, a sign of increased aggressiveness.

Accordingly, the high expression levels observed for CK2 $\alpha$  in GBM, in comparison with wt brain, reinforces the potential of CK2 $\alpha$  as a valid therapeutic target [124, 275] to investigate in GL261 GBM. In this sense, recent studies have reported that promiscuous iCK2s such as APG have shown relevant effects in the growth inhibition of established human GBM cultured cells lines [168]. Additionally, a more specific iCK2, CX-4945, has been reported as the first iCK2 to reach clinical stage testing for the treatment of multiple types of cancer [121, 124]. Moreover, there are other promising iCK2s in development, such as TDB which is a dual inhibitor of CK2 and PIM-1 [125].

Finally, the preclinical GL261 mice GBM model has been widely used for molecular imaging studies and to evaluate TMZ therapy response. Accordingly, the results here described warrant further work with CK2 $\alpha$  inhibition in this GBM model as standalone or combination therapeutic strategies.

#### **4.1.5 Conclusion**

The expression level of the CK2 catalytic subunit (CK2 $\alpha$ ) was found higher in GL261 GBM tumor (about 4-fold) and in contralateral brain parenchyma (more than 2-fold) than in wt brain parenchyma ( $p < 0.05$ ). In contrast, no significant changes were found in the CK2 regulatory subunit (CK2 $\beta$ ) expression, suggesting a predominance of CK2 $\alpha$  overexpression in the evaluated tumors and possibly pointing to a differential role for the two subunit types in GBM tumor development in our investigated model. This should also be taken into account in future studies with preclinical GBM and therapeutic CK2 targeting.

## **4.2 TARGETING PROTEIN KINASE CK2: EVALUATING CX-4945 POTENTIAL FOR GL261 GLIOBLASTOMA THERAPY IN IMMUNOCOMPETENT MICE**

Most of the content of this section has been accepted for publication in the *Pharmaceuticals Journal* with the title of “*Targeting protein kinase CK2: Evaluating CX-4945 potential for GL261 glioblastoma therapy in immunocompetent mice*” by Ferrer-Font L, Villamañan L, Arias-Ramos N, Vilardell-Vila J, Plana M, Ruzzene M, Pinna LA, Itarte E, Arús C and Candiota AP.

### **4.2.1 Specific objectives**

- Assessment of iCK2 effects over cultured GL261 cells viability to select the best potential candidates for *in vivo* preclinical studies.
- Collection of MTD information in C57BL/6 mouse model for the best iCK2 candidates and TMZ.
- Tumor targeting effects assessment and survival rate evaluation in longitudinal studies with C57BL/6 mice bearing GL261 tumors (immunocompetent model) treated with iCK2.

### **4.2.2 Specific materials and methods**

#### **Cell viability assay**

GL261 cells were plated at 5000 cells per well in 96-well multiwell plates (*Sigma-Aldrich, Madrid, Spain*). Cells were allowed to adhere for 24 h before drugs were added to the medium at increasing concentrations: for TMZ, 0  $\mu$ M, 0.8  $\mu$ M, 4  $\mu$ M, 20  $\mu$ M, 100  $\mu$ M, 200  $\mu$ M, 500  $\mu$ M, 1000  $\mu$ M, 5000  $\mu$ M and 10000  $\mu$ M, APG and TBB: 0  $\mu$ M, 0.8  $\mu$ M, 4  $\mu$ M, 20  $\mu$ M, 100  $\mu$ M, 200  $\mu$ M and 500  $\mu$ M, and CX-4945: 0  $\mu$ M, 0.2  $\mu$ M, 2  $\mu$ M, 5  $\mu$ M, 20  $\mu$ M, 50  $\mu$ M, 100  $\mu$ M, 200  $\mu$ M and 500  $\mu$ M. Controls in each plate included cell culture RPMI medium and dimethyl sulfoxide (DMSO) (0.4% for CX-4945, TBB and APG, and 0.8% for TMZ). Drug-treated and control wells were run in triplicate. After 72 h of drug exposure, cell viability was measured using XTT Assay (*Sigma-Aldrich, Madrid, Spain*) as per the manufacturer’s instruction. DMSO-treated wells

were considered as “100% viability” for each treatment plate. In the case of combined TMZ and CX-4945 treatment, MTT assay (*Sigma-Aldrich, Madrid, Spain*) was used for cell viability assay. Two compound combinations were used to assess possible synergy: CX-4945 30  $\mu$ M plus TMZ 1 mM, and CX-4945 50  $\mu$ M plus TMZ 1.5 mM, compared to control (medium and DMSO) and TMZ or CX-4945 alone. Controls included RPMI medium and DMSO (0.8%). Half maximal effective concentration ( $EC_{50}$ ) was calculated using Graphpad Prism software (*version 5, <http://www.graphpad.com/>*).

### **Antibodies**

CK2 $\alpha$ -subunit rabbit antiserum (*dil. 1:1000*) was raised against [376– 391] region of the human protein, corresponding to the specific C-terminal sequence. CK2 $\beta$  (*Monoclonal, dil. 1:750, rabbit, Ref Ab76025*) and Phospho-AKT (S129) (*dil. 1:1000, rabbit, Ref 133458*) were purchased from Abcam (*Cambridge, UK*).  $\beta$ -actin (*dil.1:2000, mouse, Ref A2228*) and  $\alpha$ -tubulin (*dil.1:2000, mouse, Ref A5441*) were obtained from *Sigma-Aldrich (Madrid, Spain)*, and  $\beta$ -tubulin (*dil. 1:1000, rabbit, Ref 2146*) and AKT1 (*dil 1:500, rabbit, Ref C3H10*) were purchased from Cell Signalling technology (*Beverly, MA, USA*). Secondary antibodies towards rabbit and mouse IgG (*dil.1:2000*), conjugated to horse radish peroxidase, were purchased from PerkinElmer (*Waltham, MA, USA*).

### **Target evaluation in GL261 cultured cells with CX-4945 treatment**

For the CK2 expression and activity studies, a total of 18 flasks (75 cm<sup>2</sup>) of GL261 cells were cultured (n=3 as controls, n=3 as CX-4945 treatment during 1h, 4h, 8h, 12h and 24h). Cells were cultured in flasks until 50% confluence and at that moment, CX-4945 was added to the “treatment” flasks, and an equal amount of the vehicle (DMSO) was added to the control cells. The CX-4945 concentration used was 67.2 $\mu$ M (four times the  $EC_{50}$ , as stated by other authors [276]). Still, this concentration was included in the range of maximum CX-4945 effect in cell viability assay. An *in vitro* dose-response study was also conducted in cultured GL261 cells in

order to check for increasing target effects. For this, 300,000 cells/well were plated in 6-well plates and concentrations of CX-4945 of 0, 5, 10, 20, 30 and 60  $\mu$ M were added. Treatments were performed during 8 and 24 hours.

#### **Therapeutic agent preparations (CK2 inhibitors and TMZ)**

CX-4945 sodium salt (*Glix laboratories, Southborough, USA*) was dissolved in 0.4% DMSO (cell experiments), or in phosphate buffer 25 mM pH 7.2 (*in vivo* studies), as described in [122]. For APG (*Sigma-Aldrich, Madrid, Spain*) and TBB (*Calbiochem, Merck KGaA, Darmstadt, Germany*), used for cell experiments, 0.4% DMSO was used as dissolvent. Regarding TMZ (*Sigma-Aldrich, Madrid, Spain*), it was dissolved in 0.8% DMSO for cell experiments, and in 10% DMSO in saline solution (0.9% NaCl) for *in vivo* experiments.

#### **Animal model for *in vivo* studies**

A total of 60 C57BL/6 female wt mice weighting  $21.2 \pm 1.3$  g were used for this study. Tumors were induced in C57BL/6 mice by intracranial stereotactic injection of  $10^5$  GL261 cells, as explained in general materials and methods section 3.2.1. Mice were weighed every day and tumor volumes were followed using  $T_{2w}$  MRI acquisition as in [237] the day 6 and 10 or 11 after implantation. Mice with most homogeneous weights and tumor sizes were chosen to make experimental groups after randomization (usually  $n=6$  per studied condition), and therapy started. The volume and weight averages did not show significant differences between the experimental groups (Table 4.2-4.4).

DAY 11 (Tumor volume and body weight)								
CONTROL	Mice	C940	C942	C943	C944	C945	C946	AV±SD
	Weight	21.7	21.2	20.4	22.6	19.5	20.9	21.1±1.1
	Volume	11.7	12.4	17.9	22.9	12.5	10.9	14.7±4.7
CX-4945 every day	Mice	C947	C948	C949	C951	C952	C953	AV±SD
	Weight	21.0	21.8	22.1	22.3	22.6	22.3	22.0±0.6
	Volume	17.7	17.9	17.3	25.4	11.5	13.3	17.2±4.8

Table 4.2 Average ± standard deviation (AV ± SD) for tumor volume (mm<sup>3</sup>) and body weight (g) for mice before starting CX-4945 therapy every day (day 11 p.i.). No significant differences (p>0.05) were found between CX-4945 every day treated group (n=6) and control mice (n=6) neither for tumor volumes, nor for mice body weight, with Student's t-test.

DAY 11 (Tumor volume and weight)								
CONTROL	Mice	C955	C956	C957	C958	C960	C965	AV±SD
	Weight	25.5	20.0	19.5	22.0	20.1	22.7	21.6±2.3
	Volume	10.7	7.1	22.6	4.9	15.8	11.4	12.1±6.4
CX-4945 alternated days	Mice	C961	C962	C963	C964	C067	C950	AV±SD
	Weight	21.0	19.5	22.3	20.8	20.8	21.7	21.0±0.9
	Volume	22.2	14.8	11.1	18.2	10.9	11.9	14.9±4.6

Table 4.3 Average ± standard deviation (AV± SD) for tumor volume (mm<sup>3</sup>) and body weight (g) for mice before starting CX-4945 therapy in alternated days (day 11 p.i.). No significant differences (p>0.05) were found between CX-4945 alternated days treated group (n=6) and control mice (n=6) neither for tumor volumes, nor for mice body weight, with Student's t-test.

DAY 11 (Tumor volume and weight)								
CONTROL	Mice	C991	C992	C996	C997	C998	C999	AV±SD
	Weight	21.3	21.9	21.1	21.4	20.0	19.6	20.8±0.9
	Volume	10.6	23.9	8.8	6.8	24.0	8.0	13.7±8.0
TMZ and CX-4945	Mice	C984	C985	C988	C990	C994	C995	AV±SD
	Weight	22.4	22.1	21.7	22.6	21.5	24.4	22.5±1.0
	Volume	13.0	14.6	9.5	8.8	22.5	11.6	13.3±5.0

Table 4.4 Average ± standard deviation (AV± SD) for tumor volume (mm<sup>3</sup>) and body weight (g) for mice before starting combined TMZ±CX-4945 therapy (day 11 p.i.). No significant differences (p>0.05) were found between 3 cycles TMZ + CX-4945 every day treated group (n=6) and control mice (n=6) neither for tumor volumes, nor for mice body weight, with Student's t-test.



DAY 10 (Tumor volume and weight)								
CX	Mice	C1144	C1158	C1147	C1148	C1149	C1150	AV±SD
	Weight	20.6	20.6	20.6	20.4	19.9	20.8	20.5±0.3
	Volume	5.3	5.1	6.5	7.5	2.3	3.0	5.0±2.0
CX±TMZ	Mice	C1151	C1152	C1153	C1154	C1155	C1156	AV±SD
	Weight	21.9	20.7	21.0	20.1	22.5	24.1	21.7±1.4
	Volume	5.9	7.7	3.1	5.2	4.6	2.9	4.9±1.8
TMZ	Mice	C1166	C1167	C1168	C1169	C1170	C1171	AV±SD
	Weight	19.7	20.7	22.0	21.1	17.1	21.0	20.3±1.7
	Volume	4.9	5.3	5.8	6.9	5.3	8.0	6.0±1.2
CONTROL	Mice	C1157	C1145	C1160	C1161	C1162	C1165	AV±SD
	Weight	20.9	20.2	21.1	21.1	21.1	20.0	20.7±0.5
	Volume	5.2	4.1	6.9	3.6	10.1	7.1	6.2±2.4

Table 4.5 Average ± standard deviation (AV± SD) for tumor volume (mm<sup>3</sup>) and body weight (g) for mice before starting metronomic therapy: CX-4945, TMZ, CX-4945 and TMZ, and control mice (day 10 p.i.). No significant differences ( $p>0.05$ ) were found between the different groups ( $n=6$ ) neither for tumor volumes, nor for mice body weight, with Student's t-test.

#### CX-4945, TDB and TMZ tolerability assay

Two phases were performed for this study, based on the work described in [277] and under the advice of Dr. Jordi Llorens (*Department of Physiological Sciences, Faculty of Medicine and Health Sciences, Universitat de Barcelona*): in phase 1,  $n=1$  was used and the starting TMZ dose was the one described by us (60mg/kg/day) [237] For CX-4945, the dose was the one described in [123, 276] (150mg/kg/day), as no adverse effects have been observed with these doses, and for TDB, the dose used was the *molar* equivalent as the dose used for CX-4945. Administrations were performed with an oral gavage. Doses were increased (Table 4.6) until detection of toxicity symptoms (Table 4.7). Once MTD was estimated in this first phase, a second phase took place and a group of  $n=3$  mice were administered with the calculated MTD. If toxicity signs were detected, phase 2 was repeated with a lower dose. Mice follow-up (weight+welfare parameters) was carried out every day for up to 30 days.

Day	0	4	8	12	16	20
<b>CX-4945 (mg/Kg)</b>	150	300	600	1200	2400	4800
<b>TDB (mg/Kg)</b>	269.9	539.8	1079.6	2159.2	4318.4	
<b>TMZ (mg/Kg)</b>	60	120	240	480	920	1890

**Table 4.6 Doses for CX-4945, TDB and TMZ administration in MTD calculation experiments. The final volume administration and doses were adjusted to actual animal weights.**

Parameter for endpoint	Means of verification
<b>Weight loss of above 20% regarding the previous register</b>	Scale readings
<b>Marked piloerection</b>	Piloerection detected during animal observation
<b>Animal shows subdued behaviour patterns even when provoked</b>	Apathic behaviour during weighting procedure, in comparison with control animals.
<b>Intermittent or persistent tremors</b>	Observation of animals before and after weighting procedure

**Table 4.7 Symptoms and signals guidance to decide the MTD. Adapted from [278]. If at least two parameters are detected, there is indication of adverse side effects and further dose increasing is discouraged.**

Despite tolerability assays were performed with TMZ, CX-4945 and TDB, we decided to focus first on CX-4945 [122–124], because unlike the other one, TDB, it has been already used in clinical trials<sup>5,6</sup>.

### **Use of iCK2 in tumor-bearing animals**

#### ***Preliminary studies of target validation***

CX-4945 therapy was administered to tumor-bearing mice (n=2) during three days (150mg/kg split into two administrations per day). The CX-4945 vehicle (phosphate buffer 25mM pH 7.2) was administered to control mice (n=2). Administrations were performed with an oral gavage. Mice were euthanized at 2h, 6h and 24h after the last administration for both treated and

<sup>5</sup> <http://www.cancer.gov/clinicaltrials/search/view?cdrid=642699&version=HealthProfessional>

<sup>6</sup> <http://www.prnewswire.com/news-releases/cylene-presents-encouraging-clinical-data-for-oral-ck2-inhibitor-at-asco-123219423.html>

control mice to assess CK2 activity compared to control mice. Tumor samples were stored in liquid nitrogen until further processing.

***Longitudinal studies with iCK2 (alone or in combination)***

CX-4945 therapy was administered to tumor-bearing mice, every day or in alternated days, 150mg/Kg/day [124] (Figure 4.2A and B). Total dose of CX-4945 was 150 mg/Kg/day, split into two times per day (75 mg/kg at 8h, and 75 mg/kg at 16h) and dissolved in vehicle administration, which was phosphate buffer 25mM pH 7.2. For the combined CX-4945+TMZ therapy (Figure 4.2C), CX-4945 was administered every day whereas TMZ (60mg/Kg) was prepared and administered as previously described by the group in three administration cycles [237] (Figure 4.2G). Both treatments were administered using an oral gavage and the administration volume for CX-4945 and TMZ was the same that has been used in our group for the TMZ administration (10 $\mu$ l/g weight animal) [237]. CX-4945 therapy was given until the end point of animal survival, when animals were euthanized because of welfare parameters (annex 1). Animals were euthanized by cervical dislocation, the brain was removed and tumor resected. Samples were stored in liquid nitrogen until further processing for CK2 activity and expression analysis.

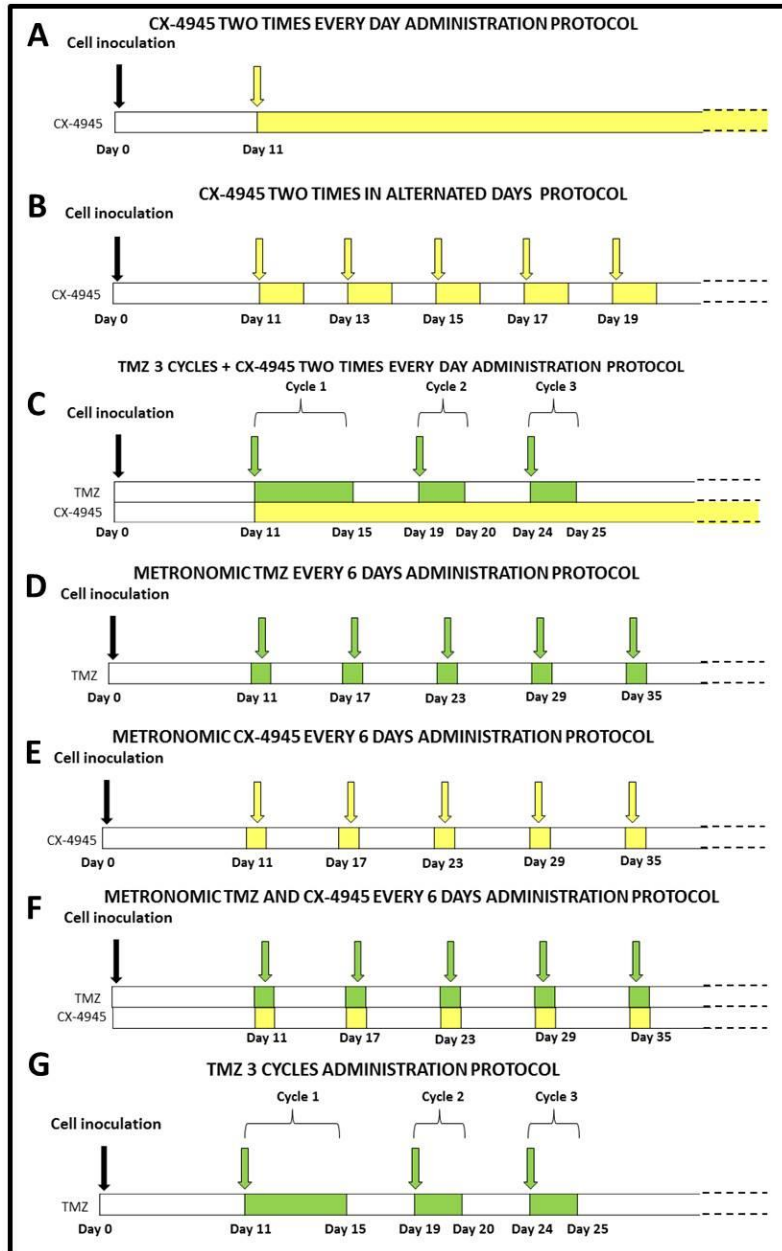


**Figure 4.2 Therapy administration scheme protocols (A)** for every day CX-4945 at 150 mg/kg (75mg/kg at 8h and 75mg/kg at 16h) **(B)** for alternated days CX-4945 at 150 mg/kg (75mg/kg at 8h and 75mg/kg at 16h) **(C)** for TMZ ± CX-4945 administration protocol. TMZ 60 mg/kg was administered at days 11-15, 19-20 and 24-25 p.i. and CX-4945 150mg/kg (75mg/kg at 8h and 75mg/kg at 16h, every day) **(D)** for metronomic TMZ (60mg/Kg) every 6 days protocol **(E)** for metronomic CX-4945 (75mg/kg at 8h and 75mg/kg at 16h) every 6 days protocol and **(F)** for metronomic TMZ ± CX-4945 every 6 days administration protocol. TMZ 60 mg/kg and 150mg/kg of CX-4945 were administered as follows: CX-4945 75mg/kg at 8h, TMZ 60 mg/Kg at 12h and CX-4945 75mg/kg at 16h). **(G)** for 3-cycles of TMZ, 60 mg/kg were administered at days 11-15, 19-20 and 24-25 p.i.

Regarding metronomic (every 6 days) administration protocol, 8 doses of CX-4945 (150 mg/Kg; 75 mg/kg at 8h and 75 mg/kg at 16h) were administered to CX-4945 treated group (Figure 4.2D), 8 doses of TMZ (60mg/Kg at 12h) were administered to TMZ treated group (Figure 4.2E) and 8 doses of CX-4945 (150 mg/Kg 75 mg/kg at 8h, and 75 mg/kg at 16h) plus TMZ (60 mg/Kg at 12h) were administered to CX-4945 and TMZ combined therapy group (Figure 4.2F). Control mice received TMZ and CX-4945 vehicles. In all cases, the maximum cumulative dose administered was of 1200 mg/Kg for CX-4945 and 480 mg/kg for TMZ.

### **Tissue homogenization and protein extraction**

Tissue samples were weighed and 250 µl of cold lysis buffer for each 100 mg of tissue were added (cold lysis buffer: 20 mM Tris-HCl pH 7.4, 150 mM NaCl, 1 mM EDTA, 0.2% sodium deoxycholate, 2x proteases inhibitor EDTA free (*Roche, Madrid, Spain*), 1x phosphatases inhibitors (*Sigma-Aldrich, Madrid, Spain*): Phosphatase inhibitor cocktail 2 (*Ref P5726*), Phosphatase inhibitor cocktail 3 (*Ref P0044*) and 1% Triton-x-100 (*Sigma-Aldrich, Madrid, Spain*). Samples were homogenized with a 20G needle 10 times and with a 26G needle 10 more times. Sonication (*Vibra-cell, Newtown, USA*) was performed 5 times for 5-second intervals at 30% amplification. After remaining 30 min on ice, the lysate was centrifuged at 25,000g for 20 min at 4 °C. Supernatants were used for WB and CK2 activity analysis. On the other hand, GL261 cells were lysed as described in [203].

### **CK2 activity assay**

CK2 activity was measured in 1–2 µg of lysate proteins (total protein extract of cell lysates) and 5-10 µg (total protein extract of brain mice samples), previously incubated 10 min at 30°C with 0.1 mM CK2-tide (specific CK2 substrate peptide), by means of radioactive assays with [ $\gamma$ -<sup>33</sup>P] ATP, in the presence of phosphorylation reaction mixture as described in [279].

### **MRI acquisition**

MR studies were carried out as explained in general materials and methods section (3.4.1).

### **WB analysis**

Protein concentration was determined by Bradford method [272] and equal amounts of protein (25 µg) were loaded on 11% SDS-PAGE, blotted on PVDF Immobilon-P membranes (*Millipore, Darmstadt, Germany*), and immunodetected with the corresponding antibodies using a chemiluminescent detection method. Chemiluminescent signal obtained was quantified in a Kodak Image Station 440MMPRO and analysed with the Kodak 1DImage software. For tumor samples, 40 µg of tissue homogenate protein was loaded.

### **Statistical analysis**

Variance homogeneity was assessed with the Levene's test. A two-tailed Student's t-test for independent measurements was used for comparisons, for samples of equal or different variances (depending on the Levene's test result). Dixon's and Grubb's tests were used to detect outliers. The global evolution of tumor growth curves or body weight control was evaluated with the UNIANOVA test. Comparisons of survival rates were performed with the Log-Rank test. The significance level for all tests was  $p < 0.05$ .

## **4.2.3 Results**

### **GL261 cell viability under CK2 inhibition treatment**

Cultured GL261 cells sensitivity to different treatments was assessed. Figure 4.3A and B showed a low  $EC_{50}$  ( $12.9 \pm 2.3 \mu\text{M}$ ) for APG, similar to CX-4945 ( $16.5 \pm 5.5 \mu\text{M}$ ), but the final viability reached with APG was only up to 40% of the initial value. Instead, TBB and CX-4945 both decreased viability to about 20% of the initial value. Regarding to TBB, a concentration of  $91.4 \pm 8.3 \mu\text{M}$  produced a 50% viability decrease, whereas for CX-4945, a concentration of  $16.5 \pm 5.5 \mu\text{M}$  produced the same results. In the case of TDB, it showed the lowest  $EC_{50}$  ( $8.1 \pm 1.5 \mu\text{M}$ ), and the final viability obtained was similar to CX-4945. TMZ  $EC_{50}$  was  $747.6 \pm 63.3 \mu\text{M}$ .

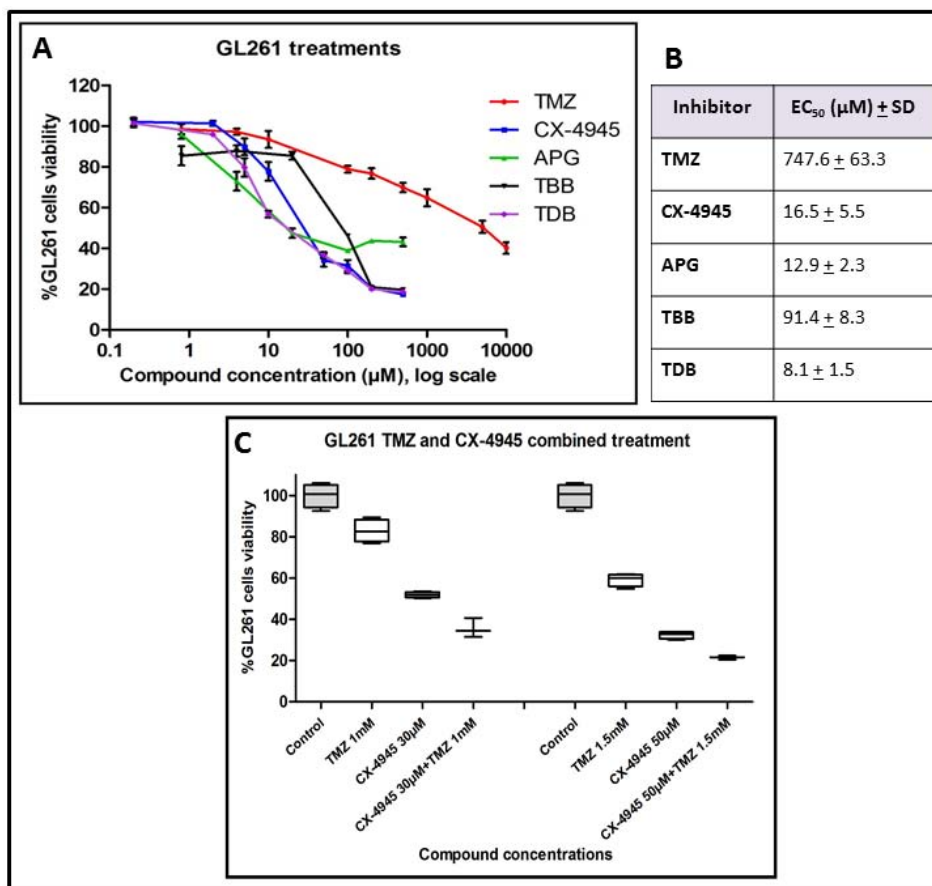


**Figure 4.3 GL261 cells viability after treatment (A)** GL261 cells viability (%) with the “XTT assay” after 72h of treatment (TMZ: 0 μM, 0.8 μM, 4 μM, 20 μM, 100 μM, 200 μM, 500 μM, 1000 μM, 5000 μM and 10000 μM, APG and TBB: 0 μM, 0.8 μM, 4 μM, 20 μM, 100 μM, 200 μM and 500 μM, CX-4945 and TDB: 0 μM, 0.2 μM, 2 μM, 5 μM, 20 μM, 50 μM, 100 μM, 200 μM and 500 μM); 100% cell viability was assigned to control cells treated with 0.8% DMSO (v/v). Experiments were performed with n=3-9, and mean ± SD values are shown. **(B)** EC<sub>50</sub> mean ± SD values obtained with the different treatments to GL261 cells after 72h of incubation with the drug<sup>7</sup>. **(C)** Boxplot of GL261 cells viability after TMZ and CX-4945 treatment. GL261 cells viability (%) with the “MTT assay” after 72h of treatment. On the left side, control (n=4), CX-4945 30 μM (n=4), TMZ 1 mM (n=4) and CX-4945 30 μM plus TMZ 1 mM (n=3); on the right side, control (n=4), CX-4945 50 μM (n=4), TMZ 1.5 mM (n=4) and CX-4945 50 μM and TMZ 1.5 mM (n=3); 100% cell viability was assigned to control cells treated with 0.8% DMSO (v/v). As both experiments were

<sup>7</sup> Half maximal effective concentration (EC<sub>50</sub>) refers to the concentration of a drug, antibody or toxicant which induces a response halfway between the baseline and maximum after a specified exposure time.

performed at the same time, controls were acquired only once and, accordingly, the same control results are shown for both experimental conditions. Experiments were performed with  $n=3-4$ , and mean  $\pm$  SD values are shown. In boxplots, the limits of the box represent quartiles 1 (Q1) and 3 (Q3) of the distribution, the central line corresponds to the median (quartile 2), and the whiskers symbolize the maximum and minimum values in each distribution.

Additionally, an *in vitro* experiment with combined treatment of GL261 cells was outlined, and as it can be seen in Figure 4.3C, we could demonstrate that the combined administration of CX-4945 and TMZ to GL261 cultured cells presented an increased efficacy in comparison with treatments of single substances alone. TMZ alone reduced cell viability to  $82.8\pm 5.6\%$  (at 1 mM) and  $59.2\pm 3.2\%$  (at 1.5 mM) in comparison to controls, whereas CX-4945 alone reduced cell viability to  $52.0\pm 1.4\%$  (at 30  $\mu$ M) and  $31.9\pm 2.1\%$  (at 50  $\mu$ M). The combined administration of both therapeutic agents resulted in a cell viability reduction to  $35.6\pm 4.7\%$  (TMZ 1 mM + CX-4945 30  $\mu$ M), and to  $21.5\pm 1.0\%$  (TMZ 1.5 mM + CX-4945 50  $\mu$ M) in comparison to controls, being clearly superior to the efficacy of each substance separately. Concentrations chosen were above the  $EC_{50}$  (Figure 4.3A and B), to ensure enough cell viability reduction. This would point to a possible synergy between both agents as described by [280], although additional combination experiments would be needed to fully confirm this hypothesis.

In the remainder of this study, we decided to focus first on CX-4945 [122–124], one of the two most effective iCK2s tested on GL261 cell viability (Figure 4.3) because unlike the other one (TDB), CX-4945 has been already used in clinical trials<sup>8,9</sup>.

---

<sup>8</sup> <http://www.cancer.gov/clinicaltrials/search/view?cdrid=642699&version=HealthProfessional>

<sup>9</sup> <http://www.prnewswire.com/news-releases/cylene-presents-encouraging-clinical-data-for-oral-ck2-inhibitor-at-asco-123219423.html>



**CK2 activity in GL261 cells treated with CX-4945**

CK2 activity was analysed in GL261 cells treated with CX-4945 and in control, non-treated cells. As a reporter of endocellular CK2 activity, the phosphorylation state of the well-known CK2 target AKT(S129) [203] was analysed. In Figure 4.4A, p-AKT(S129) normalized to total AKT1 expression was obtained (at 8h and 24h post-treatment) and CX-4945 presented a dose-scale response, being p-AKT(S129) lower when higher concentrations of the inhibitor were applied.

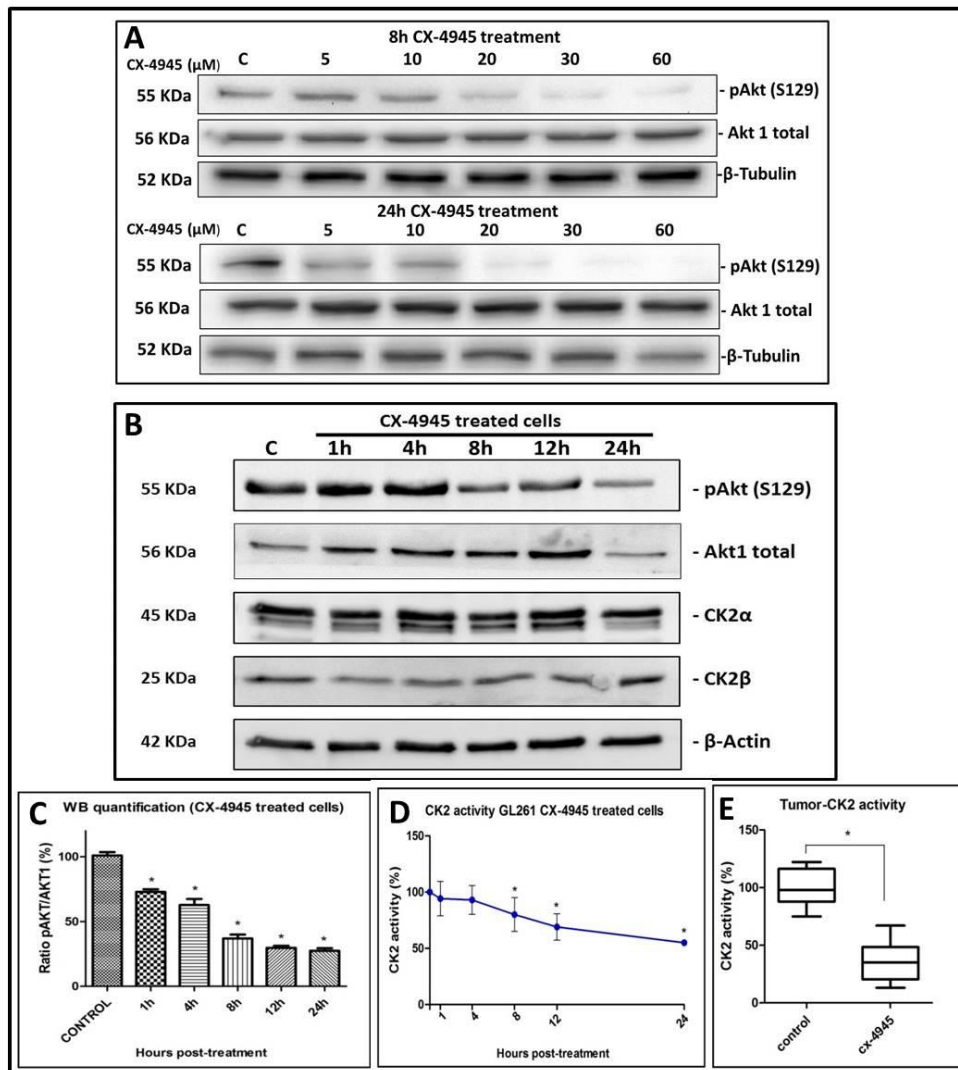


**Figure 4.4 CK2 activity in GL261 cells and tumor samples (A)** Western blot for GL261 cell protein extracts (25μg) treated with increasing doses of CX-4945 (from left to right: control (C) and CX-4945 treated cells 5 μM, 10 μM, 20 μM, 30 μM and 60 μM). This experiment was performed with n=1 for each condition and for 8h (upper part) or 24h (lower part). p-AKT(S129), AKT1 total and β-Tubulin proteins were analysed. **(B)** Western blot for GL261 cell protein extracts (25μg) treated with 67.2μM CX-4945

(from left to right: control (C) and CX-4945 treated cells for 1h, 4h, 8h, 12h and 24h). The experiment was performed with  $n=3$  for each condition. p-AKT(S129), AKT1 total, CK2 $\alpha$ , CK2 $\beta$  and  $\beta$ -Actin proteins were analysed. **(C)** Quantification of Western blot for GL261 cell protein extracts (25 $\mu$ g) treated with CX-4945 ( $n=3$  per each condition). Ratio (%) of p-AKT(S129) content divided by AKT1 total content, while the control values (C) for this ratio are taken as the 100% start value.  $\ast = p < 0.05$  for Student's *t*-test for the comparison of control and treated groups. **(D)** CK2 activity measured on a CK2-specific synthetic peptide in lysates from GL261 cells treated with 67.2 $\mu$ M CX-4945 ( $n=3$  for each condition). Treatment during 1h, 4h, 8h, 12h and 24h.  $\ast = p < 0.05$  for Student's *t*-test for the comparison of control (100% initial value) and treated groups. **(E)** Boxplot of CK2 activity in CX-4945 treated mice compared to control mice. CX-4945 was administered to treated mice during 3 days (a total of 150mg/Kg/day split into two administrations per day) and mice were euthanized 2h, 6h and 24h after the last CX-4945 administration. As no CK2 activity differences ( $p > 0.05$ ) were detected between euthanization time points (2h, 6h and 24h), they were grouped in a single CX-4945 treated group. ( $\ast = p > 0.05$  for Student's *t*-test for the comparison of control and treated groups). CK2 activity was measured on tissue homogenates by means of radioactive assays towards a CK2-specific peptide. Boxplot features as in Figure 4.3 legend.

In addition, Figure 4.4B and C show that p-AKT(S129), normalized to total AKT1, is significantly ( $p < 0.05$ ) less phosphorylated in GL261 cells treated with 67.2  $\mu$ M CX-4945 compared to control cells. No differences were found for CK2 $\alpha$  and CK2 $\beta$  expression ( $p > 0.05$ ) between treated and non-treated cells as it is shown in Figure 4.4B. CK2 activity was also measured in cell lysates, exploiting a highly specific peptide substrate [279] and significant differences ( $p < 0.05$ ) were found between CX-4945 treated cells (Figure 4.4D) and control cells (pre-treatment). These results indicate that CX-4945 reduces endogenous CK2 activity when used to treat cultured GL261 cells, but not the total amount of CK2 subunits present in those cells.

#### **CX-4945 mice tolerability**

Before starting longitudinal *in vivo* treatment experiments, tolerability evaluation was performed for CX-4945, TDB and TMZ. As it can be observed in Figure 4.5A, in the first phase, an MTD of 920mg/kg was estimated for TMZ, and of 1200mg/kg for CX-4945. These MTD

values were chosen because the doses of 1840mg/kg (TMZ) and 2400mg/kg (CX-4945) produced toxicity/adverse effects to the treated mice. In the case of TDB, no MTD could be found due to TDB solubility restrictions (the maximal concentration that could be used was 2,159.2 mg/Kg).

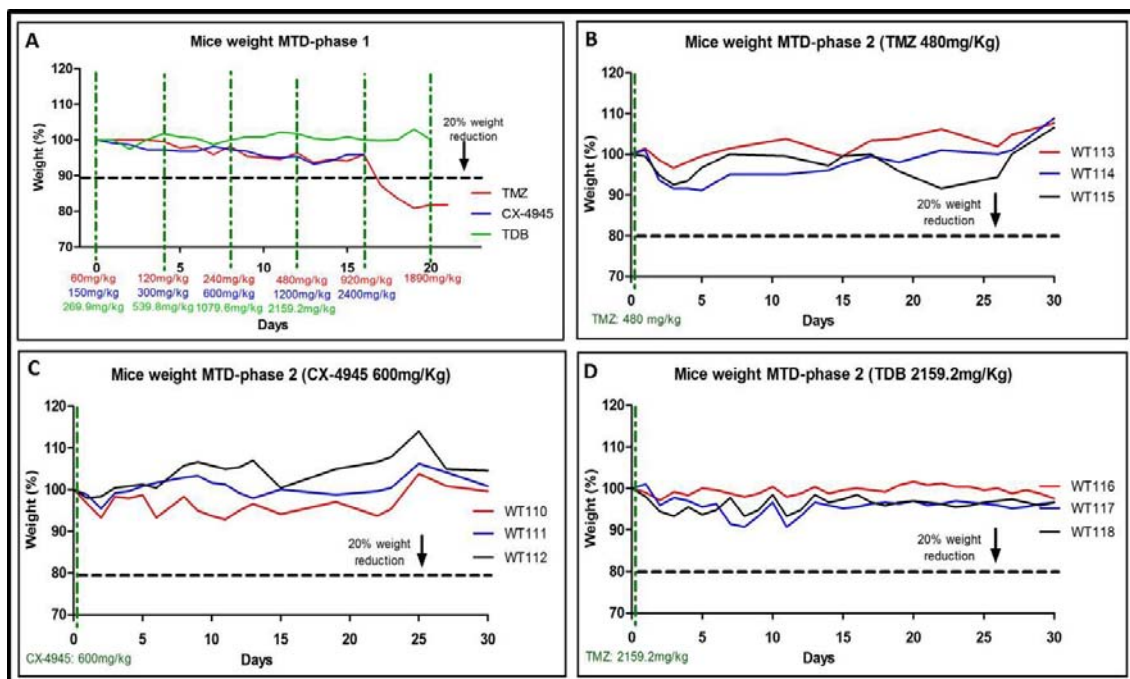


**Figure 4.5 Mice body weight (MTD studies)** (A) Body weight of mice treated with increasing doses of TMZ (red line), CX-4945 (blue line) and TDB (green line) (B) Body weight of mice treated with TMZ single dose (480mg/kg) (n=3) and (C) Body weight of mice treated two times a day with CX-4945 (600mg/kg total dose) (n=3). (D) Body weight of mice treated two times a day with TDB (2,159.2mg/kg total dose) (n=3). In all cases, the weight is expressed in %, considering 100% as the initial weight, and the dashed black line indicates the 20% weight reduction point.

In phase 2, when n=3 mice were administered with a dosage of 920mg/kg of TMZ, 9 days after this single TMZ administration, noticeable body weight decrease was detected in all mice. For this reason, the experiment was repeated with an n=3 at the next lower dose, 480mg/kg (Figure 4.5B). A similar situation was observed for CX-4945 when 1200mg/kg of CX-4945 were administered per n=3, one mouse was found dead, the day after administration so the experiment was repeated at 600 mg/kg (Figure 4.5C). For TDB, we could not find the MTD,

as the maximal soluble dose (2,159.2 mg/Kg), did not produce toxicity signs to our studied model, Figure 4.5D. These results indicate that the MTD (acute dose) is 480 mg/kg for TMZ, 600 mg/Kg for CX-4945 and higher than 2,159.2 mg/Kg for TDB, under our experimental conditions.

#### **CK2 activity in CX-4945 treated mice**

In preliminary *in vivo* target validation studies, CK2 activity was found significantly ( $p < 0.05$ ) reduced in all samples analysed, in comparison to controls (Figure 4.4E). Values obtained at the different time points (2h, 6h and 24h) did not present significant differences when compared ( $p > 0.05$ ), and results were grouped in  $n=6$  treated and  $n=6$  control mice. These results indicate that CX-4945 successfully reached tumors and exerted the expected effect on its target.

#### **Non-metronomic longitudinal treatments with CX-4945 and/or TMZ in tumor-bearing mice**

CX-4945 treatment (either every day or alternated days administration at the classical dose/schedule described by others [122–124]) was performed in GL261 tumor-bearing mice, and no improvement was detected regarding tumor evolution (Figure 4.6A and B) or survival rate ( $p > 0.05$ , Figure 4.6C and D) in comparison with control mice. Figure 4.6C and D show the survival rate for every day CX-4945 treatment ( $20.5 \pm 2.0$  vs.  $20.0 \pm 2.1$  days for control mice) and for alternated days CX-4945 treatment ( $20.5 \pm 1.8$  days vs.  $20.5 \pm 1.6$  days for control mice). Body weight was inspected every day and no significant differences ( $p > 0.05$ ) were observed between groups (Figure 4.7A). Examples of  $T_{2w}$  images for CX-4945 treated mice are shown in Figure 4.8.

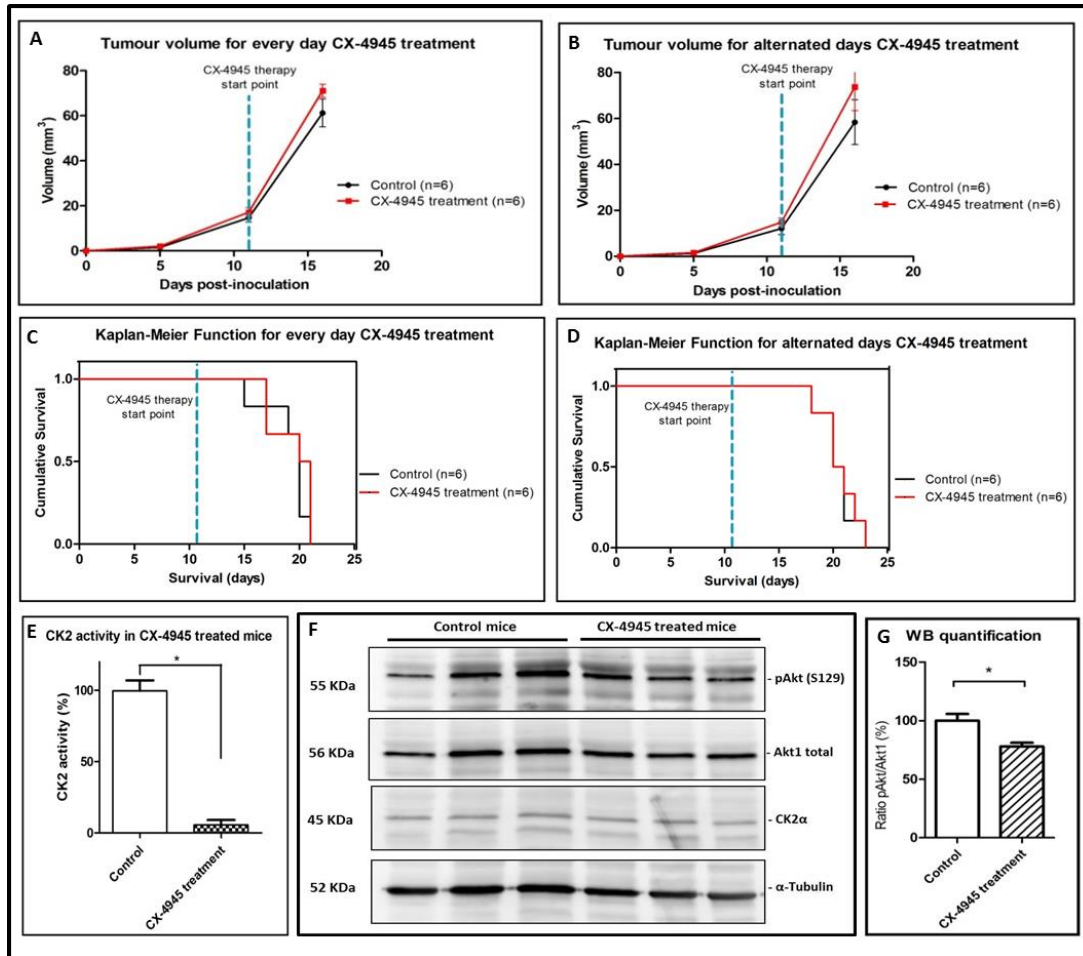


**Figure 4.6** Tumor volumes, survival rate and CK2 activity and expression in CX-4945 treated mice.

Tumor volumes (recorded at days 5, 11 and 16 p.i) of treated (black line) and control non-treated tumor bearing mice (red line) for **(A)** CX-4945 treated every day GL261 implanted mice and **(B)** CX-4945 treated alternated days GL261 implanted mice. No significant differences were observed between groups ( $p > 0.05$ ). The dashed blue line indicates the CX-4945 therapy starting point. **(C)** Survival Kaplan-Meier curve for CX-4945 treated every day mice and control mice **(D)** Survival Kaplan-Meier curve for CX-4945 treated alternated days mice and control mice. No significant differences were found between groups ( $p > 0.05$ ). The dashed blue line indicates the CX-4945 therapy start point. **(A-D)** For all conditions and studies,  $n = 6$  was used **(E)** Tumor CK2 activity (%) in mice treated with CX-4945,  $n = 3$ , compared with control mice,  $n = 3$ . (\* =  $p < 0.05$  for Student's t-test for the comparison of control and treated groups). **(F)** WB for tumor total protein homogenate (40µg) from different mice treated with CX-4945,  $n = 3$ , compared with control mice,  $n = 3$ . p-AKT(S129), AKT1 total, CK2α, and α-tubulin proteins were analyzed. **(G)** Quantification of WB for tumor total protein homogenate (40µg) from mice treated with CX-4945,

## RESULTS – Section 4.2: CX-4945 in GBM treatment

$n=3$ , compared with control mice,  $n=3$ . Ratio (%) of  $p$ -AKT(S129) content divided by AKT1 total content.

\*=  $p<0.05$  for Student's  $t$ -test for the comparison of control and treated groups.

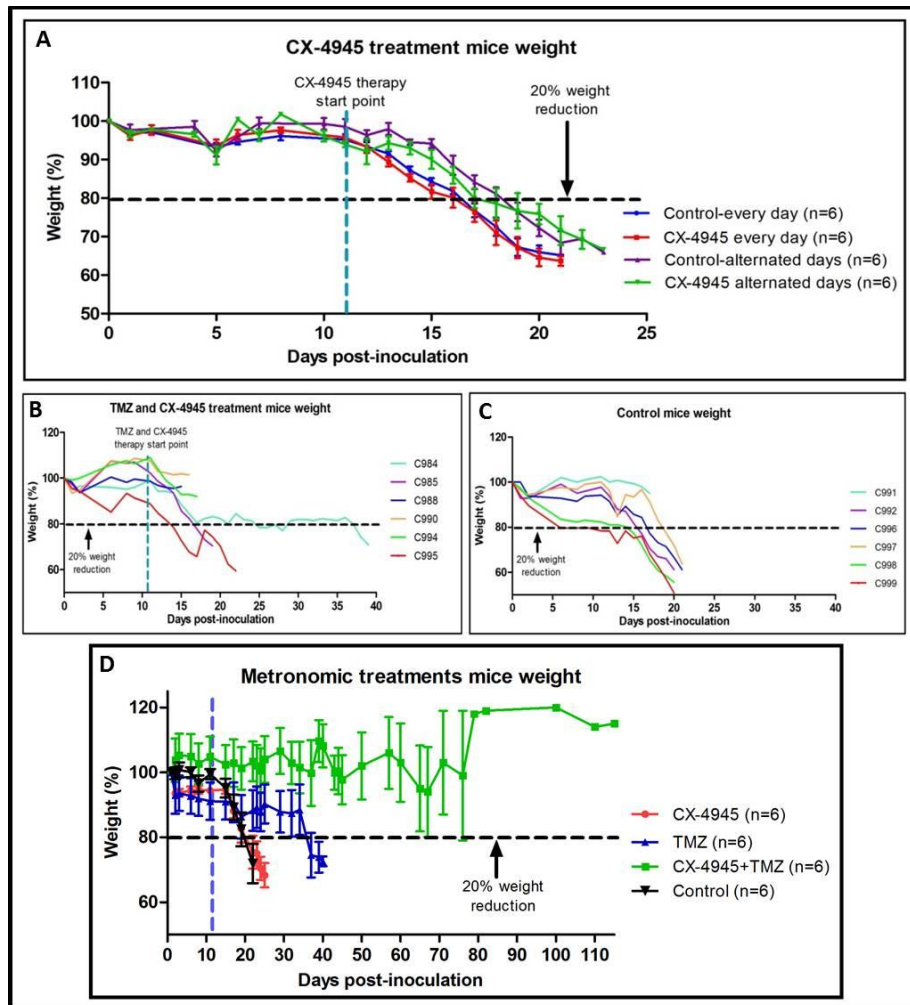


**Figure 4.7 Body weight averages of treated and control mice (A)** Weight (average $\pm$ SD) of mice treated two times every day with CX-4945 (red line) and control vehicle (blue line), and for mice treated two times a day in alternated days with CX-4945 (green line) and control vehicle (purple line). The dashed blue line indicates CX-4945 therapy start point. No differences were observed between groups ( $p>0.05$ ). **(B)** Weights of individual mice treated with a combination of TMZ cycles (5-2-2) [237] and CX-4945 two times every day until death or euthanasia for ethical reasons. The dashed blue line indicates TMZ and CX-4945 therapy start point. Case C984 was considered an outlier according to Grubbs' and Dixon's tests ( $p<0.05$ ). **(C)** Body weight of each control mice (controls of mice represented in B) until death or euthanasia for ethical reasons. Administration of vehicles: phosphate buffer two times a day (CX-4945 vehicle) and 10% DMSO solution in 0.9% NaCl (TMZ vehicle) in 3 cycles, were performed. In all cases, the

weight is expressed in %, assuming that at day 0 the initial weight corresponds to 100%. The dashed black line indicates the 20% weight reduction point. **(D)** Weight (average±SD) of mice treated with CX-4945 metronomic treatment (red line), of mice treated with TMZ metronomic treatment (blue line), of mice treated with CX-4945 and TMZ metronomic treatment (green line) and control mice (blue line). The dashed blue line indicates therapies start point. Significant differences were observed between all groups (control vs. treated groups and different treatments between them ( $p < 0.05$ )). For all conditions and studies,  $n=6$  was used.

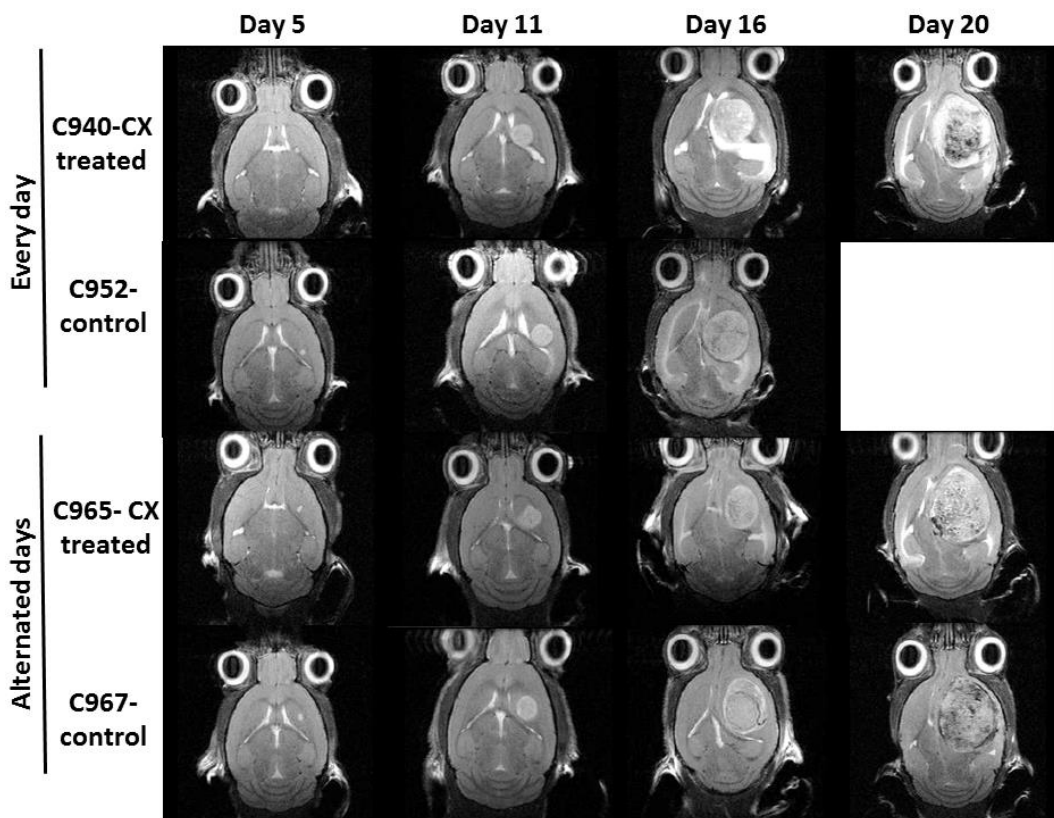


**Figure 4.8 MRI of CX-4945 treated mice.** Follow up of tumor volume evolution by  $T_{2w}$  MRI axial images of CX-4945- treated tumor bearing mice (at days 5, 11, 16 and 20 p.i.). C940: treated with CX-4945 every day, C952: control of every day treatment (phosphate buffer CX-4945 vehicle administration), C965: CX-4945 treated in alternated days and C967: control for alternated days (vehicle administration). CX-4945 dosage was 150mg/kg split into two times per day (75mg/kg 8h and 75mg/kg 16h). MRI is not displayed for C952 day 20 because this mouse was found dead the day 17 p.i. C940 was euthanized at day 20 p.i. for ethical reasons, and C965 and C967 were euthanized the days 21 and 20, respectively. Cxxx corresponds to a unique alpha-numeric animal identifier code in the GABRMN group.

To ensure that CX-4945 reached the tumor, even when no effect on survival could be detected, 6 arbitrarily chosen tumor samples from the CX-4945 treatment every day (n=3 treated, n=3 controls) were analysed for CK2 activity and p-AKT(S129) WB. The CK2 activity was more than seventeen-fold reduced in CX-4945 treated tumor compared to control tumor after  $10.0 \pm 2.0$  days of treatment (Figure 4.6E) and p-AKT(S129)/AKT1 ratio (Figure 4.6F-G) was found around 20% reduced in CX-4945 treated mice, indicating that CX-4945 had reached the desired target and inhibited CK2 activity, despite no increase of the survival rate was observed.

An additional experiment with combined 3 cycles TMZ and CX-4945 administered every day (Figure 4.2C), produced significantly worse results than 3 cycles TMZ treatment alone (see [237], Figure 4.9 and Figure 4.10). In other words, CX-4945 treatment *in vivo*, in these conditions, seems to inhibit the beneficial effect produced by TMZ. Tumor volume curves are shown in Figure 4.9A. As shown in Figure 4.7B, 3 out of the 6 treated mice died around day 16 p.i. without noticeable weight reduction. Control mice weight evolution can be observed in Figure 4.7C. To compare survival rates between groups, Kaplan-Meier survival curves were elaborated, and no significant differences were found between TMZ 3 cycles+CX-4945 every day treated group and control group ( $p > 0.05$ , Figure 4.9B). The average survival rate was  $21.3 \pm 9.0$  days for treated mice (TMZ 3 cycles+CX-4945 every day) vs.  $19.8 \pm 1.5$  days for control mice, while for TMZ 3 cycles only treated mice from previous work (Figure 4.10) average survival time found was  $33.9 \pm 11.7$  days. In addition, no significant differences were found when comparing TMZ 3 cycles+CX-4945 every day and CX-4945 everyday alone (survival rates of  $19.8 \pm 1.5$  vs  $20.5 \pm 2.0$  days, respectively). C984 mouse was proven to be an outlier both in Grubbs' and Dixon's tests for single outliers (survival rate of 39 days,  $p < 0.05$ ), but still it was maintained for survival analysis calculations. Overall average survival for control (untreated) GL261 harbouring mice was  $20.8 \pm 1.8$  days, n=18, while previous work from our group had obtained  $21.5 \pm 3.7$  days, n=61 (Figure 4.10), without significant difference ( $p > 0.05$ ) with the present cohort of mice.



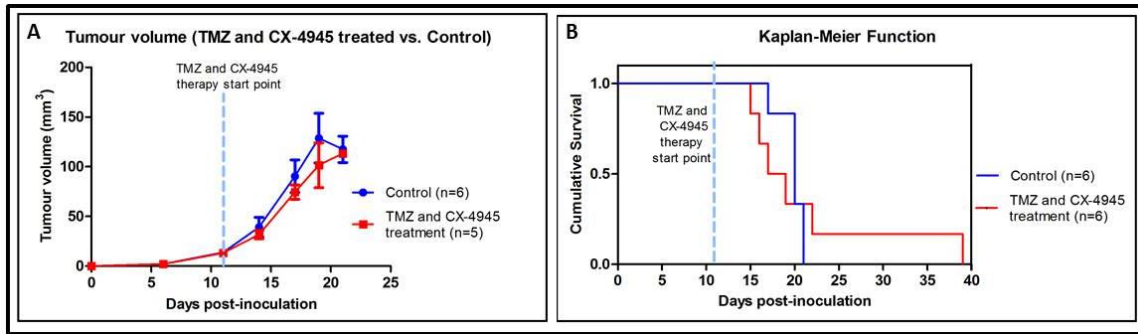


**Figure 4.9 Tumor volume and Kaplan-Meier survival curve of mice treated with TMZ combined with CX-4945. (A)** Tumor volumes (recorded at days 6, 11, 14, 17, 19 and 21 p.i) of control GL261 implanted mice (n=6, blue line) and combined TMZ - CX-4945 cycles in GL261 implanted mice (n=5, red line). The dashed blue line indicates TMZ and CX-4945 therapy starting point. No significant differences were observed between groups for comparisons of control and treated mice tumor volumes at each time point ( $p>0.05$ ). C984 has been excluded from tumor volume comparisons because it has been proven an outlier with Grubb's and Dixon's tests. **(B)** Survival Kaplan-Meier curves for TMZ+CX-4945 treated mice (n=6) and control mice (n=6). No significant differences were found between groups ( $p>0.05$ ). The dashed blue line indicates TMZ and CX-4945 therapy starting point.

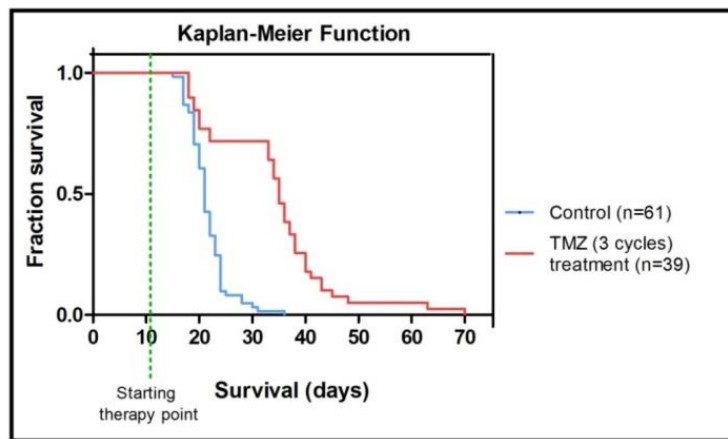


**Figure 4.10 Survival Kaplan-Meier curve for 3 cycles of TMZ vs. control.** Control mice (n=61, blue line) and TMZ treatment (n=39, red line). Survival rate average was  $21.5\pm 3.7$  days for control mice and  $33.9\pm 11.7$  days for TMZ (3 cycles) treated mice. Significant differences were found between groups ( $p<0.05$ ) when comparing control mice with TMZ treated mice. The dashed green line indicates the therapy start point. Results for control and TMZ treatment extracted from [237] and unpublished data from our group. For therapy protocol see Figure 4.2G.

**Metronomic longitudinal treatments with CX-4945 and/or TMZ in tumor-bearing mice**

Three metronomic (every 6 days) administration treatments were performed: CX-4945 (n=6), TMZ (n=6) and a combination of CX-4945+TMZ (n=6), Figure 4.11.

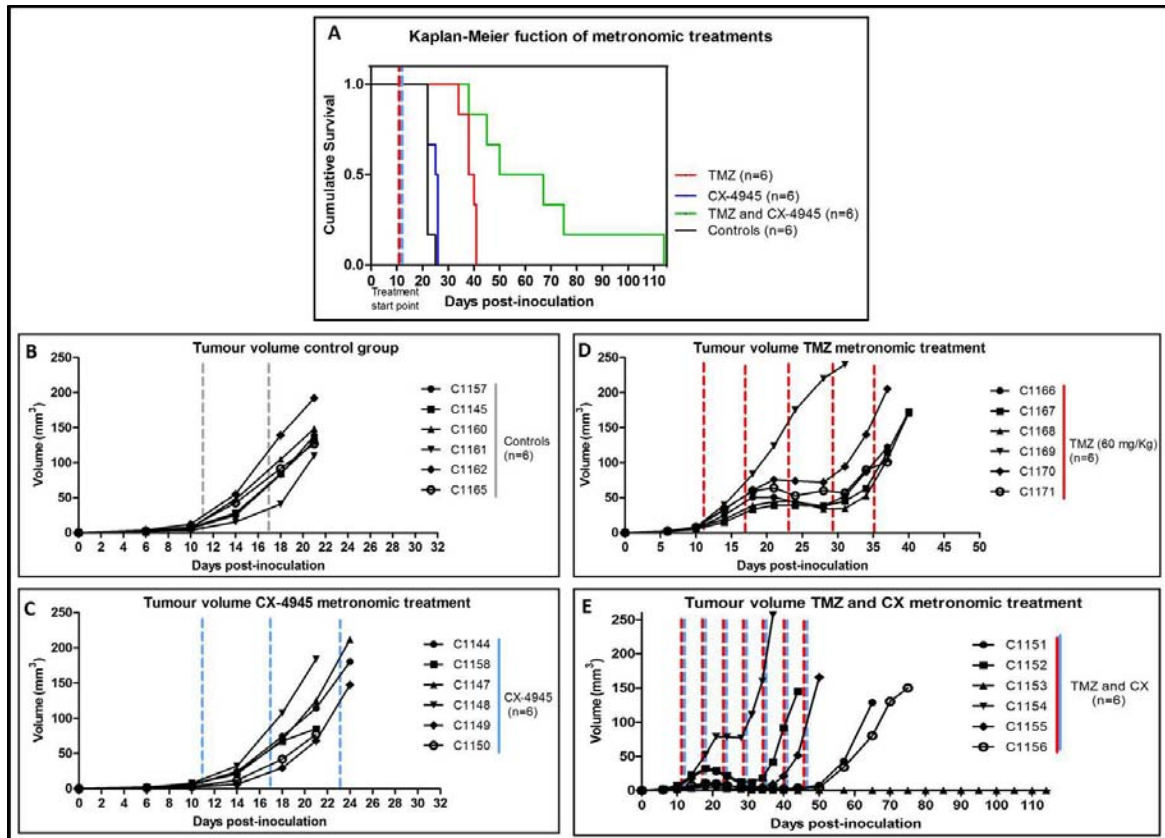


**Figure 4.11 Tumor volumes and survival rate for 6-day metronomic treatment. (A)** Survival Kaplan-Meier curve for metronomic CX-4945 treated mice (blue line), metronomic TMZ treated mice (red line), CX-4945 and TMZ metronomic treated mice (green line), and control mice (black line). Significant differences ( $p < 0.05$ ) were observed between all treatment groups analysed in comparison with control mice. **(B)** Tumor volumes of control GL261 mice **(C)** Tumor volumes of metronomic CX-treated GL261 mice **(D)** Tumor volumes of metronomic TMZ-treated GL261 mice and **(E)** Tumor volumes of metronomic CX and TMZ- treated GL261 mice. For all conditions and studies,  $n=6$  was used. Significant differences were found between groups ( $p < 0.05$ ) when comparing control mice with treated mice, and when comparing different treatments between them (TMZ, CX-4945 and combined TMZ and CX-4945). The dashed lines indicate therapy administration points. Cxxxx corresponds to a unique alpha-numeric animal identifier code in the GABRMN group.

For the CX-4945 metronomic treatment, a survival rate of  $24.5 \pm 2.0$  days was found, whereas for TMZ treatment, the survival rate was  $38.7 \pm 2.7$ . For the combined TMZ and CX-metronomic treatment, the survival rate was of  $64.8 \pm 27.8$  days. All groups offered significantly higher survival rate ( $p > 0.05$ ) compared to control mice group ( $22.5 \pm 1.2$  days), Figure 4.11A. Besides, TMZ alone produced better survival rate than CX-4945 alone, while combined TMZ and CX-4945 was significantly better than any of the two alone. Moreover, tumor volume evolution (Figure 4.11B-E) was significantly different ( $p < 0.05$ ) when comparing treated groups with control group. Body weight was also inspected every day (Figure 4.7D). At the time of comparing the different treated groups, significant differences were found regarding weight, tumor volume evolution and survival rate, being the best results always obtained with the metronomic treatment combining TMZ with CX-4945.

It is interesting to remark that mouse C1153 was cured from its GBM (presented substantial tumor reduction until only a small, but stable abnormal mass could be detected by MRI), but after 114 days p.i, it was found dead. C1553 mouse did not present body weight reduction. This mouse was euthanized according to animal welfare parameters, necropsy was performed and samples stored in 4% formaldehyde. A thymic lymphoma mass was detected, being probably the main cause of its death.

#### **4.2.4 Discussion**

##### **Effect of iCK2 on GL261 cultured cells**

GL261 cultured cells sensitivity was variable for the different iCK2 evaluated. CX-4945 decreased cell viability to about 20% of the control value. The  $EC_{50}$  found for CX-4945 ( $16.5 \pm 5.5$   $\mu$ M) is similar to the  $EC_{50}$  found in breast cancer cell lines by others [122], who reported values between 1.7 and 20  $\mu$ M. The lowest  $EC_{50}$  ( $8.1 \pm 1.5$ ) was found for TDB, concurring with a previous study [125], where a half maximal cell death concentration ( $DC_{50}$ ) of  $2.45 \pm 0.84$   $\mu$ M was observed for the human HeLa cell line and of  $3.45 \pm 0.2$   $\mu$ M for human T lymphoblastoid

cells. The standard GBM chemotherapeutic agent, TMZ, reached the EC<sub>50</sub> at 747.6±63.3 μM, which agrees with high values of half maximal inhibitory concentration (IC<sub>50</sub>) found by others that varied between cell lines: the IC<sub>50</sub> value of TMZ in SKNMC, NOS1, HS-SY-II, SYO-1 and 402-92 cells was <300 μM and In U87-MG cells, the IC<sub>50</sub> was 348 μM [281]. In addition, the combined TMZ and CX-4945 treatment carried out with GL261 cells *in vitro* presented increased efficacy regarding cell viability reduction, in comparison with both therapeutic agents administered separately (Figure 4.3C).

The low EC<sub>50</sub> of CX-4945 and TDB, combined with a significant decrease in cell viability, indicated that they should be suitable for future preclinical evaluation with GL261 tumors *in vivo*. CX-4945 was eventually chosen because it has been already described in clinical and preclinical studies [122–124]<sup>10,11</sup>.

As expected, we observed a significant reduction of CK2 activity in CX-4945 treated GL261 cells (Figure 4.4D). This was accompanied by the decrease of the phosphorylation of the CK2 target AKT(S129) (Figure 4.4B), similarly to the reported in [123] in prostate PC3 cancer cells. In addition, the AKT phosphorylation was found reduced as the CX-4945 concentration was increased, in a dose-dependent manner (Figure 4.4A). It has been described that the antiapoptotic effect of CK2 can be partially mediated by upregulation of the AKT/PKB pathway [203], thus the reduced viability found in GL261 cultured cells treated with CX-4945 can be also related to the downregulation of this pathway. These results reinforced the idea that CX-4945 could be a promising candidate for non-mutagenic brain tumor therapy in our preclinical GBM model.

---

<sup>10</sup> <http://www.cancer.gov/clinicaltrials/search/view?cdrid=642699&version=HealthProfessional>

<sup>11</sup> <http://www.prnewswire.com/news-releases/cylene-presents-encouraging-clinical-data-for-oral-ck2-inhibitor-at-asco-123219423.html>

### **Effects of CX-4945 in *in vivo* studies**

In *in vivo* studies, CX-4945 was described to inhibit the activation of STAT-3, NF- $\kappa$ B p65 and AKT, in nude mice with intracranial human GBM X1046 xenografts [124]. In our work, we could demonstrate that 3 days of CX-4945 administration to GL261 tumor-bearing mice caused a decrease in CK2 activity of tumor samples analysed to 35% of control values (Figure 4.4E). This confirms that CX-4945 reached the target tissue and caused the expected effect, as also reported in [124], although no further detailed study of the affected pathway was performed in our case. Regarding CX-4945 pharmacokinetics, described extensively elsewhere [123], it has a long half-life (more than 5 hours) and high oral bioavailability (20%) in mice, without detectable mutagenicity, genotoxicity or cardiac toxicity. The results described in our work agree with this, showing that CX-4945 was well tolerated in mice as assessed by minimal changes in body weight during the course of treatment compared to control vehicle (Figure 4.7A).

### **Non-metronomic CX-4945 longitudinal *in vivo* studies**

Although *in vitro* results indicated that CX-4945 should be a promising candidate for preclinical GBM therapy, unexpectedly, the non-metronomic *in vivo* treatment of GL261 tumor-bearing mice did not produce a better outcome. No tumor growth arrest and no survival improvement were detected (Figure 4.6A-D). This disagrees with a previous *in vivo* study [124] with intracranial human xenografts treated with CX-4945 which showed significant effects in mice survival (50.2-67.8 days for treated mice, versus 35.6-40.4 days for control mice). However, there are relevant differences between work reported in [124] and our work, which could explain, at least partially, the differences observed. In [124], athymic nude mice were used, while in our experiment, immunocompetent C57BL/6 mice have been used, because we consider that they mimic better the clinical patient situation. Moreover, despite authors in [124] inoculated more cells for tumor generation ( $5 \times 10^5$  cells vs.  $10^5$  cells, in our study), their tumor growth pattern was much slower (survival rate for their control mice was 35.6-40.4

days, whereas our control mice survived 17-21 days). In this sense, it is widely accepted that small, slow-growing tumors are easier to treat than established, fast-growing tumor [282, 283].

It is also worth mentioning that longitudinal *in vivo* studies reported by other authors did not present satisfactory results with CX-4945 in the same doses used in this work, although they studied other tumor types [284]. In this sense, using a drug combination for therapy involving CX-4945 was already suggested by authors in [284, 285], with an additive effect recorded, which is also in line with our decision to study a drug combination (CX-4945 and TMZ) in order to perhaps improve the therapy response results produced by CX-4945 alone.

#### **Non-metronomic combined CX-4945 and TMZ longitudinal *in vivo* studies**

Thus, the unexpected result obtained with the *in vivo* longitudinal study using CX-4945 alone in GL261 tumor-bearing mice lead us to hypothesize that a combined therapy with CX-4945 superimposed with TMZ could produce better results. The TMZ treatment in preclinical GBM mice has been proved useful in our group [237] with an average survival of  $33.9 \pm 11.7$  days for treated animals (Figure 4.10), significantly higher than control mice ( $21.5 \pm 3.7$  days). TMZ cytotoxicity is predominantly mediated by O6-MeG DNA lesions, which are repaired by the DNA repair protein MGMT [286]. Consequently, GBM patients whose tumors express low MGMT level, due to promoter hypermethylation, are more responsive to TMZ based therapy [60, 287]. Protein Kinase CK2 is a novel interaction partner of JAK1/2, potentiating JAK and STAT-3 activation [207]. A iCK2 could reduce STAT-3, which has been implicated in the resistance of GBM to TMZ, downregulating MGMT and diminishing TMZ resistance [288], highlighting the potential of use of iCK2 combined with standards of care like TMZ. Nevertheless, the combined treatment (standard 3-cycle TMZ described by our group [237] superimposed with non-metronomic schedule for CX-4945) did not produce the expected improvement, except by case C984, classified as an outlier (Figure 4.7C), which followed an evolution pattern similar to TMZ-treated cases described in [237]. Except for this case, the

combined TMZ+CX-4945 therapy showed similar results than control mice (survival of  $17.8 \pm 2.8$  days for treated mice vs  $19.8 \pm 1.5$  days for control mice), reversing the beneficial effect of TMZ 3 cycles treatment. However, the combined TMZ and CX-4945 treatment carried out with GL261 cells *in vitro* presented increased efficacy regarding cell viability reduction, in comparison with both therapeutic agents administered separately (Figure 4.3C). This reinforced the idea that an increased efficacy, instead of an antagonistic effect, should have been observed *in vivo* with the combined therapy.

One of the possible explanations for those results could be due to dramatic CX-4945 ‘off target’ effects, e.g. leading to strong splicing inhibition [289]. We cannot discard that these effects, rather than CK2 inhibition, are responsible for reversing TMZ efficacy. Another explanation could be related to the role of the immune system in therapy response [77] (see below), which would help to explain why a synergistic effect was observed *in vitro* with GL261 treated cells, but it was not seen in our early non-metronomic *in vivo* approach.

#### **Metronomic CX-4945 and/or TMZ longitudinal *in vivo* studies and possible implication of the immune system in therapy response**

The disappointing results obtained with non-metronomic administration schedules of CX-4945 both alone or in combination with TMZ lead us to raise the hypothesis that a possible interference with the host immune system was taking place, and it was the cause of the unfavourable outcome. Thus, we decided to move to a metronomic approach to discard or confirm this hypothesis. The so-called “metronomic therapy” [91], referring to equally spaced, low doses of chemotherapeutic drugs without extended rest periods, has been studied by several groups in the preceding years. Also, new therapeutic regimens with conventional drugs have been evaluated in order to activate immune responses that enhance tumor regression and prevent tumor regrowth. Recent studies with CPA metronomic therapy proved that this type of administration not only activates antitumor CD8<sup>+</sup> T-cell response, but also induces

long-term, specific T-cell tumor memory in GL261 tumors growing subcutaneously in immunocompetent mice [231, 290]. These authors have also proven that a 6-day intermittent was the optimum timing for this therapy and this could agree with the 7-day cycle for immune cell recruitment described in [81], and accordingly this was the schedule chosen for our metronomic treatments. Indeed, the metronomic (every 6 days) therapy carried out in our study offered a much better mice outcome, being the best results produced by CX-4945 and TMZ combined ( $64.8 \pm 27.8$  days) metronomic therapy, which was better than CX-4945 or TMZ metronomic therapies alone. These results reinforce the idea of the role of the immune system in therapy response [77] in GBM, and could explain the variation in our results depending on the therapy administration protocol used.

Regarding the immune system cycle involved in tumor response, we should consider that the cytotoxic T-lymphocytes (CTLs) have a relevant role in the defence against cancer recognizing antigens presented on the surface of transformed cells, following a complex cycle described in [80]. Also, the whole cycle for immune cell response could take around 7 days in mouse brain [81], which is in agreement with the 6-day interleave that we have used in our work. It was also described the need of a functional cluster of differentiation 5 (CD5)-dependent CK2 signalling for efficient differentiation of naive  $CD4^+$ T cells into Th2 and Th17 cells [80, 291], involved in monocytes differentiation into DCs subsets [292]. Moreover, authors in [293] have recently described impairment of Th17 cells development by CK2 inhibition with CX-4945 in a C57BL/6 mouse model of experimental autoimmune encephalomyelitis. Accordingly, CK2 inhibition (which could take place in every day or alternated days CX-4945 administration) could impair proper attraction of immune response triggered by immunogenic cell death signals. In this respect, several authors have described immunogenic death caused by TMZ therapy in GBM [294, 295]. All this combined could explain the reversal of beneficial effects observed in the non-metronomic combined therapy. Additionally, CK2 inhibition *in vitro* has been shown to compromise normal T-cell viability of cultured peripheral blood T-lymphocytes



harvested from chronic lymphocytic leukemia patients [296], while other authors [284] demonstrated cytotoxic effects of CX-4945 administration, alone, in head and neck cancer cultured cell lines and xenograft models. Further work will be needed to clarify, *in vitro* and *in vivo*, the extent of immunogenic cell death produced by TMZ and CX-4945, alone or in combination, in the GL261 GBM model.

In summary, it is tempting to speculate that when CX-4945 is administered every day or in alternated days, it could cause an impairment of immune system elements needed for tumor response. Furthermore, when it is administered combined with TMZ (3 cycles of therapy), CX-4945 reversed the beneficial effect of TMZ. When TMZ and CX-4945 are administered in a metronomic scheme every 6 days, the activation of the immune cell recruitment and response, which can take around 7 days [81], would not be significantly compromised. Accordingly, a word of caution should be said when treating immunocompetent preclinical tumors with CX-4945: the continued administration of a drug could impair the proper attraction of immune response contributing to therapeutic effects being evaluated.

#### **4.2.5 Conclusions**

CX-4945 has a noticeable effect in decreasing GL261 GBM cell viability and CK2 activity *in vitro*. Additionally, CK2 activity analysis confirmed that CX-4945 reached the target tissue *in vivo*. Notable differences in mice outcome were obtained with CX-4945 every day/alternated days (alone or combined with 3 cycles of TMZ), in comparison with metronomic administration of CX-4945 and/or TMZ, the highest survival rates being obtained with the metronomic protocol combining TMZ ± CX-4945 every 6 days.

An appealing explanation for this fact would be related to the immune system role in tumor response and the possible impairment of cytotoxic T-cell maturation cycle due to continued administration of CX-4945, which was overcome by the 6-day schedule metronomic administration. Further histopathological studies will be needed to confirm this hypothesis.

Accordingly, due care should be exercised when treating immunocompetent mice harbouring preclinical tumors with CX-4945 to ensure optimal results.

### **4.3 CYCLOPHOSPHAMIDE AND TEMOZOLOMIDE METRONOMIC TREATMENT IN IMMUNOCOMPETENT MICE: POTENTIAL FOR GL261 GLIOBLASTOMA TREATMENT**

Most of the content of this section have been submitted (and it is currently under revision) to the *NMR in Biomedicine* Journal with the title of “*Metronomic treatment in immunocompetent preclinical GL261 glioblastoma: effects of cyclophosphamide and temozolomide*” by Ferrer-Font L, Arias-Ramos N, Lope-Piedrafita S, Julià-Sapé M, Pumarola M, Arús C and Candiota AP.

#### **4.3.1 Specific objectives**

- Evaluating CPA and TMZ metronomic treatment in our GL261 implanted C57BL/6 immunocompetent mice model for therapy response monitored using MRSI-based PR techniques and nosological imaging.

#### **4.3.2 Specific materials and methods**

##### **GL261 cells**

GL261 mouse glioma cells were grown as previously described [270] and explained in section 3.1.

##### **Animal model for *in vivo* studies**

A total of 48 C57BL/6 female wt mice weighing  $21.7 \pm 1.3$  g were used for this study. Tumors were induced in C57BL/6 mice by intracranial stereotactic injection of  $10^5$  GL261 cells as explained in general materials and methods section 3.2.1 Mice were weighed every day and tumor volumes were followed twice a week using  $T_{2w}$  MRI acquisition as in [237] the day 6 and 11 after implantation. Mice with the most homogeneous weights and tumor sizes were chosen before therapy start to make experimental groups. Volume and weight averages measured before treatment did not show significant differences ( $p > 0.05$ ) (Table 4.8).

Tumor volume and body weight									
Therapy start point day 8 p.i									
CONTROL_TMZ_8	CONTROL	Mice	C1075	C1081	C1068	C1079	C1071	C1088	AV±SD
		Weight	22.5	22.5	20.9	20.6	24.7	22.1	22.2±1.5
		Volume	8.3	7.4	4.3	4.0	2.9	2.9	5.0±2.3
TMZ140_8	TMZ 140mg/kg/day	Mice	C1070	C1069	C1087	C1082	C1073	C1076	AV±SD
		Weight	21.4	21.8	19.3	19.4	22.5	22.8	21.2±1.5
		Volume	10.7	9.3	9.0	1.6	1.3	1.3	5.5±4.6
TMZ200_8	TMZ 200mg/kg/day	Mice	C1085	C1078	C1086	C1080	C1072	C1077	AV±SD
		Weight	22.1	19.1	19.9	19.5	21.3	21.3	20.5±1.2
		Volume	7.5	7.0	4.3	3.6	2.9	1.9	4.5±2.3
Therapy start point day 11 p.i									
CONTROL_CPA_11	CONTROL	Mice	C1032	C1036	C1039	C1042	C1038	C1047	AV±SD
		Weight	20.8	20.1	19.4	23.0	22.7	21.3	21.2±1.4
		Volume	6.8	23.1	8.9	20.8	5.5	26.5	15.3±9.2
CPA140_11	CPA 140mg/kg/day	Mice	C1033	C1034	C1035	C1040	C1041	C1043	AV±SD
		Weight	23.0	21.6	21.4	21.6	20.2	21.6	21.6±0.9
		Volume	8.2	9.3	9.4	5.4	16.0	19.4	11.2±5.3
CONTROL_TMZ_11	CONTROL	Mice	C1000	C1001	C1004	C1006	C1007	C1009	AV±SD
		Weight	20.8	22.1	22.2	22.4	23.8	23.1	22.4 ±1.0
		Volume	20.6	10.4	21.7	14.5	6.6	20.5	15.7±6.3
TMZ140_11	TMZ 140mg/kg/day	Mice	C1002	C1010	C1011	C1012	C1013	C1014	AV±SD
		Weight	20.9	23.4	22.8	20.1	23.8	21.2	22.0±1.5
		Volume	5.2	16.6	14.2	19.7	15.8	14.3	14.3±4.9
TMZ240_11	TMZ 240mg/kg/day	Mice	C1003	C1005	C1015	C1037	C1045	C1046	AV±SD
		Weight	21.3	20.1	23.6	20.5	21.5	20.1	21.2±1.3
		Volume	22.6	3.1	2.4	10.24	14.7	21.0	12.3±8.7

**Table 4.8 Average ± standard deviation (AV±SD) for tumor volume (mm<sup>3</sup>) and body weight (g) for mice before starting therapy, at day 8 p.i. (groups: CONTROL\_TMZ\_8, TMZ140\_8 and TMZ\_200\_8) and at day 11 p.i. (groups: CONTROL\_CPA\_11, CPA140\_11, CONTROL\_TMZ\_11, TMZ140\_11 and TMZ240\_11). No significant differences (p>0.05) were found between TMZ or CPA treated group (n=6) and control mice (n=6) neither for tumor volumes, nor for mice body weight before starting therapy. Cxxxx corresponds to a unique alpha-numeric animal identifier code in the GABRMN.**

**Animal treatments**

CPA and TMZ therapy were administered to tumor-bearing mice every six days. Different experiments and groups were used (Table 4.9): CPA was administered at a dosage of 140 mg/kg for 7 times (980 mg/Kg cumulative dose). TMZ was administered at different dosages: dosage of 140 mg/kg for 10 times (1400 mg/Kg cumulative dose) and for 7 times (980 mg/Kg cumulative dose). TMZ dosage of 200 mg/Kg was administered 6 times (cumulative dose of 1200 mg/Kg), and dosage of 240 mg/Kg was administered 7 times (cumulative dose of 1200 mg/Kg). The therapy starting day was not always the same (see Table 4.9). Some groups started therapy at day 11 p.i. (tumor volume average  $13.8 \pm 6.8 \text{ mm}^3$ ), as previously described by our group [237], whereas other groups started therapy at day 8 p.i. in order to assess the possible effect of starting therapy at smaller tumor volumes ( $5.0 \pm 3.1 \text{ mm}^3$ ).

Acronym	Treatment	MRI days (p.i)	Therapy starting day	Number of doses administered	Cumulative dose	Tumor volume at therapy start point ( $\text{mm}^3$ )	Survival rate (days)
TMZ140_8 (n=6)	140 mg/kg TMZ	6 and 8	Day 8	7 doses	980 mg/Kg	C: $4.2 \pm 2.3$ T: $5.5 \pm 4.6$	C: $19.7 \pm 2.7$ T: $46.7 \pm 28.4$
TMZ200_8 (n=6)	200 mg/kg TMZ	6 and 8	Day 8	6 doses	1200 mg/Kg	C: $4.2 \pm 2.3$ T: $4.0 \pm 2.3$	C: $19.7 \pm 2.7$ T: $34.5 \pm 8.0$
CPA140_11 (n=6)	140 mg/kg CPA	7 and 11	Day 11	7 doses	980 mg/Kg	C: $15.2 \pm 9.2$ T: $11.2 \pm 5.3$	C: $19.7 \pm 2.7$ T: $36.7 \pm 15.2$
TMZ140_11 (n=6)	140 mg/kg TMZ	5 and 11	Day 11	10 doses	1400 mg/Kg	C: $15.7 \pm 6.3$ T: $14.3 \pm 4.9$	C: $19.0 \pm 2.1$ T: $43.2 \pm 32.2$
TMZ240_11 (n=6)	240 mg/kg TMZ	5 and 11	Day 11	6 doses	1440 mg/Kg	C: $15.7 \pm 6.3$ T: $12.3 \pm 8.7$	C: $19.0 \pm 2.1$ T: $32.2 \pm 15.8$
TMZ140_8 + TMZ140_11 (n=12)	140 mg/kg TMZ	6 and 8	Day 8	7 doses	980 mg/Kg	C: $4.2 \pm 2.3$ T: $5.3 \pm 4.6$	C: $19.5 \pm 2.3$ T: $44.9 \pm 29.0$
		5 and 11	Day 11	10 doses	1400 mg/Kg	C: $15.7 \pm 6.3$ T: $14.3 \pm 4.9$	

**Table 4.9 Treatments performed with CPA and TMZ therapy: type and dose of treatment, MRI time points for volume measurement before treatment, therapy starting point, number of doses administered, cumulative dose, tumor volume average ( $\pm$ SD) at therapy starting points and survival rate ( $\pm$ SD). C: control and T: treated.**

If tumor volume mass was found to be equal or lower from the previous measurement, the tumor was considered to show signs of response to therapy. In this respect, control GL261

tumors monitored in our group (unpublished results) display an average increase of  $11.7 \pm 3.8$   $\text{mm}^3/\text{day}$  ( $n = 61$ ) between day 8 p.i. and death of the animal (average of  $21.5 \pm 3.7$  days p.i.).

Acronyms to name each group have been established and will be used along this section (Table 4.9): TMZ140\_8 (TMZ 140 mg/Kg with therapy start point at day 8 p.i.), TMZ200\_8 (TMZ 200 mg/Kg with therapy start point at day 8 p.i.), CPA140\_11 (CPA 140 mg/Kg with therapy start point at day 11 p.i.), TMZ140\_11 (TMZ 140 mg/Kg with therapy start point at day 11 p.i.) and TMZ240\_11 (TMZ 240 mg/Kg with therapy start point at day 11 p.i.)

After treatment, animals with progressive tumor growth were euthanized by cervical dislocation as animal welfare protocols advice for ethical restrictions (annex 1). Animals cured from GBM (cured in this study meaning to have only a small,  $<2 \text{ mm}^3$ , stable residual mass) were followed-up (weighed twice a week and regular weekly MRI explorations performed).

TMZ (*Sigma-Aldrich, Madrid, Spain*) was dissolved in 10% DMSO in saline solution (0.9% NaCl) for *in vivo* experiments and it was administered using an oral gavage at doses of 140 mg/kg, 200 mg/kg and 240 mg/kg. CPA (*Sigma-Aldrich, Madrid, Spain*) was administered as a monohydrate and was dissolved in 1x PBS (final pH 7.2), filter sterilized (*Steriflip, Merckmillipore, Spain*) and administered at dose of 140 mg/kg by intraperitoneal injection using a 1 ml syringe and 27.5 gauge needle as in [297].

### **Necropsies**

In the case of “cured” animals, when a 20% or higher percentage of weight reduction was detected, animals were euthanized, necropsy performed and tissue samples kept in paraformaldehyde 4%. Organs analysed were encephalon, salivary glands, thymus, heart, lungs, LNs, stomach, small and large intestine, liver, spleen, kidneys, pancreas, urinary bladder, reproductive organs, skin and skeletal muscle. HE staining was performed and samples analysed by histopathology.

### ***In vivo MRI and MRSI studies***

#### ***Data Acquisition***

- ***MRI studies***

MR studies were carried out as explained in general materials and methods section (3.4.1). In this case, the 7T Bruker BioSpec 70/30 USR was equipped with a mini-imaging gradient set (400mT/m) and used a linear volume coil with 72 mm inner diameter as transmitter, and a mouse brain surface coil as a receiver for brain MRI studies. Furthermore, for body MRI, a rat brain phased array 4-channel coil located over the thorax of the mouse was used.

GL261 tumor-bearing mice were screened by acquiring HR coronal  $T_{2w}$  images using RARE sequence to detect brain tumor presence and to monitor its evolution stage. The acquisition parameters are described in general materials and methods, section 3.4.1.

For body MRI, images were acquired with respiration gating. Low resolution  $T_{2w}$  fast SE images were initially obtained in axial planes to be used as reference scout images. Acquisition parameters for these images were: TR/TE<sub>eff</sub>=3600/36 ms; echo train length (ETL)=8; FOV=3×3 cm<sup>2</sup>; MTX=128×128; ST=1 mm; NS=30; NA=2. HR  $T_{2w}$  fast SE images were acquired afterwards in axial, sagittal and coronal planes. Experimental parameters for coronal and sagittal images were: TR/TE<sub>eff</sub>=3000/26 ms; ETL=4; FOV=4.8×3.2 cm<sup>2</sup>; MTX=384×256; ST= 1 mm (sagittal) and 0.5 mm (coronal); NS=15 (sagittal) and 21 (coronal); NA=4. Experimental parameters for axial images were: TR/TE<sub>eff</sub>=4200/36 ms; ETL=8; FOV=3×1.5cm<sup>2</sup>; MTX=256×128; ST= 1 mm; NS=35; NA=4. An intragate FLASH sequence (with retrospective gating) was also used to acquire a coronal image (TR/TE=150/2.5ms flip angle=40°, 30 repetitions, FOV=7×3.5cm<sup>2</sup>; MTX=256×256; NS=15; ST= 1 mm)

- ***Diffusion Weighted Imaging (DWI) studies of the brain***

DWI sequences were performed in the coronal and axial planes using a diffusion-weighted SE pulse sequence. A total of 11 coronal and 8 axial contiguous 1mm-thick sections were imaged

using the following parameters: TR= 3s (coronal) and 1.5s (axial), TE=22 ms, MTX=128x128, FOV=1.92 x 1.92 cm<sup>2</sup>, with two diffusion weightings at b=100 and 900 s/mm<sup>2</sup> ( $\Delta=10$ ms and  $\delta=5$ ms). ADC maps were estimated from DWI images as in [298].

- ***MRSI studies of the brain***

MRSI was acquired once a week, but if tumor size was unchanged or reduced in comparison with the previous exploration, MRSI was acquired twice a week. For these studies, a reference T<sub>2w</sub> high-resolution image and a 14 ms TE basal MRSI with PRESS localization were acquired. The MRSI grid was spatially located such that the volume of interest (VOI) included most of the tumoral mass as well as normal/peritumoral brain parenchyma. Acquisition parameters were as described in [237], except by matrix size (12x12 in this study).

#### **MRI and MRSI processing and post processing**

- ***Tumor and edema volume calculation***

Manual segmentation of abnormal brain mass in T<sub>2w</sub> images and edema in ADC maps was performed. Edema volume was considered to be represented by the hyperintensity zone in DWI and T<sub>2w</sub> images, while for estimation of tumor volume, the abnormal mass in T<sub>2w</sub> images was used, without taking into account the possible hyperintensity edema zone (example in Figure 4.12A). Tumor or edema volumes were calculated from T<sub>2w</sub> HR horizontal images using the equation 6 in section 3.4.1.1.



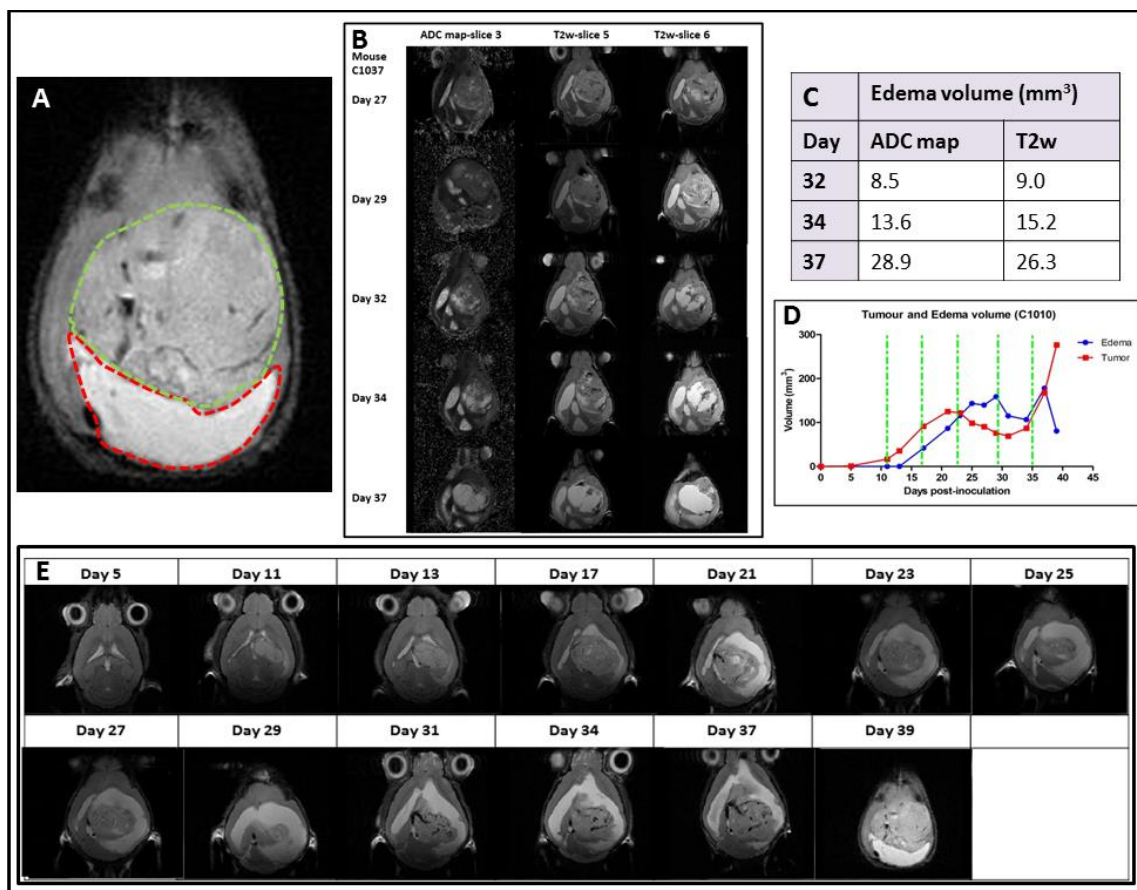


**Figure 4.12 Tumor and edema volumes of mice treated with TMZ (A)** C1010 mouse (metronomic TMZ treatment with 140 mg/kg) at day 39 p.i. axial  $T_{2w}$  MRI image. Cxxxx corresponds to a unique alphanumeric animal identifier code in the GABRMN research group. Manual segmentation of tumor and edema is shown. Slashed green line approximately surrounds the tumor zone and slashed red line, the edema. **(B)** Apparent diffusion coefficient (ADC) maps and  $T_{2w}$  axial images acquired at days 27, 29, 32, 34 and 37p.i. from case C1037 with TMZ metronomic treatment (240 mg/kg/day). **(C)** Quantification of the edema volume in both ADC and  $T_{2w}$  axial images acquired at days 32, 34 and 37p.i. from case C1037 TMZ with metronomic treatment (240 mg/kg/day). Edema quantification from  $T_{2w}$  images and ADC maps did not present significant differences ( $p>0.05$ ). **(D and E)** Tumor and edema volume evolution of mouse C1010 (TMZ 140 mg/Kg).  $T_{2w}$  axial images at different days p.i.

- **Brain MRSI post-processing and nosological imaging**

MRSI data were post-processed essentially as described in [270, 299]. Briefly, data were initially pre-processed at the MR workstation with ParaVision 5.1 (Bruker BioSpin), and then post-processed with 3D Interactive Chemical Shift Imaging (3DiCSI) software package (courtesy

of Truman Brown, Ph.D., Columbia University, New York, NY, USA) for line broadening adjustment (Lorentzian filter, 4 Hz), zero-order phase correction and exporting the data in American Standard Code for Information Interchange (ASCII) format. Dynamic MRSI processing Module (DMPM, <http://gabrmn.uab.es/dmpm>), running over MatLab (*The MathWorks Inc., Natick, MA, USA*) was used to align all spectra within each MRSI matrix (using the Cho containing compounds peak as reference, 3.21 part per million (ppm)). The 0 – 4.5 ppm region of each spectrum in the MRSI matrix was individually normalized to UL2 and the normalized matrix was exported in ASCII format for performing the PR analysis.

NMF methods belong to a group of multivariate data analysis techniques designed to estimate meaningful latent components, also known as sources, from non-negative data. Standard NMF methods decompose the data matrix into two non-negative matrices  $S$  (the sources) and  $A$  (the mixing matrix). The differences between these NMF methods are given by the different cost functions used for measuring the divergence between 'X' and  $S \cdot A$ . Convex NMF, used in this work, is also able to handle negative data [249, 300].

From the biochemical viewpoint, the source extraction technique to classify MRS data assumes that in each voxel there is a mixture of heterogeneous tissues, from which the contribution of each source can be obtained [262]. Three different sources (normal brain parenchyma, actively proliferating tumor and tumor responding to treatment) were extracted and used for calculating nosologic maps representing the spatial response to treatment, as in [262]. In this work, the green colour is used for nosological image coding when GBM responding to treatment source contributes the most, blue for normal brain parenchyma, red for actively proliferating GBM and black for undetermined tissue [262].

### **Statistical analysis**

Variance homogeneity was assessed with the Levene's test. Sample distribution was assessed with the Kolmogorov-Smirnov test. A two-tailed Student's t-test for independent measurements was used for comparisons, for samples of equal or different variances (depending on the Levene's test result). The global evolution of tumor growth curves or body weight measurements was evaluated with the UNIANOVA test. A bivariate correlation test with analysis of Pearson coefficient was carried out to assess the interrelation between the tumor volume at therapy starting point and the survival of each individual. Comparisons of survival rates were performed with the Log-Rank test. The significance level for all tests was  $p < 0.05$ .

### **4.3.3 Results**

#### **Longitudinal metronomic treatment with CPA in tumor-bearing mice**

A significant improvement was detected regarding tumor evolution (Figure 4.13A) and survival rate (Figure 4.13B) for CPA140\_11 in comparison with non-treated mice.

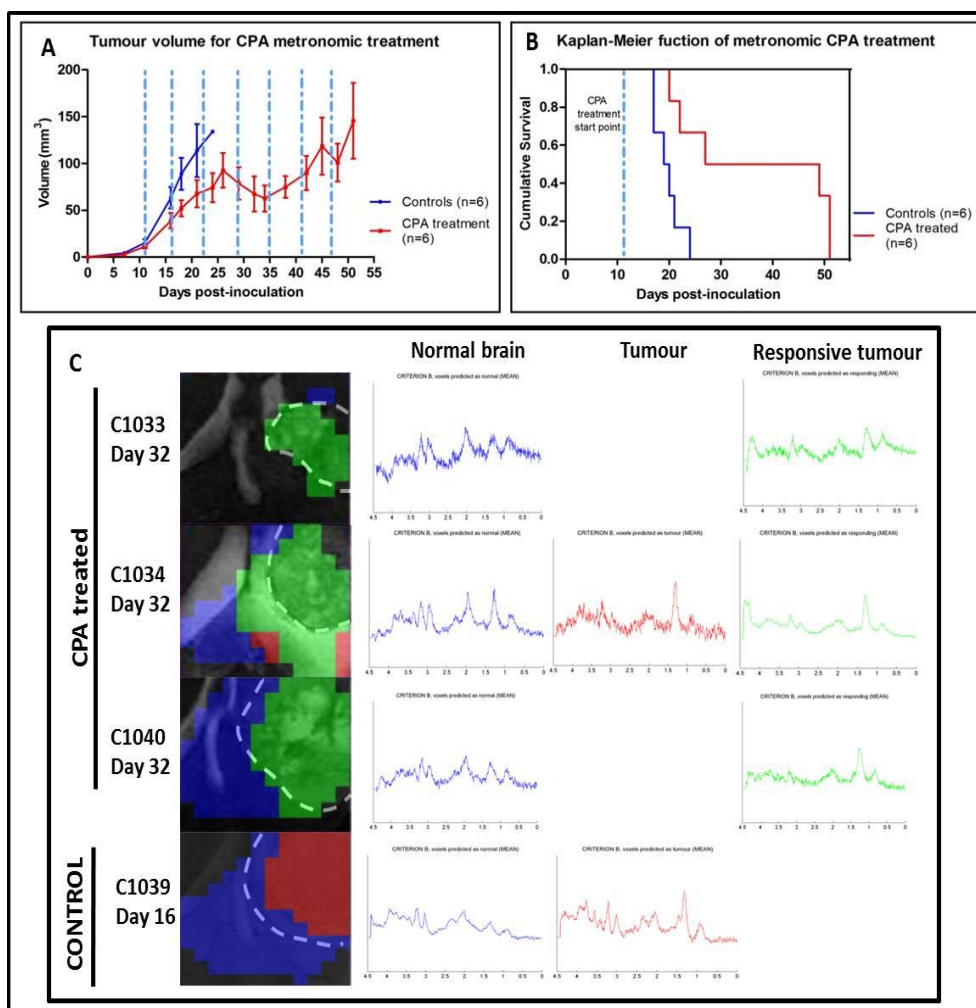


**Figure 4.13 Tumor volumes, survival rate and nosological images of mice treated with CPA (A) Tumor volumes  $\pm$  SD (acquired at days 7, 11, 16, 18, 21, 24, 26, 27, 29, 32, 34, 38, 42, 45, 48 and 51 p.i) of control mice (blue line) and CPA treated mice (red line). The dashed blue line indicates CPA therapy administration days. Significant differences were observed between groups for comparisons between control and treated mice tumor volumes along therapy ( $p < 0.05$ ). (B) Survival Kaplan-Meier curves for control mice (blue line) and CPA treated mice (red line). Significant differences were found between groups ( $p < 0.05$ ). The dashed blue line indicates CPA therapy starting point. For all conditions and studies,  $n = 6$  was used (C) Nosological maps superimposed on  $T_{2w}$  reference images acquired at day 32 p.i. in cases C1033, C1034 and C1040 (CPA treated) and at day 16 in case C1039 (control). CPA dosage was 140mg/kg administered every 6 days, at this time point (32 days), mice had received a total of 560 mg/kg of CPA. For each map, blue represents normal tissue; red, actively proliferating tumor; green, tumor responding to therapy; and black undetermined tissue. Mean spectra calculated from individual**

**RESULTS – Section 4.3: CPA and TMZ metronomic GBM treatment**

spectra of cases C1033, C1034 and C1040 at day 32, and C1039 at day 16. For mouse C1033, left, normal tissue (average of 2 blue pixels), and right, tumor responsive tissue (average of 23 green pixels). For mouse C1034, left, normal tissue (average of 23 blue pixels), in the centre, actively proliferating tumor tissue (average of 6 red pixels) and in the right, tumor responsive tissue (average of 54 green pixels). For mouse C1040, left, normal tissue (average of 46 blue pixels), and right, tumor responsive tissue (average of 50 green pixels). For mouse C1039, left, normal tissue (average of 67 blue pixels), in the centre, actively proliferating tumor tissue (average of 41 red pixels).

The survival rate for CPA140\_11 treatment was 36.7+15.2 vs. 19.7+2.7 days in control mice (Figure 4.13B). Significant differences ( $p < 0.05$ ) were observed for body weight evolution between groups (Figure 4.14A). At the therapy starting point, no significant differences ( $p > 0.05$ ) were observed neither for tumor volume nor for body weight between groups (Table 4.8 and Table 4.9).

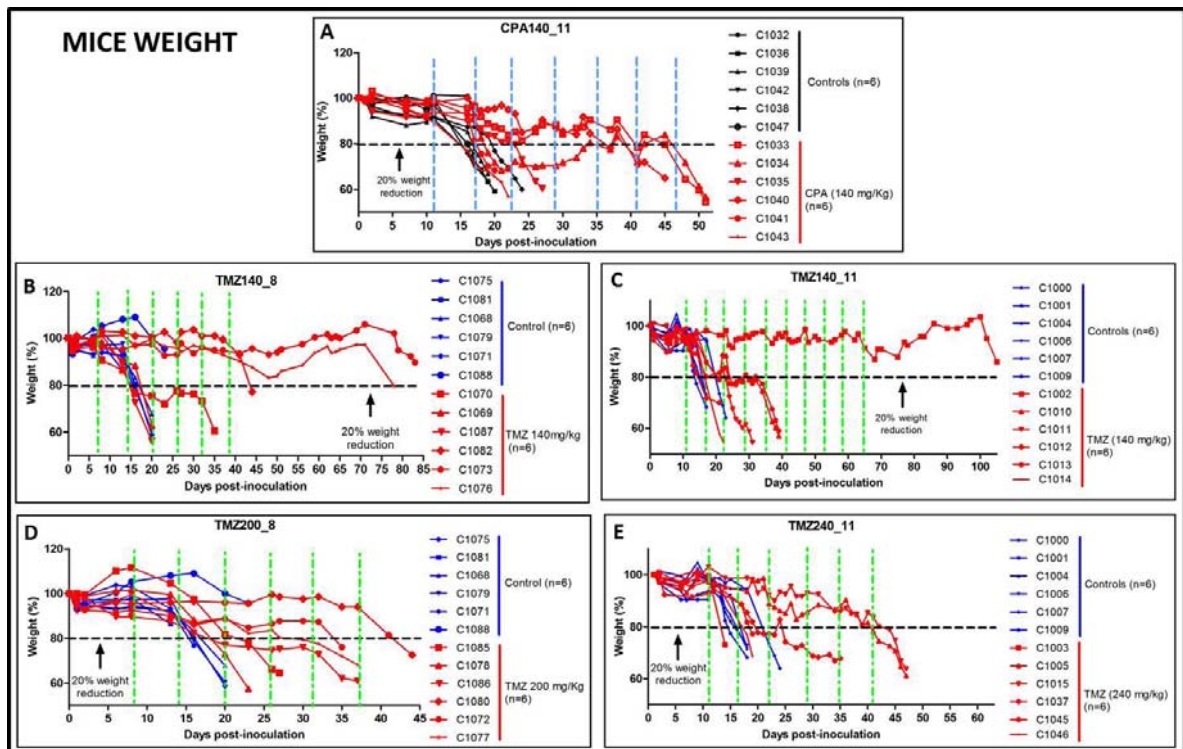


**Figure 4.14 Body weight of mice from different experimental groups (A) Weight of mice treated with 140 mg/Kg metronomic CPA (red lines) and control vehicle (black lines), the dashed blue lines indicates CPA therapy administration time points. Therapy start point is at day 11 day p.i. Significant differences**

## RESULTS – Section 4.3: CPA and TMZ metronomic GBM treatment

were observed between groups ( $p < 0.05$ ). **(B-E)** Weight of mice treated with metronomic TMZ (red lines) and control vehicle (blue lines), the dashed green lines indicates TMZ therapy administration time points. Significant differences were observed between treatment and control in each individual therapy experimental groups ( $p < 0.05$ ). **(B)** 140 mg/kg metronomic therapy starting at day 8 p.i. **(C)** 140 mg/kg metronomic therapy starting at day 11 p.i. **(D)** 200 mg/kg metronomic therapy starting at day 8 p.i. **(E)** 240 mg/kg metronomic therapy starting at day 11 p.i. For all conditions and studies,  $n=6$  was used.

### Longitudinal metronomic treatments with TMZ in tumor-bearing mice

TMZ metronomic treatment was carried out in GL261 tumor-bearing mice and significant improvement ( $p < 0.05$ ) in survival rate was detected for all doses used (140, 200 and 240 mg/Kg, Figure 4.15), in comparison with non-treated mice.

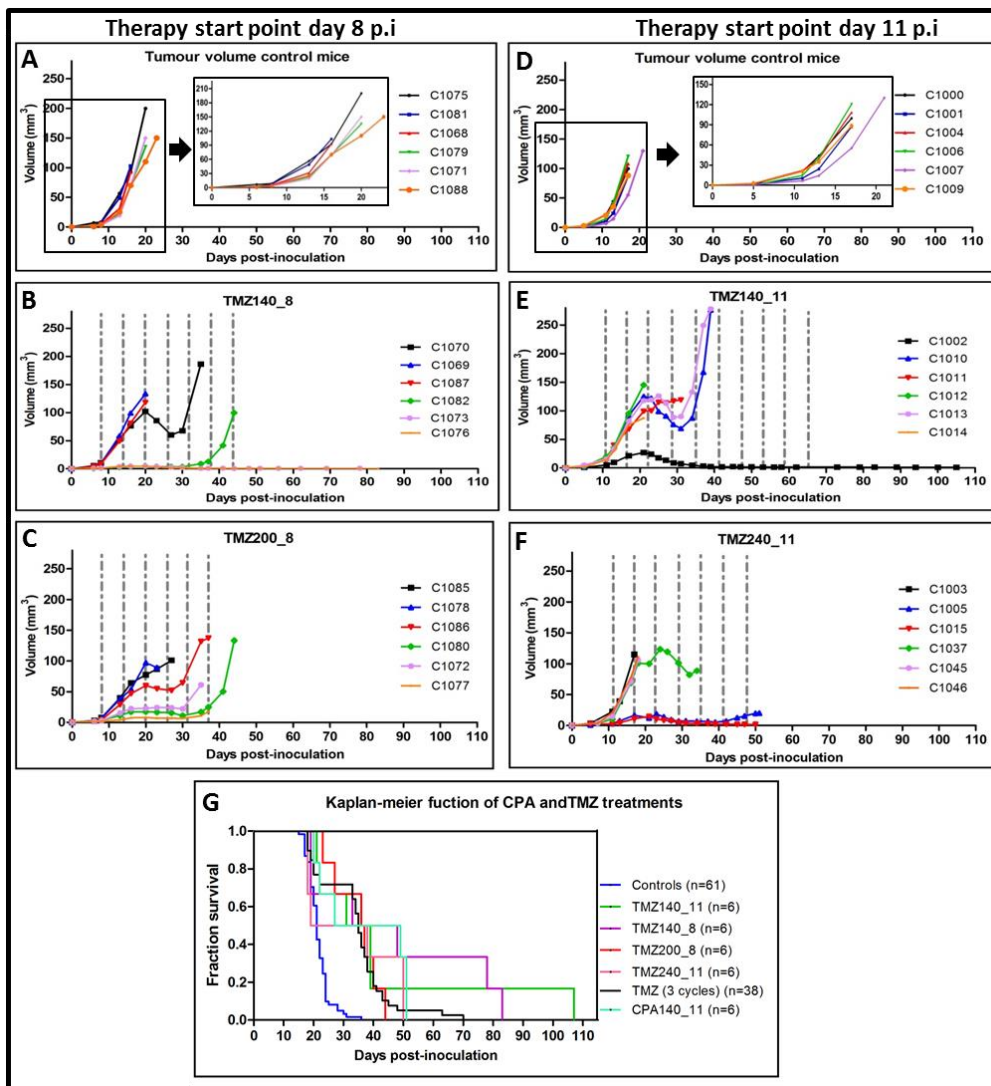


**Figure 4.15 Tumor volumes and Kaplan-Meier curve of control mice and metronomic TMZ treated mice**

**(A-F)** Tumor volumes of control mice and metronomic TMZ treated mice (metronomic administration every 6 days). Significant differences were observed between control and treated mice tumor volumes along therapy ( $p < 0.05$ ). **(A)** Control mice of therapy start point at day 8 p.i. **(B)** Treatment of 140 mg/Kg with 7 doses, therapy start point at day 8 p.i. **(C)** Treatment of 200 mg/Kg with 6 doses, therapy start point at day 8 p.i. **(D)** Control mice of therapy start point at day 11 p.i. **(E)** Treatment of 140 mg/Kg, with 10 doses, therapy start point at day 11 p.i. **(F)** Treatment of 240 mg/Kg with 7 doses, therapy start point at day 11 p.i. **(G)** Survival Kaplan-Meier curves for control mice from this study, from [237] and unpublished data from GABRMN ( $n=61$ , dark blue line), TMZ 140 mg/Kg treatment ( $n=6$ , green line), TMZ 140 mg/Kg treatment with therapy start point at day 8 p.i ( $n=6$ , purple line), TMZ 200 mg/Kg treatment with therapy start point day at 8 p.i ( $n=6$ , red line), TMZ 240 mg/Kg treatment ( $n=6$ , pink line), 3 cycles TMZ from [237] and unpublished data from GABRMN ( $n=38$ , black line) and 140 mg/Kg CPA treated mice ( $n=6$ , clear blue line). Significant differences ( $p < 0.05$ ) were found between treated group and controls, and for TMZ 140mg/Kg groups compared to the other treatments (TMZ 200 mg/Kg, TMZ 240 mg/Kg, CPA 140 mg/Kg and 3 cycles of TMZ). Inserts in A and D show results in an expanded x-axis scale.

The composition of the experimental groups can be found in Table 4.9. At the start of each treatment, no significant differences were found between treated and control groups regarding tumor volume or body weight (Table 4.8 and Table 4.9).

- **TMZ metronomic treatment at 140mg/Kg (TMZ140\_8 and TMZ140\_11)**

For the 140 mg/kg metronomic TMZ treatment assessment, two different groups were studied. In one of the groups, TMZ administration started at day 8 p.i (TMZ140\_8), and in the other group, at day 11 p.i. (TMZ140\_11).

With the first group, TMZ140\_8 (Table 4.9), a Kaplan-Meier survival curve was elaborated to compare the survival rate with the control group (Figure 4.15G), and significant differences ( $p < 0.05$ ) were found between them. For control mice, the average survival rate was  $19.7 \pm 2.7$  days and for the metronomic TMZ-treated ones,  $46.7 \pm 28.4$  days. A significant improvement

( $p < 0.05$ ) was detected regarding tumor evolution as well (Figure 4.15A and B). With TMZ140\_11 (Table 4.9), a Kaplan-Meier survival curve was elaborated to compare the survival rate with the control group (Figure 4.15G), and significant differences ( $p < 0.05$ ) were found between them. For control mice, the average survival rate was  $19.0 \pm 2.1$  days and for the metronomic TMZ-treated ones,  $43.2 \pm 32.2$  days. For this group, significant improvement ( $p < 0.05$ ) was also detected regarding tumor evolution (Figure 4.15D and E). On the other hand, no significant differences ( $p > 0.05$ ) were recorded regarding survival time for different therapy start days.

- **Grouping of both treatment groups at 140mg/Kg of TMZ**

At the starting point of each treatment, body weight and tumor volume were assessed. While significant differences ( $p < 0.05$ ) were recorded for different therapy start days comparing tumor volume of both groups (at day 8 p.i,  $5.0 \pm 3.1$  mm<sup>3</sup> and day 11 p.i,  $13.8 \pm 6.8$  mm<sup>3</sup>), no significant differences ( $p > 0.05$ ) could be detected when comparing TMZ140\_8 and TMZ140\_11 survival rates. So both groups have been grouped for further analysis (140 mg/Kg TMZ,  $n=12$  and control,  $n=12$ ).

- **TMZ metronomic treatment at 200 mg/Kg (TMZ200\_8)**

For TMZ200\_8 treatment assessment, TMZ administration started at day 8 p.i. and significant differences ( $p < 0.05$ ) were found regarding tumor evolution along treatment (Figure 4.15A and C). The survival rate comparison between groups, Figure 4.15G, showed significant differences between groups ( $p < 0.05$ ): TMZ-treated mice showed a survival rate of  $34.5 \pm 8.0$  days, and control mice,  $19.7 \pm 2.7$  days.

- **TMZ metronomic treatment at 240mg/Kg (TMZ240\_11)**

For TMZ240\_11 treatment assessment, TMZ administration started at day 11 p.i. Significant differences ( $p < 0.05$ ) were found between treated and control group for tumor volume



evolution (Figure 4.15D and F), as well as for survival rates (Figure 4.15G): For control mice, the average survival rate was  $19.0 \pm 2.1$  days and for the metronomic TMZ treated ones,  $32.2 \pm 15.8$  days.

#### **Non-invasive assessment of therapy response**

In Figure 4.13C, nosological images generated through semi-supervised source analysis are shown for three CPA metronomic treated cases at day 32 and one control case at day 16. Figure 4.13C also shows the mean spectra calculated from the segmented tumor zones. The three treated cases shown (out of  $n=6$  total treated cases) presented reduced volume (2-30% reduction) at day 32 p.i in comparison with the previous exploration at day 29 p.i. All mice presenting tumor volume reduction during treatment show predominantly a “responding pattern” (green pixels in the nosological image) in the tumor zone, and a “normal parenchyma pattern” in the normal brain zone (blue pixels in the nosological image). On the other hand, the control mouse show “actively proliferating tumor pattern ” (red pixels in the nosological image) instead of “responding pattern” in the tumor zone.

Regarding TMZ-treated cases with 140 mg/Kg, three groups were identified based on tumor growth: one group (33.3%,  $n= 4$ ) did not show volume reduction at any time (Figure 4.16A), the second (41.7%,  $n= 5$ ) showed a transient volume reduction (ranging 1.8-45% reduction in comparison with previous highest volume measurement) and tumor started growing again after a certain point (Figure 4.16B), and a third group (25%,  $n= 3$ ) considered to be “cured” (Figure 4.16C) since tumor volume was reduced until only a small remaining abnormal mass was detected by MRI (Figure 4.17). Regarding the representative nosological images (Figure 4.16B), when GL261 tumors showed volume growth arrest, there was a predominance of green pixels (responding tumor). During the phase of tumor shrinkage, red pixels (proliferating tumor) seem to predominate again, preceding the regrowth of the tumor. A further exploration (day 31 p.i) seems to point to an oscillatory behaviour with an increase in green

pixels again, although no further acquisitions were obtained. Tumors smaller than 5 mm<sup>3</sup> could not be properly segmented from normal tissue due to the limiting pixel size, Figure 4.16C.

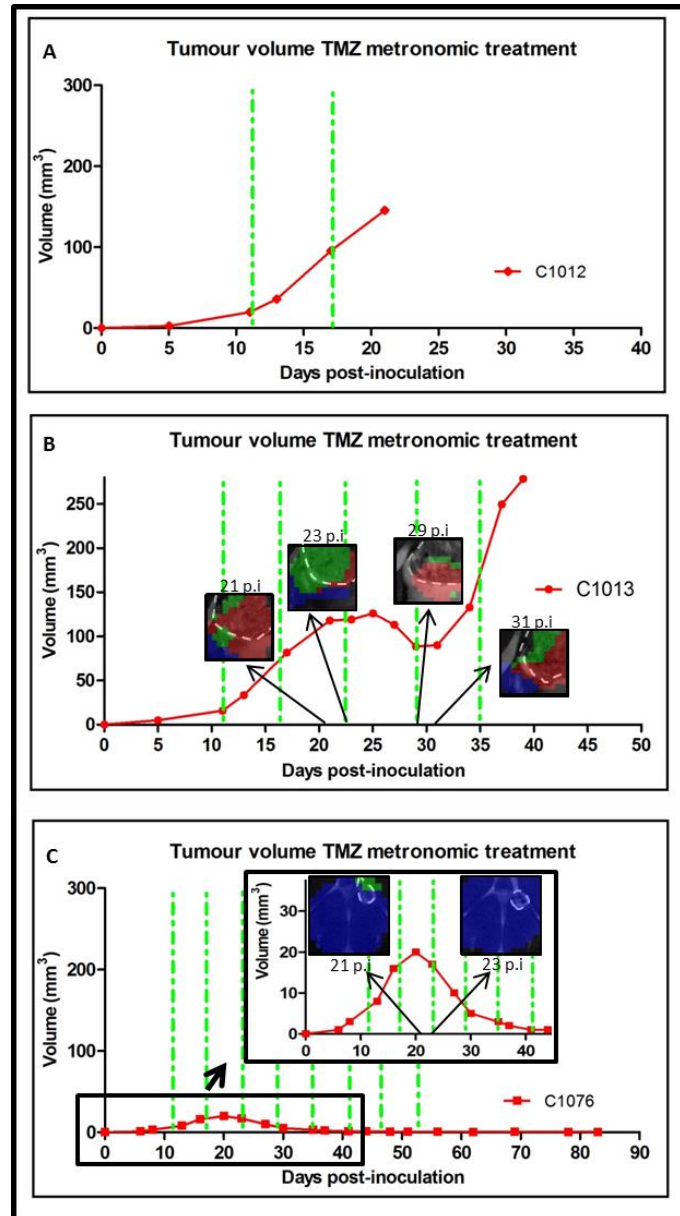


**Figure 4.16** Examples of volume evolution follow-up and MRSI acquisitions of (A) one mouse that did not respond to therapy (C1012), in this instance no MRI acquisition was performed. (B) one mouse that responded to therapy but with posterior tumor relapse (C1013). (C) and a “cured” mouse (C1076). Mice were treated with 140 mg/Kg of TMZ every six days. Green lines indicate the days of therapy administration and MRSI was acquired once a week, and if tumor size was unchanged or reduced, twice a week. Some MRSI acquisitions could not be used due to the small tumor mass or the bad quality of

spectra obtained due to the heterogeneity of the investigated tissue. For each map, blue represents normal tissue, red, actively proliferating tumor, green, tumor responding to therapy, and black undetermined tissue. Numbers p.i. above or below nosological images refer to p.i acquisition time.

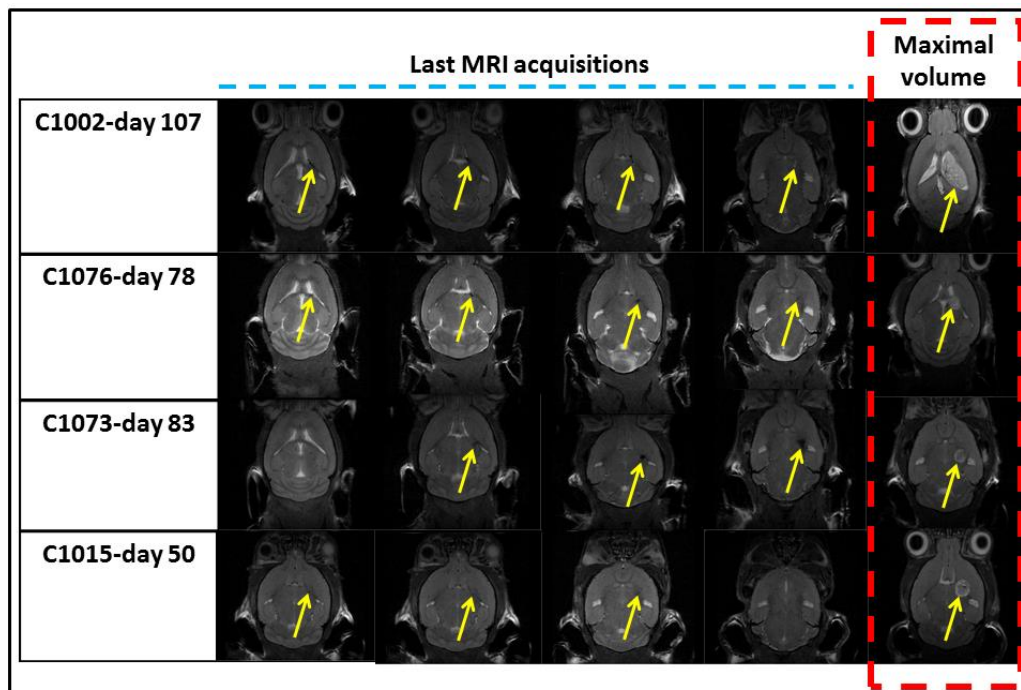


**Figure 4.17** Coronal  $T_{2w}$  MRI of “cured” mice from TMZ 140 mg/Kg metronomic therapy treatment. Consecutive slices from dorsal (left) to ventral (right), for the last day before euthanization, marked with slashed blue line. In some images, a remaining small abnormal mass is observed (either hypo or hyperintense) marked with a yellow arrow, but always lower than  $1.5\text{mm}^3$  in size and no changes were observed during, at least, 4 weeks after the last therapy administration. In the last column (marked with a slashed red line) the maximum tumor volume achieved in each case is shown. Mouse C1002,  $26.8\text{mm}^3$ , day 21 p.i.; mouse C1076,  $4.6\text{mm}^3$ , day 16 p.i.; mouse C1073,  $4.8\text{mm}^3$ , day 20 p.i. and mouse C1015,  $18.5\text{mm}^3$ , day 23 p.i.

#### **Diffusion parameters in CPA and TMZ treated mice**

Some of the CPA and TMZ-treated mice displayed clear signs of peritumoral brain edema (PTBE) (Figure 4.12). DWI was acquired for these mice, as densely cellular tissues or those with intracellular swelling exhibit lower water diffusion coefficients when compared to an edematous hypocellular region, which allow their differentiation. Figure 4.12B and C show

that ADC maps indicated that there was PTBE, compatible with an increased content of free water. Mice presenting edema were all from the group showing transient tumor volume reduction followed by final tumor regrowth.

Figure 4.12D and E and Figure 4.18 also show that PTBE zones surrounding the tumor seem to have sometimes opposed evolution in comparison with tumoral tissue growth: the enlargement of the edema zone was accompanied by a decrease in tumor volume, and when tumor started growing again, edema decreased.

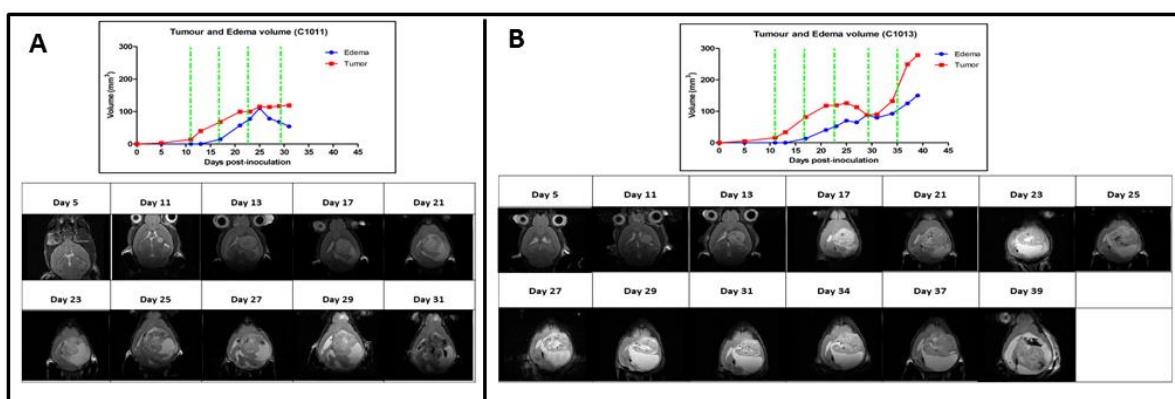


**Figure 4.18 Tumor and edema volume evolution (A) of mouse C1011.  $T_{2w}$  axial images at days 5, 11, 13, 17, 21, 23, 25, 27, 29, 31, 34, 37 and 39 p.i. and (B) of mouse C1013.  $T_{2w}$  axial images at days 5, 11, 13, 17, 21, 23, 25, 27, 29, 31, 34, 37 and 39 p.i. Dashed green lines represent TMZ therapy administrations (140 mg/Kg).**

#### **Follow-up of cured mice after TMZ therapy and assessment of final cause of death**

One mouse from the TMZ240\_11 treatment (mouse C1015) was cured from its GBM, but after 50 days p.i, it was found dead. In the TMZ140 groups, 25% of the mice (n=3) presented substantial tumor reduction until only a small, but stable abnormal mass could be detected by MRI (Figure 4.17 and also Figure 4.16C). These GBM-cured mice survived between 50 and 107 days p.i and they were screened by whole body MRI examinations when their body weight decreased beyond 20% (Figure 4.14) to check for possible abnormal masses in other organs. Mice were euthanized according to animal welfare parameters, necropsy was performed and

samples stored in 4% formaldehyde. In about 75% of these mice (n=3), the most probable cause of death was a lymphoma mass (Figure 4.19 shows an example of a treated mouse (C1076) from the TMZ140\_8 group, with thymic lymphoma detection, compared to a control mouse) with metastases in the surrounding structures and organs. The other 25% (n=1) died due to other dysfunctions in intestine, liver and kidney.

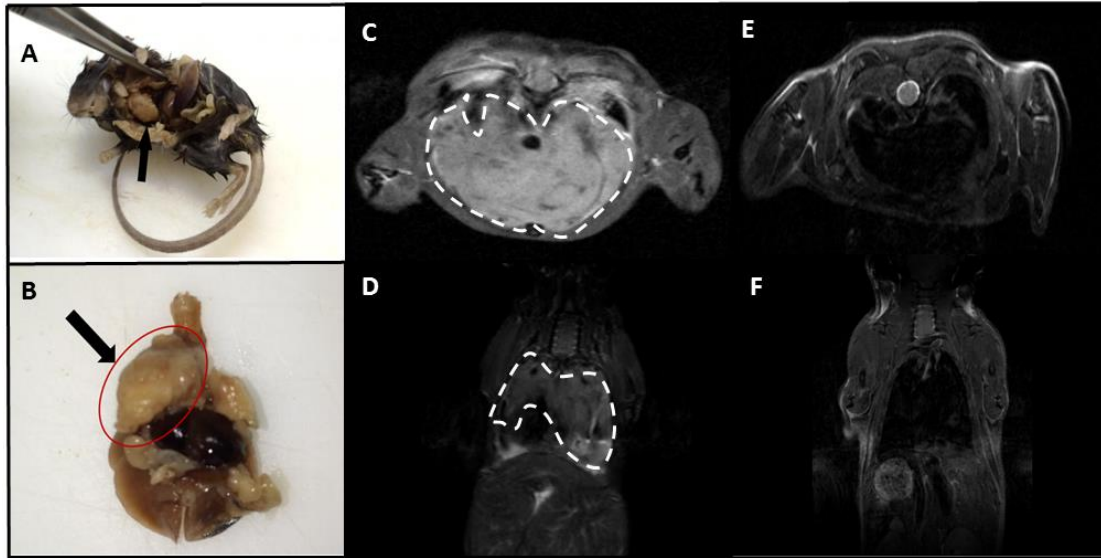


**Figure 4.19 Example of thymic lymphoma appearance in one mouse treated with TMZ metronomic 140 mg/Kg (C1076 at day 78 p.i.) (A-D) compared to a control mice with no lymphoma (E and F). (A) Whole body necropsy with the lymphoma localization marked with a black arrow (B) Mediastinum zone with the lymphoma localization marked with a black arrow and a red oval (C) C1076 mouse axial  $T_{2w}$  MRI image. Slashed white line marked the tumor zone, occupying the zone of the mediastinum. (D) C1076 mouse coronal  $T_{2w}$  MRI image. Slashed white line marked the tumor zone. (E) Control mouse axial  $T_{2w}$  MRI image and (F) Control mouse coronal  $T_{2w}$  MRI image.**

Regarding the residual mass observed in brain MRI examinations of the cured mice (Figure 4.17), the histopathological analysis did not find tumoral cells. Instead, scar tissue with macrophages and lymphocytic cells was detected in the initially inoculated region. In addition, no abnormal features were found in the rest of normal-appearing brain parenchyma.

#### **4.3.4 Discussion**

##### **Longitudinal metronomic treatments with CPA or TMZ in tumor-bearing mice**

Metronomic approaches have been followed for chemotherapeutic treatment of mice bearing GL261 tumors, with TMZ (140, 200 and 240 mg/Kg) and CPA (140 mg/Kg). These protocols were chosen according to previous studies describing that a 6-day interleave between administrations was the ideal resting period [231], because it could improve therapy response by enhancing the participation of the host immune system in such response. Authors in [231] also studied GL261 GBM in immunocompetent C57BL/6 mice using CPA 140 mg/Kg, achieving a cure in all of them, this being effective in 67% of the investigated mice even when animals were re-challenged with injection of new GL261 cells for tumor growth. Nevertheless, their model was ectopic, having GL261 cells inoculated subcutaneously into the posterior flank. Our goal was to assess if this metronomic scheme was also effective in our immunocompetent orthotopic GL261 model or, at least, whether it would help to improve our previous results obtained with non-metronomic TMZ treatment [237, 262]. In the case of CPA treatment, our results did not reproduce those described in [231]; despite the survival rate of treated animals being higher than controls ( $36.7 \pm 15.2$  vs.  $19.7 \pm 2.7$  days, Figure 4.13B), no cure was achieved in our model. In addition, no significant differences ( $p > 0.05$ ) were found between the average survival of CPA-treated mice and results reported previously by our group with non-metronomic TMZ treated mice [237, 262] and unpublished group data,  $33.9 \pm 11.7$  days ( $n = 38$ ). The main hypothesis to explain these differences could be that the tumor environment is relevant, and the therapy response becomes more complex in an orthotopic GBM, compared to the ectopic inoculation, an environment which does not mimic intracranial conditions. For example, niches for SCs (and CSCs) may be different in orthotopic with respect to ectopic locations.

The brain was considered as a relatively 'immune-privileged' site [301]. This was thought to reflect, in part, the protective nature of the BBB. Thus, the brain environment may be better protected as opposed to the subcutaneous location of tumors developed in [231]. Accordingly, there is a need to examine the antitumor activity of agents in the context of the appropriate tumor micro-environment, and an ectopic model could lead to false-positive response with the evaluated drugs [232]. In an orthotopic model, relevant host interactions are analysed, as well as aspects deriving from site-specific dependence. Therefore, CPA effect could be impaired in our orthotopic model due to the brain microenvironment protection and in relation with the performance of the immune system in the different locations.

In the case of TMZ metronomic therapy studies, 140 mg/kg treatment offered the best results. Mice from these groups (TMZ140\_8 + TMZ140\_11, Table 1) survived  $44.9 \pm 29.0$  days (n=12), being significantly better ( $p < 0.05$ ) than the ones treated with TMZ 3 cycles of treatment [237, 262] and unpublished group data ( $33.9 \pm 11.7$  days, n=38). With metronomic TMZ140 administration, three types of tumor evolution were observed: cured (25%, n=3), transient tumor volume reduction with relapse after a certain point (41.7%, n=5) and no apparent response to therapy (33.3%, n=4), Figure 4.16.

TMZ treatment achieved better results regarding tumor volume reduction and survival rate than CPA, but without achieving curation of the GBM afflicted mice, in contrast with all mice cured results obtained for subcutaneous GL261 in [231] for CPA treatment. Still, the significant survival increase produced by CPA and TMZ in our orthotopic GBM model indicates a potential interest in the combination/alternation of the two compounds in future therapy studies.

#### **Influence of the tumor volume at the therapy starting point on survival**

No significant differences were found ( $p > 0.05$ ) when comparing survival rates between groups starting therapy with tumor volumes of  $5.0 \pm 3.1$  mm<sup>3</sup> and those with tumor volumes of  $13.8 \pm 6.8$  mm<sup>3</sup> (corresponding to days 8 and 11 p.i. respectively), regardless of the therapeutic

agent or dosage utilized. Nevertheless, in order to assess the interrelation between the tumor volume at the therapy starting point and the survival rate, we decided to delimit the studied group to ensure that the only variable between groups would be the starting tumor volume. In this sense, only the groups receiving TMZ at 140mg/Kg were used and the linear regression test performed showed that the correlation between the initial volume and the overall survival time was significant (Pearson coefficient= -0.66,  $p < 0.05$ ), Figure 4.20. This would agree with what has been described by others, as it is well known that smaller “early stage” tumors may respond better to therapy than “advanced stage” tumors [283]. Decreasing the number of implanted cells usually slows down tumor growth [221], accordingly we would expect tumor volumes in [295] to be clearly below that of our day 8 tumors, still their average survival time was not better than the one found in this work and in [262]. On the other hand, results described in [302] when comparing survival of C57BL/6 mice harbouring GL261 GBM (intracerebral injection of  $10^5$  GL261-luc2 cells), treated with antibodies against CTLA-4 and/or PD-1 and starting therapy on day 6 p.i. or on day 14 p.i., showed better survival in the case of smaller (6 day) tumors at therapy start day. In this respect, it may be wise to recognize that in some of the mice groups being evaluated in the present work, differences between the smallest and the largest tumor volume at the starting therapy point was substantial (Table 4.8), with the smaller (slow growing) ones producing a better therapy outcome, which is the case of mice C1076, C1071 and C1002, with survival times in the range of 50-107 days. On the other hand, smaller (slow growing) tumors in non-treated mice did not display major survival differences with respect to larger ones. In summary, although no significant differences could be demonstrated for average survival values of the evaluated groups analysed altogether, there were hints of possible influence of initial tumor volume at treatment start in therapy response also in our model, as it can be noted with the significant correlation obtained within the TMZ 140mg/Kg groups (Figure 4.20).



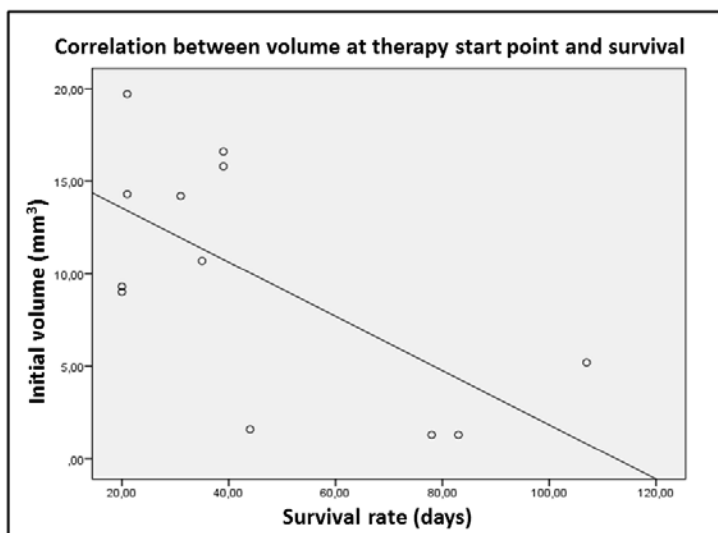


**Figure 4.20** Correlation between volume at therapy starting point (metronomic TMZ at 140mg/Kg) and survival.

#### Non-invasive assessment of therapy response

MRSI grids were acquired once a week, or two times a week if tumor volume stayed constant or decreased in comparison with previous MRI acquisitions. So, not all time points of tumor evolution have a corresponding MRSI data acquisition. A semi-supervised source analysis, as described in [262], was applied to MRSI data and nosologic images were generated (Figure 4.13, Figure 4.16). Clearly responding tumors (according to tumor volume changes and response evaluation criteria in solid tumors (RECIST) criteria [262, 303]) showed a predominance of green pixels (“responding” spectral pattern). A predominance of red pixels (“actively proliferating” spectral pattern) was also seen in some cases at times of tumor volume reduction, for example in Figure 4.16B (day 29 p.i.). In this case, it was followed by a mostly “actively proliferating” metabolomics pattern with tumor volume regrowth (days >31 in Figure 4.16B), suggesting an oscillatory behaviour for the response/regrowth patterns being sampled by MRSI, which may merit further evaluation in future work. These results are in agreement with previous results from our group [262], and offer an additional non-invasive window to assess the effectiveness of TMZ and CPA chemotherapy through a surrogate biomarker. Even before changes in tumor volume expected increase are observed in MRI

acquisitions, spectral pattern changes can be seen (e.g. day 21 p.i. in mouse C1013 in Figure 4.16B).

The reference sources used in the semi-supervised methodology were the same ones used for the conventional 3 cycles TMZ experiment [262]. Those sources have been robust enough to differentiate responding from non-responding tumors under different therapies (TMZ and CPA), which suggests that metabolic changes contributing to those response patterns are reproducible and, possibly, similar between TMZ and CPA (Figure 4.21), being both recognized by the previously extracted source. If we accept that both therapeutic agents produce immunogenic death, as stated in [295] for TMZ, and in [304] for CPA, these metabolic changes sampled by the response source could be explained due to the mobilization of the immune system to fight against the tumor (*see below Relevance of host immune system in therapy response* section) producing similar metabolomic patterns due to immune system-caused tumor cell death. This would provide a rationale for the recognition by the same source in the response caused by both therapeutic agents.

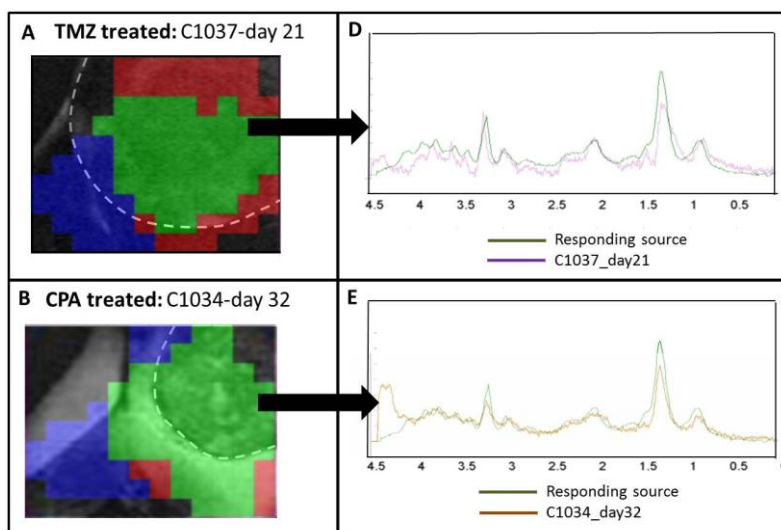


**Figure 4.21** Responding pattern average spectra after semi-supervised source analysis of (A) TMZ treated mouse (C1037 at day 21 p.i.), tumor responsive tissue (average of 44 green pixels) and (B) CPA

*treated mouse (C1034 at day 32 p.i.), tumor responsive tissue (average of 54 green pixels). Both average spectra are visually compared with the TMZ responding source obtained from the training group [262].*

One of the handicaps for this part of our work is that there were some situations that could impair the correct acquisition of MRSI data. Namely, when tumor reached a large volume (about 150 mm<sup>3</sup>), occupying most of the acquired MRSI grid and becoming MRI-wise heterogeneous, the presence of edema and extravasated blood could impair local homogeneity adjustments and, accordingly, the spectral MRSI quality could be worsened. On the other hand, when tumor volumes became very small (for example C1076 at day 23 p.i., volume of 2.9 mm<sup>3</sup>) partial volume effects from peritumoral brain parenchyma could limit the accuracy in the nosological images obtained from the sampled region, Figure 4.16C.

#### **Diffusion MRI studies in CPA and TMZ treated mice: edema appearance**

A new feature observed in this study, compared to previous work from our group [237, 262] and other work with orthotopic GBM [295], was the appearance of PTBE zones surrounding the tumor, which seem to have in some instances an opposing behaviour in comparison with tumor evolution. This was observed in T<sub>2w</sub> MRI and confirmed by diffusion MRI. The underlying mechanism for these events has not been elucidated yet, but one possible explanation is that chemotherapy causes a higher degree of (desired) tumor-cell and endothelial-cell killing than basal effects produced by standard tumor growth with concomitant nutrient access restriction. Thus, it is known that TMZ induced DNA damage may harm proliferating endothelial cells. This overall increased cell death might lead to secondary inflammatory reactions analogous to the wound-healing response [305], originating abnormal vessel permeability and subsequent edema formation in the (peri)tumoral area [306]. Furthermore, some authors state that PTBE is a consequence of tissue reconstruction resulting from tumor cell invasion and could also act as an appropriate suitable niche for the growth and spread of glioma cells [307], indicating an increased probability of tumor regrowth/relapse.

It may be relevant to mention here the phenomenon named “pseudoprogression” (increased contrast uptake volume faking relapse) known to appear in humans during or after classical radiochemical GBM treatment, which has been described to correlate with increased PTBE. This PTBE has also been seen in glioma patients treated with dendritic cell-based immunotherapy [308]. In this respect, the PTBE detected in our GBM cases could well have a similar origin as in the pseudoprogression human instances. Accordingly, the large PTBE recorded from our investigated mice would also agree with the participation of the immune system of the host mice in the response mechanism, producing inflammatory regions detectable by MRI.

#### **Hazardous effects due to cumulative TMZ dosage in brain-tumor “cured” mice**

A total of 3 mice out of 12 (25%) of the TMZ140 treatments presented tumor regression (Figure 4.16C) and their survival rate ranged between 74 and 114 days. In addition, one mouse from TMZ240\_11 survived for 50 days. However, they had to be euthanized after 20% weight reduction, and concomitant worsening of the health status of the animal. In 3 out of these 4 mice (75%), a lymphoma was found in necropsy studies (Figure 4.19). TMZ has a strong mutagenic potential on mouse bone marrow cells *in vivo* [309]. Also, clinical patients treated with high dose regimens of TMZ for extended periods might present with particular risk for secondary malignancy (like lymphoma appearance [310]) because of treatment-associated immunosuppression and a high cumulative dose of a potentially carcinogenic alkylating drug [311].

The cumulative dosages used for this study are shown in Table 4.9. For all treatments, the lower cumulative dosage used for TMZ was of 980 mg/Kg, and the higher cumulative dosage used was of 1400mg/Kg, which is equivalent to 2940 mg/m<sup>2</sup> and 4200 mg/m<sup>2</sup>, respectively,

taking into account the conversion factors for mouse data<sup>12</sup>. For human patients, TMZ is used in a different administration schedule [312], with 75 mg/m<sup>2</sup>/day x 7 days/week for 6 weeks, plus 150-200 mg/m<sup>2</sup>/day x 5 days, every 28 days for six cycles. This results in a cumulative dose of 7650-9150 mg/m<sup>2</sup>. The cumulative dosage given by us in our study in mice is indeed lower than the human dosage, but it is concentrated in a much shorter period of time (42-60 days in mice vs. around 240 days in human patients, in addition to large interleave rest periods), which could explain a higher incidence of other malignancies due to TMZ treatment in our preclinical studies in the GBM “cured” mice.

Until the present study, the TMZ cumulative dosage used in our group was of 540 mg/Kg (1620 mg/m<sup>2</sup> concentrated in 15 days) and no toxic effects had been found. One of the possible reasons to explain this absence of toxic effects could be that animals previously evaluated in our group did not survive beyond 33.9±11.7 days and the toxic effects (or tumor promoting effects) would appear at a later time, in case of animal survival due to first-line therapy. In chapter 4.2 (Figure 4.5), we have found that TMZ MTD in acute dosage was 480 mg/Kg for C57BL/6 mice (1440 mg/ m<sup>2</sup>), but no systematic study has been performed about TMZ cumulative toxicity. On the other hand, there is a study of cumulative MTD in human glioma patients [313], where they affirm that the MTD is 350 mg/m<sup>2</sup>/day, as at this dose level they observed evidence of severe toxicity occurring beyond cycle two (3 days every other week), producing a cumulative dose of 2400 mg/m<sup>2</sup>. Their toxicity evidence included neutropenia in 33% of patients and severe thrombocytopenia in 42% of patients. Therefore, a daily dose of 300 mg/m<sup>2</sup> was considered to be the recommended dose for TMZ for use in repeated cycles administration (8 cycles) in humans.

---

<sup>12</sup> <https://ncifrederick.cancer.gov/lasp/acuc/frederick/Media/Documents/ACUC42.pdf>

As many studies have reported, one of the advantages of metronomic chemotherapy administration schedules with low dosages would be the decreased toxic effects compared to MTD chemotherapy [314]. In this sense, and given the results described in this work, a decrease in the TMZ dosage would be advisable in order to avoid the appearance of hazardous effects due to TMZ cumulative dosage upon metronomic administration.

It is also worth mentioning that the lymphoma occurrence found in our treated mice took place around 3 months p.i., but most of the studies dedicated to preclinical brain tumor therapy in literature do not perform long-term follow-up studies in their treated animals. Without these follow-up explorations, it is impossible to check for tumor relapse or development of other malignancies due to the usually high doses of mutagenic chemotherapeutics administered [65], and accordingly, it is not possible to compare our data in this with those of other authors. For example, authors in [231] describe a resting period after the last CPA administration of 33 days, with an additional re-challenge period of about 30 additional days but there was no longer-term follow-up described.

#### **Relevance of host immune system in therapy response**

The possibility of using the patient's immune system for the treatment of cancer was first theorized more than 100 years ago, but only in the last decades this field has advanced toward clinical applications.

Since its inception in 2000, metronomic chemotherapy [91], has undergone major advances as an antiangiogenic therapy. Furthermore, the discovery of the pro-immune properties of chemotherapy through mechanisms of immunogenic death and its indirect effects on cancer cells has established the intrinsic multitargeted nature of this therapeutic approach [315]. The past 15 years have seen a marked rise in clinical trials of metronomic chemotherapy, which is being increasingly combined in the clinic with conventional treatments, as well as with novel

therapeutic strategies, such as drug repurposing, targeted agents and immunotherapy [314]. Our results perfectly link with results described by others [231, 290] which worked with GL261 subcutaneous tumors in immunocompetent mice treated with CPA metronomic therapy. This treatment was proven to activate antitumor CD8+ T-cell response, and also to induce long-term, specific T-cell tumor memory [231, 290]. The same authors also proved that a 6-day intermittent was the optimum timing for this therapy, which could agree with the 7-day cycle for immune cell recruitment in mouse brain described in [81].

Other approaches taking into account the immune response are being developed with satisfactory results. For example, immune vaccines used in GL261 C57BL/6 mice produced increased survival with respect to control mice [316] or even cure for up to 50% of the investigated mice [317]. Moreover, direct treatment of GL261 orthotopic tumors growing in C57BL/6 mice with monoclonal antibodies against CTL4 or PD1 T-lymphocyte ligands cures up to 75% of treated animals [302], highlighting that the immune factor cannot be neglected in the therapy response context. Nevertheless, GL261 cells used in [302, 316] also expressed a transduced firefly luciferase gene for non-invasive follow-up, and luciferase has been reported to trigger an immune response on its own [218] which suggests that caution may be required to untangle the possible contribution of the mouse-alien protein to the favourable results obtained with the immune checkpoint blockade alone.

Results obtained in our study would point to the metronomic schedule of administration (best results at 140mg/Kg dosage) as a good alternative for preclinical GBM treatment. Moreover, the improvement of results in comparison with the traditional administration scheme described in [237] suggests that the 6-day cycle is performing better than classical more continuous drug administration approaches. This would agree with a possible better recruitment of the host immune system as described in [231, 304]. Further work will be needed to validate this hypothesis, with longitudinal studies and histopathological analysis at

different time points, taking into account non-invasive information from nosological images as guidance to decide euthanization time points for ex-vivo tumor infiltrating immune cells characterization through immunohistochemistry.

#### **4.3.5 Conclusions**

Results in this work indicate that orthotopic GL261 inoculated mice did not produce the same outcome under metronomic CPA therapy than ectopic GL261 GBM mice. Thus, the correct choice of the preclinical model is essential to obtain relevant information about treatment. On the other hand, both the CPA and the TMZ metronomic protocols produced a satisfactory effect, reducing tumor volume and increasing mice survival, while 25% of mice experienced tumor regression and cure. This is an improvement in comparison with the previous 3-cycle TMZ treatment approach previously described by us. Further studies will be needed to evaluate the possible contribution of the host immune system recruitment due to metronomic schedule administration in our experimental model. Despite these promising results, the incidence of lymphoma in some animals indicate that further optimization experiments must be performed with lower TMZ cumulative dose and/or less administrations or with combination therapies while maintaining or increasing cured mice percentage.



## 5 GENERAL DISCUSSION

In the attempt of finding a suitable non-mutagenic GBM therapy for our GL261 implanted C57BL/6 mice (intended to be used alone or in combination), we focused into protein CK2, an oncogenic protein kinase which contributes to tumor development, proliferation, migration and invasion, as well as apoptosis suppression in cancer [115, 164]. Our results in preclinical GL261 GBM pointed to higher expression levels of CK2 $\alpha$  in tumor in comparison with the normal tissue (Figure 4.1 and Table 4.1), which is in agreement with other authors that affirmed that high levels of CK2 $\alpha$  are expressed in solid human tumors [165, 166]. So these results reinforced the potential of CK2 $\alpha$  as a valid therapeutic target [124, 275] to investigate in preclinical GL261 GBM. In this sense, recent studies have reported that diverse iCK2 exert inhibitory effects over cell growth, such as the very specific iCK2, CX-4945, which has been reported as the first iCK2 to reach clinical stage testing for the treatment of multiple types of cancer [121, 124]. Moreover, there are other promising iCK2s in development, such as TDB [125].

When culturing GL261 cells with different iCK2, cells sensitivity was variable for the different iCK2 evaluated, being CX-4945 and TDB the ones producing the most significant decrease in GL261 cell viability (Figure 4.3A and B), although CX-4945 was chosen for further experiments because it has been already described in clinical and preclinical studies [122–124]<sup>13,14</sup>. Moreover, as expected, a significant reduction of CK2 activity in CX-4945 treated GL261 cells, accompanied by the decrease of the phosphorylation of the CK2 target AKT(S129) (Figure 4.4A-D), similarly to [123] in prostate PC3 cancer cells, was detected. In addition, AKT phosphorylation was found reduced as the CX-4945 concentration was increased in GL261

---

<sup>13</sup> <http://www.cancer.gov/clinicaltrials/search/view?cdrid=642699&version=HealthProfessional>

<sup>14</sup> <http://www.prnewswire.com/news-releases/cylene-presents-encouraging-clinical-data-for-oral-ck2-inhibitor-at-asco-123219423.html>

cultured cells, in a dose-dependent manner. It has been described that the antiapoptotic effect of CK2 can be partially mediated by upregulation of the AKT/PKB pathway [203], thus the reduced viability found in GL261 cultured cells treated with CX-4945 can be also related to the downregulation of this pathway. These results reinforced the idea that CX-4945 could be a promising candidate for non-mutagenic brain tumor therapy in our preclinical GBM model.

Despite CK2 activity was found reduced in GL261 GBM tissue from investigated mice after CX-4945 administration, confirming us that CX-4945 had reached the target tissue (Figure 4.4E), in agreement with [124], surprisingly, the *in vivo* treatment of GL261 tumor-bearing mice did not produce a better outcome (Figure 4.6). These results were in disagreement with a previous *in vivo* study [124] with intracranial human xenografts treated with CX-4945, which showed significant effects in mice survival. These unexpected results lead us to hypothesize that a combined therapy with CX-4945 superimposed with TMZ could produce better results, as TMZ treatment in preclinical GBM mice has been proved useful in our group [237]. Nevertheless, the combined treatment did not produce the expected improvement (Figure 4.9). On the contrary, the combined TMZ+CX-4945 therapy showed similar results than control mice, even reversing the beneficial effect of the TMZ 3 cycles treatment (Figure 4.10). After these results, we checked for any possible antagonistic interaction between the two agents in GL261 cells *in vitro*, for example through TMZ-induced indirect AKT activation [318]. Nevertheless, we found increased efficacy regarding cell viability reduction in comparison with both therapeutic agents administered separately (Figure 4.3A).

The more appealing explanation for the initially disappointing *in vivo* results with non-metronomic therapeutic schema could be related to the role of the immune system in therapy response [77], which could explain why different results are obtained when comparing *in vitro* and *in vivo* results for CX-4945 in our hands. The CTLs have a relevant role in the defence against cancer recognizing antigen presented on the surface of transformed cells, following a

complex cycle described in [80] and also in Figure 1.8. It was also described the need of a functional CD5-dependent CK2 signalling for efficient differentiation of naive CD4<sup>+</sup> T cells into Th2 and Th17 cells [80, 291], involved in monocytes differentiation into DC subsets [292]. Moreover, authors in [293] have recently described impairment of Th17 cells development by CK2 inhibition with CX-4945 in a C57BL/6 mouse model of experimental autoimmune encephalomyelitis. Accordingly, CK2 inhibition could impair proper attraction of immune response triggered by immunogenic cell death signals. In this respect several authors have described immunogenic death caused by TMZ therapy in GBM [294, 295]. Additionally, CK2 inhibition *in vitro* has been shown to compromise normal T-cell viability of cultured peripheral blood T-lymphocytes harvested from chronic lymphocytic leukemia patients [296]. All this combined would provide an explanation for the lack of tumor response detection or even reversal of the TMZ effect, and accordingly, no survival increase in our treated GBM mice.

In this respect, in preceding years, several groups started to study the so-called “metronomic therapy” [91] approach, referring to equally spaced, low doses of chemotherapeutic drugs without extended rest periods. Also, new therapeutic regimens with conventional drugs have been evaluated in order to activate immune responses that enhance tumor regression and prevent tumor regrowth. Specifically in GL261 tumors growing subcutaneously in immunocompetent mice, CPA metronomic therapy has proven to not only activate antitumor CD8<sup>+</sup> T-cell response, but also to induce long-term, specific T-cell tumor memory [231, 290]. These authors have also proven that a 6-day intermittent was the optimum timing for this therapy and this could agree with the 7-day cycle for immune cell recruitment described in [81] and Figure 1.8. Authors in [231] studied GL261 GBM in immunocompetent C57BL/6 mice using CPA 140 mg/Kg, achieving a cure in all of them, this being effective even when animals were re-challenged with new GL261 cells for tumor growth. Nevertheless, their model was ectopic, having GL261 cells inoculated by subcutaneous injection into the posterior mice flanks. In the case of CPA treatment, our results were not able to reproduce the ones

described in [231]. The metronomic CPA treatment (140 mg/kg, every 6 days) in orthotopic GL261 GBM showed an increased survival rate with respect to control GL261 (Figure 4.13), although without significant differences in comparison with the standard TMZ 5-3-3 cycle previously described by our group of non-metronomic TMZ treated mice [237, 262]. These differences could be because the environment of the tumor is relevant, and the response to therapy becomes more complex when the GBM is growing orthotopically inside the brain, in comparison with an ectopic inoculation, an environment which does not mimic intracranial conditions due to the brain microenvironment protection and related with the actuation of the immune system.

After observing that CPA metronomic therapy produced a promising outcome, TMZ metronomic therapy protocols were performed. Different dosages of TMZ were used (60, 140, 200 and 240 mg/Kg) and we also assessed the influence of starting therapy with smaller tumor volumes. The best results were obtained with 60 and 140 mg/kg treatment (with no significant differences between them,  $p>0.05$ ) with survival rates of  $44.9\pm 29.0$  days and  $38.7\pm 2.7$ , respectively. From TMZ\_140 group, a 25% of mice were cured, 41% of mice had transient tumor volume reduction with relapse after a certain point and a 33.3% of mice did not significantly respond to therapy (Figure 4.16). TMZ treatment achieved better results regarding tumor volume reduction in growth curves and survival rates than the ones obtained with CPA, but without achieving 100% curation of the GBM afflicted mice as described for subcutaneous GL261 GBM in [231]. Still, the significant survival increase produced by CPA and TMZ in our orthotopic GBM model suggests a potential interest in the combination or alternation of the two compounds in future studies.

A new feature observed in this study with metronomic therapy compared to previous work from our group [237, 262] and that of others with orthotopic GBM [295] was the appearance of PTBE zones surrounding the tumor, which seem to have delayed or even opposing

behaviour in comparison with tumor evolution (Figure 4.12). It may be interesting to mention here the phenomenon named “pseudoprogression” (increased contrast uptake volume faking relapse) known to appear in humans during classical radiochemical GBM treatment, which has been described to correlate with increased PTBE. This PTBE has also been seen in glioma patients treated with dendritic cell-based immunotherapy [308, 319]. In this respect, the PTBE detected in our GBM cases could well have a similar origin as in the “pseudoprogression” human instances. Accordingly, the large PTBE recorded from our investigated mice would also agree with the participation of the immune system in the response environment of host mice in the response mechanism, producing inflammatory regions detectable by MRI. Further histopathological studies would be needed to confirm or discard this hypothesis.

The appearance of lymphomas was observed in necropsy studies (Figure 4.19) from mice treated with high TMZ cumulative dosage (480-1440mg/Kg). The lymphoma formation could be due to the strong mutagenic potential of TMZ on mouse bone marrow cells *in vivo* [309]. Also, patients treated with high dose regimens of TMZ for extended periods might present with particular risk for secondary malignancy (like lymphoma appearance [310]) because of treatment-associated immunosuppression and a high cumulative dose of a potentially carcinogenic alkylating drug [311]. Despite improving therapy outcome with TMZ metronomic administration in mice GBM, the incidence of lymphoma in some animals indicates that further optimization experiments must be performed with lower TMZ cumulative dose and/or less administrations or with combination therapies while maintaining or increasing cured mice percentage. This was partially the case of metronomic every 6-day TMZ (60mg/Kg/day) and CX-4945 (150mg/Kg/day) administration treatment, with a cumulative total dose of 480mg/kg for TMZ and 1200mg/Kg for CX-4945. Nevertheless, mouse C1153, receiving the aforementioned treatment, died in consequence of a lymphoma at day 114 p.i. Accordingly, this cumulative dose need to be further reduced for improving mice GBM outcome without generating TMZ derived secondary malignancies, such as thymic lymphoma.

Taking into account MRSI analysis performed in this study, clearly responding tumors (according to tumor volume changes, tumor growth arrest or tumor volume decrease) showed a predominance of green pixels (referring to “responding” spectral pattern). A predominance of red pixels (“actively proliferating” spectral pattern) in semi-supervised MRSI analysis was also seen in some cases of tumor volume reduction, although in these cases a relapse and resume of tumor growth was seen after 3-4 days, Figure 4.16B. These results are in agreement with previous results from our group [262], and offer an additional non-invasive window to assess the effectiveness of a therapy through a surrogate biomarker, even before changes in anatomical information gathered from MRI acquisitions (tumor volume changes) can be seen (e.g. day 21 p.i. in mouse C1013 in Figure 4.16B). Still, an unexpected further increase in the green (“responding”) pixels in a posterior acquisition at day 31 (see last nosological image shown in Figure 4.16B) seems to suggest an oscillating behaviour for the responding pattern detectable from nosologic images, which may merit further evaluation.

Other results from our group performed in parallel with this thesis (reported in [320]), with TMZ 5-3-3 cycles schedule instead of metronomic schedule, offered interesting complementary information. Thus, in Figure 5.1, regarding to tumor volume, we can clearly appreciate growth arrest starting after the second TMZ cycle (day 20 p.i.), with small changes until day 31 p.i. (stable disease following RECIST parameters [303]), whereas the relative percentage of responding pixels (the volume of “responding” tumor) presents an oscillating pattern peaking every 5-7 days, approximately. This apparent discrepancy between lack of tumor volume changes and response detected by *in vivo* metabolomics would fit with the “waves” of host immunological response triggered by initial immunogenic death of tumor cells after treatment with TMZ, as described in [294, 295], and Figure 1.8. New “repopulation” of the tumor mass with actively proliferating GL261 cells with new clonal characteristics would cause the oscillating peaks of non-responding tumor (red pixels). The initially activated CD8<sup>+</sup> T cells would not be effective against those new GL261 cells done and another cycle of DC

priming and new T cells clones activation would be required. However, although it seems that 7-day oscillations of “responding pixels” are present, it is important to remark that the 5-2-2 cycle scheme was not designed for metronomic performance, or to maximize immune system attraction, with concomitant avoidance of interference with the immune attack to the tumor.

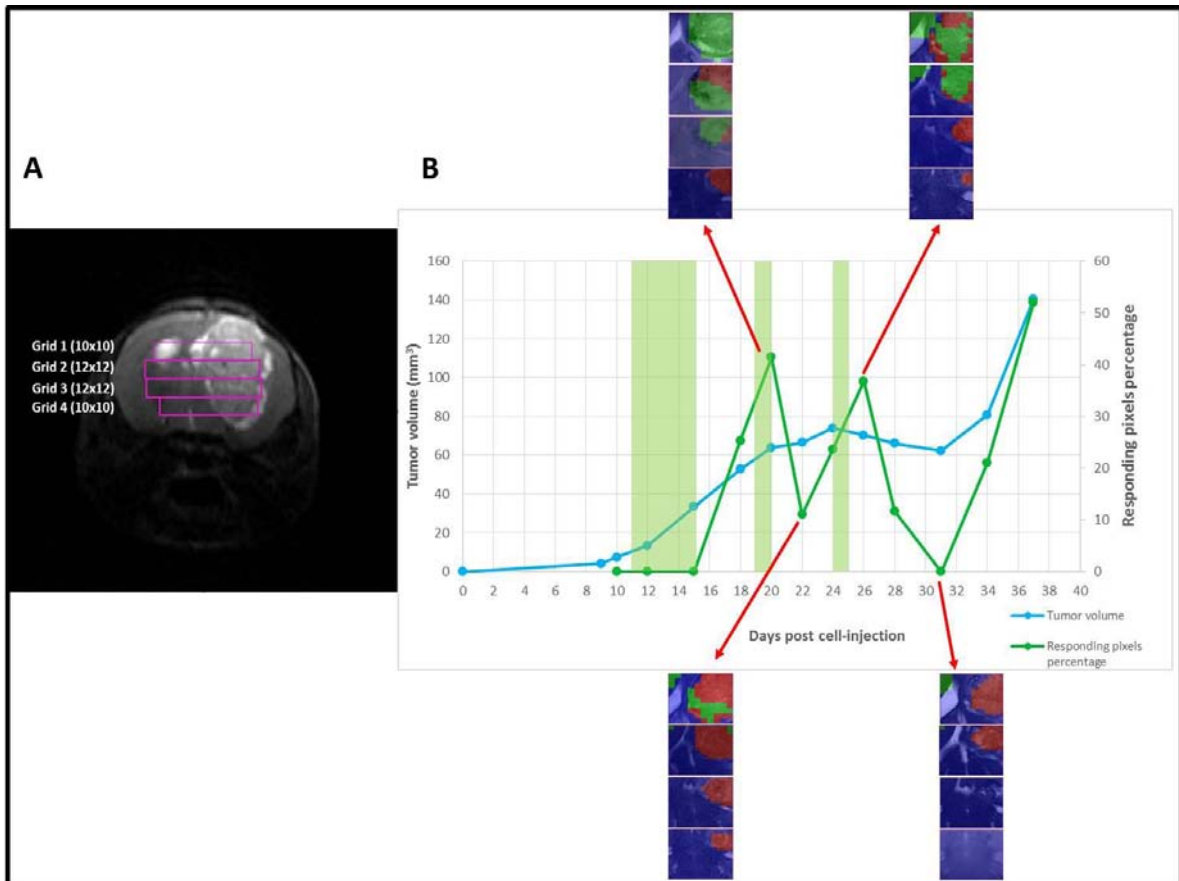


**Figure 5.1 Relationship between tumor volume evolution and nosological images obtained (A)  $T_{2w}$  MRI (axial orientation) from one GL261 tumor-bearing mouse. These acquisitions allow an accurate tumor volume calculation. The pink rectangles represent the scheme of the multislice MRSI used for the nosological image calculation, orientation perpendicular to the axial view. (B) Graphical representation of the tumor volume evolution (in  $\text{mm}^3$ , blue line, left scale), and the percentage of responding “green” pixels obtained after NMF analysis of MRSI data acquired in the multislice set as in [262] (in %, green line, right scale). For chosen time points, the evolution of the nosological images obtained with the semisupervised source extraction system is shown in four columns of colour coded grids, superimposed to the  $T_{2w}$ -MRI for each slice. The green shaded columns indicate TMZ administration periods. (from [320]).**

On the contrary, it is possible that the timing of the TMZ cycles was partially preventing the detection of a full immune cycle development. If the 7-day cycle for immune system activation is proven correct in our GBM preclinical system, the interleave between the first and second cycle should have been 6-7 days, instead of the 3 days shown in Figure 5.1. Premature TMZ administration could trigger cell death, both from tumor cells and also from proliferating primed CD8<sup>+</sup> lymphocytes in the LN (see Figure 1.8) which should later infiltrate the tumor. The next “response” peak would be a mixture of new immune system attraction through tumor cell death caused by the previous TMZ treatment, and a wave of the remaining CD8<sup>+</sup> lymphocytes not killed by TMZ administration.

All this taken into account, it can be suggested that the timing of administration of an iCK2 as therapeutic agent may be crucial for obtaining optimal therapeutic results in case immune response is involved. In this respect we should remind the reader that CX-4945 treatment every day, alternate days, or every 6 days metronomic did not produce any benefit (Figure 4.6A and B and Figure 4.11C). It was only when TMZ and CX-4945 combined metronomic treatment was applied that significant, and the best survival results in the group were obtained ( $64.5 \pm 27.1$  days). This may be interpreted as meaning that CX-4945 administered every 6 days could help TMZ to kill tumor cells producing better immunogenic death than with TMZ or CX-4945 alone without impairing the immune system CTL amplification time in the middle of the 7-day immune cycle. Despite this, it is important to mention that it is unclear the extent to which CX-4945 or TMZ cause immunological cell death in GL261 GBM cells. This is a study progress in our group.

Other approaches taking into account the immune response from the host for GBM therapy are being developed by other authors with satisfactory results. For example, immune vaccines used in GL261 C57BL/6 mice, in which treated mice survived longer than control mice [316], or plain treatment of GL261 orthotopic tumor growing in C57BL/6 mice with monoclonal



antibodies against CTL4 or PD1 T-lymphocyte ligands which cure up to 75% of treated animals [302], highlighting that the immune factor cannot be neglected in the GBM therapy response context.

The improvement of results with metronomic TMZ administration in comparison with the traditional administration scheme described in [237] suggests that the 6-day cycle is performing better. This would agree with a possible higher recruitment of the host immune system in our case as described by [98, 304], although no histopathological validation of this has been carried out yet in our case. Further studies are needed to confirm or discard this hypothesis, with longitudinal studies and histopathological analysis at different time points profiting from the evaluable non-invasive characterization of response through nosological images and using different histochemistry approaches for immune cells characterization.

We consider that it is possible to enhance or modulate the host immune system fight against GBM triggered by cell death due to treatment. Moreover, we also consider it possible to non-invasively assess this immune system performance with our molecular imaging strategies, gathering information about tumor response even when the tumor volume evolution is stable and no apparent changes are seen in the volume of the tumor. If proven correct, in the future it would be interesting to use the non-invasive information gathered from tumors along treatment to adjust the therapy administration in each case. We would expect in this case that a 6-7-day metronomic cycle would produce a responding pattern. But, still, we cannot discard that some natural deviations of the standard 6-7-day cycle for immune system recruitment and action could take place. If it was possible to detect these variations in a non-invasive way, the therapy administration could be adjusted to match with the first signal of tumor response compromise.

It is worth noting the potential interest in attempting the clinical translation of this approach. Nowadays, patients under treatment have follow-ups each 3 months for therapy response

assessment, and based essentially in MRI features. If our nosological imaging approach strategy is robust enough, this would provide an additional window for effectiveness assessment and therapy change in case of no-response or, on the contrary, maintain a therapeutic schedule if signals of clear response are seen.

## 6 GENERAL CONCLUSIONS

1. The content of the CK2 catalytic subunit (CK2 $\alpha$ ) was found higher in GL261 GBM tumor (about 4-fold) and in contralateral brain parenchyma (more than 2-fold) compared to wt brain parenchyma.
2. No significant changes were found in the CK2 regulatory subunit (CK2 $\beta$ ) expression, suggesting a predominance of CK2 $\alpha$  overexpression in the evaluated GL261 tumors and possibly pointing to a differential role for the two subunit types in GBM tumor development in our investigated model.
3. CX-4945 and TDB had a noticeable effect in decreasing GL261 GBM cell viability and CK2 activity *in vitro*. Additionally, we found that CX-4945 reached the target tissue *in vivo* and inhibited its CK2 target.
4. No beneficial effect was observed for tumor growth or survival rate in longitudinal *in vivo* experiments in GL261 tumor-bearing mice treated with CX-4945 every day or in alternated days. The combination of CX-4945 every day and TMZ 5-2-2 therapy also showed poor results, reversing the beneficial effect of TMZ in GL261 tumor-bearing mice survival, although an increased effect had been observed in the combined *in vitro* treatment of GL261 cells.
5. The TMZ metronomic protocol produced a satisfactory effect increasing survival rate in GL261 harbouring C57BL/6 mice. Some mice experienced tumor regression and cure, which is an improvement in comparison with the previous 3-cycle TMZ treatment approach previously described by us.
6. CX-4945 administration every day or in alternated days could be impairing cytotoxic T-cell amplification cycle and, consequently, blunting proper immunotherapy related response. Otherwise, metronomic TMZ and CX-4945 combined therapy offered the best results obtained in our group increasing survival rate, which could explain the

- poor results obtained with the non-metronomic schedule. This would reinforce the idea of the immune system participation of host C57BL/6 mice in response to therapy.
7. Orthotopic GL261 inoculated mice did not produce the same outcome under metronomic CPA therapy than ectopic GL261 GBM mice described in previous literature, but survival rate was significantly higher than with control mice.
  8. In mice treated with TMZ 140 mg/Kg PTBE zones surrounding the tumor were found, which seem to have delayed or even opposing behaviour in comparison with tumor evolution and could be related to the “*pseudoprogression*” concept described for human patients.
  9. High doses of TMZ metronomic treatment produced lymphoma in some animals, indicating that further optimization experiments must be performed with lower TMZ cumulative dose and/or less administrations while maintaining or increasing cured mice percentage.
  10. The semi-supervised source extraction methodology used for nosological image generation was able to characterize the response to TMZ and CPA in preclinical GBM both at a defined time-point and along the therapy protocol.
  11. The semi-supervised source extraction methodology used for nosological image generation bears a translational application potential for monitoring response to treatment in patients and allowing early decision making with respect to second line personalized therapeutic strategies.

**7 BIBLIOGRAPHY**

1. Ferlay J, Soerjomataram I, Dikshit R, et al (2015) Cancer incidence and mortality worldwide: Sources, methods and major patterns in GLOBOCAN 2012. *Int J Cancer* 136:E359–E386. doi: 10.1002/ijc.29210
2. Barnholtz-Sloan JS, Sloan AE, Davis FG, et al (2004) Incidence proportions of brain metastases in patients diagnosed (1973 to 2001) in the Metropolitan Detroit Cancer Surveillance System. *J Clin Oncol* 22:2865–72. doi: 10.1200/JCO.2004.12.149
3. Schouten LJ, Rutten J, Huveneers HAM, Twijnstra A (2002) Incidence of brain metastases in a cohort of patients with carcinoma of the breast, colon, kidney, and lung and melanoma. *Cancer* 94:2698–705.
4. Louis DN, Ohgaki H, Wiestler OD, et al (2007) The 2007 WHO classification of tumours of the central nervous system. *Acta Neuropathol* 114:97–109. doi: 10.1007/s00401-007-0243-4
5. Louis DN, Perry A, Reifenberger G, et al (2016) The 2016 World Health Organization Classification of Tumors of the Central Nervous System: a summary. *Acta Neuropathol* 131:803–20. doi: 10.1007/s00401-016-1545-1
6. Ostrom QT, Gittleman H, Liao P, et al (2015) CBTRUS Statistical Report: Primary Brain and Central Nervous System Tumors Diagnosed in the United States in 2007-2011. *Neuro Oncol* 16 Suppl 4:iv1-iv63. doi: 10.1093/neuonc/nou223
7. Mahaley MS, Mettlin C, Natarajan N, et al (1989) National survey of patterns of care for brain-tumor patients. *J Neurosurg* 71:826–836. doi: 10.3171/jns.1989.71.6.0826
8. Buckner JC (2003) Factors influencing survival in high-grade gliomas. *Semin Oncol* 30:10–14. doi: 10.1053/j.seminoncol.2003.11.031
9. Ohgaki H, Kleihues P (2011) Genetic profile of astrocytic and oligodendroglial gliomas. *Brain Tumor Pathol* 28:177–83. doi: 10.1007/s10014-011-0029-1
10. Rouse C, Gittleman H, Ostrom QT, et al (2016) Years of potential life lost for brain and CNS tumors relative to other cancers in adults in the United States, 2010. *Neuro Oncol* 18:70–77. doi: 10.1093/neuonc/nov249
11. Stupp R, Mason WP, van den Bent MJ, et al (2005) Radiotherapy plus concomitant and adjuvant temozolomide for glioblastoma. *N Engl J Med* 352:987–96. doi: 10.1056/NEJMoa043330
12. Ohgaki H, Kleihues P (2013) The definition of primary and secondary glioblastoma. *Clin Cancer Res* 19:764–72. doi: 10.1158/1078-0432.CCR-12-3002
13. Vogelstein B, Kinzler KW (1993) The multistep nature of cancer. *Trends Genet* 9:138–41.
14. Hanahan D, Weinberg RA, Aplin A., et al (2000) The Hallmarks of Cancer. *Cell* 100:57–70. doi: 10.1016/S0092-8674(00)81683-9
15. Furnari FB, Fenton T, Bachoo RM, et al (2007) Malignant astrocytic glioma: genetics, biology, and paths to treatment. *Genes Dev* 21:2683–710. doi: 10.1101/gad.1596707
16. Agnihotri S, Burrell KE, Wolf A, et al (2013) Glioblastoma, a brief review of history, molecular genetics, animal models and novel therapeutic strategies. *Arch Immunol Ther Exp (Warsz)* 61:25–41. doi: 10.1007/s00005-012-0203-0
17. Ohgaki H, Kleihues P (2007) Genetic Pathways to Primary and Secondary Glioblastoma. *Am J Pathol* 170:1445–53. doi: 10.2353/ajpath.2007.070011
18. Zhao S, Lin Y, Xu W, et al (2009) Glioma-derived mutations in IDH1 dominantly inhibit IDH1 catalytic activity and induce HIF-1 $\alpha$ . *Science* 324:261–5. doi: 10.1126/science.1170944
19. Reitman ZJ, Yan H (2010) Isocitrate dehydrogenase 1 and 2 mutations in cancer: alterations at a crossroads of cellular metabolism. *J Natl Cancer Inst* 102:932–41. doi: 10.1093/jnci/djq187

20. Yan H, Parsons DW, Jin G, et al (2009) IDH1 and IDH2 mutations in gliomas. *N Engl J Med* 360:765–73. doi: 10.1056/NEJMoa0808710
21. Weller M, Pfister SM, Wick W, et al (2013) Molecular neuro-oncology in clinical practice: a new horizon. *Lancet Oncol* 14:e370-9. doi: 10.1016/S1470-2045(13)70168-2
22. Yang H, Ye D, Guan K-L, Xiong Y (2012) IDH1 and IDH2 mutations in tumorigenesis: mechanistic insights and clinical perspectives. *Clin Cancer Res* 18:5562–71. doi: 10.1158/1078-0432.CCR-12-1773
23. Bonnet D, Dick JE (1997) Human acute myeloid leukemia is organized as a hierarchy that originates from a primitive hematopoietic cell. *Nat Med* 3:730–737. doi: 10.1038/nm0797-730
24. Galli R, Binda E, Orfanelli U, et al (2004) Isolation and characterization of tumorigenic, stem-like neural precursors from human glioblastoma. *Cancer Res* 64:7011–21. doi: 10.1158/0008-5472.CAN-04-1364
25. Singh SK, Hawkins C, Clarke ID, et al (2004) Identification of human brain tumour initiating cells. *Nature* 432:396–401. doi: 10.1038/nature03128
26. Reya T, Morrison SJ, Clarke MF, Weissman IL (2001) Stem cells, cancer, and cancer stem cells. *Nature* 414:105–11. doi: 10.1038/35102167
27. Gao X, McDonald JT, Naidu M, et al (2014) A Proposed Quantitative Index for Assessing the Potential Contribution of Reprogramming to Cancer Stem Cell Kinetics. doi: 10.1155/2014/249309
28. Hanahan D, Weinberg RA, Adams JM, et al (2011) Hallmarks of Cancer: The Next Generation. *Cell* 144:646–74. doi: 10.1016/j.cell.2011.02.013
29. Odoux C, Fohrer H, Hoppo T, et al (2008) A stochastic model for cancer stem cell origin in metastatic colon cancer. *Cancer Res* 68:6932–41. doi: 10.1158/0008-5472.CAN-07-5779
30. Cho RW, Clarke MF (2008) Recent advances in cancer stem cells. *Curr Opin Genet Dev* 18:48–53. doi: 10.1016/j.gde.2008.01.017
31. Lobo NA, Shimono Y, Qian D, Clarke MF (2007) The biology of cancer stem cells. *Annu Rev Cell Dev Biol* 23:675–99. doi: 10.1146/annurev.cellbio.22.010305.104154
32. Zhao W, Ji X, Zhang F, et al (2012) Embryonic Stem Cell Markers. *Molecules* 17:6196–236. doi: 10.3390/molecules17066196
33. Bao S, Wu Q, McLendon RE, et al (2006) Glioma stem cells promote radioresistance by preferential activation of the DNA damage response. *Nature* 444:756–60. doi: 10.1038/nature05236
34. Liu G, Yuan X, Zeng Z, et al (2006) Analysis of gene expression and chemoresistance of CD133+ cancer stem cells in glioblastoma. *Mol Cancer* 5:67. doi: 10.1186/1476-4598-5-67
35. Huang Z, Cheng L, Guryanova OA, et al (2010) Cancer stem cells in glioblastoma--molecular signaling and therapeutic targeting. *Protein Cell* 1:638–55. doi: 10.1007/s13238-010-0078-y
36. Yan K, Yang K, Rich JN (2013) The evolving landscape of glioblastoma stem cells. *Curr Opin Neurol* 26:701–7. doi: 10.1097/WCO.0000000000000032
37. Gatenby RA, Silva AS, Gillies RJ, Frieden BR (2009) Adaptive therapy. *Cancer Res* 69:4894–903. doi: 10.1158/0008-5472.CAN-08-3658
38. Wang R, Chadalavada K, Wilshire J, et al (2010) Glioblastoma stem-like cells give rise to tumour endothelium. *Nature* 468:829–33. doi: 10.1038/nature09624
39. Auffinger B, Tobias AL, Han Y, et al (2014) Conversion of differentiated cancer cells into cancer stem-like cells in a glioblastoma model after primary chemotherapy. *Cell Death Differ* 21:1119–31. doi: 10.1038/cdd.2014.31
40. Kelly PJ (2010) Gliomas: Survival, origin and early detection. *Surg Neurol Int* 1:96. doi: 10.4103/2152-7806.74243
41. Chang SM, Parney IF, Huang W, et al (2005) Patterns of care for adults with newly

- diagnosed malignant glioma. *JAMA* 293:557–64. doi: 10.1001/jama.293.5.557
42. Stupp R, Brada M, van den Bent MJ, et al (2014) High-grade glioma: ESMO clinical practice guidelines for diagnosis, treatment and follow-up. *Ann Oncol* 25:93–101. doi: 10.1093/annonc/mdu050
  43. Westphal M, Ram Z, Riddle V, et al (2006) Gliadel® wafer in initial surgery for malignant glioma: long-term follow-up of a multicenter controlled trial. *Acta Neurochir (Wien)* 148:269–75. doi: 10.1007/s00701-005-0707-z
  44. Keime-Guibert F, Chinot O, Taillandier L, et al (2007) Radiotherapy for Glioblastoma in the Elderly. *N Engl J Med* 356:1527–35. doi: 10.1056/NEJMoa065901
  45. Chinot O-L, Barrie M, Frauger E, et al (2004) Phase II study of temozolomide without radiotherapy in newly diagnosed glioblastoma multiforme in an elderly populations. *Cancer* 100:2208–14. doi: 10.1002/cncr.20224
  46. Balaña C, López-Pousa A, Berrocal A, et al (2004) Phase II study of temozolomide and cisplatin as primary treatment prior to radiotherapy in newly diagnosed glioblastoma multiforme patients with measurable disease. A study of the Spanish Medical Neuro-Oncology Group (GENOM). *J Neurooncol* 70:359–69. doi: 10.1007/s11060-004-9175-1
  47. Stummer W, Reulen H-J, Meinel T, et al (2008) Extent of resection and survival in glioblastoma multiforme: identification of and adjustment for bias. *Neurosurgery* 62:564–76. doi: 10.1227/01.neu.0000317304.31579.17
  48. Sanai N, Berger MS (2011) Extent of resection influences outcomes for patients with gliomas. *Rev Neurol (Paris)* 167:648–54. doi: 10.1016/j.neurol.2011.07.004
  49. Spetzler RF, Sanai N (2012) The quiet revolution: retractorless surgery for complex vascular and skull base lesions. *J Neurosurg* 116:291–300. doi: 10.3171/2011.8.JNS101896
  50. Sanai N, Mirzadeh Z, Berger MS (2008) Functional Outcome after Language Mapping for Glioma Resection. *N Engl J Med* 358:18–27. doi: 10.1056/NEJMoa067819
  51. Gasser T, Ganslandt O, Sandalcioglu E, et al (2005) Intraoperative functional MRI: implementation and preliminary experience. *Neuroimage* 26:685–93. doi: 10.1016/j.neuroimage.2005.02.022
  52. Senft C, Bink A, Franz K, et al (2011) Intraoperative MRI guidance and extent of resection in glioma surgery: a randomised, controlled trial. *Lancet Oncol* 12:997–1003. doi: 10.1016/S1470-2045(11)70196-6
  53. Begg AC, Stewart FA, Vens C (2011) Strategies to improve radiotherapy with targeted drugs. *Nat Rev Cancer* 11:239–53. doi: 10.1038/nrc3007
  54. Andersen AP (1978) Postoperative irradiation of glioblastomas. Results in a randomized series. *Acta Radiol Oncol Radiat Phys Biol* 17:475–84.
  55. Walker MD, Green SB, Byar DP, et al (1980) Randomized comparisons of radiotherapy and nitrosoureas for the treatment of malignant glioma after surgery. *N Engl J Med* 303:1323–9. doi: 10.1056/NEJM198012043032303
  56. Desouky O, Ding N, Zhou G (2015) Targeted and non-targeted effects of ionizing radiation. *J Radiat Res Appl Sci* 8:247–54. doi: 10.1016/j.jrras.2015.03.003
  57. Leksell L (1951) The stereotaxic method and radiosurgery of the brain. *Acta Chir Scand* 102:316–9.
  58. Ken S, Vieilleville L, Franceries X, et al (2013) Integration method of 3D MR spectroscopy into treatment planning system for glioblastoma IMRT dose painting with integrated simultaneous boost. *Radiat Oncol* 8:1. doi: 10.1186/1748-717X-8-1
  59. Baumann M, Krause M, Thames H, et al (2009) Cancer stem cells and radiotherapy. *Int J Radiat Biol* 85:391–402. doi: 10.1080/09553000902836404
  60. Stupp R, Hegi ME, Mason WP, et al (2009) Effects of radiotherapy with concomitant and adjuvant temozolomide versus radiotherapy alone on survival in glioblastoma in a randomised phase III study: 5-year analysis of the EORTC-NCIC trial. *Lancet Oncol* 10:459–66. doi: 10.1016/S1470-2045(09)70025-7

61. Yoshimoto K, Mizoguchi M, Hata N, et al (2012) Complex DNA repair pathways as possible therapeutic targets to overcome temozolomide resistance in glioblastoma. *Front Oncol* 2:186. doi: 10.3389/fonc.2012.00186
62. Friedman HS, Kerby T, Calvert H (2000) Temozolomide and treatment of malignant glioma. *Clin Cancer Res* 6:2585–97.
63. Newlands ES, Foster T, Zaknoen S (2003) Phase I study of temozolamide (TMZ) combined with procarbazine (PCB) in patients with gliomas. *Br J Cancer* 89:248–51. doi: 10.1038/sj.bjc.6601043
64. Glas M, Happpold C, Rieger J, et al (2009) Long-term survival of patients with glioblastoma treated with radiotherapy and lomustine plus temozolomide. *J Clin Oncol* 27:1257–61. doi: 10.1200/JCO.2008.19.2195
65. Kaina B, Ochs K, Grösch S, et al (2001) BER, MGMT, and MMR in defense against alkylation-induced genotoxicity and apoptosis. *Prog Nucleic Acid Res Mol Biol* 68:41–54.
66. Niewald M, Berdel C, Fleckenstein J, et al (2011) Toxicity after radiochemotherapy for glioblastoma using temozolomide—a retrospective evaluation. *Radiat Oncol* 6:141. doi: 10.1186/1748-717X-6-141
67. Allen JC, Helson L (1981) High-dose cyclophosphamide chemotherapy for recurrent CNS tumors in children. *J Neurosurg* 55:749–56. doi: 10.3171/jns.1981.55.5.0749
68. Longee DC, Friedman HS, Albright RE, et al (1990) Treatment of patients with recurrent gliomas with cyclophosphamide and vincristine. *J Neurosurg* 72:583–8. doi: 10.3171/jns.1990.72.4.0583
69. Chamberlain MC, Tsao-Wei DD (2004) Salvage Chemotherapy with Cyclophosphamide for Recurrent, Temozolomide-Refractory Glioblastoma Multiforme. *Cancer* 100:1213–20. doi: 10.1002/cncr.20072
70. Anderson P, Aguilera D, Pearson M, Woo S (2008) Outpatient chemotherapy plus radiotherapy in sarcomas: Improving cancer control with radiosensitizing agents. *Cancer Control* 15:38–46.
71. Sládek N, Kollander R, Sreerama L, Kiang D (2002) Cellular levels of aldehyde dehydrogenases (ALDH1A1 and ALDH3A1) as predictors of therapeutic responses to cyclophosphamide-based chemotherapy of breast cancer: a retrospective study. *Cancer Chemother Pharmacol* 49:309–21. doi: 10.1007/s00280-001-0412-4
72. Emadi A, Jones RJ, Brodsky RA (2009) Cyclophosphamide and cancer: golden anniversary. *Nat Rev Clin Oncol* 6:638–47. doi: 10.1038/nrclinonc.2009.146
73. Demirci U, Buyukberber S, Ozdemir N, et al (2013) Combination of Cyclophosphamide and Carboplatin in Recurrent Malignant Gliomas. *Int J Hematol Oncol* 23:178–83. doi: 10.4999/uhod.12030
74. Viñolas N, Gil M, Verger E, et al (2002) Pre-irradiation semi-intensive chemotherapy with carboplatin and cyclophosphamide in malignant glioma: a phase II study. *Anticancer Drugs* 13:163–7.
75. Noronha V, Krishna M V, Patil V, et al (2013) Metronomic therapy: chemotherapy revisited. *Indian J Cancer* 50:142–8. doi: 10.4103/0019-509X.117027
76. Kerbel RS, Kamen BA (2004) The anti-angiogenic basis of metronomic chemotherapy. *Nat Rev Cancer* 4:423–36. doi: 10.1038/nrc1369
77. Vacchelli E, Aranda F, Eggermont A, et al (2014) Trial Watch: Chemotherapy with immunogenic cell death inducers. *Oncoimmunology* 3:e27878. doi: 10.4161/onci.27878
78. Zitvogel L, Apetoh L, Ghiringhelli F, Kroemer G (2008) Immunological aspects of cancer chemotherapy. *Nat Rev Immunol* 8:59–73. doi: 10.1038/nri2216
79. Weinberg RA (2007) *The biology of cancer* (2nd edition). John Wiley & Sons
80. Tabbekh M, Mokrani-Hammani M, Bismuth G, Mami-Chouaib F (2013) T-cell modulatory properties of CD5 and its role in antitumor immune responses. *Oncoimmunology* 2:e22841. doi: 10.4161/onci.22841
81. Karman J, Ling C, Sandor M, Fabry Z (2004) Initiation of immune responses in brain is



- promoted by local dendritic cells. *J Immunol* 173:2353–61. doi: 10.4049/jimmunol.173.4.2353
82. Gajewski TF, Meng Y, Blank C, et al (2006) Immune resistance orchestrated by the tumor microenvironment. *Immunol Rev* 213:131–45. doi: 10.1111/j.1600-065X.2006.00442.x
  83. Heimberger AB, Sampson JH (2011) Immunotherapy coming of age: what will it take to make it standard of care for glioblastoma? *Neuro Oncol* 13:3–13. doi: 10.1093/neuonc/noq169
  84. Platten M, Wick W, Weller M (2001) Malignant glioma biology: role for TGF-beta in growth, motility, angiogenesis, and immune escape. *Microsc Res Tech* 52:401–10. doi: 10.1002/1097-0029(20010215)52:4<401::AID-JEMT1025>3.0.CO;2-C
  85. Beatty PL, Cascio S, Lutz E (2011) Tumor Immunology: Basic and Clinical Advances. *Cancer Res* 71:4338–43. doi: 10.1158/0008-5472.CAN-11-0717
  86. Sadun RE, Sachsman SM, Chen X, et al (2007) Immune Signatures of Murine and Human Cancers Reveal Unique Mechanisms of Tumor Escape and New Targets for Cancer Immunotherapy. *Clin Cancer Res* 13:4016–25. doi: 10.1158/1078-0432.CCR-07-0016
  87. De Bonis P, Albanese A, Lofrese G, et al (2011) Postoperative infection may influence survival in patients with glioblastoma: simply a myth? *Neurosurgery* 69:864–9. doi: 10.1227/NEU.0b013e318222adfa
  88. Lohr J, Ratliff T, Huppertz A, et al (2011) Effector T-cell infiltration positively impacts survival of glioblastoma patients and is impaired by tumor-derived TGF- $\beta$ . *Clin Cancer Res* 17:4296–308. doi: 10.1158/1078-0432.CCR-10-2557
  89. Takimoto CH (2009) Maximum tolerated dose: clinical endpoint for a bygone era? *Target Oncol* 4:143–7. doi: 10.1007/s11523-009-0108-y
  90. Walid MS (2008) Prognostic factors for long-term survival after glioblastoma. *Perm J* 12:45–8.
  91. Hanahan D, Bergers G, Bergsland E (2000) Less is more, regularly: metronomic dosing of cytotoxic drugs can target tumor angiogenesis in mice. *J Clin Invest* 105:1045–7. doi: 10.1172/JCI9872
  92. Doloff JC, Waxman DJ (2012) VEGF receptor inhibitors block the ability of metronomically dosed cyclophosphamide to activate innate immunity-induced tumor regression. *Cancer Res* 72:1103–15. doi: 10.1158/0008-5472.CAN-11-3380
  93. Galluzzi L, Senovilla L, Zitvogel L, Kroemer G (2012) The secret ally: immunostimulation by anticancer drugs. *Nat Rev Drug Discov* 11:215–33. doi: 10.1038/nrd3626
  94. Pasquier E, Kavallaris M, André N (2010) Metronomic chemotherapy: new rationale for new directions. *Nat Rev Clin Oncol* 7:455–65. doi: 10.1038/nrclinonc.2010.82
  95. Browder T, Butterfield CE, Kråling BM, et al (2000) Antiangiogenic scheduling of chemotherapy improves efficacy against experimental drug-resistant cancer. *Cancer Res* 60:1878–86.
  96. Emmenegger U, Man S, Shaked Y, et al (2004) A comparative analysis of low-dose metronomic cyclophosphamide reveals absent or low-grade toxicity on tissues highly sensitive to the toxic effects of maximum tolerated dose regimens. *Cancer Res* 64:3994–4000. doi: 10.1158/0008-5472.CAN-04-0580
  97. Pasquier E, Tuset M-P, Street J, et al (2013) Concentration- and schedule-dependent effects of chemotherapy on the angiogenic potential and drug sensitivity of vascular endothelial cells. *Angiogenesis* 16:373–86. doi: 10.1007/s10456-012-9321-x
  98. Liikanen I, Ahtiainen L, Hirvonen MLM, et al (2013) Oncolytic adenovirus with temozolomide induces autophagy and antitumor immune responses in cancer patients. *Mol Ther* 21:1212–23. doi: 10.1038/mt.2013.51
  99. Klement G, Baruchel S, Rak J, et al (2000) Continuous low-dose therapy with vinblastine and VEGF receptor-2 antibody induces sustained tumor regression without overt toxicity. *J Clin Invest* 105:R15-24. doi: 10.1172/JCI8829

100. Man S, Bocci G, Francia G, et al (2002) Antitumor effects in mice of low-dose (metronomic) cyclophosphamide administered continuously through the drinking water. *Cancer Res* 62:2731–5.
101. Penel N, Adenis A, Bocci G (2012) Cyclophosphamide-based metronomic chemotherapy: after 10 years of experience, where do we stand and where are we going? *Crit Rev Oncol Hematol* 82:40–50. doi: 10.1016/j.critrevonc.2011.04.009
102. Lien K, Georgsdottir S, Sivanathan L, et al (2013) Low-dose metronomic chemotherapy: a systematic literature analysis. *Eur J Cancer* 49:3387–95. doi: 10.1016/j.ejca.2013.06.038
103. Yaddanapudi K, Mitchell R a, Eaton JW (2013) Cancer vaccines: Looking to the future. *Oncoimmunology* 2:e23403. doi: 10.4161/onci.23403
104. Vauleon E, Avril T, Collet B, et al (2010) Overview of cellular immunotherapy for patients with glioblastoma. *Clin Dev Immunol*. doi: 10.1155/2010/689171
105. Kanaly CW, Ding D, Heimberger AB, Sampson JH (2010) Clinical applications of a peptide-based vaccine for glioblastoma. *Neurosurg Clin N Am* 21:95–109. doi: 10.1016/j.nec.2009.09.001
106. Kreisl TN, Kim L, Moore K, et al (2009) Phase II trial of single-agent bevacizumab followed by bevacizumab plus irinotecan at tumor progression in recurrent glioblastoma. *J Clin Oncol* 27:740–5. doi: 10.1200/JCO.2008.16.3055
107. Dillman RO (2011) Cancer immunotherapy. *Cancer Biother Radiopharm* 26:1–64. doi: 10.1089/cbr.2010.0902
108. Yamanaka R (2008) Cell- and peptide-based immunotherapeutic approaches for glioma. *Trends Mol Med* 14:228–35. doi: 10.1016/j.molmed.2008.03.003
109. Phuphanich S, Wheeler CJ, Rudnick JD, et al (2013) Phase I trial of a multi-epitope-pulsed dendritic cell vaccine for patients with newly diagnosed glioblastoma. *Cancer Immunol Immunother* 62:125–135. doi: 10.1007/s00262-012-1319-0
110. Fadul CE, Fisher JL, Gui J, et al (2011) Immune modulation effects of concomitant temozolomide and radiation therapy on peripheral blood mononuclear cells in patients with glioblastoma multiforme. *Neuro Oncol* 13:393–400. doi: 10.1093/neuonc/noq204
111. de Groot JF, Gilbert MR (2007) New molecular targets in malignant gliomas. *Curr Opin Neurol* 20:712–8. doi: 10.1097/WCO.0b013e3282f15650
112. Sul J, Fine HA (2010) Malignant Gliomas: New Translational Therapies. *Mt Sinai J Med* 77:655–66. doi: 10.1002/msj.20223
113. Minniti G, Muni R, Lanzetta G, et al (2009) Chemotherapy for glioblastoma: current treatment and future perspectives for cytotoxic and targeted agents. *Anticancer Res* 29:5171–84.
114. Cohen P, Alessi DR (2013) Kinase drug discovery-What's next in the field? *ACS Chem Biol* 8:96–104. doi: 10.1021/cb300610s
115. Duncan JS, Litchfield DW (2008) Too much of a good thing: the role of protein kinase CK2 in tumorigenesis and prospects for therapeutic inhibition of CK2. *Biochim Biophys Acta* 1784:33–47. doi: 10.1016/j.bbapap.2007.08.017
116. Tapia JC, Torres VA, Rodriguez DA, et al (2006) Casein kinase 2 (CK2) increases survivin expression via enhanced beta-catenin-T cell factor/lymphoid enhancer binding factor-dependent transcription. *Proc Natl Acad Sci U S A* 103:15079–84. doi: 10.1073/pnas.0606845103
117. Dixit D, Ahmad F, Ghildiyal R, et al (2016) CK2 inhibition induced PDK4-AMPK axis regulates metabolic adaptation and survival responses in glioma. *Exp Cell Res*. doi: 10.1016/j.yexcr.2016.03.017
118. Romieu-Mourez R, Landesman-Bollag E, Seldin DC, et al (2001) Roles of IKK Kinases and Protein Kinase CK2 in Activation of Nuclear Factor- $\kappa$ B in Breast Cancer. *Cancer Res* 61:3810–8.
119. Das A, Banik NL, Ray SK (2010) Flavonoids activated caspases for apoptosis in human

- glioblastoma T98G and U87MG cells but not in human normal astrocytes. *Cancer* 116:164–76. doi: 10.1002/cncr.24699
120. Zanin S, Borgo C, Girardi C, et al (2012) Effects of the CK2 inhibitors CX-4945 and CX-5011 on drug-resistant cells. *PLoS One* 7:e49193. doi: 10.1371/journal.pone.0049193
  121. Kim J, Hwan Kim S (2013) CK2 inhibitor CX-4945 blocks TGF- $\beta$ 1-induced epithelial-to-mesenchymal transition in A549 human lung adenocarcinoma cells. *PLoS One* 8:e74342. doi: 10.1371/journal.pone.0074342
  122. Siddiqui-Jain A, Drygin D, Streiner N, et al (2010) CX-4945, an orally bioavailable selective inhibitor of protein kinase CK2, inhibits prosurvival and angiogenic signaling and exhibits antitumor efficacy. *Cancer Res* 70:10288–10298. doi: 10.1158/0008-5472.CAN-10-1893
  123. Pierre F, Chua PC, O'Brien SE, et al (2011) Pre-clinical characterization of CX-4945, a potent and selective small molecule inhibitor of CK2 for the treatment of cancer. *Mol Cell Biochem* 356:37–43. doi: 10.1007/s11010-011-0956-5
  124. Zheng Y, McFarland BC, Drygin D, et al (2013) Targeting protein kinase CK2 suppresses prosurvival signaling pathways and growth of glioblastoma. *Clin Cancer Res* 19:6484–94. doi: 10.1158/1078-0432.CCR-13-0265
  125. Cozza G, Girardi C, Ranchio A, et al (2014) Cell-permeable dual inhibitors of protein kinases CK2 and PIM-1: Structural features and pharmacological potential. *Cell Mol Life Sci* 71:3173–85. doi: 10.1007/s00018-013-1552-5
  126. Lander ES, Linton LM, Birren B, et al (2001) Initial sequencing and analysis of the human genome. *Nature* 409:860–921. doi: 10.1038/35057062
  127. Meggio F, Pinna LA (2003) One-thousand-and-one substrates of protein kinase CK2? *FASEB J* 17:349–68. doi: 10.1096/fj.02-0473rev
  128. Lozeman FJ, Litchfield DW, Piening C, et al (1990) Isolation and characterization of human cDNA clones encoding the alpha and the alpha' subunits of casein kinase II. *Biochemistry* 29:8436–47.
  129. Shi X, Potvin B, Huang T, et al (2001) A novel casein kinase 2 alpha-subunit regulates membrane protein traffic in the human hepatoma cell line HuH-7. *J Biol Chem* 276:2075–82. doi: 10.1074/jbc.M008583200
  130. Moreno-Romero J, Armengot L, Marquès-Bueno MM, et al (2011) About the role of CK2 in plant signal transduction. *Mol Cell Biochem* 356:233–240. doi: 10.1007/s11010-011-0970-7
  131. Bibby AC, Litchfield DW (2005) The Multiple Personalities of the Regulatory Subunit of Protein Kinase CK2: CK2 Dependent and CK2 Independent Roles Reveal a Secret Identity for CK2 $\beta$ . *Int J Biol Sci* 1:67–79.
  132. Pinna LA (1990) Casein kinase 2: an “eminence grise” in cellular regulation? *Biochim Biophys Acta* 1054:267–84. doi: 10.1016/0167-4889(90)90098-X
  133. Meek DW, Simon S, Kikkawa U, Eckhart W (1990) The p53 tumour suppressor protein is phosphorylated at serine 389 by casein kinase II. *EMBO J* 9:3253–60.
  134. Meggio F, Marin O, Pinna LA (1994) Substrate specificity of protein kinase CK2. *Cell Mol Biol Res* 40:401–9.
  135. Gietz RD, Graham KC, Litchfield DW (1995) Interactions between the Subunits of Casein Kinase II. *J Biol Chem* 270:13017–21. doi: 10.1074/jbc.270.22.13017
  136. Litchfield DW, Lüscher B (1993) Casein kinase II in signal transduction and cell cycle regulation. *Mol Cell Biochem* 127–128:187–99.
  137. Litchfield DW (2003) Protein kinase CK2: structure, regulation and role in cellular decisions of life and death. *Biochem J* 369:1–15. doi: 10.1042/BJ20021469
  138. Pinna LA, Meggio F (1997) Protein kinase CK2 (“casein kinase-2”) and its implication in cell division and proliferation. *Prog Cell Cycle Res* 3:77–97.
  139. Litchfield DW, Lozeman FJ, Cicirelli MF, et al (1991) Phosphorylation of the beta subunit of casein kinase II in human A431 cells. Identification of the autophosphorylation site

- and a site phosphorylated by p34cdc2. *J Biol Chem* 266:20380–9.
140. Canton DA, Zhang C, Litchfield DW (2001) Assembly of protein kinase CK2 : investigation of complex formation between catalytic and regulatory subunits using a zinc-finger-deficient mutant of CK2 $\beta$ . *Biochem J* 358:87–94.
  141. Chantalat L, Leroy D, Filhol O, et al (1999) Crystal structure of the human protein kinase CK2 regulatory subunit reveals its zinc finger-mediated dimerization. *EMBO J* 18:2930–40. doi: 10.1093/emboj/18.11.2930
  142. Leroy D, Heriche J-K, Filhol O, et al (1997) Binding of Polyamines to an Autonomous Domain of the Regulatory Subunit of Protein Kinase CK2 Induces a Conformational Change in the Holoenzyme: A proposed role for the kinase stimulation. *J Biol Chem* 272:20820–7. doi: 10.1074/jbc.272.33.20820
  143. Allende J, Allende C (1995) Protein kinases. 4. Protein kinase CK2: an enzyme with multiple substrates and a puzzling regulation. *FASEB J* 9:313–323.
  144. Boldyreff B, Issinger OG (1997) A-Raf kinase is a new interacting partner of protein kinase CK2 beta subunit. *FEBS Lett* 403:197–9.
  145. Chen M, Li D, Krebs EG, Cooper JA (1997) The casein kinase II beta subunit binds to Mos and inhibits Mos activity. *Mol Cell Biol* 17:1904–12.
  146. Guerra B, Issinger O-G, Wang JYJ (2003) Modulation of human checkpoint kinase Chk1 by the regulatory beta-subunit of protein kinase CK2. *Oncogene* 22:4933–42. doi: 10.1038/sj.onc.1206721
  147. Pinna LA (2002) Protein kinase CK2: a challenge to canons. *J Cell Sci* 115:3873–8. doi: 10.1242/jcs.00074
  148. Litchfield DW, Dobrowolska G, Krebs EG (1994) Regulation of casein kinase II by growth factors: a reevaluation. *Cell Mol Biol Res* 40:373–81.
  149. Marin O, Meggio F, Pinna LA (1999) Structural Features Underlying the Unusual Mode of Calmodulin Phosphorylation by Protein Kinase CK2: A Study with Synthetic Calmodulin Fragments. *Biochem Biophys Res Commun* 256:442–6. doi: 10.1006/bbrc.1999.0348
  150. Homma MK, Homma Y (2008) Cell cycle and activation of CK2. *Mol Cell Biochem* 316:49–55. doi: 10.1007/s11010-008-9823-4
  151. Bosc DG, Lüscher B, Litchfield DW (1999) Expression and regulation of protein kinase CK2 during the cell cycle. *Mol Cell Biochem* 191:213–22. doi: 10.1023/A:1006840329973
  152. Luscher B, Litchfield DW (1994) Biosynthesis of casein kinase II in lymphoid cell lines. *Eur J Biochem* 220:521–26. doi: 10.1111/j.1432-1033.1994.tb18651.x
  153. Filhol O, Martiel J-L, Cochet C (2004) Protein kinase CK2: a new view of an old molecular complex. *EMBO Rep* 5:351–5. doi: 10.1038/sj.embor.7400115
  154. Lupp S, Gumhold C, Ampofo E, et al (2013) CK2 kinase activity but not its binding to CK2 promoter regions is implicated in the regulation of CK2 $\alpha$  and CK2 $\beta$  gene expressions. *Mol Cell Biochem* 384:71–82. doi: 10.1007/s11010-013-1782-8
  155. Pawson T, Nash P (2000) Protein-protein interactions define specificity in signal transduction. *Genes Dev* 14:1027–47.
  156. Li D, Meier UT, Dobrowolska G, Krebs EG (1997) Specific interaction between casein kinase 2 and the nucleolar protein Nopp140. *J Biol Chem* 272:3773–9.
  157. Miyata Y, Nishida E (2005) CK2 binds, phosphorylates, and regulates its pivotal substrate Cdc37, an Hsp90-cochaperone. *Mol Cell Biochem* 274:171–9.
  158. Faust M, Schuster N, Montenarh M (1999) Specific binding of protein kinase CK2 catalytic subunits to tubulin. *FEBS Lett* 462:51–6. doi: 10.1016/S0014-5793(99)01492-1
  159. Messenger MM, Saulnier RB, Gilchrist AD, et al (2002) Interactions between protein kinase CK2 and Pin1. Evidence for phosphorylation-dependent interactions. *J Biol Chem* 277:23054–64. doi: 10.1074/jbc.M200111200
  160. Finlan LE, Kernohan NM, Thomson G, et al (2005) Differential effects of 5-

- aminolaevulinic acid photodynamic therapy and psoralen + ultraviolet A therapy on p53 phosphorylation in normal human skin in vivo. *Br J Dermatol* 153:1001–10. doi: 10.1111/j.1365-2133.2005.06922.x
161. Donella-Deana A, Cesaro L, Sarno S, et al (2001) Autocatalytic tyrosine-phosphorylation of protein kinase CK2 alpha and alpha' subunits: implication of Tyr182. *Biochem J* 357:563–7.
  162. Kramerov AA, Ljubimov A V (2012) Focus on Molecules: Protein kinase CK2. *EXp Eye Res* 101:111–112. doi: 10.1016/j.exer.2010.12.011
  163. Faust M, Jung M, Günther J, et al (2001) Localization of individual subunits of protein kinase CK2 to the endoplasmic reticulum and to the Golgi apparatus. *Mol Cell Biochem* 227:73–80.
  164. Ji H, Lu Z (2013) The Role of Protein Kinase CK2 in Glioblastoma Development. *Clin Cancer Res* 19:6335–7. doi: 10.1158/1078-0432.CCR-13-2478
  165. Ruzzene M, Pinna LA (2010) Addiction to protein kinase CK2: a common denominator of diverse cancer cells? *Biochim Biophys Acta* 1804:499–504. doi: 10.1016/j.bbapap.2009.07.018
  166. Münstermann U, Fritz G, Seitz G, et al (1990) Casein kinase II is elevated in solid human tumours and rapidly proliferating non-neoplastic tissue. *Eur J Biochem* 189:251–7. doi: 10.1111/j.1432-1033.1990.tb15484.x
  167. Ortega CE, Seidner Y, Dominguez I (2014) Mining CK2 in cancer. *PLoS One* 9:e115609. doi: 10.1371/journal.pone.0115609
  168. Dixit D, Sharma V, Ghosh S, et al (2012) Inhibition of Casein kinase-2 induces p53-dependent cell cycle arrest and sensitizes glioblastoma cells to tumor necrosis factor (TNF $\alpha$ )-induced apoptosis through SIRT1 inhibition. *Cell Death Dis* 3:e271. doi: 10.1038/cddis.2012.10
  169. Hanna DE, Rethinaswamy A, Glover C V (1995) Casein kinase II is required for cell cycle progression during G1 and G2/M in *Saccharomyces cerevisiae*. *J Biol Chem* 270:25905–14.
  170. St-Denis NA, Derksen DR, Litchfield DW (2009) Evidence for regulation of mitotic progression through temporal phosphorylation and dephosphorylation of CK2alpha. *Mol Cell Biol* 29:2068–81. doi: 10.1128/MCB.01563-08
  171. Faust RA, Tawfic S, Davis AT, et al (2000) Antisense oligonucleotides against protein kinase CK2-alpha inhibit growth of squamous cell carcinoma of the head and neck in vitro. *Head Neck* 22:341–6.
  172. Ford JW, Mcvicar DW (2010) NIH Public Access. *Cancer* 19:38–46. doi: 10.1016/j.ccr.2009.12.020.An
  173. Lorenz P, Pepperkok R, Ansorge W, Pyerin W (1993) Cell biological studies with monoclonal and polyclonal antibodies against human casein kinase II subunit beta demonstrate participation of the kinase in mitogenic signaling. *J Biol Chem* 268:2733–9.
  174. Pepperkok R, Lorenz P, Ansorge W, Pyerin W (1994) Casein kinase II is required for transition of G0/G1, early G1, and G1/S phases of the cell cycle. *J Biol Chem* 269:6986–91.
  175. Yu IJ, Spector DL, Bae YS, Marshak DR (1991) Immunocytochemical localization of casein kinase II during interphase and mitosis. *J Cell Biol* 114:1217–32.
  176. Krek W, Maridor G, Nigg EA (1992) Casein kinase II is a predominantly nuclear enzyme. *J Cell Biol* 116:43–55.
  177. Russo GL, Vandenberg MT, Yu IJ, et al (1992) Casein kinase II phosphorylates p34cdc2 kinase in G1 phase of the HeLa cell division cycle. *J Biol Chem* 267:20317–25.
  178. Escargueil AE, Plisov SY, Filhol O, et al (2000) Mitotic phosphorylation of DNA topoisomerase II alpha by protein kinase CK2 creates the MPM-2 phosphoepitope on Ser-1469. *J Biol Chem* 275:34710–8. doi: 10.1074/jbc.M005179200
  179. Kikkawa U, Mann SK, Firtel RA, Hunter T (1992) Molecular cloning of casein kinase II

- alpha subunit from *Dictyostelium discoideum* and its expression in the life cycle. *Mol Cell Biol* 12:5711–23.
180. Vilk G, Saulnier RB, St Pierre R, Litchfield DW (1999) Inducible expression of protein kinase CK2 in mammalian cells. Evidence for functional specialization of CK2 isoforms. *J Biol Chem* 274:14406–14.
  181. Ahmad KA, Wang G, Unger G, et al (2008) Protein kinase CK2--a key suppressor of apoptosis. *Adv Enzyme Regul* 48:179–87. doi: 10.1016/j.advenzreg.2008.04.002
  182. Shin S, Lee Y, Kim W, et al (2005) Caspase-2 primes cancer cells for TRAIL-mediated apoptosis by processing procaspase-8. *EMBO J* 24:3532–42. doi: 10.1038/sj.emboj.7600827
  183. Guo C, Yu S, Davis AT, et al (2001) A potential role of nuclear matrix-associated protein kinase CK2 in protection against drug-induced apoptosis in cancer cells. *J Biol Chem* 276:5992–9. doi: 10.1074/jbc.M004862200
  184. Kato T, Delhase M, Hoffmann A, Karin M (2003) CK2 Is a C-Terminal I $\kappa$ B Kinase Responsible for NF- $\kappa$ B Activation during the UV Response. *Mol Cell* 12:829–39.
  185. Keller DM, Zeng X, Wang Y, et al (2001) A DNA damage-induced p53 serine 392 kinase complex contains CK2, hSpt16, and SSRP1. *Mol Cell* 7:283–92.
  186. Loizou JI, El-Khamisy SF, Zlatanou A, et al (2004) The protein kinase CK2 facilitates repair of chromosomal DNA single-strand breaks. *Cell* 117:17–28.
  187. Yang J, Weinberg RA (2008) Epithelial-mesenchymal transition: at the crossroads of development and tumor metastasis. *Dev Cell* 14:818–29. doi: 10.1016/j.devcel.2008.05.009
  188. Zou J, Luo H, Zeng Q, et al (2011) Protein kinase CK2 $\alpha$  is overexpressed in colorectal cancer and modulates cell proliferation and invasion via regulating EMT-related genes. *J Transl Med* 9:97. doi: 10.1186/1479-5876-9-97
  189. Chen X, Halberg RB, Burch RP, Dove WF (2008) Intestinal adenomagenesis involves core molecular signatures of the epithelial-mesenchymal transition. *J Mol Histol* 39:283–94. doi: 10.1007/s10735-008-9164-3
  190. Deshiere A, Duchemin-Pelletier E, Spreux E, et al (2013) Unbalanced expression of CK2 kinase subunits is sufficient to drive epithelial-to-mesenchymal transition by Snail1 induction. *Oncogene* 32:1373–83. doi: 10.1038/onc.2012.165
  191. Jouanneau E (2008) Angiogenesis and gliomas: current issues and development of surrogate markers. *Neurosurgery* 62:31–52. doi: 10.1227/01.NEU.0000311060.65002.4E
  192. Belden CJ, Valdes PA, Ran C, et al (2011) Genetics of glioblastoma: a window into its imaging and histopathologic variability. *Radiographics* 31:1717–40. doi: 10.1148/rg.316115512
  193. Noy P, Sawasdichai A, Jayaraman P-S, Gaston K (2012) Protein kinase CK2 inactivates PRH/Hhex using multiple mechanisms to de-repress VEGF-signalling genes and promote cell survival. *Nucleic Acids Res* 40:9008–20. doi: 10.1093/nar/gks687
  194. Ljubimov A V, Caballero S, Aoki AM, et al (2004) Involvement of protein kinase CK2 in angiogenesis and retinal neovascularization. *Invest Ophthalmol Vis Sci* 45:4583–91. doi: 10.1167/iovs.04-0686
  195. Feng D, Welker S, Körbel C, et al (2012) Protein kinase CK2 is a regulator of angiogenesis in endometriotic lesions. *Angiogenesis* 15:243–52. doi: 10.1007/s10456-012-9256-2
  196. Huse JT, Holland E, DeAngelis LM (2013) Glioblastoma: molecular analysis and clinical implications. *Annu Rev Med* 64:59–70. doi: 10.1146/annurev-med-100711-143028
  197. Ghosh S, May MJ, Kopp EB (1998) NF- $\kappa$ B and Rel proteins: evolutionarily conserved mediators of immune responses. *Annu Rev Immunol* 16:225–60. doi: 10.1146/annurev.immunol.16.1.225
  198. Chen L-F, Williams SA, Mu Y, et al (2005) NF- $\kappa$ B RelA phosphorylation regulates RelA acetylation. *Mol Cell Biol* 25:7966–75. doi: 10.1128/MCB.25.18.7966-7975.2005

199. Wang D, Westerheide SD, Hanson JL, Baldwin AS (2000) Tumor necrosis factor alpha-induced phosphorylation of RelA/p65 on Ser529 is controlled by casein kinase II. *J Biol Chem* 275:32592–7. doi: 10.1074/jbc.M001358200
200. Zoncu R, Efeyan A, Sabatini DM (2011) mTOR: from growth signal integration to cancer, diabetes and ageing. *Nat Rev Mol Cell Biol* 12:21–35. doi: 10.1038/nrm3025
201. Suzuki Y, Shirai K, Oka K, et al (2010) Higher pAkt expression predicts a significant worse prognosis in glioblastomas. *J Radiat Res* 51:343–348. doi: 10.1269/jrr.09109
202. Di Maira G, Brustolon F, Pinna LA, Ruzzene M (2009) Dephosphorylation and inactivation of Akt/PKB is counteracted by protein kinase CK2 in HEK 293T cells. *Cell Mol Life Sci* 66:3363–73. doi: 10.1007/s00018-009-0108-1
203. Di Maira G, Salvi M, Arrigoni G, et al (2005) Protein kinase CK2 phosphorylates and upregulates Akt/PKB. *Cell Death Differ* 12:668–77. doi: 10.1038/sj.cdd.4401604
204. Kim RH, Mak TW (2006) Tumours and tremors: how PTEN regulation underlies both. *Br J Cancer* 94:620–4. doi: 10.1038/sj.bjc.6602994
205. Brantley EC, Nabors LB, Gillespie GY, et al (2008) Loss of protein inhibitors of activated STAT-3 expression in glioblastoma multiforme tumors: implications for STAT-3 activation and gene expression. *Clin Cancer Res* 14:4694–704. doi: 10.1158/1078-0432.CCR-08-0618
206. McFarland BC, Ma J-Y, Langford CP, et al (2011) Therapeutic potential of AZD1480 for the treatment of human glioblastoma. *Mol Cancer Ther* 10:2384–93. doi: 10.1158/1535-7163.MCT-11-0480
207. Zheng Y, Qin H, Frank SJ, et al (2011) A CK2-dependent mechanism for activation of the JAK-STAT signaling pathway. *Blood* 118:156–66. doi: 10.1182/blood-2010-01-266320
208. Manni S, Brancalion A, Mandato E, et al (2013) Protein Kinase CK2 Inhibition Down Modulates the NF- $\kappa$ B and STAT3 Survival Pathways, Enhances the Cellular Proteotoxic Stress and Synergistically Boosts the Cytotoxic Effect of Bortezomib on Multiple Myeloma and Mantle Cell Lymphoma Cells. *PLoS One*. doi: 10.1371/journal.pone.0075280
209. Gordon MD, Nusse R (2006) Wnt signaling: multiple pathways, multiple receptors, and multiple transcription factors. *J Biol Chem* 281:22429–33. doi: 10.1074/jbc.R600015200
210. Nager M, Bhardwaj D, Cantí C, et al (2012)  $\beta$ -Catenin Signalling in Glioblastoma Multiforme and Glioma-Initiating Cells. *Chemother Res Pract* 2012:192362. doi: 10.1155/2012/192362
211. Song DH, Dominguez I, Mizuno J, et al (2003) CK2 phosphorylation of the armadillo repeat region of beta-catenin potentiates Wnt signaling. *J Biol Chem* 278:24018–25. doi: 10.1074/jbc.M212260200
212. Seldin DC, Landesman-Bollag E, Farago M, et al (2005) CK2 as a positive regulator of Wnt signalling and tumourigenesis. *Mol Cell Biochem* 274:63–7.
213. Wang Y, Zhang Y, Qian C, et al (2013) GSK3B/B-catenin signaling is correlated with the differentiation of glioma cells induced by Wogonin. *Toxicol Lett* 222:212–223. doi: 10.1016/j.toxlet.2013.07.013
214. Drygin D, Ho CB, Omori M, et al (2011) Protein kinase CK2 modulates IL-6 expression in inflammatory breast cancer. *Biochem Biophys Res Commun* 415:163–7. doi: 10.1016/j.bbrc.2011.10.046
215. Buontempo F, Orsini E, Martins LR, et al (2014) Cytotoxic activity of the casein kinase 2 inhibitor CX-4945 against T-cell acute lymphoblastic leukemia: targeting the unfolded protein response signaling. *Leukemia* 28:543–53. doi: 10.1038/leu.2013.349
216. Antunes L, Angioi-Duprez K, Bracard S, et al (2000) Analysis of Tissue Chimerism in Nude Mouse Brain and Abdominal Xenograft Models of Human Glioblastoma Multiforme: What Does It Tell Us About the Models and About Glioblastoma Biology and Therapy? *J Histochem Cytochem* 48:847–58.
217. Cha S, Johnson G, Wadghiri YZ, et al (2003) Dynamic, contrast-enhanced perfusion MRI

- in mouse gliomas: correlation with histopathology. *Magn Reson Med* 49:848–55. doi: 10.1002/mrm.10446
218. Podetz-Pedersen KM, Vezys V, Somia N V, et al (2014) Cellular Immune Response Against Firefly Luciferase After Sleeping Beauty–Mediated Gene Transfer In Vivo. *Hum Gene Ther* 25:955–65. doi: 10.1089/hum.2014.048
  219. Newcomb EW, Zagzag D (2009) The Murine GL261 Glioma Experimental Model to Assess Novel Brain Tumor Treatments. In: *CNS Cancer*. Humana Press, Totowa, NJ, pp 227–41
  220. Simões R V, García-Martín ML, Cerdán S, Arús C (2008) Perturbation of mouse glioma MRS pattern by induced acute hyperglycemia. *NMR Biomed* 21:251–64. doi: 10.1002/nbm.1188
  221. Szatmári T, Lumniczky K, Désaknai S, et al (2006) Detailed characterization of the mouse glioma 261 tumor model for experimental glioblastoma therapy. *Cancer Sci* 97:546–53. doi: 10.1111/j.1349-7006.2006.00208.x
  222. Scott O (1991) Tumor Transplantation and Tumor Immunity: A Personal View. *CANCER Res* 51:757–63.
  223. Aldape K, Colman H, James CD (2006) Models of malignant glioma. *Drug Discov Today Dis Model* 3:191–6. doi: 10.1016/j.ddmod.2006.06.002
  224. Guther H, Schmidt N, Phillips H, et al (2008) Glioblastoma-derived stem cell-enriched cultures form distinct subgroups according to molecular and phenotypic criteria. *Oncogene* 27:2897–909. doi: 10.1038/sj.onc.1210949
  225. Eichhorn PJA, Rodón L, González-Juncà A, et al (2012) USP15 stabilizes TGF- $\beta$  receptor I and promotes oncogenesis through the activation of TGF- $\beta$  signaling in glioblastoma. *Nat Med* 18:429–35. doi: 10.1038/nm.2619
  226. Joo KMM, Kim J, Jin J, et al (2013) Patient-Specific Orthotopic Glioblastoma Xenograft Models Recapitulate the Histopathology and Biology of Human Glioblastomas In Situ. *Cell Rep* 3:260–73. doi: 10.1016/j.celrep.2012.12.013
  227. Craveiro M, Clément-Schatlo V, Marino D, et al (2014) In vivo brain macromolecule signals in healthy and glioblastoma mouse models: <sup>1</sup>H magnetic resonance spectroscopy, post-processing and metabolite quantification at 14.1 T. *J Neurochem* 129:806–15. doi: 10.1111/jnc.12673
  228. Anido J, Sáez-Borderías A, González-Juncà A, et al (2010) TGF- $\beta$  Receptor Inhibitors Target the CD44<sup>high</sup>/Id1<sup>high</sup> Glioma-Initiating Cell Population in Human Glioblastoma. *Cancer Cell* 18:655–68. doi: 10.1016/j.ccr.2010.10.023
  229. Pelleitier M, Montplaisir S (1975) The nude mouse: a model of deficient T-cell function. *Methods Achiev Exp Pathol* 7:149–66.
  230. Bankert RB, Egilmez NK, Hess SD (2001) Human–SCID mouse chimeric models for the evaluation of anti-cancer therapies. *Trends Immunol* 22:386–93. doi: 10.1016/S1471-4906(01)01943-3
  231. Wu J, Waxman DJ (2015) Metronomic cyclophosphamide eradicates large implanted GL261 gliomas by activating antitumor Cd8(+) T-cell responses and immune memory. *Oncoimmunology* 4:e1005521. doi: 10.1080/2162402X.2015.1005521
  232. Killion JJ, Radinsky R, Fidler IJ (1998) Orthotopic models are necessary to predict therapy of transplantable tumors in mice. *Cancer Metastasis Rev* 17:279–84.
  233. Gutmann DH, Baker SJ, Giovannini M, et al (2003) Mouse models of human cancer consortium symposium on nervous system tumors. *Cancer Res* 63:3001–4.
  234. Weiss WA, Burns MJ, Hackett C, et al (2003) Genetic determinants of malignancy in a mouse model for oligodendroglioma. *Cancer Res* 63:1589–95.
  235. Ciezka M, Acosta M, Herranz C, et al (2016) Development of a transplantable glioma tumour model from genetically engineered mice: MRI/MRS/MRSI characterisation. *J Neurooncol*. doi: 10.1007/s11060-016-2164-3
  236. Ausman JI, Shapiro WR, Rall DP (1970) Studies on the chemotherapy of experimental



- brain tumors: development of an experimental model. *Cancer Res* 30:2394–400.
237. Delgado-Goni T, Julia-Sape M, Candiota AP, et al (2014) Molecular imaging coupled to pattern recognition distinguishes response to temozolomide in preclinical glioblastoma. *NMR Biomed* 27:1333–45. doi: 10.1002/nbm.3194
  238. Lauterbur PC (2003) Nobel Lecture: All Science is Interdisciplinary - from Magnetic Moments to Molecules to Men. In: Nobel Prize Physiol. or Med. [https://www.nobelprize.org/nobel\\_prizes/medicine/laureates/2003/lauterbur-lecture.html](https://www.nobelprize.org/nobel_prizes/medicine/laureates/2003/lauterbur-lecture.html).
  239. Jiménez Xarrié E (2013) Caracterización de la proliferación celular en las zonas subventriculares y de la evolución del infarto mediante espectroscopía de resonancia magnética en un modelo preclínico de isquemia cerebral. TDX (Tesis Dr en Xarxa). doi: <http://www.tesisenred.net/handle/10803/131309>
  240. Ridgway JP, Balaban R, Peters D, et al (2010) Cardiovascular magnetic resonance physics for clinicians: part I. *J Cardiovasc Magn Reson* 12:71. doi: 10.1186/1532-429X-12-71
  241. Hattingen E, Jurcoane A, Bähr O, et al (2011) Bevacizumab impairs oxidative energy metabolism and shows antitumoral effects in recurrent glioblastomas: a <sup>31</sup>P/<sup>1</sup>H MRSI and quantitative magnetic resonance imaging study. *Neuro Oncol* 13:1349–63. doi: 10.1093/neuonc/nor132
  242. Ortega-Martorell S, Julià-Sapé M, Lisboa P, Arus C (2016) Pattern recognition analysis of MR spectra in Handbook of Magnetic resonance Spectroscopy in vivo: MRS theory, practice and applications. Bottomley PA, Griffiths JR (eds). John Wiley and Sons Ltd, Chichester UK. *Handb Magn Reson Spectrosc vivo MRS theory, Pract Appl* Bottomley PA, Griffiths JR (eds) John Wiley Sons Ltd, Chichester UK 343–358.
  243. Laudadio T, Carmen Martínez-Bisbal M, Celda B, Huffel S Van (2008) Fast nosological imaging using canonical correlation analysis of brain data obtained by two-dimensional turbo spectroscopic imaging. *NMR Biomed* 21:311–21. doi: 10.1002/nbm.1190
  244. Luts J, Laudadio T, Idema AJ, et al (2009) Nosologic imaging of the brain: segmentation and classification using MRI and MRSI. *NMR Biomed* 22:374–90. doi: 10.1002/nbm.1347
  245. Spottiswoode BS (2012) Cardiac magnetic resonance imaging. *Contin Med Educ* 30:4,6,8,9,10,11.
  246. Lai PH, Ho JT, Chen WL, et al (2002) Brain abscess and necrotic brain tumor: discrimination with proton MR spectroscopy and diffusion-weighted imaging. *AJNR Am J Neuroradiol* 23:1369–77.
  247. Souza E, Castellano G, Baldissin M, Costa E Comparison of ADC values obtained in 2D and 3D for differentiation between healthy brain tissues, glioblastoma and meningioma (May 26-31, 2012) World Congress on Medical Physics and Biomedical Engineering. 40:289–298. doi: 10.1007/s00261-014-0215-9
  248. De Edelenyi FS, Rubin C, Estève F, et al (2000) A new approach for analyzing proton magnetic resonance spectroscopic images of brain tumors: nosologic images. *Nat Med* 6:1287–9. doi: 10.1038/81401
  249. Ortega-Martorell S, Lisboa PJG, Vellido A, et al (2012) Convex non-negative matrix factorization for brain tumor delimitation from MRSI data. *PLoS One* 7:e47824. doi: 10.1371/journal.pone.0047824
  250. Tate a R (1996) Pattern recognition of in vivo magnetic resonance spectra.
  251. Govindaraju V, Young K, Maudsley AA (2000) Proton NMR chemical shifts and coupling constants for brain metabolites. *NMR Biomed* 13:129–53.
  252. Horská A, Barker PB (2010) Imaging of brain tumors: MR spectroscopy and metabolic imaging. *Neuroimaging Clin N Am* 20:293–310. doi: 10.1016/j.nic.2010.04.003
  253. Glunde K, Bhujwala ZM, Ronen SM (2011) Choline metabolism in malignant transformation. *Nat Rev Cancer* 11:835. doi: 10.1038/nrc3162

254. Chernov MF, Hayashi M, Izawa M, et al (2006) Proton magnetic resonance spectroscopy (MRS) of metastatic brain tumors: variations of metabolic profile. *Int J Clin Oncol* 11:375–84. doi: 10.1007/s10147-006-0589-y
255. Rudkin TM, Arnold DL (1999) Proton magnetic resonance spectroscopy for the diagnosis and management of cerebral disorders. *Arch Neurol* 56:919–26.
256. Vander Heiden MG, Cantley LC, Thompson CB (2009) Understanding the Warburg Effect: The Metabolic Requirements of Cell Proliferation. *Science* (80- ) 324:1029–1033. doi: 10.1126/science.1160809
257. Candiota AP, Majós C, Julià-Sapé M, et al (2011) Non-invasive grading of astrocytic tumours from the relative contents of myo-inositol and glycine measured by in vivo MRS. *JBR-BTR organe la Société R belge Radiol = orgaan van K Belgische Ver voor Radiol* 94:319–29.
258. Hattingen E, Lanfermann H, Quick J, et al (2009) <sup>1</sup>H MR spectroscopic imaging with short and long echo time to discriminate glycine in glial tumours. *MAGMA* 22:33–41. doi: 10.1007/s10334-008-0145-z
259. Zoula S, Hérigault G, Ziegler A, et al (2003) Correlation between the occurrence of <sup>1</sup>H-MRS lipid signal, necrosis and lipid droplets during C6 rat glioma development. *NMR Biomed* 16:199–212. doi: 10.1002/nbm.831
260. Laurenti G, Benedetti E, D’Angelo B, et al (2011) Hypoxia induces peroxisome proliferator-activated receptor  $\alpha$  (PPAR $\alpha$ ) and lipid metabolism peroxisomal enzymes in human glioblastoma cells. *J Cell Biochem* 112:3891–901. doi: 10.1002/jcb.23323
261. Simões RV, Ortega-Martorell S, Delgado-Goñi T, et al (2012) Improving the classification of brain tumors in mice with perturbation enhanced (PE)-MRSI. *Integr Biol (Camb)* 4:183–91. doi: 10.1039/c2ib00079b
262. Delgado-Goñi T, Ortega-Martorell S, Ciezka M, et al (2016) MRSI-based molecular imaging of therapy response to temozolomide in preclinical glioblastoma using source analysis. *NMR Biomed* 29:732–43. doi: 10.1002/nbm.3521
263. Hakumäki JM, Poptani H, Sandmair a M, et al (1999) <sup>1</sup>H MRS detects polyunsaturated fatty acid accumulation during gene therapy of glioma: implications for the in vivo detection of apoptosis. *Nat Med* 5:1323–7. doi: 10.1038/15279
264. Tate AR, Griffiths JR, Martínez-Pérez I, et al (1998) Towards a method for automated classification of <sup>1</sup>H MRS spectra from brain tumours. *NMR Biomed* 11:177–91.
265. Mountford CE, Stanwell P, Lin A, et al (2010) Neurospectroscopy: the past, present and future. *Chem Rev* 110:3060–86. doi: 10.1021/cr900250y
266. Ortega-Martorell S, Olier I, Julià-Sapé M, Arús C (2010) SpectraClassifier 1.0: a user friendly, automated MRS-based classifier-development system. *BMC Bioinformatics* 11:106. doi: 10.1186/1471-2105-11-106
267. Sajda P, Du S, Brown TR, et al (2004) Nonnegative matrix factorization for rapid recovery of constituent spectra in magnetic resonance chemical shift imaging of the brain. *IEEE Trans Med Imaging* 23:1453–65. doi: 10.1109/TMI.2004.834626
268. Ortega-Martorell S, Ruiz H, Vellido A, et al (2013) A novel semi-supervised methodology for extracting tumor type-specific MRS sources in human brain data. *PLoS One* 8:e83773. doi: 10.1371/journal.pone.0083773
269. Amari S (2001) Information geometry on hierarchy of probability distributions. *IEEE Trans Inf Theory* 47:1701–11. doi: 10.1109/18.930911
270. Simões R V, Delgado-Goñi T, Lope-Piedrafita S, Arús C (2010) <sup>1</sup>H-MRSI pattern perturbation in a mouse glioma: the effects of acute hyperglycemia and moderate hypothermia. *NMR Biomed* 23:23–33. doi: 10.1002/nbm.1421
271. Mangiola A, Saulnier N, De Bonis P, et al (2013) Gene expression profile of glioblastoma peritumoral tissue: an ex vivo study. *PLoS One* 8:e57145. doi: 10.1371/journal.pone.0057145
272. Bradford MM (1976) A rapid and sensitive method for the quantitation of microgram

- quantities of protein utilizing the principle of protein-dye binding. *Anal Biochem* 72:248–54. doi: 10.1016/0003-2697(76)90527-3
273. Lama G, Mangiola A, Anile C, et al (2007) Activated ERK1/2 expression in glioblastoma multiforme and in peritumor tissue. *Int J Oncol* 30:1333–42.
274. Plotnikov A, Chuderland D, Karamansha Y, et al (2011) Nuclear extracellular signal-regulated kinase 1 and 2 translocation is mediated by casein kinase 2 and accelerated by autophosphorylation. *Mol Cell Biol* 31:3515–30. doi: 10.1128/MCB.05424-11
275. Agarwal M, Nitta RT, Li G (2013) Casein Kinase 2: a novel player in glioblastoma therapy and cancer stem cells. *J Mol Genet Med*. doi: 10.4172/1747-0862.1000094
276. Martins LR, Lúcio P, Melão a, et al (2014) Activity of the clinical-stage CK2-specific inhibitor CX-4945 against chronic lymphocytic leukemia. *Leukemia* 28:179–82. doi: 10.1038/leu.2013.232
277. Saldaña-Ruiz S, Soler-Martín C, Llorens J (2012) Role of CYP2E1-mediated metabolism in the acute and vestibular toxicities of nineteen nitriles in the mouse. *Toxicol Lett* 208:125–32. doi: 10.1016/j.toxlet.2011.10.016
278. LASA and NC3Rs, Guidance on dose level selection for regulatory general toxicology studies for pharmaceuticals, R.a.R.o.A.i.R. Laboratory Animal Science Association & National Centre for the Replacement, Editor. 2009: London. <http://www.lasa.co.uk/PDF/LAS>.
279. Ruzzene M, Di Maira G, Tosoni K, Pinna LA (2010) Assessment of CK2 constitutive activity in cancer cells. *Methods Enzymol* 484:495–514. doi: 10.1016/B978-0-12-381298-8.00024-1
280. Chou T-C (2010) Drug Combination Studies and Their Synergy Quantification Using the Chou-Talalay Method. *Cancer Res* 70:440–6. doi: 10.1158/0008-5472.CAN-09-1947
281. Kusabe Y, Kawashima H, Ogose A, et al (2015) Effect of temozolomide on the viability of musculoskeletal sarcoma cells. *Oncol Lett* 10:2511–8. doi: 10.3892/ol.2015.3506
282. McConville P, Hambardzumyan D, Moody JB, et al (2007) Magnetic resonance imaging determination of tumor grade and early response to temozolomide in a genetically engineered mouse model of glioma. *Clin Cancer Res* 13:2897–904. doi: 10.1158/1078-0432.CCR-06-3058
283. Plowman J, Waud WR, Koutsoukos AD, et al (1994) Preclinical antitumor activity of temozolomide in mice: Efficacy against human brain tumor xenografts and synergism with 1,3-bis(2-chloroethyl)-1-nitrosourea. *Cancer Res* 54:3793–9.
284. Bian Y, Han J, Kannabiran V, et al (2015) MEK inhibitor PD-0325901 overcomes resistance to CK2 inhibitor CX-4945 and exhibits anti-tumor activity in head and neck cancer. *Int J Biol Sci* 11:411–22. doi: 10.7150/ijbs.10745
285. Siddiqui-Jain A, Bliesath J, Macalino D, et al (2012) CK2 inhibitor CX-4945 suppresses DNA repair response triggered by DNA-targeted anticancer drugs and augments efficacy: mechanistic rationale for drug combination therapy. *Mol Cancer Ther* 11:994–1005. doi: 10.1158/1535-7163.MCT-11-0613
286. Drabløs F, Feyzi E, Aas PA, et al (2004) Alkylation damage in DNA and RNA--repair mechanisms and medical significance. *DNA Repair (Amst)* 3:1389–407. doi: 10.1016/j.dnarep.2004.05.004
287. Hegi ME, Diserens A-C, Godard S, et al (2004) Clinical trial substantiates the predictive value of O-6-methylguanine-DNA methyltransferase promoter methylation in glioblastoma patients treated with temozolomide. *Clin Cancer Res* 10:1871–4.
288. Kohsaka S, Wang L, Yachi K, et al (2012) STAT3 inhibition overcomes temozolomide resistance in glioblastoma by downregulating MGMT expression. *Mol Cancer Ther* 11:1289–99. doi: 10.1158/1535-7163.MCT-11-0801
289. Kim H, Choi K, Kang H, et al (2014) Identification of a novel function of CX-4945 as a splicing regulator. *PLoS One* 9:1–8. doi: 10.1371/journal.pone.0094978
290. Wu J, Waxman DJ (2014) Metronomic cyclophosphamide schedule-dependence of

- innate immune cell recruitment and tumor regression in an implanted glioma model. *Cancer Lett* 353:272–80. doi: 10.1016/j.canlet.2014.07.033
291. Sestero CM, McGuire DJ, De Sarno P, et al (2012) CD5-dependent CK2 activation pathway regulates threshold for T cell anergy. *J Immunol* 189:2918–30. doi: 10.4049/jimmunol.1200065
  292. Alonso MN, Wong MT, Zhang AL, et al (2011) T(H)1, T(H)2, and T(H)17 cells instruct monocytes to differentiate into specialized dendritic cell subsets. *Blood* 118:3311–20. doi: 10.1182/blood-2011-03-341065
  293. Ulges A, Witsch EJ, Pramanik G, et al (2016) Protein kinase CK2 governs the molecular decision between encephalitogenic TH17 cell and Treg cell development. *Proc Natl Acad Sci U S A* 113:10145–50. doi: 10.1073/pnas.1523869113
  294. Kim T-G, Kim C-H, Park J-S, et al (2010) Immunological factors relating to the antitumor effect of temozolomide chemoimmunotherapy in a murine glioma model. *Clin Vaccine Immunol* 17:143–53. doi: 10.1128/CI.00292-09
  295. Fritzell S, Sandén E, Eberstål S, et al (2013) Intratumoral temozolomide synergizes with immunotherapy in a T cell-dependent fashion. *Cancer Immunol Immunother* 62:1463–74. doi: 10.1007/s00262-013-1449-z
  296. Martins LR, Lúcio P, Silva MC, et al (2010) Targeting CK2 overexpression and hyperactivation as a novel therapeutic tool in chronic lymphocytic leukemia. *Blood* 116:2724–31.
  297. Jordan M, Waxman DJ (2016) CpG-1826 immunotherapy potentiates chemotherapeutic and anti-tumour immune responses to metronomic cyclophosphamide in a preclinical glioma model. *Cancer Lett* 373:88–96. doi: 10.1016/j.canlet.2015.11.029
  298. Jennings D, Hatton BN, Guo J, et al (2002) Early response of prostate carcinoma xenografts to docetaxel chemotherapy monitored with diffusion MRI. *Neoplasia* 4:255–62. doi: 10.1038/sj/neo/7900225
  299. Simões R V., Candiota AP, Julià-Sapé M, Arús C (2013) In Vivo Magnetic Resonance Spectroscopic Imaging and Ex Vivo Quantitative Neuropathology by High Resolution Magic Angle Spinning Proton Magnetic Resonance Spectroscopy. In: *In Neuromethods*. pp 329–65
  300. Ding C, Li T, Jordan MI (2010) Convex and semi-nonnegative matrix factorizations. *IEEE Trans Pattern Anal Mach Intell* 32:45–55. doi: 10.1109/TPAMI.2008.277
  301. Cserr HF, Harling-Berg CJ, Knopf PM (1992) Drainage of brain extracellular fluid into blood and deep cervical lymph and its immunological significance. *Brain Pathol* 2:269–76.
  302. Reardon DA, Gokhale PC, Klein SR, et al (2015) Glioblastoma Eradication Following Immune Checkpoint Blockade in an Orthotopic, Immunocompetent Model. *Cancer Immunol Res* 4:124–35. doi: 10.1158/2326-6066.CIR-15-0151
  303. Eisenhauer EA, Therasse P, Bogaerts J, et al (2009) New response evaluation criteria in solid tumours: Revised RECIST guideline (version 1.1). *Eur J Cancer* 45:228–47. doi: 10.1016/j.ejca.2008.10.026
  304. Wu J, Jordan M, Waxman DJ (2016) Metronomic cyclophosphamide activation of anti-tumor immunity: tumor model, mouse host, and drug schedule dependence of gene responses and their upstream regulators. *BMC Cancer* 16:623. doi: 10.1186/s12885-016-2597-2
  305. Zong W-X, Thompson CB (2006) Necrotic death as a cell fate. *Genes Dev* 20:1–15. doi: 10.1101/gad.1376506
  306. Brandsma D, Stalpers L, Taal W, et al (2008) Clinical features, mechanisms, and management of pseudoprogression in malignant gliomas. *Lancet Oncol* 9:453–61. doi: 10.1016/S1470-2045(08)70125-6
  307. Wang X, Liu X, Chen Y, et al (2015) Histopathological findings in the peritumoral edema area of human glioma. *Histol Histopathol* 30:1101–9. doi: 10.14670/HH-11-607

308. Calinescu A-A, Kamran N, Baker G, et al (2015) Overview of current immunotherapeutic strategies for glioma. *Immunotherapy* 7:1073–104. doi: 10.2217/imt.15.75
309. Geiger H, Schleimer D, Nattamai KJ, et al (2006) Mutagenic potential of temozolomide in bone marrow cells in vivo. *Blood* 107:3010–1. doi: 10.1182/blood-2005-09-3649
310. Clark SW, Taylor J, Wang DL, et al (2013) Plasmablastic lymphoma after standard-dose temozolomide for newly diagnosed glioblastoma. *Neurology* 81:93–4. doi: 10.1212/WNL.0b013e318297eea6
311. Neyns B, Cordera S, Joosens E, Nader P (2008) Non-Hodgkin's Lymphoma in Patients With Glioma Treated With Temozolomide. *J Clin Oncol* 26:4518–9. doi: 10.1200/JCO.2008.18.8177
312. Stupp R, Dietrich P-Y, Ostermann Kraljevic S, et al (2002) Promising survival for patients with newly diagnosed glioblastoma multiforme treated with concomitant radiation plus temozolomide followed by adjuvant temozolomide. *J Clin Oncol* 20:1375–82. doi: 10.1200/jco.2002.20.5.1375
313. Vera K, Djafari L, Faivre S, et al (2004) Dose-dense regimen of temozolomide given every other week in patients with primary central nervous system tumors. *Ann Oncol Off J Eur Soc Med Oncol* 15:161–71. doi: 10.1093/ANNONC/MDH003
314. Romiti A, Cox MC, Sarcina I, et al (2013) Metronomic chemotherapy for cancer treatment: a decade of clinical studies. *Cancer Chemother Pharmacol* 72:13–33. doi: 10.1007/s00280-013-2125-x
315. Bracci L, Schiavoni G, Sistigu A, Belardelli F (2014) Immune-based mechanisms of cytotoxic chemotherapy: implications for the design of novel and rationale-based combined treatments against cancer. *Cell Death Differ* 21:15–25. doi: 10.1038/cdd.2013.67
316. Kindy MS, Yu J, Zhu H, et al (2016) A therapeutic cancer vaccine against GL261 murine glioma. *J Transl Med* 14:1. doi: 10.1186/s12967-015-0757-9
317. Garg AD, Vandenberk L, Koks C, et al (2016) Dendritic cell vaccines based on immunogenic cell death elicit danger signals and T cell-driven rejection of high-grade glioma. *Sci Transl Med* 8:328ra27. doi: 10.1126/scitranslmed.aae0105
318. Caporali S, Levati L, Graziani G, et al (2012) NF- $\kappa$ B is activated in response to temozolomide in an AKT-dependent manner and confers protection against the growth suppressive effect of the drug. *J Transl Med* 10:252. doi: 10.1186/1479-5876-10-252
319. Pollack IF, Jakacki RI, Butterfield LH, et al (2014) Antigen-specific immune responses and clinical outcome after vaccination with glioma-associated antigen peptides and polyinosinic-polycytidylic acid stabilized by lysine and carboxymethylcellulose in children with newly diagnosed malignant brainstem and n. *J Clin Oncol* 32:2050–58. doi: 10.1200/JCO.2013.54.0526
320. Arias-Ramos N, Mocioiu V, Julia-Sape M, et al (2016) ESMRMB 33rd Annual Scientific Meeting, Vienna, AT, September 29 – October 1: Abstract 314. *Magn Reson Mater Physics, Biol Med* 29:294–5. doi: 10.1007/s10334-016-0570-3



## 8 ANNEXES

### 8.1 ANNEX 1: SUPERVISION OF LABORATORY ANIMALS

MONITORING PARAMETERS (scale: 0-3 points):

Weight Loss

- 0) Normal Weight
- 1) Less than 10% loss
- 2) Between 10 and 15% loss
- 3) Consistent or rapid, exceeding 20% loss maintained for 72h

Physical appearance

- 0) Normal
- 1) More than 10% dehydration, skin tenting
- 2) Erected hair. Cyanosis
- 3) Hunched back. Loss of muscle mass

Clinical signs

- 0) None
- 1) Circular motion of the animal
- 2) Mucous secretions and/or bleeding from any orifice. Detectable hypertrophy of organs (lymph nodes, spleen, liver)
- 3) Shortness of breath (particularly if accompanied by nasal discharge and / or cyanosis). Cachexia.

Changes in behaviour

- 0) No
- 1) Inability to move normally
- 2) Inability to get to the food / drink. Isolation from the rest of the animals in the cage
- 3) Unconsciousness or comatose. Lack of response (Dying)

Wounds

- 0) No
- 1) Scratches
- 2) Nonhealing wounds. Infection at the surgical site
- 3) Ulcerating, festering wounds. Ulcerating or necrotic tumors

**The animal condition according to the parameters and overall score:**

- a) 0 points: Healthy animal
- b) 1-2 points: Minor signs, follow established protocol
- c) 3-11 points: Daily supervision of the animal. Analgesics\* or sacrifice of the animal \*\*
- d) 12-30 points: sacrifice \*\*

\* Analgesic: Meloxicam (subcutaneously: 1 mg /kg)

\*\* The *Servei d'Estabulari* veterinary staff informs a group member as soon as possible to consider halting of the protocol / experiment.

**NOTE:** As the tumor grows, it affects the motor function of the brain. Animals may suffer from: paresis, decreased strength, plegia, paralysis. In these cases, food and water (i.e. hydrogel or water-soaked food) should be placed inside the cage to facilitate access by the animal.





## 8.2 ANNEX 2: Article of "Protein kinase CK2 content in GL261 mouse glioblastoma"

Pathol. Oncol. Res.  
DOI 10.1007/s12253-015-9987-7



SHORT COMMUNICATION

## Protein Kinase CK2 Content in GL261 Mouse Glioblastoma

Laura Ferrer-Font<sup>1,2,3</sup> · Estefania Alcaraz<sup>1</sup> · Maria Plana<sup>1</sup> · Ana Paula Candiota<sup>1,2,3</sup> · Emilio Itarte<sup>1</sup> · Carles Arús<sup>1,2,3</sup>

Received: 15 March 2015 / Accepted: 24 August 2015  
© Arányi Lajos Foundation 2015

**Abstract** Glioblastoma (GBM) is the most prevalent and aggressive human glial tumour with a median survival of 14–15 months. Temozolomide (TMZ) is the standard chemotherapeutic choice for GBM treatment. Unfortunately, chemoresistance always ensues with concomitant tumour regrowth. Protein kinase CK2 (CK2) contributes to tumour development, proliferation, and suppression of apoptosis in cancer and it is overexpressed in human GBM. Targeting CK2 in GBM treatment may benefit patients. With this translational perspective in mind, we have studied the CK2 expression level by Western blot analysis in a preclinical model of GBM: GL261 cells growing orthotopically in C57BL/6 mice. The expression level of the CK2 catalytic subunit (CK2 $\alpha$ ) was higher in tumour (about 4-fold) and in contralateral brain parenchyma (more than 2-fold) than in normal brain parenchyma ( $p < 0.05$ ). In contrast, no significant changes were found in CK2 regulatory subunit (CK2 $\beta$ ) expression, suggesting an increased unbalance of CK2 $\alpha$ /CK2 $\beta$  in GL261 tumours with respect to normal brain parenchyma, in agreement with a differential role of these two subunits in tumours.

**Keywords** Glioma · CK2 content · Preclinical brain tumor · GBM therapeutic targets

### Abbreviations

GBM Glioblastoma  
CK2 Protein kinase CK2  
TMZ Temozolomide

### Introduction

Glioblastoma (GBM) is the most prevalent and aggressive glial tumour in humans with a median survival of 14–15 months even when an aggressive treatment is applied (surgical resection, chemotherapy and radiation) [1]. Temozolomide (TMZ) plus radiotherapy is the standard therapeutic choice for GBM treatment and, at present, it is the one producing the best survival rates [2]. Unfortunately, cancer stem cells (CSCs) are known to mediate chemoresistance, indicating that CSCs persist in these tumours even after the standard treatment [3]. Due to its poor outcome and resistance to standard therapy, efficient alternative treatments are urgently needed for these tumours.

The use of animal models in brain tumour research is mandatory in the search for new therapeutic targets due to obvious ethical restrictions related to human patients. The ideal animal model of GBM should reproduce the main characteristics of this neoplasm: characteristic growth pattern, infiltrative, but non-metastatic, tumour growth and poor immunogenicity [4]. However, none of the currently available models is able to mimic all aspects of human high-grade glioma. One of the most investigated murine brain tumour models is GL261 growing into C57BL/6 mice, and it has been used for more than 20 years in different approaches in therapy evaluation

✉ Ana Paula Candiota  
AnaPaula.Candiota@uab.cat

Carles Arús  
Carles.Arús@uab.cat

- <sup>1</sup> Departament de Bioquímica i Biologia Molecular, Unitat de Bioquímica de Biociències, Edifici Cs, Universitat Autònoma de Barcelona, 08193 Cerdanyola del Vallès, Spain
- <sup>2</sup> Centro de Investigación Biomédica en Red en Bioingeniería, Biomateriales y Nanomedicina (CIBER-BBN), Cerdanyola del Vallès, Spain
- <sup>3</sup> Institut de Biotecnologia i Biomedicina (IBB), Universitat Autònoma de Barcelona, Cerdanyola del Vallès, Spain

studies [5]. Furthermore, non-invasive biomarkers of therapy response have been evaluated in this model [6].

Protein kinase CK2 is an oncogenic protein kinase which contributes to tumour development, proliferation, and suppression of apoptosis in multiple cancer types [7]. It is composed of two catalytic ( $\alpha$  and/or  $\alpha'$ ) and two  $\beta$  regulatory subunits. Protein kinase CK2 is a constitutively active serine-threonine kinase and elevated CK2 expression levels have been demonstrated in several cancer types [8]. It has been also demonstrated that it is overexpressed in mice xenograft models of human GBM [9] where it plays a fundamental role regulating multiple signalling pathways involved in tumour cell survival, proliferation, migration and invasion [10]. These characteristics identify CK2 as an active therapeutic target, and in this sense, targeting CK2 in GBM treatment could benefit patients.

Although some authors have reported higher CK2 expression levels in tumours, in comparison with normal tissue [8, 11], to our knowledge this has not been studied in the GL261 GBM model. Accordingly, before evaluating CK2 inhibitors [12, 13] for therapy response studies we felt it advisable to assess the CK2 content in GL261 GBM.

## Methods

### Animal Models

A total of 6 C57BL/6 female wt mice weighting  $18 \pm 2$  g were used for this study. They were obtained from Charles River Laboratories (Charles River Laboratories Internacional, l'Abresle, France) and housed in the animal facility of the *Universitat Autònoma de Barcelona*. The GL261 mouse glioma cells were obtained from the Tumour Bank Repository of the National Cancer Institute, Frederick, MD, USA, and were cultured as described in [14]. Tumours were induced in 3 C57BL/6 mice by intracranial stereotactic injection of  $10^5$  GL261 cells in the caudate nucleus, as previously described by us [14].

Tumour volumes were followed using  $T_2$ -weighted MRI acquisitions (see below and (6)), until the tumour reached the desired size, taking into account previous work from our group, that is  $77.3 \pm 10.9$  mm<sup>3</sup> (15 days after implantation). Both tumour-bearing and control animals were euthanized with an intraperitoneal injection of pentobarbital (200 mg/kg, 60 mg/ml), their brains were removed and tumour resected (in case of tumour-bearing animals). The brain parenchyma from three wt mice was used as control, while contralateral brain parenchyma was employed to determine the possible effects outside the tumour volume recently described by other authors [15]. The contralateral tissue was obtained after visual inspection of the whole brain and tumour, avoiding as much as possible the tumoral zone. Samples were stored in liquid nitrogen until further processing. All studies were carried out following protocols approved by the local/institutional ethics

committee, according to the regional and state legislation (CEEAH 2449 and 1176).

### In Vivo MRI Studies

These studies were carried out at the joint NMR facility of the *Universitat Autònoma de Barcelona* and CIBER-BBN (*Cerdanyola del Vallès*), unit 25 of NANBIOSIS, using a 7 T horizontal magnet (*BioSpec 70/30, Bruker BioSpin, Ettlingen, Germany*).  $T_2$ -weighted images (TR/TE<sub>eff</sub> = 4200/36 ms) were acquired as in [6] to detect brain tumour evolution and to calculate the abnormal mass volume.

### Protein Extraction

Tissue samples were weighted and 250  $\mu$ l of cold lysis buffer for each 100 mg of tissue was added (cold lysis buffer: 50 mM Tris-HCl pH 7.7, 150 mM NaCl, 15 mM MgCl<sub>2</sub>, 0.4 mM EDTA, 0.5 mM DTT, 100  $\mu$ g/mL Leupeptin, 100  $\mu$ g/mL Aprotinin, 10 mM Benzamidin, 2 mM phenylmethylsulfonyl fluoride). Samples were homogenized with a Sonic sicator (*Vibra-cell, Newtown, USA*) 10 times for 10-s intervals, and after, 0.5 % Triton-X-100 was added. After remaining 15 min on ice, the lysate was centrifuged at  $13,000 \times g$  for 20 min at 4 °C. Supernatants were used for Western blot analysis.

### Western blot Analysis

The differential expression of protein CK2 $\alpha$  and CK2 $\beta$  in mice brain was assessed for control brain parenchyma, GL261 tumour and contralateral brain parenchyma (non tumoral). The protein content of tissue extracts was quantified with the Bradford assay [16]. For Western blot analysis, 50  $\mu$ g of total protein were separated by 12 % Sodium Dodecyl Sulfate Polyacrylamide Gel Electrophoresis (SDS-PAGE) and transferred onto Polyvinylidene fluoride (PVDF) membranes by electroblotting. The membranes were then blocked in 5 % milk powder in 0.02 % Tween Phosphate buffered saline (T-PBS) for 1 h and washed three times for 10 min with T-PBS. Membranes were incubated with antibodies against CK2 $\alpha$  (CK2 $\alpha$  (sc-6479 C-18), 42 kD, 1:300, *Santacruz, Texas USA*) or CK2 $\beta$  (CK2 $\beta$  EP1995Y, 24-25kD, 1:200, *Merck Millipore, Darmstadt, Germany*), and tubulin was used as a loading control ( $\beta$ -tubulin, 55 kD, 1:1000, Cell signalling technology (*Danvers, Massachusetts, USA*)) overnight at 4 °C. Next day, three T-PBS washing steps were carried out and incubation with the secondary antibodies took place during 1 h (anti-goat for CK2 $\alpha$  and anti-rabbit for CK2 $\beta$  and tubulin, 1:5000, *Biorad, Hercules, California*) and washing steps with T-PBS were repeated. The specific antibody binding was detected with the enhanced chemiluminescence technique with Lumi-Light Western blotting substrate (*Roche, Basel, Germany*). Western blot films were scanned and quantified with the *ImageJ* software

## Protein kinase CK2 in preclinical glioma

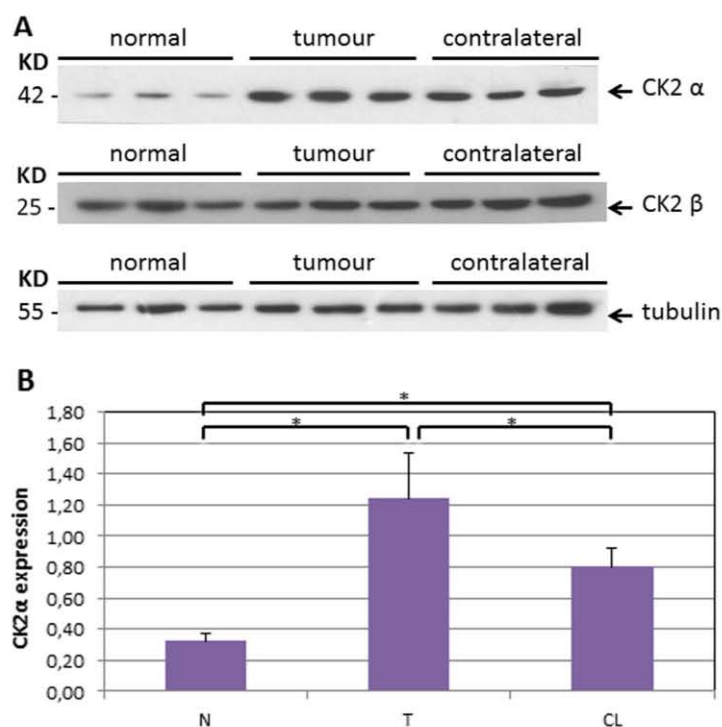


**Fig. 1** Immunoblotting of CK2 subunits in mouse brain tumour samples. **a** Western blots of characteristic tissue samples using 50  $\mu$ g of total protein, detection with anti-CK2 $\alpha$  antibody, anti-CK2 $\beta$  antibody and with anti-tubulin antibody. From left to right, normal brain parenchyma samples, tumour samples and contralateral brain parenchyma samples.

**b** Quantification (bar;  $\pm$ SD) carried out of the normalized CK2 $\alpha$  to tubulin expression in tissue samples using 50  $\mu$ g of total protein,  $n = 9$ . N = normal brain parenchyma, T = tumour, CL = contralateral brain parenchyma \* =  $p < 0.05$

(National Institutes of Health, USA, <http://imagej.nih.gov/ij/>) and data obtained was normalized to tubulin.

### Statistical Analysis

Normality was first inspected in each group by the Kolmogorov-Smirnov test and variance homogeneity assessed with the Levene's test. A two-tailed Student's t-test for independent measurements was used for comparisons when data followed a normal Gaussian distribution. If data presented a non-normal distribution, Mann-Whitney U test

was used for comparisons. The significance level for all tests was  $p < 0.05$ .

### Results and Discussion

The expression level of CK2 catalytic subunit alpha (CK2 $\alpha$ ) was about four-fold higher in tumour and more than two-fold higher in contralateral brain parenchyma than in normal brain parenchyma (Fig. 1 and Table 1). On the other hand, no significant changes were detected in the expression of the CK2

**Table 1** Expression values for CK2 $\alpha$  and CK2 $\beta$  and their ratios in mouse brain tumour samples

CK2 $\alpha$		CK2 $\beta$				CK2 $\alpha$ /CK2 $\beta$			
N	$0.32 \pm 0.1^{\text{y}}$	T/N	$3.88 \pm 1.3^{\text{e}}$	N	$1.07 \pm 0.4$	T/N	$1.13 \pm 0.6$	N	$0.30 \pm 0.15^{\text{y}}$
T	$1.24 \pm 0.1^*$	CL/N	$2.51 \pm 0.8^{\text{s}}$	T	$1.21 \pm 0.4$	CL/N	$1.03 \pm 0.5$	T	$1.02 \pm 0.4^*$
CL	$0.8 \pm 0.1^{\text{xy}}$	T/CL	$1.55 \pm 0.2^{\text{es}}$	CL	$1.1 \pm 0.3$	T/CL	$1.09 \pm 0.5^{\text{e}}$	CL	$0.73 \pm 0.2^{\text{xy}}$

Normalized expression values ( $\pm$ SD) and their T/N, CL/N and T/CL ratios ( $\pm$ SD) of the quantification carried out for CK2 $\alpha$  and CK2 $\beta$ ,  $n = 9$ . Abbreviations as in Fig. 1 legend. (\*) significance compared with N, (y) significance compared with T, (e) significance compared with T/N and (S) significance compared with CL/N

regulatory subunit (CK2 $\beta$ ), as shown in Fig. 1, for selected samples, and quantitatively summarized in Table 1. Furthermore, the here named “unbalancedness” ratio CK2 $\alpha$ /CK2 $\beta$ , significantly increased more than three-fold in tumours with respect to normal brain parenchyma.

It has been consistently reported by other authors that high levels of CK2 $\alpha$  are expressed in solid human tumours [8], for example in colorectal carcinomas and breast carcinomas [11]. Our results in preclinical GL261 GBM agree with [11], in the fact that we found higher expression levels of CK2 $\alpha$  in tumour, in comparison with the normal brain parenchyma. In our study, the Tumour/Normal brain parenchyma ratio of CK2 $\alpha$  normalized expression values was of 3.88 (Table 1). For CK2 $\beta$ , a non significant increased expression was detected for the Tumour/Normal brain parenchyma ratio (1.13).

A somewhat unexpected result found in our study was the significantly higher CK2 $\alpha$  expression level detected in the contralateral non-affected brain parenchyma, which has not been described in the literature as far as we are aware. In this respect, Figs. 1A and 1B show a significantly higher CK2 $\alpha$  expression in contralateral tissue in comparison with the normal brain parenchyma, although this expression is clearly lower than the expression found in tumours (Table 1). This could be partially explained due to the well known infiltration pattern of the GBM, invading adjacent non-tumoral tissue and even producing a precancerous stage in apparently uninvolved parenchyma [15]. In this respect, Lama and collaborators [17] also described an increased ERK1/2 expression in GBM peritumoral tissue from patients. Taking into account that ERK1/2 seems to be activated for translocation to the nucleus by CK2 phosphorylation [18] our results on the increased CK2 content in the contralateral/peritumoral area would agree with those reports and reinforce the idea of a “precancerous stage” away from the tumour mass, also for the CK2 content.

Regarding the different CK2 subunits evaluated (CK2 $\alpha$  and CK2 $\beta$ ), our results suggest that an unbalanced expression is taking place in the GL261 GBM (see Figs. 1A, 1B and Table 1), with a predominance of an overexpression of CK2 $\alpha$  in the studied tumours. This imbalance of CK2 subunits was also seen in [18], being produced in this case by a relative decrease in the CK2 $\beta$  regulatory subunit in biopsies of human breast cancer tumours having suffered epithelial-to-mesenchymal transition, a sign of increased aggressivity.

Accordingly, the high expression levels observed for CK2 $\alpha$  in GBM, in comparison with normal brain parenchyma, reinforces the potential of CK2 $\alpha$  as a valid therapeutic target [19, 20] to investigate in GL261 GBM. In this sense, recent studies have reported that promiscuous CK2 inhibitors such as apigenin have shown relevant effects in the growth inhibition of established human GBM cultured cells lines [9]. Additionally, a more specific CK2 inhibitor, CX-4945, has been reported as the first CK2 inhibitor to reach clinical stage

testing for the treatment of multiple types of cancer [13, 20]. Moreover, there are other promising CK2 inhibitors in development, such as tetra-bromo-deoxyribofuranosyl-benzimidazole (TDB) which is a dual inhibitor of CK2 and Proviral Integration of Moloney virus (PIM-1) [12].

Finally, the preclinical GL261 mice GBM model has been widely used for molecular imaging studies and to evaluate TMZ therapy response. Accordingly, the results here described warrant further work with CK2 $\alpha$  inhibition in this GBM model as standalone or combination therapeutic strategies.

## Conclusions

The expression level of the CK2 catalytic subunit (CK2 $\alpha$ ) was found higher in GL261 GBM tumour (about 4-fold) and in contralateral brain parenchyma (more than 2-fold) than in normal brain parenchyma ( $p < 0.05$ ). In contrast, no significant changes were found in the CK2 regulatory subunit (CK2 $\beta$ ) expression, suggesting a predominance of CK2 $\alpha$  overexpression in the evaluated tumours and possibly pointing to a differential role for the two subunit types in GBM tumour development in our investigated model. This should also be taken into account in future studies with preclinical GBM and therapeutic CK2 targeting.

**Acknowledgments** This work was supported by: SAF 2011-23870, SAF2014-52332-R, SGR191-2014 and Centro de Investigación Biomédica en Red – Bioingeniería, Biomateriales y Nanomedicina (CIBER-BBN, [<http://www.ciber-bbn.es/en>]), an initiative of the Instituto de Salud Carlos III (Spain) co-funded by EU FEDER funds.

**Conflict of interest disclosures** The authors have no financial conflicts to disclose.

## References

1. Buckner JC (2003) Factors influencing survival in high-grade gliomas. *Semin Oncol* 30(6 Suppl 19):10–14
2. Stupp R, Mason WP, van den Bent MJ, Weller M, Fisher B, Taphoorn MJ, et al. (2005) Radiotherapy plus concomitant and adjuvant temozolomide for glioblastoma. *N Engl J Med* 10;352(10):987–996.
3. Huang Z, Cheng L, Guryanova OA, Wu Q, Bao S (2010) Cancer stem cells in glioblastoma - molecular signalling and therapeutic targeting. *Protein Cell* 1(7):638–655
4. Ausman JI, Shapiro WR, Rall DP (1970) Studies on the chemotherapy of experimental brain tumors: development of an experimental model. *Cancer Res* 30:2394–2400
5. Szatmári T, Lumniczky K, Désaknai S, Trajcevski S, Hidvégi EJ, Hamada H, et al. (2006) Detailed characterization of the mouse glioma 261 tumor model for experimental glioblastoma therapy. *Cancer Sci* 97(6):546–553
6. Delgado-Goñi T, Julià-Sapè M, Candiota AP, Pumarola M, Artís C (2014) Molecular imaging coupled to pattern recognition

## Protein kinase CK2 in preclinical glioma

- distinguishes response to temozolomide in preclinical glioblastoma. *NMR Biomed* 27(11):1333–1345
7. Ducan JS, Litchfield DW (2008) Too much of a good thing: the role of protein kinase CK2 in tumorigenesis and prospects for therapeutic inhibition of CK2. *Biochim Biophys Acta* 1784:33–47
  8. Ruzzene M, Pinna LA (2010) Addiction to protein kinase CK2: a common denominator of diverse cancer Cells? *Biochim Biophys Acta* 1804(3):499–504
  9. Dixit D, Sharma V, Ghosh S, Mehta VS, Sen E (2012) Inhibition of Casein kinase-2 induces p53-dependent cell cycle arrest and sensitizes glioblastoma cells to tumor necrosis factor (TNF $\alpha$ )-induced apoptosis through SIRT1 inhibition. *Cell Death Dis* 3:e271
  10. Ji H, Lu Z (2013) The role of protein kinase CK2 in glioblastoma development. *Clin Cancer Res* 19:6335–6337
  11. Münstermann U, Fritz G, Seitz G, Yiping L, Schneider HR, Issinger OG (1990) Casein kinase II is elevated in solid human tumours and rapidly proliferating non-neoplastic tissue. *Eur J Biochem* 189:251–257
  12. Cozza G, Girardi C, Ranchio A, Liolli G, Samo S, Orzeszko A, et al. (2014) Cell-permeable dual inhibitors of protein kinases CK2 and PIM-1: structural features and pharmacological potential. *Cell Mol Life Sci* 71:3173–3185
  13. Kim J, Hwan KS (2013) CK2 inhibitor CX-4945 blocks TGF- $\beta$ 1-induced epithelial-to-mesenchymal transition in A549 human lung adenocarcinoma cells. *PLoS One* 8(9):e74342
  14. Simoes RV, Garcia-Martin ML, Cerdan S, Arus C (2008) Perturbation of mouse glioma MRS pattern by induced acute hyperglycemia. *NMR Biomed* 21(3):251–264.
  15. Mangiola A, Saulnier N, De Bonis P, Orteschi D, Sica G, Lama G, et al. (2013) Gene expression profile of glioblastoma peritumoral tissue: an ex vivo study. *PLoS One* 8:e57145.
  16. Bradford MM (1976) A rapid and sensitive method for the quantitation of microgram quantities of protein utilizing the principle of protein-dye binding. *Anal Biochem* 72:248–254
  17. Lama G, Mangiola A, Anile C, Sabatino G, De Bonis P, Lauriola L, et al. (2007) Activated ERK1/2 expression in glioblastoma multiforme and peritumor tissue. *Int J Oncol* 30:1333–1342
  18. Plotnikov A, Chuderland D, Karamanisha Y, Livnah O, Seger R (2011) Nuclear extracellular signal-regulated kinase 1 and 2 translocation is mediated by casein kinase 2 and accelerated by autophosphorylation. *Mol Cell Biol* 31(17):3515–3530
  19. Agarwal M, Nitta RT, Li G (2014) Casein kinase 2: A novel player in glioblastoma therapy and cancer stem cells. *Mol Genet Metab* 8: pii: 1000094.
  20. Zheng Y, McFarland BC, Drygin D, Yu H, Bellis SL, Kim H, et al. (2013) Targeting protein kinase CK2 suppresses pro-survival signaling pathways and growth of glioblastoma. *Clin Cancer Res* 19(23): 6484–6494



### **8.3 ANNEX 3: Article of “*Improving Ribosomal RNA Integrity in Surgically Resected Human Brain Tumor Biopsies*”.**

During this thesis, collaboration with Xavier Castells in RNA analysis was performed. This study focused on biopsies extracted from brain cancer patients. Often, these biopsies display degraded ribosomal RNA, which makes them unusable for transcriptomic experiments. The main objective of this work was to determine RNA integrity in a large cohort of human brain cancer biopsies and also to evaluate different factors that may influence RNA integrity in both a murine model of glioblastoma and in additional subsets of patient biopsies. Total RNA was isolated from 255 biopsies of various human brain tumors and processed on a Bioanalyzer. The time-dependent effect of *ex vivo* ischemia was evaluated in a murine model, whose results were tested in a new collection of 27 human biopsies. Multiple biopsy sampling was considered in a further set of 32 biopsies.

LFF carried out the experimental studies of the multiple biopsy sampling of (32 biopsies), and helped to draft the manuscript.

## Improving Ribosomal RNA Integrity in Surgically Resected Human Brain Tumor Biopsies

Xavier Castells Domingo,<sup>1,2</sup> Laura Ferrer-Font,<sup>3,4,2</sup> Myriam Davila,<sup>3</sup> Ana Paula Candiota,<sup>4,3,2</sup>  
 Rui V. Simões,<sup>3,\*</sup> Alejandro Fernández-Coello,<sup>5,4</sup> Andreu Gabarrós,<sup>5</sup>  
 Susana Boluda,<sup>6</sup> Anna Barcoló,<sup>1</sup> Joaquín Ariño,<sup>1,2</sup> and Carles Arús<sup>3,4,2</sup>

**Background:** Biopsies extracted from brain cancer patients often display degraded ribosomal RNA, which makes them unusable in transcriptomic experiments. This has not been properly documented in previous works aimed at refining the molecular classification of brain cancer.

**Objective:** To determine RNA integrity in a large cohort of human brain cancer biopsies and to evaluate different factors that may influence RNA integrity in both a murine model of glioblastoma and in additional subsets of patient biopsies.

**Methods:** Total RNA was isolated from 255 biopsies of various human brain tumors (HBTs) and processed on a Bioanalyzer. Correct RNA integrity was considered for samples showing either the ribosomal 28S/18S peak ratio  $\geq 1.2$  or RNA integrity number  $\geq 6$ . The time-dependent effect of *ex vivo* ischemia was evaluated in a murine model, whose results were tested in a new collection of 27 human biopsies. Multiple biopsy sampling was considered in a further set comprising 32 biopsies.

**Results:** The 255 human biopsies revealed a substantial percentage of samples displaying degraded RNA (27.5%). The murine model confirmed the known relevance of *ex vivo* ischemia time in increased RNA degradation. Human biopsies extracted immediately after cauterization showed a trend toward less RNA degradation. Combining snap freezing and multiple sampling of biopsies, the percentage of patients with degraded RNA was reduced by twofold (15.6%).

**Conclusions:** We provide a first concise study of factors influencing RNA degradation in HBT biopsies. Immediate biopsy removal after cauterization of the tumor area, snap freezing, and multiple sampling improve RNA quality.

### Introduction

STUDIES BASED ON GENE expression microarrays revolutionized the oncology field by providing in single experiments a broader insight on transcript levels of explored cells or tissues than previous approaches based on investigation of one or few genes.<sup>1-4</sup> The field of neuro-oncology also experienced an impressive outbreak of works that re-

fined the molecular features of histopathological types and proposed new subtypes.<sup>5-8</sup> Nowadays, the state-of-the-art technique for transcriptomic studies is massive RNA sequencing (RNA-seq), which has also contributed to an improved delineation of molecular traits in human brain tumors (HBTs).<sup>9-11</sup>

However, most of those studies did not describe in adequate detail the integrity of RNA obtained from the samples.

<sup>1</sup>Servei de Genòmica i Bioinformàtica, Universitat Autònoma de Barcelona, Cerdanyola del Vallès, Spain.

<sup>2</sup>Institut de Biotecnologia i de Biomedicina & Departament de Bioquímica i Biologia Molecular, Universitat Autònoma de Barcelona, Cerdanyola del Vallès, Spain.

<sup>3</sup>Grup d'Aplicacions Biomèdiques de la RMN (GABRMN). Departament de Bioquímica i Biologia Molecular. Facultat de Biociències, Universitat Autònoma de Barcelona, Cerdanyola del Vallès, Spain.

<sup>4</sup>Centro de Investigación Biomédica en Red en Bioingeniería, Biomateriales y Nanomedicina (CIBER-BBN), Cerdanyola del Vallès, Spain.

<sup>5</sup>Departament de Neurocirurgia, Institut d'Investigació Biomèdica de Bellvitge (IDIBELL). Hospital Universitari de Bellvitge, L'Hospitalet de Llobregat, Spain.

<sup>6</sup>Institut de Neuropatologia, Servei d'Anatomia Patològica, Institut d'Investigació Biomèdica de Bellvitge (IDIBELL), Hospital Universitari de Bellvitge, L'Hospitalet de Llobregat, Spain.

\*Current Address: BCNatal—Barcelona Center for Maternal-Fetal and Neonatal Medicine (Hospital Clínic and Hospital Sant Joan de Deu), Fetal i-D Fetal Medicine Research Center, IDIBAPS, Universitat de Barcelona, Barcelona, Spain.



## IMPROVING RNA INTEGRITY IN BRAIN TUMOR BIOPSIES

157

Usually, it is well stated in published articles that only biopsies with proper RNA integrity are used, but no information about the percentage of biopsies displaying degraded RNA is reported. While this issue has been commonly omitted, it is a crucial point to be addressed for any molecular tool to be implemented in clinical settings.

Commonly, parameters used to estimate the RNA quality are obtained using microcapillary-based electrophoretic systems, such as the Bioanalyzer and the Experion.<sup>12,13</sup> In short, there are two main parameters measured in this assay, the ratio of ribosomal RNAs 28S and 18S peak area (28S/18S ratio) and the RNA integrity number (RIN). RIN is a parameter proposed by Agilent that considers the entire electrophoretic profile for its estimation.<sup>14</sup> On the contrary, the 28S/18S ratio is limited to the area under the peaks. It is stipulated that RNA samples display proper integrity when the 28S/18S ratio value is within the range of 1.2–1.5 or the RIN value is  $\geq 5$ .<sup>13–15</sup>

Previous studies have reported the proportion of fresh-frozen biopsies displaying degraded RNA. For instance, Mücke et al. showed a high percentage (96%) of samples with good integrity RNA in a set of 47 samples comprising several cancer types and normal tissue.<sup>19</sup> In another study comprising 37 fresh-frozen biopsies from prostate cancer, almost all samples (97%) displayed a RIN value above seven.<sup>20</sup> In contrast, Strand et al. observed a rate of biopsies with degraded RNA that ranged between 25% and 37.5%, depending on the criterion used, in a set of 24 invasive breast cancer samples.<sup>18</sup> However, to our knowledge, there is no study addressing this topic in HBTs.

Some research teams have studied the factors leading to RNA degradation in biopsies. The elapsed time between surgical resection and freezing in liquid nitrogen is one of the main causes.<sup>19,21</sup> The physiological explanation for this effect is the induced *ex vivo* ischemia period during surgical resection. Hatzis et al. determined in 17 invasive breast cancers that 40 minutes of *ex vivo* ischemia time increased the RNA degradation in terms of ribosomal species, but it also affected the transcript level of some genes.<sup>22</sup> In a study performed on 100 renal cell carcinoma samples, decreased RNA integrity was seen after 1 hour of *ex vivo* ischemia time.<sup>21</sup> Nevertheless, Bao et al. did not observe an effect of ischemia time in a set of 51 colorectal fresh-frozen biopsies collected at different time periods.<sup>23</sup>

Again, we have been unable to find previous studies focusing on factors affecting RNA degradation in biopsies of human brain cancers. For that reason, we aimed at evaluating the RNA degradation in a large set of 255 biopsies, and posteriorly, we assessed the effect of *ex vivo* ischemia time in a murine model and two subsets of human biopsies. Our results show that best RNA integrity results for brain tumor biopsies can be achieved by snap freezing after tumor cauterization and that multiple sampling is recommended due to tumor heterogeneity.

## Methods

### Collection of samples

**Specific grant-associated biopsies.** A total of 255 brain tumor biopsy samples were accrued during the eTUMOUR, HealthAgents, and MEDIVO2 projects between March 2004 and March 2009, accounting for several types and subtypes.

These samples were collected for the most part not only at Hospital Universitari de Bellvitge IDI-BELL ( $n=184$ ) but also at hospitals associated with Centre Diagnòstic Pedralbes-Institut d'Altes Tecnologies ( $n=59$ ), Hospital Universitari Germans Trias i Pujol IDI-Badalona ( $n=7$ ), and Hospital Sant Joan de Déu ( $n=5$ ). All samples were collected in liquid nitrogen after surgical resection, except 33 biopsies that were also collected in RNAlater (Ambion; Thermo Fisher Scientific Inc.). In the latter case, the resected biopsy aliquot was immediately transferred to a 1.5-mL tube filled with RNAlater.

**Biopsies before and after tumor resection.** A set comprising 54 biopsies was collected before and after tumor resection. Specifically, the biopsy was resected from 27 patients immediately after delimiting the tumor area by cauterization to avoid an increased ischemia time. Then, a second specimen from each patient was drawn from the resected tumor mass to test the potential role of the surgery-related ischemia time in RNA degradation. This time was normally between 15 and 30 minutes. These biopsies were collected during the time period between January and May 2012 at the Hospital Universitari de Bellvitge IDI-BELL. Tumor types represented were glioblastoma ( $n=8$ ), metastasis ( $n=6$ ), meningothelial meningioma ( $n=3$ ), unreported diagnosis ( $n=3$ ), one anaplastic astrocytoma, one atypical meningioma, one fibrous meningioma, one transitional meningioma, one neuroblastoma of the adrenal gland and the sympathetic nervous system, one oligoastrocytoma, and one pleomorphic xanthoastrocytoma.

**Triplicate biopsies per patient.** The last set comprised 32 patients. Biopsies were collected between June 2012 and February 2015 at the Hospital Universitari de Bellvitge IDI-BELL. Surgeons extracted three biopsies from each patient immediately after cauterization (see supplementary methods for the description of the procedure). Biopsies accounted for tumor types as follows: glioblastoma ( $n=13$ ), anaplastic oligoastrocytoma ( $n=7$ ), anaplastic astrocytoma ( $n=2$ ), grade II astrocytoma ( $n=2$ ), metastasis of melanoma ( $n=2$ ), and one patient for gliosarcoma, metastasis of lung adenocarcinoma, breast adenocarcinoma, breast carcinoma, anaplastic oligodendroglioma, and grade II oligoastrocytoma. The protocol agreed to with the surgeons is available as Supplementary Data.

### Storage and histopathological analysis of samples

All biopsies were placed in cryotubes and immediately snap-frozen in liquid nitrogen after surgical removal, unless otherwise indicated. Tumor samples not used for RNA extraction were fixed in 4% buffered formalin and embedded in paraffin. For routine histological examination, 4- $\mu$ m-thick sections were stained with hematoxylin and eosin (HE). Given that samples were collected from 2004 to 2015, the WHO 2000 and 2007 Nervous System Classification criteria were used for diagnosis.<sup>24,25</sup>

The local Ethics Committee approved the collection of the biopsies described above and informed consent was obtained from all patients.

### RNA isolation

Total RNA was isolated using the mirVana miRNA Isolation Kit (Ambion; Thermo Fisher Scientific Inc.), following the manufacturer's instructions. Approximately 50 mg of frozen material was split from the entire biopsy using a mortar, which

was previously chilled in liquid nitrogen. For small biopsies, all of the available material was used. RNA yield per biopsy is described in Supplementary Tables (Supplementary Data are available online at [www.liebertpub.com/bio](http://www.liebertpub.com/bio)).

Isolated RNA was characterized using a NanoDrop spectrophotometer (NanoDrop Technologies). The absence of protein contamination was monitored by the 260/280 nm ratio of absorbance. RNA samples with a ratio ranging between 1.6 and 2.3 were accepted for further processing, as specified in the eTUMOUR project.<sup>26</sup>

RNA integrity was assessed using the capillary electrophoretic system 2100 Bioanalyzer (Agilent). Only RNA samples producing a 28S/18S ratio equal or higher than 1.2 or a RIN number equal or higher than 6 were selected, as specified in the eTUMOUR project.<sup>26</sup> Measured values of 28S/18S ratio and RIN are available in Supplementary Tables S1–S3. Currently, additional approaches to assess RNA integrity apart from the abovementioned ones based on ribosomal species can be tested, such as the ones based on quantitative polymerase chain reaction (qPCR). However, 28S/18S ratio and RIN were the only measurements agreed to in those projects providing the most biopsies for this study. Thus, the use of extensive qPCR assays for RNA integrity is unfortunately beyond the scope of this work.

#### qPCR of the gene *LGALS1* on a subset of samples

Although the entire study was designed to assess the integrity of RNA through the measurement of ribosomal RNAs, an additional evaluation was performed by qPCR of the *LGALS1* gene. Duplicate biopsies from the set of patients with pre- and postcauterization specimens were assessed. They represented two pairs of samples with correct RNA integrity of the precauterization biopsy, one pair with correct integrity of the postsurgery biopsy and one pair displaying degraded RNA in both biopsies. qPCR experiments were performed using triplicate measurements per RNA sample as previously described.<sup>27</sup>

#### Generation of a murine model to simulate *ex vivo* normal body temperature ischemia in brain tumor samples

**Animals and cells.** A total of 29 C57BL/6 female mice, with a weight range of 20–23 g, were used in this study. Animals were obtained from Charles River Laboratories (France) and housed at the animal facility of the Universitat Autònoma de Barcelona (UAB). All animal studies were approved by the local ethics committee according to regional and state legislations (protocol DARP-3255/CEEAH-530). GL261 mouse glioma cells were obtained and cultured exactly as described by Simões et al.<sup>28</sup>

**Inoculation of the mouse brain with GL261 tumor glial cells.** Tumors were induced in 29 mice by intracranial stereotactic injection of  $10^5$  GL261 cells in the caudate nucleus, as previously described.<sup>28,29</sup> About 15 minutes after being given a dose of analgesia (Meloxicam subcutaneous, s.c., 1.0 mg/kg), animals were anesthetized (Ketamine-Xylazine, 80–10 mg/kg intraperitoneal, i.p.) and then immobilized in a stereotactic holder (Kopf Instruments). The skull was exposed and a high-speed microdriller (Fine Science Tools) was used to make a small hole in its surface (1 mm): 2.3 mm to the right of the midline, as measured from the *Bregma*. A 26G Hamilton syringe (Hamilton), positioned on a digital

push-pull microinjector (KD Scientific), was advanced through this hole, 2.3 mm from the cortical surface into the *striatum*, to deliver  $10^5$  GL261 cells (in 4  $\mu$ L RPMI medium) at a rate of 2  $\mu$ L/min. The syringe was slowly removed 3–5 minutes after the injection was finished and the scission site closed with suture silk (5.0). Animals were left to recover from anesthesia in a warm environment ( $\sim 25^\circ\text{C}$ ) and, as they began to wake up, a stronger analgesic (opioid) was given: Buprenorphine s.c., 0.1 mg/kg. Meloxicam analgesia was repeatedly administrated at 24 and 48 hours/postsurgery.

**Animal sacrifice and encephalon removal.** Animals were sacrificed by an intraperitoneal injection of sodium pentobarbital (60 mg/mL) at a dose of 200 mg/kg and posterior cervical dislocation. Once the animal became unresponsive to mechanical foot stimulation, posterior cervical dislocation was performed and the head sectioned from the rest of the body with sterile scissors. The upper part of the skull was then removed by an incision at each occipital condyle, which was followed by a dissection in the anterior direction up to the nasal cavity. The encephalon was removed by lifting it up with sterile dissection tweezers.

**Dissection of the tumor mass.** The hemisphere inoculated with tumor cells, together with a thin surrounding layer of the parental hemisphere, was separated from the rest of the brain by using a sterile scalpel and dissection tweezers. The cerebral parenchyma was progressively removed to keep only the tumor mass, characterized by its more mucous appearance with respect to normal brain. In the case of necrotic specimens, the tumor mass was clearly identifiable due to its dark color. In contrast, the identification of non-necrotic tumor masses was more difficult since their color was very similar to the nontumor parenchyma. However, it displayed a more mucous appearance compared with the normal brain parenchyma.

The whole procedure described in this section was performed at room temperature. The time elapsed from animal death until tumor removal ranged between 5 and 7 minutes.

**Simulation of *ex vivo* normal body temperature ischemia.** Simulation of *ex vivo* warm ischemia was performed in 4 mice displaying evident necrotic tumor masses and in 14 mice showing little necrosis or non-necrotic tumors. Immediately after tumor mass resection, an aliquot ( $<1\text{ mm}^3$ ) was submerged into formahn for posterior histological verification. Such validation was performed using standard protocols (paraffin-embedded and HE-stained tissue slides).

To simulate body temperature, tumor masses were introduced into separate 1.8-mL cryotubes prefilled with phosphate-buffered saline (PBS) at  $37^\circ\text{C}$ . Samples were incubated at  $37^\circ\text{C}$  for 30 minutes and snap-frozen in liquid nitrogen after this period. Furthermore, 7 of the 14 non-necrotic mice tumors were incubated for 15 minutes instead of 30 minutes. Remaining tumor specimens were not subjected to body temperature incubation and were snap-frozen in liquid nitrogen immediately after dissection.

#### Statistical analysis

The difference of means was assessed through a *t*-test using the *t.test* function available in R for the large dataset comprising 255 biopsies. For remaining samples, this assessment was performed using the Wilcoxon test using the R software with available *wilcox.test* function<sup>30</sup> due to the lack of normal distribution of their values.

## IMPROVING RNA INTEGRITY IN BRAIN TUMOR BIOPSIES

159

The difference of proportions between two groups was assessed using the *prop.test* function in R, which performs Pearson's chi-squared test. For the set of triple biopsies, a logistic regression model using the binomial distribution as a link function was fitted to evaluate the dependency of tumor types and surgeons on the RNA integrity (degraded or nondegraded RNA).

A linear model was fitted to either 28S/18S ratios or RIN values to determine the involvement of tumor type in RNA integrity. For this purpose, the *lm* available in the *stats* R package was used. In the same package, the function, *cor*, was used to compute the correlation between micrograms of isolated RNA and the two parameters mentioned above.

## Results

### High percentage of collected brain biopsies displayed elevated RNA degradation

The first step of the study consisted of assessing whether the collection medium for biopsies played a role in the deg-

radation of RNA. For that purpose, we collected a set of 33 biopsies in two aliquots, one in liquid nitrogen (the method usually performed by our team) and the second one in RNAlater. As it can be seen in Figure 1A, B, no difference in RNA integrity was detected between collecting biopsies in RNAlater compared with snap-frozen in liquid nitrogen. These results indicated that the collection medium was not responsible for RNA degradation, and we chose liquid nitrogen as the collection medium in the remainder of this study.

The total number of biopsies collected within the eTUMOUR project by the UAB partner was 255. Of these, 27.5% (70) showed a 28S/18S ribosomal peak ratio or RIN that did not meet the standards of RNA integrity agreed to in the eTUMOUR project (Fig. 1C). This percentage of biopsy samples, which were not suitable for microarray hybridization, was detected since the beginning of the project and it was independent of the tumor type (Fig. 1D, E). This is also supported by the absence of statistical difference based on the chi-squared test observed in the pairwise comparison of matching tumor types between RNA samples from biopsies accepted and nonaccepted (RNA quality

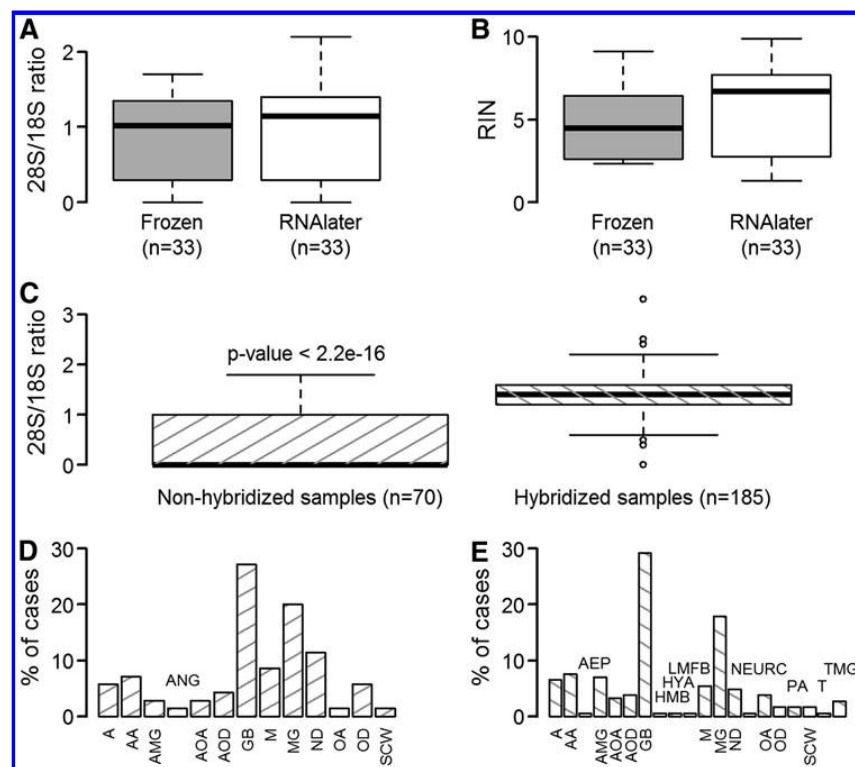


**FIG. 1.** Characterization of RNA integrity in human brain tumor samples. (A) Comparison of 28S/18S ratio for 33 biopsies simultaneously collected in liquid nitrogen and RNAlater at the surgery room is depicted in this boxplot. As indicated in the text, no significant difference was detected. (B) The same as (A), but using the RIN as measure of RNA integrity. (C) This figure shows the average 28S/18S ratio values for those biopsies hybridized and nonhybridized in Affymetrix microchips. Statistical difference between means was also computed using a two-sided *t*-test. (D) The percentage of samples per tumor type was plotted for nonhybridized biopsies. (E) The same as (D), but using those hybridized biopsies. A, low-grade astrocytoma; AA, anaplastic astrocytoma; AEP, anaplastic ependymoma; AMG, atypical meningioma; ANG, angioma; AOA, anaplastic oligoastrocytoma; AOD, anaplastic oligodendroglioma; GB, glioblastoma; HMB, hemangioblastoma; HYA, hypophysitis adenoma; LMFB, B lymphoma; M, metastasis; MG, meningioma; ND, no diagnosis; NEURC, neurocytoma; OA, low-grade oligoastrocytoma; OD, low-grade oligodendroglioma; PA, pilocytic astrocytoma; SCW, schwannoma; T, teratoma; TMG, transitional meningioma; RIN, RNA integrity number.

TABLE 1. RNA DEGRADATION BY TUMOR TYPE

	28S/18S			RIN			Isolated RNA ( $\mu\text{g}$ )	
	Mean	SD	p	Mean	SD	p	Mean	SD
Anaplastic astrocytoma (27)	1.23	0.61	Ref.	7.2	2.0	Ref.	33.2	25.5
Anaplastic oligoastrocytoma (29)	1.32	0.42	0.56	7.2	1.5	0.90	30.0	32.4
Anaplastic oligodendroglioma (13)	1.15	0.62	0.71	6.9	2.4	0.80	59.0	45.8
Atypical meningioma (17)	1.14	0.52	0.62	6.6	2.5	0.53	97.5	74.4
Glioblastoma (128)	1.02	0.60	0.09	6.2	2.5	0.08	46.9	40.2
Grade II astrocytoma (6)	1.47	0.35	0.36	7.3	0.5	0.89	16.1	16.3
Grade II oligoastrocytoma (3)	1.30	0.26	0.84	7.5	1.1	0.83	25.2	16.7
Low-grade oligoastrocytoma (8)	1.33	0.58	0.67	6.9	2.0	0.82	24.5	12.6
Low-grade astrocytoma (16)	1.33	0.47	0.59	6.1	2.2	0.25	35.0	29.0
Low-grade oligodendroglioma (7)	0.70	0.70	0.03	5.6	2.6	0.28	30.3	26.2
Meningioma (47)	1.03	0.68	0.16	5.8	2.7	0.04	49.4	32.4
Metastasis (28)	1.03	0.59	0.16	5.7	2.6	0.02	80.7	57.7
Piloicytic astrocytoma (3)	1.07	0.31	0.65	7.6	1.8	0.78	26.2	34.1
Transitional meningioma (7)	1.29	0.37	0.81	6.8	2.6	0.75	70.4	49.6

The mean and standard deviation (SD) of 28S/18S ratio, RIN, and total isolated RNA are provided per those tumor types represented at least by three biopsies. The *p*-value provides the probability that the mean of each tumor type differs from the reference group (Ref., anaplastic astrocytoma). The number of biopsies per tumor type is indicated within brackets. As duplicate and triplicate biopsies per patient (Supplementary Tables S2 and S3) were used to build the table, multiple biopsies may correspond to one single patient.

RIN, RNA integrity number.

noncompliant) for hybridization. In this respect, the average values of the 28S/18S ratio and RIN per tumor type also support the lack of correlation among specific tumor types and RNA degradation status (Table 1). Only low-grade oligodendroglioma, meningioma, and metastasis displayed a significantly lower value of 28S/18S ratio or RIN. Furthermore, the absence of correlation between these two parameters with micrograms of RNA isolated was observed ( $\text{Cor}_{28\text{S}/18\text{S}-\mu\text{g}}=0.10$  and  $\text{Cor}_{\text{RIN}-\mu\text{g}}=0.14$ ).

Therefore, we hypothesized that the time elapsed from tumor resection until snap freezing of biopsies could be critical. Thus, we generated a murine model of glioblastoma to evaluate the effect of *ex vivo* ischemia at normal body temperature in RNA from brain tumors.

#### *Ex vivo normal body temperature ischemia in a murine model increases RNA degradation in non-necrotic samples*

Incubation for 30 minutes in PBS at 37°C did not produce differences in RNA degradation for necrotic tumors compared with necrotic tumors snap-frozen in liquid nitrogen (Fig. 2A, B). In contrast, non-necrotic tumors showed a statistically significant decrease of the 28S/18S ratio for cases incubated for both 15 and 30 minutes in PBS at 37°C (Fig. 2C, D).

From our results, RNA degradation as measured from the 28S/18S ratio and RIN occurs for non-necrotic tumor specimens when simulating an *ex vivo* normal body temperature ischemia period. This phenomenon is not observed in necrotic tumors. Translating these findings into the routine clinical practice, the 25%–30% of human biopsies showing RNA degradation, and unsuitable for microarray hybridization, could be explained by an increased *ex vivo* ischemia time.

#### *Fast resection of biopsies improves RNA integrity*

Standard surgical practice during HBT removal requires surgeons halting blood flow to the tumor by cauterization

when delimiting the tumor mass. This results in variable ischemia time at body temperature before biopsy removal (between 15 and 30 minutes).

We evaluated, in a new set of human biopsies, the RNA integrity of 27 samples before and after tumor resection (the procedure undertaken for the 255 biopsies described above). The percentage of biopsies displaying acceptable RNA integrity was similar in those ones taken before and after tumor resection (59.3% [16/27] and 55.6% [15/27], respectively). However, looking at the 28S/18S ratio and RIN values in more detail, the average values were always higher, although not significantly, in samples immediately resected after cauterization than in the ones sampled at the end of the surgery, both in terms of 28S/18S (pre =  $1.02 \pm 0.48$ , post =  $0.88 \pm 0.49$ ,  $p=0.335$ ) and RIN values (pre =  $6.09 \pm 2.21$ , post =  $5.84 \pm 2.70$ ,  $p=0.843$ ).

Furthermore, we tested whether the detectable gene expression level of *LGALS1* was related to the integrity of ribosomal RNA, according to the predefined quality thresholds. For that, four pairs of biopsies extracted before and after cauterization in four different patients were evaluated (Supplementary Table S4). The expression level of *LGALS1* in those biopsies displaying correct ribosomal RNA integrity (double-02-pre, double-08-pre, and double-24-post) was at least three times higher than in the other pair (double-02-post, double-08-post, and double-24-pre). That is, a fold change<sup>pre/post</sup>  $\geq 3$  was noticed for biopsies of patients, double-02 and -08, while a fold change<sup>pre/post</sup>  $\leq 1/3$  was seen for patient double-24. The patient with degraded rRNA in both biopsies (double-19) showed twice the expression level in the postcauterization biopsy. Nevertheless, the Ct value obtained from those two biopsies was very similar to the other biopsies displaying degraded ribosomal RNA (double-02-post, double-08-post, and double-24-pre) with values close to or above 25, while Ct values from samples with correct RNA integrity (Ct<sup>double-02</sup> = 22.1, Ct<sup>double-08</sup> = 20.6, and Ct<sup>double-24</sup> = 22.2) were similar to the value observed in a previous work,<sup>27</sup> in which the average Ct value was  $21.9 \pm 1.2$ .

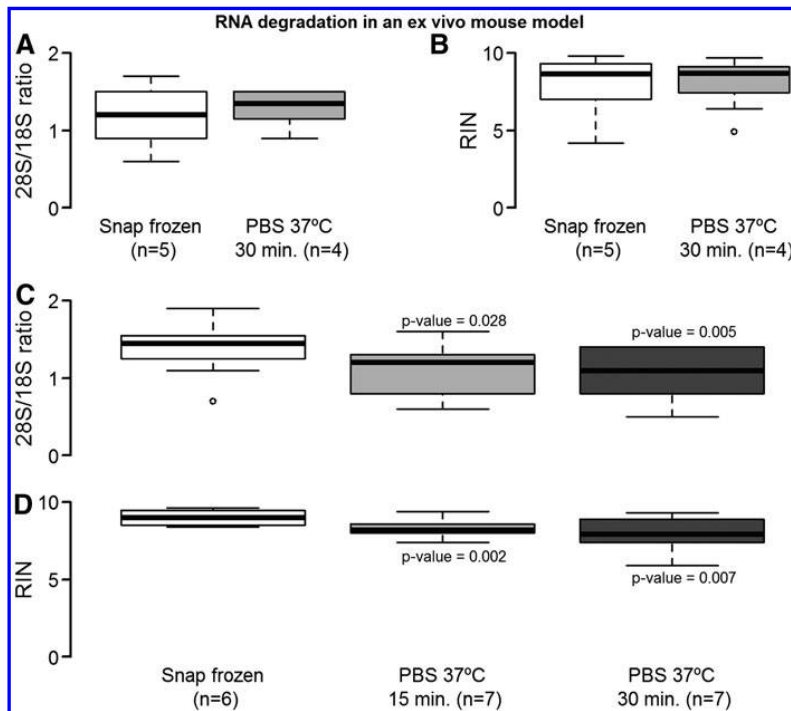


**FIG. 2.** *Ex vivo* simulation of ischemia at normal body temperature in a murine model of glioblastoma. Effect of normal body temperature ischemia on RNA degradation for both necrotic and non-necrotic mice tumors is shown. (A, B) Box plots of both 28S/18S ratio and RIN number, respectively, for necrotic tumors are shown. (C, D) Average 28S/18S ratio and RIN values for non-necrotic tumors at three time points (snap-frozen, 15 and 30 minutes) are shown. Difference between the 28S/18S ratio or RIN value of snap-frozen samples and those ones incubated for 15 or 30 minutes at 37°C was assessed using a Wilcoxon test.

These results suggest the possible advantage of taking the biopsy as the first step after cauterization of the tumor mass so that the likely effects of ischemia during the operation are avoided and maximal RNA integrity is preserved. Moreover, these data also reveal the improvement in the approach of surgeons in limiting the number of biopsies with degraded RNA. That is, if we consider the 27 biopsies collected in this subset, only 22.2% (6 of 27) had degraded RNA, which improves the rate obtained in the set of 255 biopsies mentioned above (27.5%).

#### *Multiple sampling per patient increases the percentage of biopsies with acceptable RNA integrity*

Given that the integrity of the RNA of the tissue does not vary significantly with the moment it is obtained during the surgical procedure, we hypothesized that other factors may be contributing to the RNA integrity of biopsies. The intratumor heterogeneity of cancer tissue is well known in general and particularly in brain tumors such as gliomas.<sup>31</sup> We tested whether, by sampling several biopsies per patient, the chance of having at least one biopsy with proper RNA integrity increased.

To evaluate that hypothesis, surgeons resected three biopsies per tumor mass in 32 patients. Biopsies were resected immediately after tumor cauterization to maintain possible beneficial effects in RNA quality, as demonstrated in the previous section. As shown in Table 2, half of the patients harbored nondegraded RNA and just five (15.6%) had all three biopsies displaying degraded RNA. Although this percentage is lower than the one observed in the two previous sets, there are still a non-negligible number of samples not fulfilling the standards of RNA integrity.

Although we had already observed that the tumor type is not related with RNA integrity, we fitted a logistic regression model using the binomial distribution as a function link and the tumor type as predictor variable. No tumor type had a significantly higher chance of having three degraded biopsies per patient compared with grade II astrocytoma, which was set as the reference tumor according to alphabetical order. Actually, all *p*-values were close to one (data not shown). A similar result was obtained when assessing the involvement of surgeons who had extracted the biopsies.

Considering that biopsies were sequentially extracted, we computed the percentage of patients with at least one biopsy having nondegraded RNA observed in the order of extraction. Looking at the first biopsy removed from each patient, seven patients (21.9%) had biopsies displaying degraded RNA, which is a similar percentage to the one obtained in the previous section. By extracting two biopsies, the number of patients with degraded RNA dropped to five (15.6%), which is the same figure as the one obtained after the extraction of the third biopsy.

**TABLE 2.** RNA DEGRADATION IN TRIPLE BIOPSY SAMPLING PER PATIENT

<i>No. of biopsies deg. RNA/patient</i>	<i>No. of patients</i>	<i>Patients (%)</i>
0	16	50.0
1	5	15.6
2	6	18.8
3	5	15.6

This table shows the number (number of patients) and percentage (% of patients) with none, one, two, or three biopsies with degraded RNA (number of biopsies deg. RNA/patient).

## Discussion

RNA integrity is a main issue in oncology when isolating RNA from a biopsy for subsequent molecular analyses. Acceptable RNA integrity has been mandatory to conduct reliable and reproducible gene expression microarray experiments during the past decade.<sup>14,16,17</sup> Nowadays, this requirement still prevails for RNA-seq experiments.<sup>32,33</sup> Therefore, any study aiming to establish a biomarker based on transcriptomics relies on the integrity of RNA for the proposal to be trustworthy.

In a large dataset of brain tumor biopsies, we observed a high percentage, almost 30%, of biopsies displaying RNA degradation. This was a fatidic concern given that the aim of this type of project was to identify biomarkers for different types and subtypes of brain tumors. That is, any diagnostic or prognostic assay with such a high rate of failure would not be implementable in standard clinical settings.

For that reason, we investigated the best approach for biopsy collection in the surgery room so that we could maximize the number of specimens with proper RNA integrity and thus render them usable for diagnosis and prognosis. The first question that we addressed was the involvement of *ex vivo* normal body temperature in the stability of RNA. The rationale was to reproduce the likely ischemic conditions that happen during surgery between the cauterization of the tumor tissue and the removal of the biopsy. For this purpose, we evaluated in a murine model of glioblastoma whether incubating the extracted biopsy in PBS medium at 37°C for 15 or 30 minutes increased the RNA degradation compared with snap-frozen biopsies after resection. Indeed, there was a decrease in RNA integrity with increased incubation time. However, that effect was only seen in non-necrotic tumors (Fig. 2). Lack of such an effect in necrotic tumors may be explained by the activation of hypoxia-related metabolism, which is well established as a process that is led by the expression of hypoxia-inducible factor 1 (*HIF1*).<sup>34–36</sup> *HIF1* is a transcription factor for several genes, whose expression counterbalances the effects of lack of oxygen supply. The *HIF1*-induced pathway in necrotic tumors could be already activated before surgical biopsy resection. Thus, cells of these tumors would be protected against acute damage, such as massive ribosomal RNA degradation, compared with non-necrotic specimens. This is the most plausible hypothesis that we can postulate, although its demonstration is beyond the goals of this study. Although the murine model is not totally comparable with humans, this experiment highlighted the relevance of extracting a biopsy immediately after cauterization of the tumor mass.

The promising results with the murine model led us to evaluate that effect in humans. In a set of 27 patients, we compared the RNA integrity of a first biopsy extracted immediately after cauterization and a second one taken after the complete resection of the tumor. As a result, the integrity of biopsies extracted without elapsed ischemic time was not statistically different from those resected later on. Nevertheless, 28S/18S and RIN average values were consistently higher in those specimens initially removed, and the percentage of biopsies with proper RNA integrity decreased compared with the initial set of 255 biopsies (22.2% vs. 27.5%). In addition, the expression level of *LGALS1* was more than 10 times higher in two precauterization biopsies than in

their postcauterization counterparts (fold change<sup>pre/post-double-02</sup>=11.7 and fold change<sup>pre/post-double-08</sup>=50.4). Regardless, one of the postcauterization biopsies showed higher integrity of ribosomal RNA than the precauterization one (fold change<sup>pre/post-double-24</sup>=0.3), which may be related to the known heterogeneity of HBTs.<sup>31</sup> The qPCR experiments performed confirmed that degraded ribosomal RNA implies degraded messenger RNA.

In light of these results, we speculated about additional factors potentially involved in RNA integrity. Provided that brain tumors, and specially gliomas and glioblastoma, are very heterogeneous, we hypothesized that apart from an immediate extraction of the biopsy, several specimens per patient should be taken to ensure at least one biopsy with nondegraded RNA. Interestingly, the percentage of patients displaying degraded RNA in all biopsies dropped to 15.6% (5 of 32) compared with the set of biopsies extracted after cauterization and resection (22.2%, 6 of 27). Nonetheless, the rate of unusable biopsies for molecular analyses remained prominent.

Although the type of tumor was not statistically associated with RNA integrity, all patients with three degraded biopsies suffered from high-grade tumors (three glioblastomas, one gliosarcoma, and one metastasis of breast adenocarcinoma). The lack of significance is likely to be related to the small sample size, and it cannot be ruled out that tumor type may also play a role in RNA integrity. However, high-grade brain tumors are the most commonly observed and there was also absence of significance in the set of 255 biopsies of this study. At any rate, data from our study confirm that this is an issue deserving further attention. For instance, the average 28S/18S and RIN values in one of the least aggressive tumors, meningiomas, were similar or even lower than the ones in glioblastomas, the most aggressive HBT (Table 1).

It is well known that gliomas shift their metabolism toward an increased glycolytic activity<sup>37,38</sup> and are often exposed to fluctuating hypoxic conditions.<sup>39</sup> This may imply a metabolic reorganization of tumor cells with consequences on ribosomal RNA turnover and integrity. In this respect, a fast increase in cytoplasmic turnover of ribosomes in yeast has been demonstrated upon mTOR inhibition conditions mimicking starvation.<sup>40</sup> A similar situation may be encountered under fluctuating hypoxia conditions in tumor cells.

Therefore, it appears plausible that in addition to factors identified in this study (speed of extracting the biopsy and multiple sampling), the metabolic stage of a tumor specimen, which is often undetermined before surgery, could be a relevant feature for RNA integrity.

To the best of our knowledge, this is the first work investigating in detail the causes of the high percentage of brain tumor biopsies displaying degraded RNA. Subsequent to obtaining a percentage close to 30% of degradation in the 255 human biopsy dataset, we have shown in a murine model of glioblastoma that an *ex vivo* ischemia time of 15 minutes increases the RNA degradation. Further collection and analysis of human biopsies have shown that (1) biopsies should be snap-frozen early after cauterization to restrict RNA degradation and that (2) multiple sampling is recommended to increase the chances of obtaining at least one biopsy with proper RNA integrity per patient.

The lowest rate of RNA degradation achieved in this work was 15.6%, which still remains too elevated whenever

## IMPROVING RNA INTEGRITY IN BRAIN TUMOR BIOPSIES

163

the final purpose is to use samples for routine diagnosis. Further studies should focus on linking the metabolic stage of tumors and the integrity of their RNA. In this respect, the fluorescence-guided multiple sampling scheme for tissue collection described by Sottoriva et al.<sup>31</sup> could provide a relevant avenue for further investigation.

## Acknowledgments

The authors thank Dr. Juan José Acebes, former head of the Neurosurgery Ward at Hospital Universitari de Bellvitge, for guidance and support during the initial phase of this study. Participation in biopsy and clinical data accrual by Dr. Angel Moreno and Dr. Jesús Pujol (Centre Diagnòstic Pedralbes-Institut d'Altes Tecnologies), Dr. Jaume Capellades (Hospital Universitari Germans Trias i Pujol IDI-Badalona), and Dr. Antoni Capdevila (Hospital Sant Joan de Déu) is also acknowledged. This work was funded by the EU-funded grant eTUMOUR (FP6-2002-LIFESCIHEALTH 503094) and the Spanish grants, MARESCAN (SAF2011-23870) and MOLIMAGLIO (SAF2014-52332-R), from MINECO. Additional funding was received from CIBER-BBN (Centro de Investigación Biomédica en Red—Bioingeniería, Biomateriales y Nanomedicina [www.ciber-bbn.es/en]), an initiative of the Instituto de Salud Carlos III (Spain) cofunded by EU FEDER funds.

## Author Disclosure Statement

No conflicting financial interests exist.

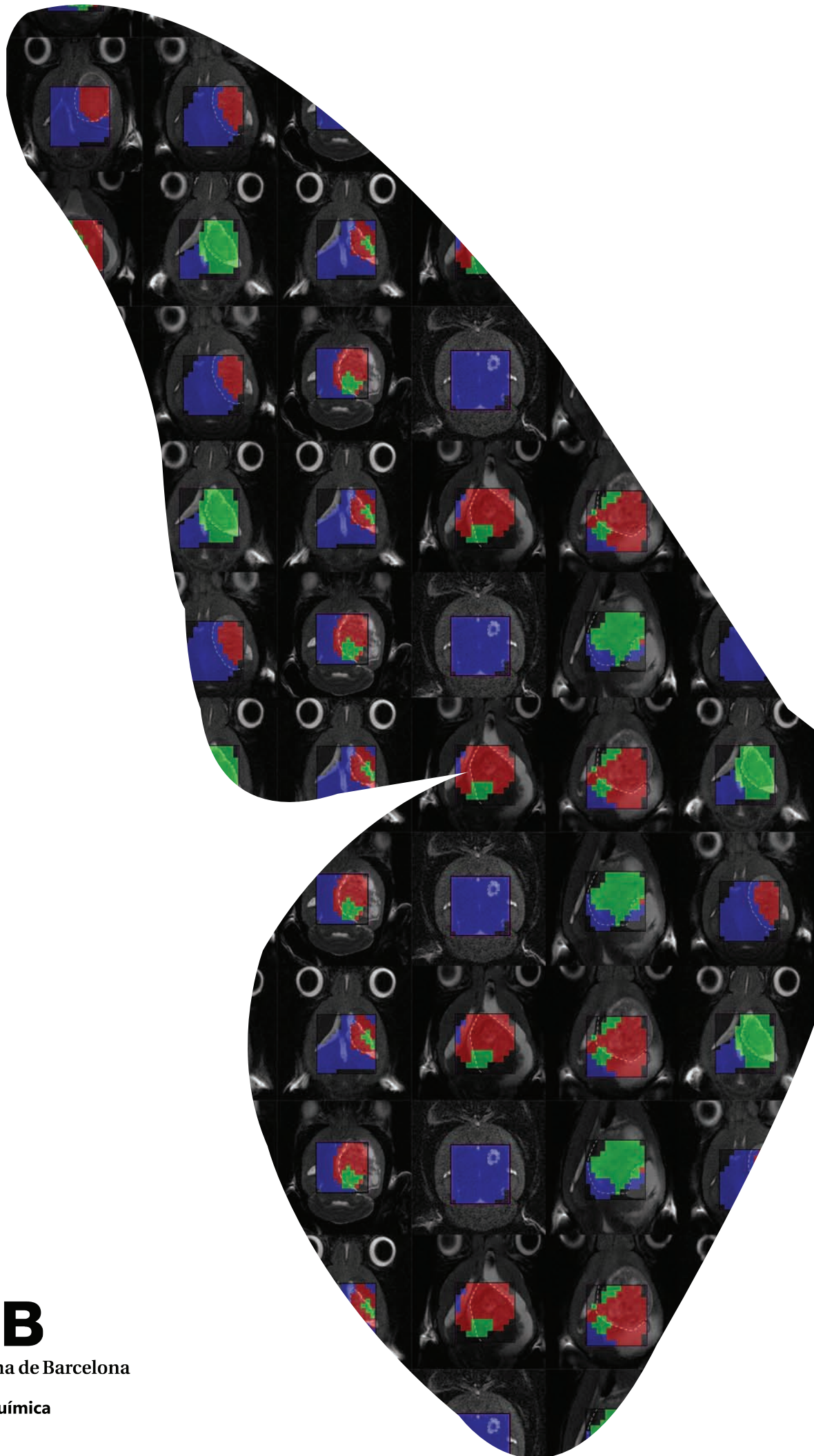
## References

- Chari R, Thu KL, Wilson IM, et al. Integrating the multiple dimensions of genomic and epigenomic landscapes of cancer. *Cancer Metastasis Rev* 2010;29:73–93.
- Nannini M, Pantaleo MA, Maleddu A, Astolfi A, Formica S, Biasco G. Gene expression profiling in colorectal cancer using microarray technologies: Results and perspectives. *Cancer Treat Rev* 2009;35:201–209.
- Weigelt B, Baehner FL, Reis-Filho JS. The contribution of gene expression profiling to breast cancer classification, prognostication and prediction: A retrospective of the last decade. *J Pathol* 2010;220:263–280.
- Yu Y, He J. Molecular classification of non-small-cell lung cancer: Diagnosis, individualized treatment, and prognosis. *Front Med* 2013;7:157–171.
- Gravendeel LAM, Kouwenhoven MCM, Gevaert O, et al. Intrinsic gene expression profiles of gliomas are a better predictor of survival than histology. *Cancer Res* 2009;69:9065–9072.
- Li A, Walling J, Ahn S, et al. Unsupervised analysis of transcriptomic profiles reveals six glioma subtypes. *Cancer Res* 2009;69:2091–2099.
- Parsons DW, Jones S, Zhang X, et al. An integrated genomic analysis of human glioblastoma multiforme. *Science* 2008;321:1807–1812.
- Phillips HS, Kharbanda S, Chen R, et al. Molecular subclasses of high-grade glioma predict prognosis, delineate a pattern of disease progression, and resemble stages in neurogenesis. *Cancer Cell* 2006;9:157–173.
- Bao Z-S, Chen H-M, Yang M-Y, et al. RNA-seq of 272 gliomas revealed a novel, recurrent PTPRZ1-MET fusion transcript in secondary glioblastomas. *Genome Res* 2014;24:1765–1773.
- Patel AP, Tirosh I, Trombetta JJ, et al. Single-cell RNA-seq highlights intratumoral heterogeneity in primary glioblastoma. *Science* 2014;344:1396–1401.
- Shah N, Lankerovich M, Lee H, Yoon J-G, Schroeder B, Foltz G. Exploration of the gene fusion landscape of glioblastoma using transcriptome sequencing and copy number data. *BMC Genomics* 2013;14:818.
- Copois V, Bibeau F, Bascoul-Mollevi C, et al. Impact of RNA degradation on gene expression profiles: Assessment of different methods to reliably determine RNA quality. *J Biotechnol* 2007;127:549–559.
- Imbeaud S, Graudens E, Boulanger V, et al. Towards standardization of RNA quality assessment using user-independent classifiers of microcapillary electrophoresis traces. *Nucleic Acids Res* 2005;33:e56.
- Shi L, Perkins RG, Fang H, Tong W. Reproducible and reliable microarray results through quality control: Good laboratory proficiency and appropriate data analysis practices are essential. *Curr Opin Biotechnol* 2008;19:10–18.
- Atz M, Walsh D, Cartagena P, et al. Methodological considerations for gene expression profiling of human brain. *J Neurosci Methods* 2007;163:295–309.
- Mane SP, Evans C, Cooper KL, et al. Transcriptome sequencing of the Microarray Quality Control (MAQC) RNA reference samples using next generation sequencing. *BMC Genomics* 2009;10:264.
- Shi L, Campbell G, Jones WD, et al. The MicroArray Quality Control (MAQC)-II study of common practices for the development and validation of microarray-based predictive models. *Nat Biotechnol* 2010;28:827–838.
- Strand C, Enell J, Hedenfalk I, Fernö M. RNA quality in frozen breast cancer samples and the influence on gene expression analysis—A comparison of three evaluation methods using microcapillary electrophoresis traces. *BMC Mol Biol* 2007;8:38.
- Micke P, Ohshima M, Tahmasebpour S, et al. Biobanking of fresh frozen tissue: RNA is stable in nonfixed surgical specimens. *Lab Invest* 2006;86:202–211.
- Brimo F, Aprikian A, Latour M, et al. Strategies for biochemical and pathologic quality assurance in a large multi-institutional biorepository: The experience of the PROCURE Quebec Prostate Cancer Biobank. *Biopreserv Biobank* 2013;11:285–290.
- Sun H, Sun R, Hao M, et al. Effect of duration of ex vivo ischemia time and storage period on RNA quality in biobanked human renal cell carcinoma tissue. *Ann Surg Oncol* 2016;23:297–304.
- Hatzis C, Sun H, Yao H, et al. Effects of tissue handling on RNA integrity and microarray measurements from resected breast cancers. *J Natl Cancer Inst* 2011;103:1871–1883.
- Bao W-G, Zhang X, Zhang J-G, et al. Biobanking of fresh-frozen human colon tissues: Impact of tissue ex-vivo ischemia times and storage periods on RNA quality. *Ann Surg Oncol* 2013;20:1737–1744.
- Kleihues P, Cavenee WK. *World Health Organization Classification of Tumours: Pathology and Genetics: Tumours of the Nervous System*. Lyon: IARC press; 2000: 1–8.
- Louis DN, Ohgaki H, Wiestler OD, et al. The 2007 WHO classification of tumours of the central nervous system. *Acta Neuropathol* 2007;114:97–109.
- Julià-Sapé M, Lurgi M, Mier M, et al. Strategies for annotation and curation of translational databases: The eTUMOUR project. *Database (Oxford)* 2012;2012:bas035.
- Castells X, Acebes JJ, Majós C, et al. Robustness of equations that define molecular subtypes of glioblastoma









**UAB**

Universitat Autònoma de Barcelona

Departament de bioquímica  
i biologia molecular